UNIVERSITY OF SOUTHAMPTON

FACULTY OF ENGINEERING AND THE ENVIRONMENT

Aerodynamics and Flight Mechanics

Pressure and velocity fluctuations in wall-bounded turbulent flows

by

Angeliki Laskari

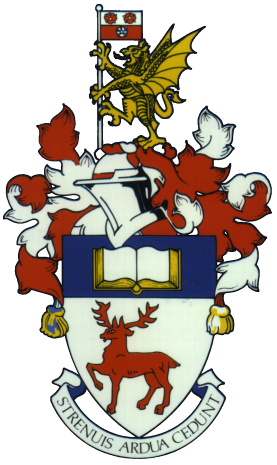

Thesis for the degree of Doctor of Philosophy

June 2017

UNIVERSITY OF SOUTHAMPTON

ABSTRACT

FACULTY OF ENGINEERING AND THE ENVIRONMENT
Aerodynamics and Flight Mechanics

Doctor of Philosophy

PRESSURE AND VELOCITY FLUCTUATIONS IN WALL-BOUNDED TURBULENT FLOWS

by Angeliki Laskari

The purpose of this work is to enhance the understanding of wall-bounded turbulent flows, with respect to both pressure and velocity fluctuations. To this end, time-resolved planar and tomographic PIV experiments were performed in a high-Reynolds-number turbulent boundary layer. Starting at the freestream boundary, the structure and evolution of velocity fluctuations within the boundary layer are analysed using the planar PIV database. Across the turbulent/non-turbulent interface, conditional profiles of velocity, vorticity, and Reynolds stress exhibit clear jumps, within an interface thickness that scales with the local Taylor microscale. The interface is tracked in time and a net positive entrainment rate is estimated, exhibiting an increasing trend for higher wall-normal locations. Below the freestream boundary, the flow is organised into zones of uniform momentum, which are detected instantaneously, while a temporal threshold is then applied to remove non-time-coherent zones. A low number of zones is found to be associated with a large-scale $Q4$ event and a decrease of the turbulent activity in the log region. On the other hand, a higher than average number of zones is linked with a large-scale $Q2$ event and an amplification of the Reynolds stress in the log region. Zones belonging to a low-zone-number structuring are shown to reside within the measurement plane on average four times longer than those belonging to a high-zone-number case. To gain further physical insight, a pressure estimation method is developed, based on Taylor's hypothesis, using both planar and volumetric velocity data without the requirement of time information. The method is validated in the case of a DNS channel flow and is found to be robust to noise and grid resolution, performing as well as a pseudo-Lagrangian approach in the case of volumetric experimental data. A 2D formulation of the proposed method, although performing significantly worse than the 3D one instantaneously, provides reliable results in a statistical sense and allows for pressure estimation also for the planar PIV database. Pressure fluctuations are shown to be correlated almost throughout the boundary layer in the wall-normal direction, while within the log region they convect slightly faster than the velocity fluctuations. A high number of uniform momentum zones is linked with an increase of pressure rms values and a larger coherence of pressure fluctuations both in the streamwise and the vertical direction, while the opposite is observed in a low zone number state.

Contents

Declaration of Authorship **xix**

Acknowledgements **xxi**

Nomenclature **xxiii**

1 The complex nature of wall-bounded turbulent flows **1**
1.1 Velocity field . . . 2
1.1.1 Mean velocity profile . . . 3
1.1.2 Instantaneous velocity/vorticity fields and coherent structures . . . 5
1.1.3 Turbulent/non-turbulent interface . . . 11
1.1.4 Internal layers and uniform momentum zones . . . 15
1.2 Pressure field . . . 16
1.2.1 Why is pressure important in turbulent flows? . . . 16
1.2.2 Direct pressure measurements and numerical simulations . . . 18
1.2.3 Indirect pressure estimation using PIV data . . . 20
1.3 Pressure and velocity in the current work . . . 22

2 Turbulent boundary layer experiments **25**
2.1 Velocity measurement with PIV . . . 25
2.1.1 Principle of operation . . . 25
2.1.2 Seeding . . . 26
2.1.3 Image mapping and calibration . . . 27
2.1.4 Displacement interrogation . . . 29
2.2 Experimental facilities and equipment . . . 30
2.3 Time-resolved planar PIV measurements . . . 32
2.4 Time-resolved tomographic PIV measurements . . . 35
2.4.1 Long vertical field of view ($\approx 2\delta$) . . . 36
2.4.2 Intermediate vertical field of view ($\approx 2/3\delta$) . . . 38

3 Determination of pressure fluctuations from PIV **41**
3.1 Methodology . . . 41
3.1.1 Eulerian approach (EU) . . . 42
3.1.2 Pseudo-Lagrangian approach (pLA) . . . 42
3.1.3 Taylor's hypothesis approach (TH) . . . 43
3.1.4 Taylor's hypothesis using 2D velocity data (TH-2D) . . . 44
3.1.5 Pressure estimation uncertainty . . . 45
3.2 Numerical assessment . . . 48

3.2.1 Numerical set up . . . 49
3.2.2 Convection velocity dependence . . . 50
3.2.3 Time-separation dependence . . . 51
3.2.4 Noise dependence . . . 53
3.2.5 Resolution dependence . . . 55
3.2.6 Pressure Statistics . . . 56
3.3 Experimental assessment - TBL long vertical field of view . . . 58
3.3.1 Instantaneous pressure fields . . . 58
3.3.2 Pressure statistics . . . 60
3.4 Experimental assessment - TBL intermediate vertical field of view . . . 66
3.4.1 Instantaneous pressure fields . . . 66
3.4.2 Pressure statistics . . . 67

4 Velocity fluctuations and entrainment at the freestream boundary 69
4.1 Detection of the freestream boundary . . . 69
4.2 Characteristics of the freestream boundary . . . 71
4.2.1 Geometrical characteristics . . . 71
4.2.2 Conditional statistics across the interface . . . 75
4.3 Entrainment . . . 82
4.3.1 Method Analysis . . . 83
4.3.2 Effects of streamwise extent . . . 84
4.3.3 Entrainment for different interface geometries . . . 87

5 Temporal evolution of velocity fluctuations within the turbulent region 91
5.1 Detection of instantaneous uniform momentum zones . . . 91
5.1.1 Influence of peak detection thresholds . . . 93
5.2 Detection of time-coherent uniform momentum zones . . . 94
5.3 Characteristics of time-coherent uniform momentum zones . . . 96
5.3.1 Velocity range . . . 96
5.3.2 Wall-normal location and thickness . . . 99
5.3.3 Total number of zones . . . 101
5.3.4 $Q2$ and $Q4$ events in the log region . . . 104
5.3.5 Conditional statistics across the internal layers . . . 108
5.3.6 A note on the influence of bin count and time-coherence . . . 111
5.4 Time-scales . . . 114
5.4.1 Number of zones . . . 114
5.4.2 Individual UMZs . . . 117

6 Structure of pressure fluctuations 123
6.1 Spatio-temporal characteristics . . . 123
6.2 Pressure statistics varying with number of UMZs . . . 127
6.3 Pressure statistics across the TNTI and internal layers . . . 130

7 Conclusions and future work 133

List of Figures

2.1 Sketch of a typical planar PIV set-up (from Raffel et al., 2007). 26
2.2 Recirculating water channel. 30
2.3 Laser beam steering. 31
2.4 Schematic (rendering) of the Planar PIV setup. 32
2.5 TBL flow, planar-PIV field ($Re_\tau = 5300$). Pdf of $\mathbf{u}/U_\infty$ for all the vectors below $y = 0.5\delta$ before and after filtering. 33
2.6 TBL flow, planar-PIV field ($Re_\tau = 5300$). Inner normalised mean velocity profile. $\times$ symbols are hotwire data from Hutchins et al. (2009). Solid black line denotes Spalding's law of the wall (Spalding, 1961). 34
2.7 TBL flow, planar-PIV field ($Re_\tau = 5300$). Inner normalised turbulence intensity profiles of the streamwise and wall-normal components and Reynolds shear stress profile. $\times$ symbols are hotwire data from Hutchins et al. (2009). 34
2.8 Schematic (rendering) of the tomo-PIV setup. 36
2.9 Tomo-PIV equipment. 37
2.10 TBL flow, tomo-PIV field ($Re_\tau = 2300$, long vertical field of view). Inner normalised mean velocity profile. Solid black line denotes Spalding's law of the wall (Spalding, 1961). 38
2.11 TBL flow, tomo-PIV field (Intermediate vertical field of view). Experimental setup capture. 39

3.1 Total uncertainty on the pressure estimation following equation (3.12)–(3.14) for all methods (top). Total uncertainty on the pressure estimation for TH with increasing levels of ε_{U_c} and ε_U (bottom). Colours: —— TH, —— EU, —— pLA. 47
3.2 Channel flow, synthetic PIV field ($Re_\tau = 1000$). Different time separations for EU and pLA approaches. 50
3.3 Channel flow, synthetic PIV field ($Re_\tau = 1000$). Convection velocity dependence for TH approach. Streamwise–wall-normal contours of rms error normalised with the dynamic range of the DNS pressure field at each snapshot, and averaged over all snapshots and spanwise locations ($\varepsilon_u/U_{max} = 1\%$, $l^+ = 12$). . 51
3.4 Channel flow, synthetic PIV field ($Re_\tau = 1000$). Average correlation coefficient with varying frame time-separation ($\varepsilon_u/U_{max} = 1\%$, $l^+ = 12$). Colours: —— EU, —— pLA. For pLA the largest timestep yields the best results. The performance of EU increases for moderate timesteps but deteriorates again for the largest timesteps used. 52
3.5 Channel flow, synthetic PIV field ($Re_\tau = 1000$). Average correlation coefficient with varying frame time-separation and noise for EU ($l^+ = 12$). When noise is present in the data a moderate increase in timestep improves the performance, while for zero noise the minimum timestep yields the most accurate results. . . 52

3.6 Channel flow, synthetic PIV field ($Re_\tau = 1000$). Time separation dependence for EU and pLA. Streamwise–wall-normal contours of rms error normalised with the dynamic range of the DNS pressure field at each snapshot, and averaged over all snapshots and spanwise locations ($\varepsilon_u/U_{max} = 0\%$ for EU, $\varepsilon_u/U_{max} = 1\%$ for pLA, $l^+ = 12$). EU performs worse with increasing time separation while pLA shows the opposite behaviour. 53
3.7 Channel flow, synthetic PIV field ($Re_\tau = 1000$). Average correlation coefficient with varying noise level ($dt^+ = 1.28$ for EU and pLA, $U_c = U$ for TH, $l^+ = 12$). Colours: —— TH, - - - TH-2D, —— EU, —— pLA. All methods show decrease in correlation with increasing noise, with TH being the least sensitive to noise and EU suffering the most. TH-2D shows a constant drop of about 40% from the 3D estimation, however it is still robust with respect to noise and outperforms EU for high noise levels. 54
3.8 Channel flow, synthetic PIV field ($Re_\tau = 1000$). Noise dependence for all methods. Streamwise–wall-normal contours of rms error normalised with the dynamic range of the DNS pressure field at each snapshot, and averaged over all snapshots and spanwise locations ($dt^+ = 1.28$ for EU and pLA, $U_c = U$ for TH, $l^+ = 12$). All methods show decrease in accuracy with increasing noise, with TH being the least sensitive to noise and EU suffering the most. 55
3.9 Channel flow, synthetic PIV field ($Re_\tau = 1000$). Average correlation coefficient with varying resolution ($dt^+ = 1.28$ for EU and pLA, $U_c = U$ for TH, $\varepsilon_u/U_{max} = 1\%$). Colours: —— TH, - - - TH-2D, —— EU, —— pLA. Decrease in correlation for lower resolution for all methods with TH showing the slowest decrease. TH-2D has the lowest accuracy for the finest grid, however performs better than either EU or pLA for the coarsest one. 56
3.10 Channel flow, synthetic PIV field ($Re_\tau = 1000$). Resolution dependence fot all methods. Streamwise–wall-normal contours of rms error normalised with the dynamic range of the DNS pressure field at each snapshot, and averaged over all snapshots and spanwise locations ($dt^+ = 1.28$ for EU and pLA, $U_c = U$ for TH, $\varepsilon_u/U_{max} = 1\%$). 57
3.11 Channel flow, synthetic PIV field ($Re_\tau = 1000$). Rms pressure normalised with inner variables for all methods ($dt^+ = 1.28$ for EU and pLA, $U_c = U$ for TH, $l^+ = 12$). ■ TH, ○ TH-2D, ■ EU, ■ pLA, —— DNS. 57
3.12 Channel flow, synthetic PIV field ($Re_\tau = 1000$), pressure volumes. Comparison of best performance for all methods ($\varepsilon_u/U_{max} = 0\%$, $l^+ = 12$). 58
3.13 TBL flow, tomo-PIV field ($Re_\tau = 2300$, long vertical field of view). Contour plots of pressure for all methods. Flow is from left to right, axes as appearing on the left, each 200^+ long. TH seems to be the least affected by noise and EU the most while pLA performs much better for very large timesteps but the resulting volume is greatly reduced. 59
3.14 TBL flow, tomo-PIV field ($Re_\tau = 2300$, long vertical field of view). Rms pressure, normalised with inner variables, using EU. (a) Results for increasing frame separation ($dt^+ = 0.38 - -11.4$). (b) Same results translated downwards using a reference pressure and replotted together with DNS (Sillero et al., 2013, 2014; Borrell et al., 2013; Simens et al., 2009) at $Re_\theta = 5000$ ($Re_\tau = 1460$) and $Re_\theta = 6500$ ($Re_\tau = 1990$), solid lines. 61

3.15 TBL flow, tomo-PIV field ($Re_\tau = 2300$, long vertical field of view). Rms pressure, normalised with inner variables, using pLA together with DNS results (Sillero et al., 2013, 2014; Borrell et al., 2013; Simens et al., 2009) at $Re_\theta = 5000$ ($Re_\tau = 1460$) and $Re_\theta = 6500$ ($Re_\tau = 1990$), solid lines. (a) Results for increasing frame separation ($dt^+ = 7.6 - 22.8$). (b) Zoomed-in region in (a) showing increasing time-scales with increasing y^+. 62

3.16 TBL flow, tomo-PIV field ($Re_\tau = 2300$, long vertical field of view). Rms pressure, normalised with inner variables, using TH together with DNS results (Sillero et al., 2013, 2014; Borrell et al., 2013; Simens et al., 2009) at $Re_\theta = 5000$ ($Re_\tau = 1460$) and $Re_\theta = 6500$ ($Re_\tau = 1990$), solid lines. 63

3.17 TBL flow, tomo-PIV field ($Re_\tau = 2300$, long vertical field of view). Average error (in %) of all methods with respect to DNS results. ♦ TH, —■— EU, —■— pLA. For pLA a moderate timestep $\sim dt^+ = 10$ yields the best results, even though for larger timesteps the error remains at similar – albeit a bit higher – levels. The performance of EU improves for moderate timesteps but deteriorates again for the largest timesteps used. TH is not time dependent and shows quite low error levels 64

3.18 TBL flow, tomo-PIV field ($Re_\tau = 2300$, long vertical field of view). Comparison of all methods together with DNS results (solid lines) (Sillero et al., 2013, 2014; Borrell et al., 2013; Simens et al., 2009). ■ TH, ○ TH-2D, ■ EU, ■ pLA. TH seems to be the least affected by noise while pLA performs much better for large timesteps ($dt^+ = 11.4$) but the resulting volume is greatly reduced. TH-2D also provides reliable pressure values in a statistical sense. 66

3.19 TBL flow, tomo-PIV field ($Re_\tau = 5300$, intermediate vertical field of view). Contour plots of pressure for all methods. Flow is from left to right, axes as appearing on the left, each 200^+ long. TH seems to be the least affected by noise and EU the most while pLA performs much better for very large timesteps but the resulting volume is greatly reduced. 67

3.20 TBL flow, tomo-PIV field ($Re_\tau = 5300$, intermediate vertical field of view). Comparison of all methods together with direct pressure measurement results (×, Tsuji et al., 2007). ■ TH, ○ TH-2D, ■ EU, ■ pLA. TH seems to be the least affected by noise while pLA performs much better for large timesteps ($dt^+ = 19$) but the resulting volume is greatly reduced. TH-2D shows again a good statistical representation of the pressure values. 68

4.1 TBL flow, planar-PIV field ($Re_\tau = 5300$). (a) Average kinetic energy deficit, $\overline{K}$ with wall normal location. Red dashed lines indicate the region where $\overline{K}$ is approximately constant in the freestream. (b) Variation of the intermittency profile with K_{th}. Fully turbulent flow at $\gamma = 0$, while no turbulent activity is considered at the limit of $\gamma = 1$. Solid red line marks the chosen threshold $K_{th} = 0.26$ and dashed red line denotes the boundary layer thickness above which the kinetic energy deficit profile should be approximately constant. 70

4.2 TBL flow, planar-PIV field ($Re_\tau = 5300$). Variation of statistics with K_{th} (open circles). (a) Mean TNTI location, Y_i. (b) $Y_i + 3\sigma_i$. Solid red circles denote the chosen threshold $K_{th} = 0.26$. 71

4.3 TBL flow, planar-PIV field ($Re_\tau = 5300$). Pdf of TNTI location, Y_i. Dashed line denotes the corresponding Gaussian distribution with $\mu = Y_i$, $\sigma = \sigma_i$. Dotted-dashed line denotes $Y_i = 0.58\delta$. 72

4.4 TBL flow, planar-PIV field ($Re_\tau = 5300$). Velocity contours of a single snapshot. The TNTI is marked with grey solid line, while the streamwise (L_x) and wall-normal (L_y) extent of the interface are shown in black. 73
4.5 TBL flow, planar-PIV field ($Re_\tau = 5300$). Pdf of total length, when normalised with (a) the streamwise extent, L_x and (b) the wall-normal extent, L_y. Dashed lines denote mean values, solid yellow lines mark lognormal fits. 74
4.6 TBL flow, planar-PIV field ($Re_\tau = 5300$). Temporal autocorrelation of L_s/L_x and L_s/L_y. 74
4.7 TBL flow, planar-PIV field ($Re_\tau = 5300$). Joint pdf of average TNTI location, $\overline{y_i}^s$ with total length, when normalised with (a) the streamwise extent, L_x and (b) the wall-normal extent, L_y. Dashed lines denote mean values. 75
4.8 TBL flow, planar-PIV field ($Re_\tau = 5300$). Conditionally averaged flow statistics across the interface, y_i. Coloured region indicates the vorticity thickness, δ_ω, estimated following Chauhan et al. (2014a). (a) Streamwise velocity, $\langle \tilde{U} \rangle / U_\infty$. (b) Wall-normal velocity, $\langle \tilde{V} \rangle / U_\infty$. (c) Out-of-plane vorticity, $\langle \tilde{\Omega}_z \rangle \delta / U_\infty$. (d) Reynolds stress, $\langle u'v' \rangle / {U_\tau}^2$. 76
4.9 TBL flow, planar-PIV field ($Re_\tau = 5300$). Vorticity jump, δ_ω/δ, with Reynolds number from Chauhan et al. (2014b). Present data denoted with ♦. 78
4.10 TBL flow, planar-PIV field ($Re_\tau = 5300$). Conditionally averaged flow statistics across the interface, conditioned upon the average interface location at each snapshot, $\overline{y_i}^s$: ♦ for $\overline{y_i}^s \geq 0.75\delta$, ♦ for $0.45 \leq \overline{y_i}^s < 0.75\delta$, and ♦ for $\overline{y_i}^s < 0.45\delta$. Coloured region indicates the global vorticity thickness, δ_ω. Dashed lines indicate the global averages in figure 4.8. (a) Streamwise velocity, $\langle \tilde{U} \rangle|_{\overline{y_i}^s} / U_\infty$. (b) Wall-normal velocity, $\langle \tilde{V} \rangle|_{\overline{y_i}^s} / U_\infty$. (c) Out-of-plane vorticity, $\langle \tilde{\Omega}_z|_{\overline{y_i}^s} \rangle \delta / U_\infty$. (d) Reynolds stress, $\langle u'v' \rangle|_{\overline{y_i}^s} / {U_\tau}^2$. 79
4.11 TBL flow, planar-PIV field ($Re_\tau = 5300$). Number of $Q2$ and $Q4$ events across the TNTI as a percentage of the total number of uv events at each wall-normal location. (a) $Q2$ and $Q4$ events for all time instances. (b) Percentage of $Q2$ events conditioned upon the average interface location at each snapshot, $\langle N_{Q2} \rangle|_{\overline{y_i}^s}$. (b) Percentage of $Q4$ events conditioned upon the average interface location at each snapshot, $\langle N_{Q4} \rangle|_{\overline{y_i}^s}$: ♦ for $\overline{y_i}^s \geq 0.75\delta$,♦ for $0.45 \leq \overline{y_i}^s < 0.75\delta$, and ♦ for $\overline{y_i}^s < 0.45\delta$. 81
4.12 TBL flow, planar-PIV field ($Re_\tau = 5300$). Velocity contours and interface outline at time t and $t + dt$ with and without subtracting local advection. (a) Velocity contours and interface outline at time t (black solid line). (b) Velocity contours and interface outline at time $t + dt$ (brown solid line). (b) Velocity contours at time t and interface outline at time $t + dt$ when the local advection is subtracted (green solid line). 84
4.13 TBL flow, planar-PIV field ($Re_\tau = 5300$). (a) Pdf of normalised length, L_{s_i}/L_{x_i}, with varying streamwise extent. Blue arrows indicate decrease of ΔL_x from 0.03δ to 0.5δ. (b) Variation of $\overline{L_{s_i}}$ with $\overline{L_{x_i}}$ for $\Delta L_x : 0.03\delta - 0.5\delta$. Dashed line indicates linear fit for $\overline{L_{s_i}}$ and dot-dashed line shows the unit slope of $\overline{L_{x_i}}$ for comparison. (c) Variation of $\overline{L_{s_i}/L_{x_i}}$ with $\overline{L_{x_i}}$ for $\Delta L_x : 0.03\delta - 0.5\delta$ (linear fit marked with dashed line). 85

4.14 TBL flow, planar-PIV field ($Re_\tau = 5300$). (a) Pdf of inner normalised entrainment velocity v_n^+ for $\Delta L_x : 0.03\delta - 0.5\delta$. Blue arrow indicates increase in the number of segments and a Gaussian fit is marked with red solid line. (b) Variation of the average entrainment velocity, $\overline{v_n}$ for $\Delta L_x : 0.03\delta - 0.5\delta$. Dashed line indicates average mass flux rate as estimated in Chauhan et al. (2014a) (see equation 4.4). 86

4.15 TBL flow, planar-PIV field ($Re_\tau = 5300$). Joint pdfs of the mass flux rate, $\dot{M}$ with (a) the average TNTI location at each time instance $\overline{y_i}^s$, (b) the interface length normalised with the streamwise interface extent, L_s/L_x, and (c) the interface length normalised with the wall-normal interface extent, L_s/L_y. Dashed lines indicate average values. 87

5.1 TBL flow, planar-PIV field ($Re_\tau = 5300$). Pdf of U/U_∞ for two independent snapshots. Detected peaks denoted with $\times$. 92

5.2 TBL flow, planar-PIV field ($Re_\tau = 5300$). Pdf of the total number of peaks detected, following a snapshot (black symbols) and a time-resolved (grey symbols) approach. 92

5.3 TBL flow, planar-PIV field ($Re_\tau = 5300$). Contours of the average number of peaks detected, with varying minimum peak height, minimum peak distance and minimum peak threshold (prominence from neighbouring points) in the peak-detection algorithm. 94

5.4 TBL flow, planar-PIV field ($Re_\tau = 5300$). Contour plot of the time evolution of the pdf of U/U_∞ for 300 consecutive images. (a) Red $\times$ symbols denote all detected modal velocities. (b) Modal peaks that have time-scales shorter than $\tau^+ \approx 20$ are removed and all remaining peaks are coloured separately. 95

5.5 TBL flow, planar-PIV field ($Re_\tau = 5300$). Classification system based on zone rank. The zone closest to the freestream is defined as rank one (▲, R_1) while the others below it follow in ascending order. (a) Pdf of U/U_∞ for an instantaneous velocity field with $N_{UMZ} = 4$. Grey dashed lines mark the internal layers that distinguish the different UMZs and the modal velocity of each zone is marked with coloured symbols according to rank. $\times$ symbol denotes an instantaneously detected, short-lived peak that was discarded. (b) Velocity contours of the same velocity snapshot as in (a). Black solid lines denote the boundaries of each zone while the TNTI is marked with grey. 97

5.6 TBL flow, planar-PIV field ($Re_\tau = 5300$). Mean values and extent of the pdf of the normalised modal velocities, varying with the total number of UMZs detected, N_{UMZ}. (a,b) Classification based on momentum deficit, $(U_\infty - U_m)/U_\tau$: ◄ 0-6, ■ 6-12, ► 12-18. (a) Symbols denote mean values and solid lines the pdf extent, taken at a constant height of 3 (grey dashed line on subfigure b). Grey coloured symbols denote the mean and extent of the example distribution shown in (b). UMZs with low momentum deficit show little variation with increasing N_{UMZ}, while the group of the largest deficit moves to lower modal velocities as new zones appear close to the wall. (c,d) Classification based on zone rank. Symbols as in figure 5.5. Pdf extent taken at a constant height of 4 (grey dashed line in subfigure d). Grey coloured symbols denote the mean and extent of the example distribution shown in (d). All ranks move to higher modal velocities as N_{UMZ} increases. 98

5.7 TBL flow, planar-PIV field ($Re_\tau = 5300$). Mean values and extent of the pdf of the normalised wall-normal location, varying with the total number of UMZs detected N_{UMZ}. Colours and symbols as in figure 5.6. (a, b) Classification based on momentum deficit, $(U_\infty - U_m)/U_\tau$. Pdf extent taken at a constant height of 11 (grey dashed line in subfigure b). For an increase in N_{UMZ}, the zones with the lowest momentum deficit move to higher wall-normal locations, to account for the newest ones that appear near the wall. (c, d) Classification based on zone rank, pdf extent taken at a constant height of 10 (grey dashed line in subfigure d). Only the first three ranks are shown for clarity, however the trend is similar for all following ranks. All ranks move upwards while new zones of higher rank appear below them. 99

5.8 TBL flow, planar-PIV field ($Re_\tau = 5300$). Mean values and extent of the pdf of the normalised zone thickness, varying with the total number of UMZs detected, N_{UMZ}. Colours and symbols as in figure 5.6. (a, b) Classification based on momentum deficit, $(U_\infty - U_m)/U_\tau$. Pdf extent, taken at a constant height of 12 (grey dashed line in subfigure b). (c, d) Classification based on zone rank, pdf extent taken at a constant height of 12 (grey dashed line in subfigure d). Only the first three ranks are shown for clarity, however the trend is similar for all following ranks. Both systems show similar trends of decreasing thickness with increasing N_{UMZ}. Zones close to the wall have shorter wall-normal extent on average and with a much narrower distribution around it. 100

5.9 TBL flow, planar-PIV field ($Re_\tau = 5300$). Variation of the mean location of the TNTI, $\overline{Y}_i$, with the number of UMZs detected below it. Colour gradient from dark to light denotes increasing number of time-coherent zones. Open symbols mark results before applying the temporal threshold. Red dotted line denotes the global average location of the TNTI. 101

5.10 TBL flow, planar-PIV field ($Re_\tau = 5300$). Conditionally averaged statistics with varying number of UMZs present in the flow. Blue arrows indicate increasing number of zones (from 1 to 8). (a) Outer normalised mean streamwise velocity profile. (b) Difference from global streamwise average. (c) Outer normalised mean wall-normal velocity profile. (b) Difference from global wall-normal average. (e) Root-mean-square profile of the Reynolds shear stress. (f) Difference from global Reynolds stress profile. 102

5.11 TBL flow, planar-PIV field ($Re_\tau = 5300$). Streamwised averaged velocity profiles for two different snapshots representing a large-scale $Q2$ (a, b) and $Q4$ (c, d) event at the log region. 105

5.12 TBL flow, planar-PIV field ($Re_\tau = 5300$). Pdf of residence times within the FOV; ■ for $Q2$ events and ■ for $Q4$ events. 106

5.13 TBL flow, planar-PIV field ($Re_\tau = 5300$). Pdf of the average number of zones present in the flow, $\overline{N}_{UMZ}$, for varying TNTI location, $\overline{Y}_i$ and magnitude of log-region events. Average number of zones (a) and pdf of realisations for large-scale $Q2$, $Q4$ events in the log region (b). In total, they occur in 74% of all cases. Average number of zones (c) and pdf of realisations (d), for large-scale $Q1$, $Q3$ events in the log region (26% of all cases). For all plots, events on the left represent lower than average streamwise velocities, while the opposite holds for events on the right. 107

5.14 TBL flow, planar-PIV field ($Re_\tau = 5300$). Conditionally averaged flow statistics across the internal layers that bound each UMZ. Dashed lines indicate the profiles across the TNTI (see chapter 4). (a) $\langle \tilde{U} \rangle / U_\infty$ (b) $\langle \tilde{V} \rangle / U_\infty$ (c) $\langle \tilde{\Omega}_z \rangle \delta / U_\infty$ (d) $\langle u'v' \rangle / {U_\tau}^2$. 109

5.15 TBL flow, planar-PIV field ($Re_\tau = 5300$). Number of $Q2$ and $Q4$ events across the internal layers that bound each UMZ as a percentage of the total number of vectors averaged at each wall-normal location. 111
5.16 TBL flow, planar-PIV field ($Re_\tau = 5300$). Pdf of U/U_∞ for two independent velocity snapshots representing lower and higher than average TNTI location and how that infulences the detection of modal peaks. Red and green triangles denote peaks with streamwise extent below and above the defined threshold respectively. White lines mark the local minimum between two consecutive peaks. (a) $\overline{Y}_i = 0.46\delta$. (b) $\overline{Y}_i = 0.98\delta$. 112
5.17 TBL flow, planar-PIV field ($Re_\tau = 5300$). Difference in vector counts, $\Delta N = N_{peak} - N_{min}$, between the modal peaks in figure 5.16 and the greater of the two local minima that surround them. Grey lines mark the uncertainty on the detection of each peak, defined as $\sqrt{N_{peak} + N_{min}}$. (a) $\overline{Y}_i = 0.46\delta$. (b) $\overline{Y}_i = 0.98\delta$. 113
5.18 TBL flow, planar-PIV field ($Re_\tau = 5300$). Conditionally averaged velocities for each characteristic region. (b) Difference from global streamwise average. (c) Difference from global wall-normal average. Colours denote the classification of N_{UMZ} into three characreistic regions: ■ for $N_{UMZ} < 3$,■ for $3 \leq N_{UMZ} < 5$,■ for $N_{UMZ} \geq 5$. 114
5.19 TBL flow, planar-PIV field ($Re_\tau = 5300$). (a) Time-evolution of the number of time-coherent peaks for the same 300 consecutive images as in figure 5.4. Background colours denote the classification of N_{UMZ} into the three regions defined in figure 5.4. Examples of how long a high number of zones resides within the measurement plane, τ_w^+, and how often it reappears, τ_f^+, denoted with black. (c,d) For how long, on average, the boundary layer is structured into a certain number of zones (left) and the frequency of repetition of this structuring (right). Squares denote each number of zones independently and triangles each group of zones: ▼ for $3 < N_{UMZ}$,▼ for $3 \leq N_{UMZ} < 5$,▼ for $N_{UMZ} \geq 5$. Solid lines mark the range of each group. Dashed lines denote the time (left) and frequency (right) for which the boundary layer is structured in an average or high number zones (⧫) or in a low or average number of zones (⧫). 116
5.20 TBL flow, planar-PIV field ($Re_\tau = 5300$). Pdf of the number of zones at time $t + dt$, based on the number of zones at time t. Grey dots denote data-points. Linear interpolation was used on a finer mesh for visual clarity. 117
5.21 TBL flow, planar-PIV field ($Re_\tau = 5300$). Frequency of appearance of time-coherent UMZs (in % of the total), depending on their residence time, τ. Dashed line denotes average residence time. 118
5.22 TBL flow, planar-PIV field ($Re_\tau = 5300$). UMZs are classified according to whether they reach at least once during their residence time, τ, a modal velocity, U_m belonging to each of the three shown velocity bands. (a) Frequency of appearance of UMZs within each velocity band (in % of the total UMZs within that band), depending on their residence time. Each UMZ might contribute to multiple bands, only once to each, according to the different modal velocities it corresponds to during its residence time. Dashed lines denote the average residence time of UMZs within each band. (b) Duration of observation of UMZs within each velocity band (in % of the total observation time of all UMZs within that band) according to their residence time. Each UMZ might contribute to multiple bands, every time it reaches a modal velocity belonging to any of them. Dashed lines denote the average observation time of UMZs in each group. . . . 119

5.23 TBL flow, planar-PIV field ($Re_\tau = 5300$). UMZs are classified according to whether they encounter at least once during their residence time, τ, any of these zone-groups: —— for $\overline{N}_{UMZ} < 3$, —— for $3 \leq \overline{N}_{UMZ} < 5$, —— for $\overline{N}_{UMZ} \geq 5$. (a) Frequency of appearance of UMZs, within each zone-number group (in % of the total within that group), depending on their residence time. Each UMZ might contribute to multiple groups, only once to each, according to the number of other zones appearing and dying away during its residence time. Dashed lines denote the average residence time of UMZs within each group. (b) Duration of observation of UMZs within each zone-number group (in % of the total observation time of all UMZs within that group) according to their residence time. Each UMZ might contribute to multiple groups, every time it encounters them. Dashed lines denote the average observation time of UMZs in each group. . . . 120

6.1 TBL flow, planar-PIV field ($Re_\tau = 5300$). (a) Probability density function (pdf) contours of inner-normalised pressure fluctuations, varying with distance from the wall. (b) Pdf profiles of inner-normalised pressure fluctuations for two wall normal locations: $y^+ = 108$ (grey symbols) and $y/\delta = 0.5$. 124

6.2 TBL flow, planar-PIV field ($Re_\tau = 5300$). Contours of constant two-point correlations of pressure fluctuations R_{pp}, as a function of streamwise and wall-normal separations for $y^+ = 108$, $y^+ = 350$, $y/\delta = 0.2$, $y/\delta = 0.5$, and $y/\delta = 1$. Contour levels ranging from 0.2 to 1 with spacing of 0.1. The maximum streamwise (Λx), and wall-normal (Λy) extents, estimated for a correlation level of 0.3, are also schematically drawn. 124

6.3 TBL flow, planar-PIV field ($Re_\tau = 5300$). Maximum extents of pressure correlations (shown schematically in figure 6.2), varying with distance from the wall.(a) Maximum streamwise (Λx) and (b) wall-normal extent (Λy). Dashed lines denote approximate pinch-off location from the wall. 125

6.4 TBL flow, planar-PIV field ($Re_\tau = 5300$). Contours of constant two-point correlations of total pressure fluctuations as a function of time and streamwise separation for $y^+ = 108$, $y^+ = 350$, $y/\delta = 0.2$, $y/\delta = 0.5$, and $y/\delta = 1$. Contour levels ranging from 0.2 to 1 with spacing of 0.1. 126

6.5 TBL flow, planar-PIV field ($Re_\tau = 5300$). Average convection velocities of pressure fluctuations varying with distance from the wall, estimated from a linear fit of the two-point correlation contours in figure 6.4. The mean velocity profile is marked with dashed line. 126

6.6 TBL flow, planar-PIV field ($Re_\tau = 5300$). Conditionally averaged pressure statistics based on the number of UMZs in the boundary layer, N_{UMZ}. (a) Inner-normalised rms pressure and difference from global rms pressure (b). Pressure rms values are computed with respect to the global time-averaged pressure field. 127

6.7 TBL flow, planar-PIV field ($Re_\tau = 5300$). Contours of constant two-point correlations of total pressure fluctuations, as a function of streamwise and wall-normal separations, conditioned upon the number of zones present in the boundary layer, N_{UMZ}, for $y^+ = 108$, $y^+ = 350$, $y/\delta = 0.2$, $y/\delta = 0.5$, and $y/\delta = 1$. (a) $N_{UMZ} < 3$. (b) $3 \leq N_{UMZ} < 5$. (c) $N_{UMZ} \geq 5$. Contour levels ranging from 0.2 to 1 with spacing of 0.1. Pressure fluctuations are computed with respect to the global time-averaged pressure field. 128

6.8 TBL flow, planar-PIV field ($Re_\tau = 5300$). Maximum extents of pressure correlations (shown schematically in figure 6.7), varying with distance from the wall and conditioned on N_{UMZ}. (a) Maximum streamwise (Λx) extent. (b) Maximum wall-normal extent (Λy). Dot-dashed horizontal lines denote approximate pinch-off location from the wall. Dashed lines denote the global values for the wall-normal and stremawise extents as were presented in figure 6.6. 129

6.9 TBL flow, planar-PIV field ($Re_\tau = 5300$). Conditionally averaged pressure fluctuations, $\langle \tilde{p} \rangle$, across the TNTI (a), conditioned upon the average interface location at each snapshot, $\overline{y_i}^s$ and across the internal layers (b) that bound each UMZ (see also chapter 5). Dashed lines indicate the global average across the TNTI. . 130

List of Tables

2.1 TBL flow, planar-PIV field ($Re_\tau = 5300$). Nominal flow conditions and processing parameters. 33
2.2 TBL flow, tomo-PIV field ($Re_\tau = 2300$, long vertical field of view). Nominal flow conditions and processing parameters. 37
2.3 TBL flow, tomo-PIV field ($Re_\tau = 5300$, intermediate vertical field of view). Nominal flow conditions and processing parameters 39

3.1 Channel flow, synthetic PIV field ($Re_\tau = 1000$), simulation Parameters. 48
3.2 Channel flow, synthetic PIV field ($Re_\tau = 1000$), grid spacing. 48
3.3 Channel flow, synthetic PIV field ($Re_\tau = 1000$), resolutions tested. 49
3.4 Channel flow, synthetic PIV field ($Re_\tau = 1000$). Average performance measures for different convection velocities ($\varepsilon_u/U_{max} = 1\%$, $l^+ = 12$). Using the streamwise mean velocity as the convection velocity yields the best results. 51

4.1 TBL flow, planar-PIV field ($Re_\tau = 5300$). Velocity jump and vorticity thickness for different wall-normal locations. Taylor microscale, λ_τ, estimated for each wall normal location as $\sqrt{\overline{u'^2}/\overline{(\partial u/\partial x^2)}}$. 78

5.1 TBL flow, planar-PIV field ($Re_\tau = 5300$). Velocity jump and vorticity thickness for internal layers bounding different zone ranks. Taylor microscale, λ_τ, estimated for each average wall-normal location as $\sqrt{\overline{u'^2}/\overline{(\partial u/\partial x^2)}}$. 110

Declaration of Authorship

I, Angeliki Laskari , declare that the thesis entitled *Pressure and velocity fluctuations in wall-bounded turbulent flows* and the work presented in the thesis are both my own, and have been generated by me as the result of my own original research. I confirm that:

- this work was done wholly or mainly while in candidature for a research degree at this University;
- where any part of this thesis has previously been submitted for a degree or any other qualification at this University or any other institution, this has been clearly stated;
- where I have consulted the published work of others, this is always clearly attributed;
- where I have quoted from the work of others, the source is always given. With the exception of such quotations, this thesis is entirely my own work;
- I have acknowledged all main sources of help;
- where the thesis is based on work done by myself jointly with others, I have made clear exactly what was done by others and what I have contributed myself;
- parts of this work have been published as: Laskari et al. (2014), Laskari et al. (2015) and Laskari et al. (2016)

Signed:.....

Date:.....

Acknowledgements

'Gratitude is one of the least articulate of the emotions, especially when it is deep.'

Felix Frankfurter

First of all I would like to thank my two supervisors, Prof. Bharathram Ganapathisubramani and Dr. Roeland de Kat, for their invaluable support throughout my PhD. This work would not have been possible without their guidance and expertise, unending patience, but mostly their faith in me, through the good and bad. I would like to thank them for challenging me constantly, giving me the freedom to work on things that inspired me and, despite my great reluctance, present the work in public in various occasions. It allowed me to be bolder, grow as a researcher and 'own the work', or well, at least aspire to.

Throughout these four years I was lucky to be part of a great group of people, who helped me one way or another in this journey, so I am grateful to all members of 'Bgroup', past and present. Especially I would like to thank Jacques, with whom we started together and who was always there to help with experiments, bike emergencies, software issues or a beer after a long day. Eda, the other member of our turbulence team, for the constant support in matters of work or life and a great listener for all kinds of philosophical discussions or complaints. Laura, for the great cultural trips and outings, that made me move out of the office once in a while and appreciate British culture. Apostolis and Vagia who made life here much more fun and less stressful the past two years. Thank you Sonia and Sonia, Rammah and Tim, residents of the Wilton Road flat for all the bbqs, and all my office mates from both the second and fifth floor office for making the long hours of work more enjoyable. I would like to thank Jason for introducing me to uniform momentum zones, a topic that became my biggest interest and focus in this work, and pushing me to think a little more positive about science in general. Special thanks to all the technicians of Tizard building for their help with various experimental problems, that invariably arise in any experimental lab. Thank you to both Alex and Jacob, for all the effort and great collaborative work in demonstrating the Aerolab for three consecutive years, it was a great experience.

This work comes at the end of a much longer journey, each part of which was a learning experience, thanks to all the people that I met along the way. Special thanks should go to all the members of the CSE lab in Zurich and especially Christian, Jana, Gery and of course Sena for making that experience an unforgettable one. Going back to where this all started in Greece, I cannot thank enough Prof. Lambros Kaiktsis from the NTUA in Athens, for his never-ending support and advice, and mostly for setting an example of work ethic and exceptional character, being a great inspiration throughout all these years.

Last but not least, I would like to thank the quiet but unwavering support of my family and friends, for putting up with me all this time, regardless of how far or how busy I was. I would not be even halfway here without all of you. Finally, I would like to thank Kimon for teaching me to look at the unknown with a little less fear.

Nomenclature

Flow Parameters

x	Streamwise direction
y	Wall-normal direction
z	Spanwise direction
$\mathbf{u}$	Velocity vector
u	Streamwise velocity component
v	Wall-normal velocity component
w	Spanwise velocity component
$\mathbf{U}$	Mean velocity vector
U	Mean streamwise velocity component
V	Mean wall-normal velocity component
W	Mean spanwise velocity component
$\mathbf{u}'$	Fluctuating velocity vector
u'	Fluctuating streamwise velocity component
v'	Fluctuating wall-normal velocity component
w'	Fluctuating spanwise velocity component
$u'v'$	Reynolds stress
$\mathbf{U_c}$	Convection velocity of velocity fluctuations
U_τ	Friction velocity ($\sqrt{\tau_w/\rho}$)
U_∞	Freestream velocity
U_b	Bulk velocity, channel flow
U_{ctr}	Centreline velocity, channel flow
p	Fluctuating pressure
δ	Boundary layer thickness
δ^*	Boundary layer displacement thickness
κ	Von Kármán constant
B	Additive constant of the log-law of the wall
ν	Kinematic viscosity
ρ	Density
τ_w	Wall shear stress
λ_τ	Taylor microscale

Re_τ Friction Reynolds number ($\frac{\delta \cdot U_\tau}{\nu}$)
Re_θ Momentum thickness Reynolds number ($\frac{\theta \cdot U_\infty}{\nu}$)

Superscripts

$+$ Inner/viscous scaling (wall units) using u_τ and ν

Performance Assessment Measures

r_{p_i} Correlation coefficient between exact and estimated pressure field

Uncertainty Analysis

ε_u Uncertainty on the instantaneous velocity field
ε_U Uncertainty on the mean velocity field
ε_{U_c} Uncertainty on the convection velocity field

Seeding Particles, Imaging and Illumination

d_p Particle diameter
ρ_p Particle density
$\mathbf{u}_p$ Particle velocity
d_τ Image particle diameter
d_s Diffraction limited image particle diameter
d_a Aberration limited image particle diameter
d_r Pixel size
d_z Depth of field
Δz_0 Laser sheet thickness
M_0 Magnification factor
λ Light source wavelength
$f^\#$ Lens f-number
F Point-wise image mapping function
$\hat{F}$ Analytical image mapping function
$R(\mathbf{s})$ Interrogation window correlation function
$\mathbf{s}$ Window displacement
I Image intensity

DNS and PIV Parameters

Δx^+ Streamwise grid spacing
Δy^+ Wall-normal grid spacing

Δz^+	Spanwise grid spacing
h	PIV grid spacing
dt	timestep
L_x	Streamwise domain length
L_y	Wall-normal domain length
L_z	Spanwise domain length
N_x	DNS streamwise grid wavemodes
N_y	DNS wall-normal grid wavemodes
N_z	DNS spanwise grid wavemodes
l^+	PIV interrogation volume size in wall units
${l_v}^+$	PIV voxel size in wall units
n	Time separation between frames in number of time steps

Turbulent/non-turbulent interface and uniform momentum zones

L_s	Total interface length
L_y	Wall-normal interface extent
y_i	Wall-normal interface location
Y_i	Average wall-normal interface location for all snapshots
$\overline{y_i}^s$	Average wall-normal interface location per snapshot
δ_ω	Vorticity thickness
K	Kinetic energy deficit
K_{th}	Kinetic energy deficit threshold
γ	Intermittency of the interface
$\langle \tilde{U} \rangle$	Conditional streamwise velocity across the interface
$\langle \tilde{V} \rangle$	Conditional vertical velocity across the interface
$\langle \tilde{\Omega}_z \rangle$	Conditional spanwise vorticity across the interface
$\langle \tilde{u}'\tilde{v}' \rangle$	Conditional Reynolds stress across the interface
$\Delta\langle \tilde{U} \rangle$	Streamwise velocity jump
$Q1$	First quadrant, outward event
$Q2$	Second quadrant, ejection event
$Q3$	First quadrant, inward event
$Q4$	Fourth quadrant, sweep event
$\dot{M}$	Mass flux rate across the interface
v_n	Entrainment velocity across the interface
N_{UMZ}	Number of uniform momentum zones
$\overline{Y}_{UMZ}$	Average wall-normal location of uniform momentum zones
$\bar{t}_{UMZ}$	Average thickness uniform momentum zones
τ_w	Residence time of a certain number of zones within the field of view
τ_f	Frequency of re-appearance of a certain number of zones within the field of view
Λx	Maximum extent of streamwise correlation

Λ_y	Maximum extent of wall-normal correlation

Chapter 1

The complex nature of wall-bounded turbulent flows

Turbulence is a chaotic, unsteady state of a flow and a representative example of an unsolved fundamental phenomenon in fluid mechanics. It is present in almost all flows in nature and even though its manifestation was observed and described very early and its governing equations have been known since 1845 (Davidson, 2004), its sheer physical complexity and unpredictable nature renders a mathematical analysis – and therefore a thorough study – quite challenging. Apart from the physical insight itself, the interest in turbulence also stems from the impact it has on a large field of engineering applications, especially with respect to drag reduction and energy efficiency.

In this context, one main point of focus is wall-bounded turbulent flows. When a solid body is present within a flow, the velocity of the fluid drops to zero at the solid boundary and reaches a freestream value at a distance δ from the wall. This thin layer of fluid is the boundary layer and δ its thickness. The majority of the drag a body immersed in a fluid experiences comes from the velocity gradient present in this layer. Therefore, any advances on its physical understanding would certainly improve the rapidly developing energy efficiency strategies that are based on drag control and reduction. However, the boundary layer's structure and evolution especially when turbulent, are issues still unresolved and often points of controversy within the research community. The goal of this project is to shed more light into some of these, still obscure, aspects of wall-bounded turbulent flows.

To accomplish this, experimental and numerical work has been carried out, aimed towards directly measuring or indirectly estimating velocity and pressure fields in different kinds of wall-bounded flows. These two quantities are essential to the description of an incompressible flow however, for complex geometries and flow conditions, no mathematical analysis, numerical simulation or experiment has been able to predict (or measure) them both. The most sophisticated and advanced experimental techniques are able to provide, at best, an estimate for the velocity field in quite limited volumes together with point-wise wall pressure measurements. Using

direct numerical simulations (DNS), the most accurate but also most expensive computational method, both fields can be extracted but the solutions are severely restricted in low Reynolds numbers and simple geometries. It is obvious that, in terms of experimental and numerical advances, the interest lies in breaking these boundaries by increasing the available computational power and developing state of the art algorithms and measuring techniques. However important these advances are, they mainly depend on financial factors and as such they are available only to a very small percentage of the research community. Even more so, it is quite debatable whether they would be able to provide accurate and complete results for large scale, complex flows in the foreseeable future. Therefore, much attention has been brought upon developing indirect techniques to bridge the existing gaps in knowledge and also on exploiting innovative statistical and mathematical tools to analyse the already available data.

Following this trend, for the present study, reasonably advanced experimental and numerical techniques have been employed together with post-processing and analysis methods. More specifically, both planar and tomographic time-resolved Particle Image Velocimetry (PIV) are used for velocity field measurements in turbulent boundary layers. The full pressure field is estimated indirectly, using the acquired PIV velocity data. The intent is to enhance physical understanding without solely relying on technological advances.

1.1 Velocity field

Historically, out of the two quantities of interest in an incompressible flow, velocity has been the main point of focus. Most of the experimental techniques for flow measurements are designed to measure velocity (Laser Doppler Anemometry, Acoustic Doppler Velocimetry, Particle Image Velocimetry, Hot Wire Anemometry), largely owing to the fact that it has been easier to measure and more intuitively understood than pressure. Therefore almost all early research studies on turbulence were based on the analysis of the velocity field. Apart from technical reasons though, knowledge of the velocity field alone, provides a quite detailed view of the flow, albeit incomplete. In the context of turbulence, where our interest lies, energy cascade processes and structure formation and – up to some level – their interactions can be adequately described with only velocity information available. Also, from a purely engineering point of view, energy efficiency studies based on controlling skin friction drag for devices operating with/in water and air environments can be carried out with information of the velocity field only, since it is the velocity gradients that are responsible for this added resistance force.

From the wealth of information that the turbulent velocity field alone provides, our main point of interest in this work will be the structural organisation of turbulence, including individual structure formation, interaction and evolution, momentum and energy transfer. These areas of study, despite the many decades of research, still raise important questions, some of them still unresolved and a few of which will be the focus of this work. In this section, an effort is made to first describe the mean velocity structure of wall-bounded turbulent flows together with some open

questions on the topic (see subsection 1.1.1). Based on this layer description, physical models of individual structures in different regions of the boundary layer are then outlined (subsection 1.1.2) with further focus on the freestream boundary (turbulent and non-turbulent interface) and the internal shear layers below it which bound zones of uniform momentum (subsection 1.1.3). Next to the existing literature on these areas, the main points of interest for our work will be outlined.

1.1.1 Mean velocity profile

Like any turbulent quantity, flow velocity, $\mathbf{u}$, can be decomposed into a mean, $\mathbf{U}$ and a fluctuating component, $\mathbf{u}'$ (Reynolds decomposition). The mean component can most commonly be defined either as a time average, an ensemble average or a volume average depending on the available data and type of study. The ensemble average (average over independent realisations) is the fundamental average of turbulence theory, however it is difficult to measure. For experimental studies, where it is hard to obtain many runs of the same experiment, time averaging is mostly used. In DNS simulations, especially for homogeneous turbulence, the volume average is the most common approach. Nonetheless, assuming ergodicity, the above measurable averages should in principle converge towards the ensemble average. Even though the mean component of the velocity doesn't include information about instantaneous phenomena, its profile alone can depict the presence of mean structural layers in wall-bounded flows and highlight scaling issues, outlined below.

Wall-bounded turbulent flows can be described using two sets of parameters. One for the region close to the wall where viscosity dominates (inner scaling) and one representative of bulk motion (outer scaling). In the inner region, denoted with a superscript +, variables scale with viscosity, ν, and the friction velocity, $U_\tau = \sqrt{\frac{\tau_w}{\rho}}$, where τ_w is the wall shear stress and ρ the density. For the outer region, the characteristic length scale is δ, which represents either the boundary layer thickness, the pipe radius, or the channel half-height depending on the type of flow. The velocity scale is U_τ, same as for the inner region, even though some normalisations use the freestream velocity, U_∞ or the centreline velocity, U_{ctr}, instead. For the intermediate layer between inner and outer regions, asymptotic arguments and dimensional analysis lead to a logarithmic variation in the mean velocity profile. The region below the logarithmic layer is commonly divided into the viscous sublayer (up to $y^+ \approx 5$) and the buffer layer (up to $y^+ \approx 30$), while the region above ($y^+ \gtrsim 0.2\delta$) is called the wake layer (Klewicki, 2010). The logarithmic law of the wall, is one of the most celebrated results in wall bounded turbulence (for a recent discussion on its importance see McKeon, 2013) and even though it has been rigorously analysed and it represents experimental data remarkably well, numerous extensions and alternatives have also been proposed over the years.

First of all, the logarithmic representation itself has been questioned, with alternative representations proposed over the years, of which the most notable is the power law distribution, which

came to prominence mainly due to the work of Barenblatt (1993) and Barenblatt and Prostokishin (1993), who proposed a non-universal, Reynolds dependent scaling law for the mean velocity distribution. The theoretical foundation was thoroughly developed and the power law was successfully implemented on experimental data from flow in tubes. The results were also compared with the ones stemming from a log-law representation. George and Castillo (1997) proposed a new approach for zero-pressure gradient boundary layers, using an Asymptotic Invariance Principle and Near-Asymptotics. Their approach also exhibited a power law behaviour for the mean velocity profile, however they specifically noted that similarity solutions are only valid for infinite Reynolds numbers and therefore no representation is expected to work perfectly for any real (finite Reynolds number) flow. On the other hand, Nagib et al. (2007) using recent flat-plate boundary layer data to study scale relations and asymptotic behaviour, re-established the log-law of the wall using both the mean velocity profile and its diagnostic function. Even though the subject has gathered particular attention and created noticeable controversy in the research community, conclusive answers cannot be given without conducting experiments of exceptional accuracy on very high Reynolds numbers that can clearly display differences between the proposed approaches (Marusic et al., 2010b), although the already available data seems to provide strong support for the universality of the logarithmic scaling (Marusic et al., 2013).

A second point of controversy is how the different layers discussed above are defined and what are their exact limits (see Zagarola and Smits, 1998; Pope, 2000; Wei et al., 2005; Klewicki et al., 2007, among others). An important extension to the mean layer structure was proposed by Wei et al. (2005), who, considering mean momentum balance, argued that the classical logarithmic representation should include at least an intermediate layer, with its own characteristic scaling, between the traditional inner and outer ones. An extensive review on the different layer divisions can be found in Klewicki (2010). The limits of the different layers – especially the extent of the logarithmic layer – are still a highly controversial point and have lately been linked with the issue of scale separation. In particular, a question raised recently and examined thoroughly due to new high Reynolds facilities available, is the required scale separation in a flow in order for it to exhibit a logarithmic region in the mean velocity distribution. Previously, it had been believed that the effects of viscosity on the mean velocity distribution were confined to regions below $y^+ < 30-50$ (Smits et al., 2011). However, recent data would seem to indicate that viscosity is in fact important in regions quite far from the wall. Besides proposing an extension to the logarithmic representation as mentioned above, Wei et al. (2005) also noted that viscous effects are dynamically significant from the wall out to a (Reynolds-number dependent) position. In particular, they observed that even though the viscous stresses themselves are a very small percentage of the Reynolds stresses outside the buffer layer, it is their gradients that are dynamically relevant outside this region. Therefore, only the outer part of the logarithmic layer, as originally described, should be considered an inertial sublayer. Following this line of work, Nagib et al. (2007) studying zero pressure boundary layers, observed a logarithmic behaviour on the mean velocity profile for $200 < y^+ < 0.15\delta$. Even more surprisingly, Zagarola and Smits (1998) who used data from a high Reynolds number pipe flow only identified a log law region for $600 < y^+ < 0.07\delta$, whereas for smaller distances a power-law behaviour was

observed ($60 < y^+ < 0.15\delta$). They also noted that the log-law was evident only for $Re_\tau > 9000$. Repeating the same experiments with a smaller Pitot probe McKeon et al. (2004), while finding different limits and constants for the regions, confirmed the presence of the power law near the wall and also identified a log region, albeit for slightly lower Reynolds numbers: $Re_\tau > 5000$. DNS studies of turbulent flows could also provide some insight regarding this behaviour, however they are still limited to much lower Reynolds numbers than the ones currently achieved experimentally. Marusic et al. (2010b) in a comprehensive review suggested that while it is still unclear how high the Reynolds number should be for the mean velocity to exhibit a logarithmic behaviour, a reasonable estimate could be $Re_\tau > 4000$–5000.

Another subject of significant debate regarding the mean velocity profile is the universality of the Kármán constant, κ, in the logarithmic representation, for different types of flow. The accuracy with which the different constants in the log region of the mean velocity profile are determined, mainly depends on the wall friction measurement (Smits et al., 2011). While for pipe and channel flows, wall friction can be estimated from the pressure gradient with good accuracy, for boundary layers its measurement is much more challenging and new techniques have to be employed, one of the most prominent being Oil Film Interferometry (OFI, see Fernholz et al., 1996; Naughton and Sheplak, 2002; Ng et al., 2007, among others). A quick review of recent studies, highlights the issue at hand. In the pipe flow measurements by McKeon et al. (2004), it was found that $\kappa = 0.421$, while $\kappa = 0.384$ was estimated for zero-pressure gradient boundary layers (Nagib et al., 2007) and pipe flow (Monty, 2005). For channel flow, Monty (2005) found $\kappa = 0.389$ while Zanoun et al. (2003) estimated the constant to be $\kappa = 0.37$, a value later confirmed from Nagib and Chauhan (2008). Adding another factor of influence, Chauhan et al. (2007) observed a variation of κ depending on the pressure gradient, with a favourable pressure gradient resulting in higher values. The question remains unanswered and further studies of high accuracy with preferably high Reynolds numbers (for an extended logarithmic region) would be required for any conclusive results.

Regardless of the many controversial issues, the important point to stress here is that the mean velocity profile can provide valuable information on the presence of different regions in a boundary layer. Notions of structure interaction and evolution or interface identification that follow, require a common spatial frame of reference and these regions provide an appropriate framework for this purpose.

1.1.2 Instantaneous velocity/vorticity fields and coherent structures

Now that the general frame of reference is defined with the help of the mean velocity, the mechanisms behind individual structure formation and interaction will be discussed, based on the study of the instantaneous velocity, its gradient tensor (linked with vorticity) and the velocity fluctuation statistics. An effort will be made to outline the history and development of some controversial issues on these topics and highlight the parts where our work will be focused. It

should be noted here that in general, distinguishing flow features according to their relationship with either the mean profile or the fluctuating component of the velocity is neither obvious nor entirely correct. The mean flow is inherently linked with turbulence since the two of them interact via the Reynolds stresses and it is this interaction that actually sustains turbulence itself (Davidson, 2004). For coherent structures in particular, their relationship with the mean flow is a matter of some confusion, with researchers arguing whether the structures draw energy from the mean flow in a similar fashion to turbulent fluctuations or, following the attached eddy hypothesis of Townsend (1976), they account for both the mean flow and the turbulent fields (Marusic et al., 2010b). While such a distinction could therefore be somewhat misplaced, it aids the classification of the broad range of studies on boundary layers, according to the statistical methods they employ.

The goal here is to use our experimental results (see Chapter 2) in order to study some aspects of the structural organisation in high *Re* number turbulent boundary layers. This includes the formation and characteristics of coherent structures and their time evolution, a topic that recently has developed a lot with the help of high *Re* DNS data and time-resolved PIV measurements (Flores and Jiménez, 2010; Lozano-Durán and Jiménez, 2011; Elsinga et al., 2012, among others). Special attention will be given to the freestream boundary of the turbulent region, the internal layers of high shear below it and the zones of uniform momentum that are bounded by those layers. To place these points of interest into a historical context, a short historical review of coherent structures will be presented in this section, followed by studies that highlight the formation and structure of Large and Very large-Scale Motions (LSMs and VLSMs respectively). Most importantly, the ways with which these structures can be linked with the shape scaling and entrainment properties of the turbulent/non-turbulent interface and the presence of internal shear layers below it will be discussed.

Coherent Structures

The structural organisation of turbulent wall bounded flows has been a focus point for researchers for several decades. Theodorsen (1952) was probably the first to identify the presence of horseshoe shaped vortical structures originating at the wall at roughly 45°. It would, however, be a long time before his observations would be further supported and longer still before these vortical structures would be associated with other structures identified near the wall. Kline et al. (1967), after a series of quantitative and qualitative studies, observed the formation of low-speed streaks near the wall. The authors also showed that the streaks interact and this process, consisting of a lift-up, an oscillation, a bursting and an ejection, suggests an instability mechanism and plays a key role in the transport of the turbulent kinetic energy. Following this work Corino and Brodkey (1969) used data from a pipe flow to analyse the structure near the wall, mainly highlighting the presence of fluid ejections in the region of $5 < y^+ < 70$ interacting with the mean flow and a sweep event following right after (axial entry of fluid from upstream). Kim et al. (1971) further established the occurrence of a series of events consisting of a low-speed streak

lift, followed by an oscillation and a breakup, which they collectively called bursts. Wallace et al. (1972), using hot-film measurements in a oil-channel flow, introduced the quadrant classification of the streamwise–wall-normal plane, u-v. They associated an upstream downwards motion ($u > 0, v < 0$, Q2 event) to the ejection process earlier identified and they attributed the opposite combination ($u < 0$, $v > 0$, Q4 event) with the sweep type motion. It wasn't until 1975 though, that Offen and Kline (1975), while trying to establish a pattern for the bursting process, associated the lift up stage of the low-speed streak with the results of a vortex roll-up and thus connected the depiction of the lifting process with the horseshoe vortex of Theodorsen (1952). Strong experimental evidence for the presence of hairpin and horseshoe vortices was further provided by Head and Bandyopadhyay (1981), who also observed that these structures were not clearly shaped for low Reynolds numbers where scale separation was small, but became increasingly elongated with higher Reynolds number. A comprehensive schematic of a hairpin vortex can be found in Adrian et al. (2000), where it is described as a structure with two counter-rotating legs (quasi-streamwise vortices) connected to the head of the vortex by vortex necks inclined at roughly 45° with the wall.

In parallel with these experimental developments, DNS data that started to become available in the late 1980's provided further insights into the structural organisation of boundary layers, allowing also for the freedom to isolate and analyse different regions of the flow separately. A representative example of that was the use of 'minimal' boxes by Jiménez and Moin (1991), to isolate minimal flow units in the near-wall region of a DNS channel flow. The results revealed an intermittent cycle of bursts of maximum activity (in terms of Reynolds stress, vorticity and average wall shear) and quiescent states where the shear stress decayed. During this cycle wall vorticity seemed to be lifted from the wall by wrapping around an inclined vortex, leaving a low-speed streak at the sublayer. The process was compared and found similar with the formation of hairpin vortices, however the resulting hairpin in this case was mostly asymmetric. Further numerical experiments (Jiménez and Pinelli, 1999) reinforced the presence of streamwise streaks and quasi-streamwise vortices in the near-wall region as well as their regeneration cycle which was shown to be autonomous and not dependent on the outer flow. This process was described as the formation of streamwise streaks from the vortices, which extract energy from the mean flow, followed by an instability of the streaks that leads to the generation of new quasi-streamwise vortices. This hypothesis of streak instability was later tested by Schoppa and Hussain (2002) who performed DNS simulations in a Poiseuille flow where only low-speed streaks were present. The authors argued that normal-mode streak instability might not be the source of vortex regeneration, since it showed only moderate mode amplification and was mitigated by viscous diffusion but it can alternatively be explained by the growth of structures in a shear (see also Jiménez, 2013). More insight into the bursting process of the streaks into vortices was given by Jiménez et al. (2005) who showed that in both minimal and full Couette and Poiseuille flows the streaks seemed to destabilise in two different occasions with the second one being faster and leading to the generation of strong streamwise vortices. They also argued that this process doesn't contribute to the Reynolds stress near the wall which, in the buffer layer, is mostly carried by 'steady structures'. Similar to the minimal structures and cycle in the

near-wall region, such units (a vortex cluster and low-speed streaks) were also observed in the logarithmic layer but they were themselves turbulent and the relevant scales were much larger (Flores and Jiménez, 2010). The regeneration cycle in this region also included bursts which were shown to destabilise the velocity streaks until they were destroyed.

Finally, temporal evolution of three-dimensional coherent structures of moderate and high Re numbers became possible only lately, owing to new DNS studies and results from time-resolved tomographic PIV experiments. Lozano-Durán and Jiménez (2011) tracked vortex clusters in a DNS channel flow ($Re_\tau = 950$) using geometrical intersection of the structures in time and found that their lifetime was dependent on their volume, they convected with velocities close to the mean in streamwise direction and both upwards and downwards in the wall-normal, with the former being slightly more probable. In a lower Reynolds number flow ($Re_\tau = 410$), LeHew et al. (2013) performed time-resolved planar PIV in different wall-normal planes and tracked swirling structures, which they subsequently separated into 'attached' and 'detached'. The results showed that the structures persisted for long times (5 turnover times) and their lifetime increased with distance from the wall. Elsinga et al. (2012) acquired time-resolved tomographic PIV data from a turbulent boundary layer of a much higher Reynolds number ($Re_\tau = 2460$) and tracked vortices in the outer region, which seemed to be passively advected by the external velocity. Their spanwise spacing was found to be close to 0.2δ and their motion was almost coherent, with very low relative velocities, in a similar fashion as the hairpin model (Adrian et al., 2000). Analysing the same data from a different perspective, Elsinga and Marusic (2010) also tracked the changes of the incompressible invariants in the outer layer. They found very large lifetimes of energy containing eddies ($\approx 14.3\delta/U_e$) with quite extended wavelengths associated with them ($\approx 11\delta$).

Clusters of structures, large and very large-scale motions

Apart from analysing single structure behaviour, significant efforts were made to explain evidence of larger structures spreading in the logarithmic layer and the wake region (Brown and Thomas, 1977), in the form of bulges with a mean streamwise extent reaching 2–3δ (Kim and Adrian, 1999). Even though the hairpin vortex model was able to incorporate several different observations throughout the years and explain many of the features of the turbulent boundary layer, some essential aspects – like the large scale motions mentioned above – could not be accounted for (Adrian et al., 2000). This led researchers to look for clusters of structures, with Zhou et al. (1999) recognising mechanisms of structure generation, followed with a forming of packets from single hairpin structures. The hairpin packet paradigm was thoroughly analysed by Adrian et al. (2000), with which they explained the very long streaks of low-momentum fluid found in the outer layer (essentially as pumping of the fluid from the legs of the many aligned vortices) and which they also linked to another very early theory of 'inactive motion' of Townsend (1976). Building on these observations, even larger, active motions in the outer layer were subsequently identified, reaching 8–16R in the experiments of Guala et al. (2006) in a pipe

flow, where R is the pipe radius, and 12–14R in the measurements from Kim and Adrian (1999). In internal flows these motions are typically named very-large-scale motions (VLSMs), while in external flows the prevalent term is superstructures (Hutchins and Marusic, 2007a; Smits et al., 2011).

These large and very-large motions are currently the subject of different studies particularly because they have been shown to carry at least half of the turbulent kinetic energy of the streamwise component and contribute more than half of the Reynolds stress (Guala et al., 2006; Balakumar and Adrian, 2007). From an engineering point of view, this fact might shift the focus of drag reduction strategies, which until now were based on the manipulation of small-near wall structures (Smits et al., 2011). Also, evidence of interaction of the large scale motions with the near wall cycle (Hutchins and Marusic, 2007b; Mathis et al., 2009; Marusic et al., 2010a) could potentially give rise to models predicting near wall events, when large scale information becomes available (see Marusic et al., 2010a).

Many of the recent insights into the behaviour of the large scale motions in the log region were brought about by examining the streamwise velocity spectra. Balakumar and Adrian (2007), analysing premultiplied spectra for streamwise velocity fluctuations in zero-pressure gradient boundary layers and channels, observed a bimodal distribution with the short-wavelength peak representing LSMs and the long-wavelength one corresponding to the VLSMs. Hutchins and Marusic (2007b), comparing premultiplied spectra for streamwise velocity fluctuations for turbulent boundary layers at $Re_\tau = 1000$ and at $Re_\tau = 7300$, observed a growing outer peak at length-scales around 6δ situated close to the mid-point of the logarithmic layer, which they associated with superstructures present in this region. A similar bimodal distribution was also found by Guala et al. (2006) in pipe flow, at length-scales around $7R$. Evolution of the same spectra with Reynolds number, presented in Marusic et al. (2010a), showed a clear increase in area, with increasing values of Re resulting from the extra energy at long wavelegths. Both Guala et al. (2006) and Balakumar and Adrian (2007) for pipe flow and channel and boundary layer flow respectively, also employed cumulative energy and Reynolds stress distribution as a function of wavelength to show that a large portion of the kinetic energy and the Reynolds stress come from the LSMs and superstructures.

Another observation that was also associated with large structure behaviour, came from the streamwise power spectrum and its k_x^{-1} region, or lack thereof. Even though the $k_x^{-5/3}$ region is well established, at least at high Re numbers, there has been recent evidence that the k_x^{-1} region can only be identified for extremely high Re numbers (Smits et al., 2011). The interactions between small, inner motions and outer-layer, larger motions and also the existence itself of LSMs and VLSMs could be some of the reasons explaining why the k_x^{-1} scaling fails (Hoyas and Jiménez, 2006; Smits et al., 2011).

The aforementioned presence of large scale structures on the outer layer and their interactions with the near-wall cycle can also be highlighted using turbulence intensity profiles and signal analysis of velocity fluctuations. Hutchins and Marusic (2007b) decomposing the streamwise

fluctuations into small (wavelength smaller than δ) and large scales, presented the corresponding turbulence intensity profiles which show that, the small-scale component is dominant near the wall and accounts for the inner spectral peak mentioned in the previous section, while the large-scale component even though strong in the log-region, has a non-trivial presence next to the wall as well, hinting at an outer influence on the near wall cycle. The authors examined also decomposed streamwise velocity signals, where it became clear that the low-wavenumber motions in the log region have a strong effect on the small-scales near the wall, quite similar to an amplitude modulation (see also Marusic et al., 2010a).

Finally, two point velocity correlations can also indicate the passage of structures and give an indication of their size. Using two-point correlations, Ganapathisubramani et al. (2005) revealed the formation of hairpin packets in the log region, which tend to be shorter in length and broader in width in the wake region. Tutkun et al. (2009) using the same technique on a high *Re* turbulent boundary layer, observed correlations spanning several boundary layer thicknesses, associating their findings with the presence of large scale coherent motions, much like the hairpin packet model of (Adrian et al., 2000). They also revealed correlations, at the same 'instant of time', between the near wall region and the outer layer which they suggest supports the amplitude modulation proposed by Hutchins and Marusic (2007b). Hot film shear-stress sensors were used to identify large-scale skin friction fluctuations at the wall which – by employing conditional averages – are found to be the footprint of large scales superstructures further away from the wall (Hutchins et al., 2011). The authors observed that the superstructures consist of a forward leaning low-momentum region framed on both sides by high-speed structures. Further, decomposing the velocity signal into small and large scale components and again using conditional average, they showed that under a low skin friction event at the wall – corresponding to a low-speed region on the log layer – small-scale energy is attenuated close to the wall and intensified farther away from it, while the exact opposite happens under the influence of a high skin-friction event (corresponding to high-speed structures on the log region). This is found to be in very good agreement with the amplitude modulation suggestion of Hutchins and Marusic (2007b), Mathis et al. (2009) and Marusic et al. (2010a), among others.

Although LSMs and VLSMs or superstructures were observed in both internal and external wall-bounded flows, in the specific case of a turbulent boundary layer the passage of these clusters of structures was further linked with an observed zonal structure (Adrian et al., 2000) of the turbulent region. Despite the importance of these observations and their influence on the general understanding of the boundary layer structure, further analysis of these zones and their characteristics arose only very recently. It was in fact Eisma et al. (2015) who, starting from the turbulent/non-turbulent interface in a boundary layer, reported again the presence of internal layers below it, which they then linked to zones of uniform momentum (UMZs). The term turbulent/non-turbulent interface (TNTI) is used to describe the sharp interface separating the flow into turbulent and non-turbulent regions which provides information on mechanisms of mass and momentum transfer. A detailed description of both the TNTI and the internal layers

and zones below it follows in the next section together with an overview of related studies and points of focus for the present work.

1.1.3 Turbulent/non-turbulent interface

The term TNTI is used to describe a region that separates a turbulent flow domain from an irrotational one. Such interfaces exist in many types of turbulent flows including jets, wakes and shear layers but also boundary layers which are of interest here. Starting from the seminal work of Corrsin and Kistler (1955) on free-stream boundaries in turbulent shear flows, researchers have been progressively interested in the properties of these interfaces (Phillips, 1955; Turner, 1986; Westerweel et al., 2005; Hunt et al., 2006; Westerweel et al., 2009; da Silva et al., 2011; Ishihara et al., 2015, among others), their intermittent nature (Townsend, 1949; Corrsin and Kistler, 1955; Bisset et al., 2002) and evolution (Kovasznay et al., 1970; Khashehchi et al., 2013).

Corrsin and Kistler (1955), combining a detailed theoretical analysis and hot-wire experiments in a turbulent boundary layer and a round jet, were among the first to corroborate and analyse the existence of the sharp front distinguishing turbulent from non-turbulent regions in these type of flows. Following the work of Townsend (1949), who first described the intermittent nature of the outer part of a turbulent cylinder wake, they analysed the intermittent signal of the front location aiming to determine its propagation and growth characteristics. They showed that viscous forces are dominant in this front – which they termed 'the laminar superlayer' – and are responsible to transfer vorticity from the turbulent towards the non-turbulent region, which they also showed is irrotational. Further, they concluded that this superlayer is very thin, owing to its propagation with respect to the surrounding fluid and the stretching of the local vortex gradient. Focusing on the non-turbulent domain outside of this superlayer, Phillips (1955) used mathematical arguments to describe the motion of the irrotational fluid in this domain and its properties and compared the results with experimental data from (Townsend, 1949, 1951), indicating reasonable agreement. A bit later, Kovasznay et al. (1970) performed a series of extensive hot-wire experiments in a turbulent boundary layer in order to study how the properties of the TNTI relate to the large-scale motions present in the outer part of the flow. This was primarily achieved by space-time autocorrelations, ensuring that the separations in time and space (in the streamwise direction) were long enough to allow for the identification of large-scale, lasting events. The detection of the interface was achieved again by exploiting the intermittent character of the turbulence signal at the free-stream boundary: a double hot-wire probe was employed, recording the time history of the wall-normal velocity gradient, which, as a measure of out-of-plane vorticity, could then be used as the detector of turbulent bursts in time. Their results confirmed a strong correlation of the interface properties with a large-scale motion and they agreed well with the potential flow theory of Phillips (1955) – a theory later validated again by Bisset et al. (2002). Further, (Kovasznay et al., 1970) were one of the first to compute a convection velocity of that front, showing that it moves at approximately the same speed as the free-stream, albeit a

bit slower. This result is of particular importance for the present work, since our main focus is the time-evolution of such interfaces. Another important conclusion from that study, regarding the dynamic processes across the interface, is that the wall-normal velocity, V, of the fluid is crucial to explain the motion of the interface, since a turbulent burst is characterized by a large positive V, while a negative one is representative of a non-turbulent valley, where irrotational fluid is entrained into the turbulent core (Kovasznay et al., 1970). In the years that followed and still in the absence of numerical results, different experimental techniques were used for the detection of TNTIs including heating the turbulent core and detecting the intermittent interface with resistance wires in cylinder wakes (LaRue and Libby, 1974; Fabris, 1979) and boundary layers (Chen and Blackwelder, 1978). The appearance of the first numerical simulations and the further development of experimental techniques bolstered the research on the subject and strengthened the theoretical framework, especially with respect to the main properties of these interfaces and the mechanisms that are involved in their formation and evolution. Some of the major points of this still growing body of research are summarised in the subsections that follow.

Structure and geometry

The sharp and irregular instantaneous shape of the TNTIs is one of their most distinctive features, making them easily observable in nature (clouds, flames, plumes and jets) and simple laboratory experiments (shadow-graphs) without the need of advanced visualisation equipment. That was one of the main reasons they gathered particular attention very early, however further understanding of their structure and geometrical characteristics was a much slower process, hampered by the absence of necessary theoretical and experimental tools needed for an in-depth quantitative analysis. One of the first observations regarding the structure of this front, was that its sharp outline was the reason behind the intermittent character of hot-wire signals at the edge of boundary layers (Corrsin and Kistler, 1955). It was this connection that allowed later studies to analyse more intricate notions of convection and entrainment (Kovasznay et al., 1970; Chen and Blackwelder, 1978) without the use of very advanced visualisation techniques like PIV that appeared much later. It was also that study of Corrsin and Kistler (1955) that first described the TNTI as a thin laminar superlayer, where viscous forces are dominant, a highly significant notion, if only for the time in which it was made, which was later adopted and expanded by almost all related studies that followed on the subject, but confirmed only much more recently (da Silva and Taveira, 2010). The first important development of the initial concept came by Bisset et al. (2002) that postulated that this 'superlayer' actually only represents the outer boundary of the TNTI, which in its entity is again a thin region of fluid, albeit turbulent and is acting as an adjustment layer (Westerweel et al., 2009), which encompasses all the necessary changes required to 'bridge' the outside irrotational region with the fully turbulent one below. It was the work of da Silva and Taveira (2010) and (da Silva and dos Reis, 2011) in high resolution DNS data though, that confirmed the presence of these two separate layers, namely the outer thin viscous 'superlayer' and the inner TNTI, where a jump in vorticity occurs, thus vindicating

the original idea of Corrsin and Kistler (1955), half a century later. A more detailed description and schematic illustration of these different layers and processes across the interface can be found in da Silva et al. (2014b). It should be noted here that, such a distinction is possible only when high-resolution data are available and therefore the finite resolution of the PIV data in the present work will render such distinction impossible.

Besides the structural layer organisation of the interface, another point of focus concerning its geometrical characteristics is the corrugation of its surface and the range of scales over which it happens. Kovasznay et al. (1970) suggested that the shape and motion of the TNTI is closely linked to a large scale motion inside the boundary layer, a notion later supported also by Chen and Blackwelder (1978) who linked it further with a bursting phenomenon near the wall. Much later, Sreenivasan and Meneveau (1986) attributed a more complex character to the the surface of the TNTI suggesting that, among other aspects of turbulent flows, its bounding surface is 'fractal' and includes a range of scales (Bisset et al., 2002). The studies that followed since then clearly made the distinction between the large-scale 'engulfing' motion which is of the order of the integral scale of the turbulent region (Bisset et al., 2002), and the small-scale 'nibbling', which is a viscous process and mostly happens at the viscous outer layer of the TNTI (da Silva and dos Reis, 2011).

Conditional statistics and dynamics

Apart from the structure and geometry of the surface, many researchers also shifted very quickly their attention towards the dynamics that take place across the interface, mainly using statistical analysis of distributions of different quantities across it. It was actually the first study on TNTIs and their general structure (Corrsin and Kistler, 1955) that, among all the aforementioned crucial concepts, also hinted at a potential jump of velocity, vorticity or of a scalar quantity across the thin interface. It was not until the work of Alexopoulos and Keffer (1971) on a turbulent wake though, that a sharp jump in temperature was observed across the TNTI and only much later that a similar behaviour could be confirmed for turbulent quantities (velocity, vorticity, Reynolds stress). More specifically it was Bisset et al. (2002), who, through the use of conditional statistics – which allowed for the jumps to be sharper – observed both a velocity and a temperature jump again in a turbulent wake, and later these observations were further extended to turbulent jets (Westerweel et al., 2005, 2009; da Silva et al., 2011) and boundary layers (Hunt et al., 2011; da Silva et al., 2014b; Philip et al., 2014; Chauhan et al., 2014a; Ishihara et al., 2015; Eisma et al., 2015). Brown and Roshko (1974) and later da Silva and Taveira (2010); Chauhan et al. (2014a); Eisma et al. (2015), among others, suggested that the presence of these jumps validates the existence of a shear layer between turbulent and non-turbulent regions and supports the very early notions of a 'superlayer' by Corrsin and Kistler (1955). As mentioned above, it was recently shown that the actual jump in vorticity happens at the turbulent adjustment layer (or interface) – just below the viscous 'superlayer' – and is indicative of its thickness, (da Silva et al., 2011), even though that distinction is not possible without very high-resolution data, so

that the terms interface and 'superlayer' are used interchangeably in literature (Chauhan et al., 2014a). Regardless of the term use however, the thickness of the jump, δ_ω, was unilaterally regarded as a direct measure for the shear across the interface and a crucial parameter of the scales that were involved in the transport mechanisms (Chauhan et al., 2014a). It was also shown that δ_ω is larger for turbulent jets than shear free, isotropic turbulence and is also a measure of the radius of the large vortical structures in the turbulent region (da Silva and Taveira, 2010). Further, following a control volume analysis (Westerweel et al., 2009) suggested that this sharp scalar jump is directly linked to the velocity, E_b, with which the interface moves outward, and could also be representative of the mechanism through which this entrainment happens (Bisset et al., 2002), a point of controversy between researchers for many years, which will be discussed below.

Entrainment

Having discussed the geometrical characteristics and dynamics of the interface, more complex notions of mass and momentum entrainment can now be better described. Apart from their importance for the physical understanding of turbulent flow, the transport phenomena taking place between the two very different flow regimes lying on either side of the interface are also of particular importance for engineering applications. One of the long-lasting debates in this particular area of research has been the determination of the dominant mechanism through which entrainment happens and its relation to the geometrical characteristics of the interface. Entrainment is the process via which, fluid particles originating at the irrotational part of the flow, acquire vorticity and become turbulent, contributing to the growth of the turbulent region below the TNTI. This transition can happen either through an advective large scale process (the aforementioned 'engulfment'), or via the small-scale, viscous 'nibbling'. Early studies (Dahm and Dimotakis, 1987; Ferré et al., 1990, among others) suggested that the large-scale motions are primarily responsible for the entrainment and mixing processes in jets and wakes. Later on, Bisset et al. (2002), in an extensive analysis of such an interface in the wake of a flat plate, also suggested that the conditional distributions of velocity and vorticity highlight that the leading mechanism of entrainment comes from 'large-scale engulfing' motions, even though the small-scale processes play also an important role. In contrast to these findings, Westerweel et al. (2005), using data of a turbulent jet, showed that the inertial flux is not responsible for transferring vorticity across the interface and that the engulfment of irrotational fluid accounts for a very small percentage of the total jet mass, thus arguing that the prominent process of entrainment is not the engulfment of the large-scale eddies but rather a spreading of smaller eddies. Further PIV and LIF measurements again on a turbulent jet by Westerweel et al. (2009) reaffirmed the notion of small-scale spreading ('nibbling') as the prominent entrainment mechanism for low Re numbers. It has since then been speculated that the two terms describe the same process albeit at different scales, with the 'nibbling' being prominent at the smallest scales and the engulfing motion at the largest with negligible viscous contributions (Wolf et al., 2012; Philip et al., 2014; Chauhan et al., 2014a). For the in-between scales both processes are actively involved and it

can be assumed that the overall entrainment rate is dominated by the large-scale motions but it actually happens on the small viscous ones (Philip et al., 2014; Eisma et al., 2015). The notion of entrainment at different scales was also recently analysed by Mistry et al. (2016) in the case of an axisymmetric jet using both time-resolved PIV and planar laser-induced fluorescence (PLIF). The authors computed entrainment velocities across the TNTI by tracking the interface in time and suggested that both entrainment velocities and the length of the interface scale with filter size in a way that the average mass flux remains constant across scales.

It is clear from the above review that the main point of focus of recent studies is the entrainment mechanism responsible for mass and momentum transfer across the interface and how this interface evolves in time. With respect to the TNTI, our work is therefore focused on these aspects in the case of a high-Reynolds number turbulent boundary layer exploiting the time information available from high-speed PIV measurements (see Chapter 4), something that seems to be lacking from most of the available studies on this subject.

1.1.4 Internal layers and uniform momentum zones

Based on the observations from these TNTI studies, Eisma et al. (2015) indicated that characteristics similar to those of TNTIs exist also in interfaces inside the boundary layer, which bound UMZs, and whose growth rate is of the same order as that of the TNTI. Following the same conditional averaging techniques that have been commonly used to analyse the dynamics of the TNTIs, the authors found that these internal layers show a similar behaviour as the TNTIs, with the conditional averages of velocity, vorticity and Reynold's stress exhibiting clear jumps, whose width grows the closer they are to the wall. They further showed that, based on theoretical concepts for the computation of the entrainment velocities, the layers move upwards faster with increasing distance from the wall. de Silva et al. (2017) using experimental datasets of turbulent boundary layer spanning a decade in friction velocity Reynolds numbers, analysed the characteristics of the internal layers, confirming the observations from Eisma et al. (2015) for all Reynolds numbers tested. The authors further suggested that the magnitude of momentum jumps across the layers is Reynolds number independent when scaled with the friction velocity.

The UMZs bounded by those layers have also been the focus of several studies, starting with the work of Meinhart and Adrian (1995), who first described the presence of instantaneous zones of uniform velocity populating a turbulent boundary layer. Adrian et al. (2000) further proposed that each zone is characterised by a 'modal velocity', which is the local peak of the probability density function (pdf) of the streamwise velocity component. The authors also suggested that these low-momentum zones are the result of the passage of hairpin vortices and their packets, whose legs induce a back-flow responsible for the lower momentum and whose heads lie on the high-shear regions that separate the zones (Adrian et al., 2000). Using Acoustic Doppler Velocimetry, Hurther et al. (2007) identified the presence of large-scale shear events within zones of uniform streamwise velocity in the case of rough-bed open channel flows of various Reynolds numbers, suggesting a link between the UMZs and the high-shear regions. Following a similar

peak detection procedure, Kwon et al. (2014) identified a region of uniform velocity magnitude in a turbulent channel. A bit later, de Silva et al. (2016) analysed the presence of UMZs within these internal layers, and showed that their number increases logarithmically with Reynolds number, their wall-normal extent diminishes closer to the wall, and their organisation follows the attached eddy model (Perry and Chong, 1982). More recently, (Chini et al., 2017) using high-Reynolds number asymptotic analysis, proposed a conceptual model able to represent the interaction between the internal high-shear layers and the UMZs that are bounded by them. The issue of Reynolds-number dependence of such structures was further investigated by Morris et al. (2007) in the case of a rough-wall atmospheric boundary layer and results supported the low-Reynolds number observations of UMZs within inclined shear layers of Meinhart and Adrian (1995) and Adrian et al. (2000).

As was mentioned previously, the presence of UMZs has been linked to the passage of hairpin vortices and their packets (Adrian et al., 2000), so further analysis on their characteristics could potentially facilitate the understanding of the boundary layer structuring and evolution. In view of the relatively small volume of available literature on the subject, we chose the UMZs as our second main point of focus apart from the TNTI discussion outlined above – in a sense moving away from the freestream to also include the structures below it.

1.2 Pressure field

However essential the velocity field is proven to be in terms of understanding the nature of turbulence, if the full picture of the physical processes is sought, acquiring the pressure field is just as crucial.

1.2.1 Why is pressure important in turbulent flows?

It is known (Pope, 2000) that the pressure fluctuations while not very important in the turbulent kinetic energy equation, play a central role in the Reynolds-stress equations. More specifically, the main effect of the pressure term is to redistribute the energy among the velocity components – extract energy from the streamwise component and transfer it to the spanwise and wall normal ones. Along with production and dissipation, redistribution is a dominant process in the balance of the Reynolds stresses (Pope, 2000). This process is represented in the Reynolds transport equation with the pressure-velocity correlation (pressure strain-rate) term $2\overline{p' S'_{ij}}$, where p' is the instantaneous pressure and S'_{ij} is the strain rate tensor based on velocity fluctuations. Due to the inability of directly measuring this term, different closure models have been proposed over the years for numerical simulations (see Rotta, 1951; Launder et al., 1975; Lumley, 1979; Speziale, 1991, among others). Later DNS studies (Rogers, 1986; Mansour et al., 1988) have provided valuable results to test these models (Speziale et al., 1992 and later Jakirlić and Hanjalić, 2013) however even today there are important limitations in terms of flow geometries and Reynolds

numbers for DNS simulations and the physical implications of this term and subsequently its modelling remain mostly obscure.

Pressure fluctuations are also related to vorticity fluctuations (Kim, 1989) which can in turn provide valuable information on the formation of turbulent structures (see Perry and Chong, 1982; Jiménez et al., 1988; Kim and Hussain, 1993; Adrian et al., 2000; Elsinga et al., 2012; Gao et al., 2013, among others). Douady et al. (1991) showed that identifying high vorticity regions can be achieved by tracking and visualising the corresponding low pressure regions. In line with this observation, Brachet (1991) performed DNS of three dimensional turbulence in the Taylor-Green vortex, confirming the strong correlation of turbulent activity with low-pressure zones. Pumir (1994) using joint pdfs of pressure and vorticity from DNS data of homogeneous isotropic turbulence, further established the relation between vortex filaments and low pressure regions and also showed that, in contrast, high positive pressure fluctuations are not associated with any well-defined structures. Kida and Miura (1998) used a swirling condition together with regions of low pressure to identify swirling vortical structures in the case of homogeneous turbulence. Recently, Naka et al. (2015) measured pressure fluctuations in the field and at the surface of a turbulent boundary layer using microphones in combination with velocity measurements using stereoscopic PIV, for three different Reynolds numbers. They computed space-time correlations of pressure and velocity in order to link turbulent coherent structures with pressure fluctuations and results showed that both positive and negative pressure fluctuations at the wall and in the field are linked to ejections and sweeping motions and also that pressure fluctuations in the field are also correlated with the passage of large coherent structures for long periods of time and could be linked to the large and very-large scale motions observed in wall-bounded flows (see also section 1.1.2). Next to the detection of such structures, their interaction with the near wall cycle – a subject already mentioned above (section 1.1.2) with respect to the velocity fluctuations – can also be examined using pressure fluctuation measurements (Tsuji et al., 2015). This highlights the significance of flow pressure information in understanding some of the important issues relevant to wall-bounded turbulent flows which, until recently were analysed using solely velocity data.

Apart from these theoretical concepts and studies, the pressure field is also of paramount importance when it comes to practical applications. For bodies immersed in a fluid, pressure is the main factor contributing to the aerodynamic loads exerted on them. Similarly to skin friction drag mentioned above, pressure drag is another important component adding to the resistance of vehicles operating within a fluid. In aeroacoustics, estimation of pressure fluctuations is essential in noise quantification (see Goldstein, 1984; Bogey and Bailly, 2007; Maaloum et al., 2004, among others). Pressure is also responsible for cavitation phenomena in turbomachinery, marine propellers, valves and pumps (see for example Wang et al., 2001). This is actually one of the most tangible manifestations of pressure as a fundamental fluid property. Even for the turbulence models widely used in industrial CFD packages, knowledge of the pressure behaviour is required so that the pressure-strain term appearing in the Reynolds-stress equations can be correctly modelled (Speziale et al., 1992; Jakirlić and Hanjalić, 2013). It is therefore clear

that whether for reasons of physical understanding or direct practical applications, information regarding the pressure field is highly valued.

1.2.2 Direct pressure measurements and numerical simulations

Acknowledging the critical role of the pressure term but on the same time being severely restricted from measuring it experimentally, several early researchers tried to approach the problem based on mathematical notions. Batchelor (1951), noting the importance of the pressure fluctuations on the boundary layer of wall-parallel flows, used the Millionshchikov hypothesis (fourth-order moments are related to second-order moments in the same way as for a normal joint distribution) to compute integral expressions for the mean-square pressure fluctuation and mean-square pressure gradient. Using second order velocity correlations in the case of isotropic turbulence, Uberoi (1953) computed the root-mean-square (rms) pressure and pressure gradients for a range of Reynolds Numbers. By Fourier transforming the integral solution of the Poisson equation for pressure, George et al. (1984) developed spectral models for turbulent pressure fluctuations. By that time, numerous technological advances have also facilitated the realisation of more complex experimental and numerical simulations and provided the researchers with new information on pressure fields, thus slowly turning the focus away from purely mathematical studies. Using DNS data from a channel flow, Kim (1989) investigated pressure fluctuations statistics. Following a frequently employed decomposition of pressure into rapid and slow parts, he demonstrated that the slow (non-linear) pressure fluctuations are larger than the rapid ones for the most part of the channel. A bit later, Farabee and Casarella (1991) analysed frequency spectra and cross-spectra of wall pressure fluctuations and identified the turbulent source regions within the boundary layer that contribute to the low-, mid-, and high frequency ranges of the wall pressure field. Attempting to tackle the more fundamental question regarding the origins of pressure fluctuations, Pumir (1994) conducted a thorough analysis of PDF's for different quantities of a isotropic homogeneous turbulent flow. Comparing the pressure PDF of a turbulent field with that obtained using a Gaussian velocity field he showed that the pressure fluctuations for the latter are always less intense than for the real and not even the pressure rms value can be accurately predicted using a Gaussian assumption. Additionally, the PDF's of pressure, vorticity and strain showed that high strain will most probably be associated with high vorticity and this in turn will render high values of pressure quite unlikely.

In parallel with mathematical and numerical developments, some efforts were made towards obtaining pressure information experimentally. In the early years, the majority of works was focused in wall pressure measurements, starting with Willmarth (1956) who performed surface pressure measurements over a flat plate, and Mull and Algranti (1956) who investigated sound pressure on the surface on an airplane wing. Later, Harrison (1958) acquired wall pressure fluctuations on a turbulent boundary layer while Blake (1970) employed microphones much smaller than those of earlier works to measure fluctuating surface pressure in rough and smooth walls. The effect of the transducer's size on the acquired signal's resolution (attenuation effects)

had been recognised from the outset (Willmarth, 1956) but possible correction methods were not proposed until later (Corcos, 1963). For a more detailed review on the early wall pressure measurements the reader is encouraged to look at Willmarth (1975). Much fewer experimental studies were oriented towards measuring static pressure away from the wall. Novel measurements were carried out by Kobashi (1957) who used a condenser microphone as a transducer together with a hot-wire to obtain static pressure fluctuations and its correlation with velocity fluctuations in the wake of a circular cylinder. Siddon (1969) developed a probe capable of measuring unsteady static pressure while correcting for the error induced from interactions with the unsteady velocity components and a bit later, Elliott (1972) built an instrument manufactured in such a way so as to allow pressure static fluctuations to be measured with minimal influence from the surrounding air velocity, and measured static pressure inside an atmospheric boundary layer. In a different kind of flow, Jones et al. (1979), measured static pressure fluctuations in the mixing layer of a subsonic circular jet.

These developments also highlighted some aspects regrading the spectral distribution of pressure fluctuations which, even until today, is much less understood than the distribution of the velocity spectra. Similarly to the velocity $k^{-5/3}$ scaling law proposed by Kolmogorov (1941), it has been speculated that the same similarity arguments can be extended to pressure, yielding a $k^{-7/3}$ scaling (Monin et al., 1975; Lumley et al., 1964; George et al., 1984, among others). In the case of wall-bounded flows, the interaction between the mean velocity field and the shear might be a source of deviation from this behaviour (Tsuji et al., 2007). Measuring static pressure at a single point inside an atmospheric boundary layer, Elliott (1972) observed a power law behaviour of the pressure spectra, with a mean slope of 1.7. For a homogeneous turbulent flow with a constant mean shear, using Fourier transform of the solution to the pressure Poisson equation, George et al. (1984) showed that the results exhibited the Kolmogorov prediction for pressure fluctuations (turbulence-turbulence interaction possess the $k^{-7/3}$ inertial subrange) and the turbulence–mean-shear contribution was shown to fall-off as $k^{-11/3}$. Later, Albertson et al. (1998) using a pressure static probe inside a near-surface atmospheric boundary layer in a grass clearing, showed that pressure spectra seemed to scale with $k^{-3/2}$ rather than $k^{-7/3}$. On the other hand, Tsuji and Ishihara (2003) measured pressure fluctuations in the case of a turbulent jet using a microphone and a piezoresistive transducer and the resulting spectra showed a scaling close to the $k^{-7/3}$ for Reynolds numbers based on the Taylor microscale, $Re_\lambda \gtrsim 600$, much higher than those required for the velocity spectra to show the Kolmogorov scaling.

As the measurement techniques and the computational power grew exponentially over the next years, researchers continued to analyse the new information bringing novel insights on the role of pressure fluctuations on turbulent flows all the while focusing on more complex geometries and flows. Kim and Sung (2006) used DNS data to examine the response of wall-pressure fluctuations to the longitudinal curvature and pressure gradient resulting from the presence of a bump in the flow. They showed that the pressure fluctuations are significantly enhanced near the trailing edge of the bump, where also large-scale structures grow and convect downstream. Following this line of work of non-equilibrium turbulent boundary layers and also using DNS

data, Bhaganagar et al. (2007) studied the effect of surface roughness on pressure fluctuations and showed that roughness decidedly alters the pressure statistics introducing new length-scales and increasing form drag. He also concluded that velocity data alone are not enough to get a complete description of inner/outer interactions. More recently, Patwardhan and Ramesh (2014) analysed pressure in DNS data of a boundary layer ($Re_\theta = 4500$) and observed a $k^{-7/3}$ scaling in the outer regions, which tends to a -1 slope closer to the wall. In the experimental field, Tsuji et al. (2007) measured wall pressure together with mean and fluctuating static pressure over a flat plate for high Reynolds numbers and showed that the rms pressure fluctuations normalised with inner variables are Reynolds number dependent, while the static pressure spectra do not show the $k^{-7/3}$ scaling but rather a -1 slope power-law. Similar experiments in even higher Reynolds numbers ($Re_\theta \approx 44000$) were later performed in different wind tunnel facilities (Tsuji et al., 2012) highlighting the influence of background noise inside the wind tunnel. Corrections of the acquired pressure values for this effect were proposed so that the statistics could then be compared with DNS profiles. Winkel et al. (2008) performed surface pressure measurements in water to study the effect of air injection on the wall pressure fluctuations and consequently on the skin-friction. The results showed a large reduction of the wall-pressure variance due to the air injection in proportion to the reduction in skin friction and a suppression of the pressure spectra in the mid-frequency range.

However, despite the obvious technological advances, the fact remains that experimental methods have not yet managed to provide full pressure and velocity fields. As mentioned already, surface pressure can be obtained using microphones or pressure transducers (whose performance is limited due to their intrusive nature), whereas for static pressure only point-wise measurements using probes are usually available, which are also intrusive and mainly provide mean flow quantities (van Oudheusden, 2013). With respect to numerical simulations, even though DNS studies can provide both pressure and velocity fields, they are still restricted to low Reynolds numbers and relatively simple geometries. Thus, there are still several applications where pressure information would be invaluable but the complexity of the flow is prohibitive for both experimental and computational methods.

1.2.3 Indirect pressure estimation using PIV data

Therefore, alongside studies that focused on further developing methods to analyse already available data, many researchers directed their attention on formulating indirect techniques to acquire pressure data, especially in those applications where it would otherwise be impossible. More specifically, they revisited the link between pressure and velocity, stemming from the Navier–Stokes equations. Like the very early studies on pressure fluctuations mentioned above, these much more recent studies, focused on the Poisson formulation of pressure, this time though bolstered by the fact that not only velocity correlations but the full field velocity measurements were available from particle image velocimetry (PIV), a method that came into prominence around that time and was rapidly established as a standard non-intrusive technique

to acquire velocity. With the velocity field known, integrating the Poisson formulation could actually provide a solution for the full pressure field and it was this fact together with the swift development of PIV that enabled the establishment of these indirect techniques.

Following this line of work, Gurka et al. (1999) using planar PIV velocity data, computed pressure distributions in water flow in a pipe and in an impinging air jet and compared the results with reported data from previous studies. Fujisawa et al. (2005) also used PIV velocity data to numerically solve the pressure Poisson equation to acquire pressure and fluid forces on a circular cylinder. Liu and Katz (2006) used a four-exposure PIV system to measure material accelerations, which were subsequently integrated employing an omni-directional virtual boundary integration scheme to obtain the pressure distribution. De Kat et al. (2008) acquired planar pressure fields, starting from time-resolved PIV velocity data of a flow past a square-section cylinder and using a Poisson solver and they compared the results with surface pressure measurements. Using artificial and real PIV velocity data, Charonko et al. (2010) presented a detailed assessment of different Eulerian methods that calculate pressure, as well as their dependence on grid resolution, sampling rate, measurement error and off-axis recording. A detailed review of studies on acquiring pressure from PIV can be found in van Oudheusden (2013). For completeness, it should be noted here that for applications where body forces are of importance, calculation of the pressure field can be avoided and the instantaneous forces can be calculated using only velocity fields and their gradients (Noca et al., 1997 and more recently DeVoria et al., 2014).

Many of these studies used Eulerian methods to compute the material acceleration term. However, the acceleration can also be determined using a Lagrangian approach and the comparison of the two methods has also been the focus of several recent works. Using PIV on surface waves to predict flow accelerations and forces, Jakobsen et al. (1997) compared Eulerian and Lagrangian approaches and the results indicated that the former approach matched closely the analytical calculations. The Lagrangian approach exhibited a small bias, which led to a systematic error in the estimation of flow acceleration and seemed to be limited due to poor tracking or deformation of fluid volume. This observation was supported by de Kat and van Oudheusden (2012), who found that a pseudo-Lagrangian approach (reconstructing fluid parcel paths from velocity fields, in contrast with particle path tracking of LA-techniques) limited in time by the turnover time of the structures, exhibited more severe restrictions than an Eulerian one, requiring thick measurement volumes to accurately reconstruct the fluid path. They also showed that the Eulerian approach suffered more from measurement noise and was limited in time by the advection of structures on the boundaries, but not as much as the pseudo-Lagrangian (de Kat and van Oudheusden, 2012). In contrast to these findings, results from pressure field evaluation of rod–airfoil flow from time-resolved PIV (Violato et al., 2010) suggested that a pseudo-Lagrangian approach managed a lower precision error with a larger timestep than an Eulerian one, which was again shown to suffer from measurement noise. In line with this, Ghaemi et al. (2012), used time-resolved, tomographic PIV on a turbulent boundary layer to estimate pressure and showed that a pseudo-Lagrangian formulation performed much better than an Eulerian one, when compared with microphone surface pressure measurements.

In view of these developments and contrasting results, an alternative method was proposed by de Kat and Ganapathisubramani (2013). It was based on an Eulerian approach but avoided its aforementioned temporal limitations by using Taylor's hypothesis for the estimation of the flow acceleration. The technique was successfully implemented on both synthetic and experimental 3C planar velocity data and results indicated that pressure could be accurately estimated with an appropriate choice of convection velocity (de Kat and Ganapathisubramani, 2013). With respect to pressure, this is the theoretical point where the present work is situated.

We extend the use of Taylor's hypothesis to estimate pressure on three-component volumetric velocity snapshots, validate our method against DNS and experimental data and compare the results with those of an Eulerian and a pseudo-Lagrangian approach.

1.3 Pressure and velocity in the current work

Following the review of existing literature in the previous sections and the related observations on unexplored areas in the field, we can now outline the main points of focus in the present work. With respect to velocity fluctuations and how they relate to the structure of the flow, our interest lies mainly on the detection and evolution of the freestream boundary and on the temporal organisation of the velocity fluctuations below it. Both are studied using time-resolved planar PIV, as described in Chapter 2. The TNTI is tracked in time and the evolution of its surface area and entrainment rates are computed (see Chapter 4), while its main geometrical characteristics are analysed. With respect to the velocity fluctuations below the TNTI and specifically the UMZs that have been shown to populate the boundary layer, a short outline on their instantaneous detection is presented, following the work of both Adrian et al. (2000) and de Silva et al. (2016). The detection process is then extended to account for temporal coherence of UMZs and results on the velocity range and thickness of the time-coherent UMZs, according to their relative position within the boundary layer and the total number of zones within a snapshot, are presented. Residence times of individual zones within the measurement plane are subsequently analysed and their dependence on modal velocity and the total number of zones within a snapshot are also discussed (see Chapter 5).

Regarding pressure, a new method of pressure estimation from PIV – introduced by de Kat and Ganapathisubramani (2013) – is expanded in order to determine pressure fluctuations in the case of three-component volumetric velocity data. The proposed approach, together with a pseudo-Lagrangian and an Eulerian method are outlined and a linear uncertainty propagation analysis is performed to estimate the uncertainty on the resulting pressure fields (Chapter 3, section 3.1). A numerical assessment is then carried out (section 3.2) using the channel flow database from John's Hopkins University (Li et al., 2008; Perlman et al., 2007; Graham et al., 2013). The dependence of all methods on grid resolution and noise levels is tested, as well as the influence of time separation between frames on the Eulerian and pseudo-Lagrangian approaches and of

different convection velocities on Taylor's hypothesis. Time-resolved tomographic PIV experiments on a turbulent boundary layer are carried out (as outlined in Chapter 2) and the methods are applied on the acquired velocity volumes. The resulting pressure fields and their statistics are then compared with each other and with available DNS and direct pressure measurement results (sections 2.4.1 and 2.4.2, respectively). Assessment of the Taylor's Hypothesis approach in the case of two-component planar PIV data is also included for both the numerical and the experimental cases. The 2D approach, although performing significantly worse than the 3D one instantaneously, provides reliable results in a statistical sense and allow us to further analyse spatio-temporal characteristics of the pressure fluctuations in the case of the time-resolved planar PIV turbulent boundary layer (Chapter 6). Finally, since both pressure and velocity could be determined using the time-resolved planar database, pressure fluctuations across the internal layers and the TNTI are also outlined and an effort is made to link the structural information of pressure fluctuations with the presence of UMZs in the flow (Chapter 6).

Chapter 2

Turbulent boundary layer experiments

2.1 Velocity measurement with PIV

Particle image velocimetry (PIV) is a non-intrusive optical flow measurement technique that extends flow visualisation into quantitative measurements to provide instantaneous flow velocity fields. In this work, we used both planar and tomographic PIV (tomo-PIV) to measure velocity in a turbulent boundary layer (see following section). Therefore, in this section, the main operating principle of the technique will be outlined together with some relevant considerations about factors that affect measurement accuracy. These considerations will cover some general aspects of the technique but they will be mainly focused on additional requirements for tomographic systems and measurements in water flows, which are of interest here. An extensive review on PIV methods and applications can be found in Raffel et al. (2007) and Adrian and Westerweel (2011).

2.1.1 Principle of operation

The main operation principle of PIV is the estimation of particle displacements during a known time interval, dt. Initially, the flow is seeded with light-reflecting particles in such a way that their distribution is roughly homogeneous. A single plane in the flow (or a volume in tomographic systems) containing the area of interest is illuminated in two time instances (t and t' in figure 2.1a) by a pulsed light source and the particle location at both instances is captured by a digital device. The most common illumination sources are lasers, while for the imaging CCD and CMOS cameras are typically used. The recorded pair of images is then divided into interrogation windows that contain a certain number of particles. The displacement of each group of particles is subsequently estimated by cross-correlation algorithms between the two successive images that identify the most probable shift in space over the time interval dt. With the displacement and time interval known, the velocity vector maps can then be estimated. Finally, post processing techniques are applied to these vector fields to remove background noise,

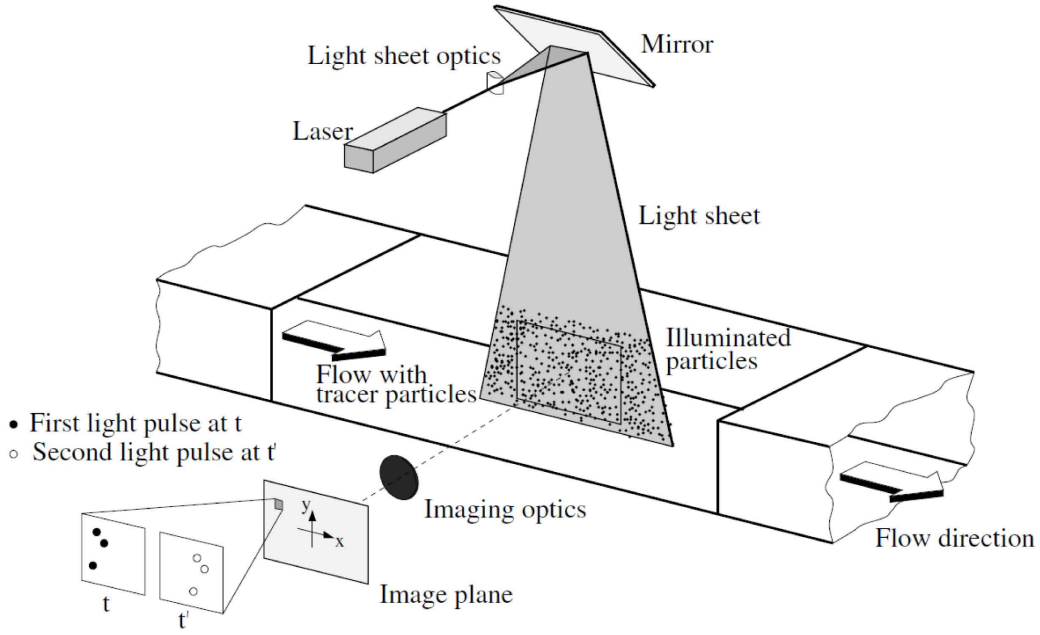

Figure 2.1. Sketch of a typical planar PIV set-up (from Raffel et al., 2007).

systematic error and spurious vectors. In the following sections some important aspects and limitations of the technique are described in more detail.

2.1.2 Seeding

As already mentioned above, PIV is based on the tracking of light-reflecting particles. Two aspects of seeding that are crucial in the measurement precision are the particle size and seeding density and they are separately discussed in the paragraphs that follow.

Particle size

The ability of the particles to accurately follow the fluid motion directly influences the precision of the measurement. Therefore, decreasing the particle size increases the flow tracking ability (Melling, 1997) and ensures the non-intrusiveness of the method. More specifically, following Tropea et al. (2007), the equation of motion for small particles is dominated by Stoke's drag and assuming that the acceleration of the particle approximates the fluid's acceleration, one can write for the difference of particle and fluid velocity (slip velocity):

$$\mathbf{u_p} - \mathbf{u} = \frac{2}{9}\frac{d_p^2(\rho_p - \rho)}{\mu}\frac{d\mathbf{u_p}}{dt} \tag{2.1}$$

where $\mathbf{u_p}$ and $\mathbf{u}$ are the particle's and fluid's velocities respectively, ρ_p and ρ their densities, d_p the particle diameter and μ the fluid's dynamic viscosity. From equation 2.1 it follows that, with

increasing particle diameter, flow tracking accuracy decreases. However, choosing neutrally buoyant particles ($\rho_p = \rho$) leads to precise flow tracking (Tropea et al., 2007). In liquid flows, as is the case of our experiments, this requirement can easily be met. Even so, small particle size is still required to ensure no particle interaction that would disturb the flow.

On the other hand, small particles have decreasing light scattering abilities. In liquid flows, the most common tracer particles used have diameters between 10–100 μm (Scarano, 2013), so for the common green laser source with wavelength $\lambda = 532$ nm, the light scattering belongs in the Mie regime, where the scattering cross-section increases roughly proportionally with the square of the particle diameter (Tropea et al., 2007). It is then obvious that a balance between the two requirements has to be found in order to obtain good image intensity and contrast in the PIV images but also achieve good tracking accuracy.

Seeding density

The concentration of particles is another important factor in PIV methods and especially for the spatial resolution of tomographic systems (Scarano, 2013). Similar to the discussion on the particle size above, there are different contradicting seeding density requirements that need to be balanced in order to achieve optimum accuracy for the measurements.

In particular, light intensity requirements in the case of tomographic systems are increased, since a three-dimensional volume needs to be illuminated rather than a plane. Additionally, for high-speed systems, which is also the case in our experiments, the operating frequency of the laser source is two or three orders of magnitude higher than the one in low-speed measurements something that results in a rapid decrease of output energy. These limitations with respect to the laser source can lead to insufficient illumination of the volume of interest and therefore dictate relatively high seeding densities to remedy the situation. Also, in terms of image analysis requirements, for tomographic systems, 5-10 particles per interrogation volume are required for an accurate cross-correlation analysis (Scarano, 2013). On the other hand, a maximum limit on the particle image density is imposed by the volumetric reconstruction algorithms as well as by the opacity of the fluid which leads to losses in optical transmission for very high seeding densities. Considering these factors and based on different experimental results, Scarano (2013) suggests for a typical tomographic set-up seeding densities of the order of 0.055 particles per pixel (ppp).

2.1.3 Image mapping and calibration

The main idea behind PIV imaging is the precise mapping of the actual particle locations onto the image plane through a mapping function. This essentially means that every three dimensional point, $\mathbf{x}$ in the real space, is mapped onto a two-dimensional point, $\mathbf{X}$, in the image plane through a function F (Soloff et al., 1997). In an ideal scenario this would be a linear relationship,

and the mapping function would simply be the magnification factor, M_0, defined as the ratio between the distances of the object and image planes from the center of the lens. However, in real measurements, there are many factors, such as variable magnification, projection effects, lens diffraction and other optical aberrations that make this relationship non-linear and in general the accurate point-wise estimation of F is impossible. However, approximations can be used to find an analytical expression for the mapping function, $\hat{F}$. Following Soloff et al. (1997), a polynomial expression for $\hat{F}$ can be used, which in its most generic form has a cubic dependence on x and y and quadratic dependence on z (Adrian and Westerweel, 2011). The coefficients of this expression can be found by inserting a 2D calibration target in the measurement location. The target usually consists of a flat surface with marks printed or engraved in known locations on a regular grid. A single image of the calibration target can be used to find the coefficients for the x and y dependence, which is usually the case in single-camera planar systems where the z-dependence cannot be resolved (Adrian and Westerweel, 2011). This leads to a perspective error due to the out-of-plane motion of particles, inherent in single-camera planar PIV, and it can only be minimised by using small viewing angles. In the case of tomo-PIV systems, where all the motions are taken into account, coplanar views of the calibration target in different z locations are needed, in order to also estimate the coefficients for the z dependence.

A further note should be made for the case of tomographic systems, where volumetric reconstruction algorithms require very high accuracy for the mapping function (less than 0.1 pixels, Wieneke, 2008), so a volume self-calibration technique is required in addition to the initial image calibration described above. The main concept behind this self-calibration technique is the accurate determination of 3D particle locations from the 2D particle images from the different cameras, by eliminating triangulation disparities. Preprocessing of the images and averaging disparity maps over a large number of recordings improves the accuracy of the technique and the whole procedure can also be repeated for further corrections. A more detailed description of the technique together with applications on experimental data can be found in Wieneke (2008).

Besides the need for a calibration procedure, the lens diffraction and other aberrations require some further practical consideration, especially for liquid flows (as is the case in our experiments) where optical distortions are amplified. More specifically, besides magnification, the combination of these effects, leads to a further increase of a particle's diameter on the image plane, d_τ (Adrian and Westerweel, 2011):

$$d_\tau \cong (M_0^2 d_p^2 + d_s^2 + d_a^2)^{1/2} \tag{2.2}$$

d_p is the actual particle diameter, M_0 is the magnification factor, d_s^2 is the particle diameter increase due to diffraction and d_a^2 is the particle diameter increase due to other aberrations. Based on the variation of bias and random errors on estimating the particle location, Adrian and Westerweel (2011) suggested an optimal particle diameter of $2d_r$, where d_r is the pixel size. The increase due to diffraction can be estimated as:

$$d_s = 2.44(1 + (M_0) f^{\#} \lambda \tag{2.3}$$

where $f^{\#}$ is the lens f-number and λ the wavelength of the light source. For a typical PIV setup and diffraction limited lens ($d_a^2 < d_s^2$), diffraction is the dominating term in equation 2.2 and d_s^2 the minimum possible particle diameter that can be obtained. Following Raffel et al. (2007) that can give an estimation about the depth of field, d_z, (equation 2.4), which is the width across which, particle images are well-focused.

$$d_z = 2f^{\#}d_s\frac{(M_0+1)}{M_0^2} \tag{2.4}$$

Because of the finite thickness of the laser sheet, Δz_0, $d_z > \Delta z_0$ is required in order to ensure that all illuminated particles are in-focus, and for a given magnification M_0, increasing the f-number is the only way to achieve this (Adrian and Westerweel, 2011). However, equation 2.3 also shows that for a given magnification, only a decrease of the f-number can minimise diffraction, sharpen the image but also allow more light into the sensor. Therefore, as with the case of particle size and seeding density, a balance has to be found, this time between tuning diffraction (2 pix) and ensuring in-focus particle images, depending on the specific experimental needs. This balance is quite crucial in tomographic experiments in water. The change of material leads to large optical distortions and the illumination of a volume dictates that all the particles inside the volume need to be in focus, so large f-numbers are needed for both reasons. On the other hand, as also mentioned above, tomographic set-ups have much higher light requirements and increasing the f-number will dramatically decrease the illumination of the acquired images, so reaching a balance in this situation is much more challenging.

2.1.4 Displacement interrogation

With the seeding, illumination and imaging considerations in mind, particle image pairs (or image time-sequences in high-speed measurements) are recorded and the next step is the estimation of the particle displacement and subsequently their velocity. The images are divided into small windows (interrogation windows or volumes for tomo-PIV usually square), which contain a certain amount of particles each. Each window intensity at a point $\mathbf{x}$, at time t, denoted by $I(\mathbf{x},t)$ is then correlated with the corresponding window intensity at a point $\mathbf{x}+\mathbf{s}$ and at the next time instant, $t+dt$ so as to find the displacement $\mathbf{s}$ that maximises this correlation:

$$R(\mathbf{s}) = \int I(\mathbf{x},t)I(\mathbf{x}+\mathbf{s},t+dt)\,\mathrm{d}\mathbf{x} \tag{2.5}$$

With $\mathbf{s}$ chosen as the most probable displacement, the velocity at each interrogation window can be found, by dividing with the known time interval, dt. It then follows that the size of the interrogation windows define the spatial resolution of the measurement. Smaller windows yield better resolution, provided that enough particles are included for an accurate correlation estimation. Spatial sampling can improve by overlapping interrogation windows at the expense of computational time. To avoid edge effects from rectangular windows and improve accuracy,

different window weight functions can be also used with round or elliptical Gauss functions being the most common ones, again at the expense of time. Further optimisation of the correlation estimation and possible random error reduction can be achieved by repeated interrogation of the same image pair (multi-pass approach, see Adrian and Westerweel, 2011). This approach is also often combined with a multi-grid technique, which decreases the size of the interrogation window at every pass. In this way, the window shift for the next pass is optimised using the information from the previous pass on the coarser grid. Finally, besides tuning of processing parameters for the raw particle images, a series of post-processing tools are also used for the acquired vector fields. These typically include the use of a median filter to remove outliers (spurious vectors) based on local information, interpolation to replace the removed vectors and also smoothing (commonly with a Gauss filter) to remove noise.

This subsection ends the theoretical background on velocity measurements using PIV methods. The different experimental techniques used in the present work are described in the section that follows.

2.2 Experimental facilities and equipment

All the PIV experiments presented in this work were carried out in the free water surface, recirculating water tunnel (figure 2.2) located at the Experimental Fluids Laboratory, which is a part of the Aerodynamics and Flight Mechanics Research Group, in the Faculty of Engineering and the Environment of the University of Southampton.

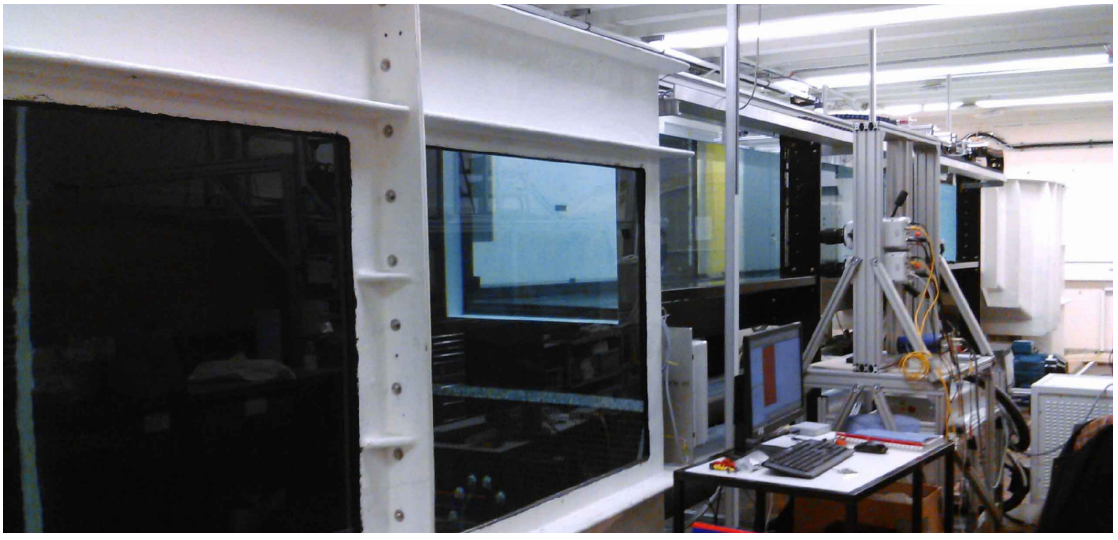

Figure 2.2. Recirculating water channel.

The channel consists of a contraction section, a settling tank with glass observation windows and a 6.75 long working section in between. This test section also has glass fitted (19 mm float glass) to provide visual access from the sides and the bottom. The overall length of the channel is 14 m with a rectangular cross-section of 1.2 m $\times$ 0.8 m (width $\times$ height) in the test section region.

A honeycomb together with a fine and a coarse turbulence grid are fitted in the contraction to reduce turbulence intensity level. Two axial flow impellers, driven by two identical electrical motors of 17.5 kW, produce maximum flow speeds of 1 m/s while double PVC return pipes complete the closed loop system.

All the experiments presented here are turbulent boundary layer experiments, where the water channel glass floor serves as the wall, with the light source and the cameras positioned at the side of the glass section (figure 2.2). The light beam (5 mm) was steered underneath the water channel and the PVC return pipes by a set of three mirrors positioned at 45° angles (figure 2.3) and then expanded by sheet (Planar PIV) or volume (Tomo-PIV) Lavision optics. The light

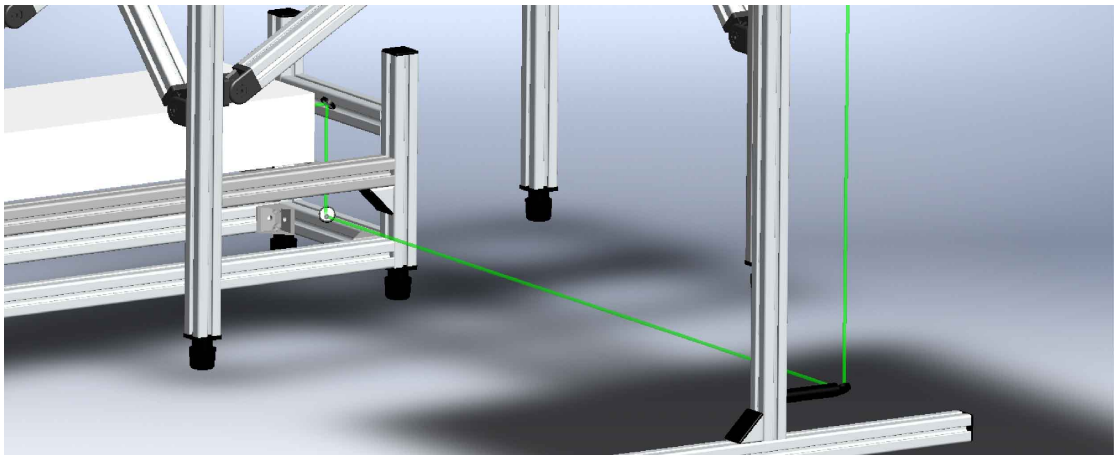

Figure 2.3. Laser beam steering.

source was mounted on a moving cart and the cameras were attached to an aluminium frame, designed and built specifically for these experiments such that it would minimise vibrations on the cameras, allow enough vertical space for them to translate for the different experimental needs and also allow the laser cart to move underneath. Finally, the volume or sheet optics together with the last beam-steering mirror were attached to a small aluminium frame positioned underneath the wind tunnel and aligned with the laser cart and the cameras accordingly.

For the illumination we used a Litron LDY 304 high-repetition rate (0.2–10 kHz) laser with output energies of up to 30 mJ at 1 kHz per cavity at 527 nm. The cameras used for all experiments were Phantom v641 32 GB high speed cameras, with a 2560×1600 pixels CMOS sensor (10 μm pixel size). The system was synchronised using a LaVision high-speed controller. The measurements were made around 5.5 m downstream of the contraction's end, in the mid-plane of the cross-section in the spanwise direction. The flow was tripped with a 10 cm wide 60-grit sandpaper at the end of the contraction section. For seeding, 50 μm neutrally buoyant polyamide particles (Vestosint 2157, $\rho = 1.016$ g/cm^3) were used. The diameter was chosen to achieve an adequate balance between light scattering and no-intrusiveness (see also section 2.1.2). The particles were mixed with washing liquid soap in order to increase the fraction of suspended particles and decrease floating or heavy particles gathering at the free surface and

water channel floor respectively. Mixing with washing liquid also decreases surface tension, preventing clustering of particles (Adrian and Westerweel, 2011).

2.3 Time-resolved planar PIV measurements

For the planar PIV measurements, a single camera was used, fitted with a Sigma f/2.8 EX DG Macro lens with a focal length of 105 mm at an aperture stop of f/16. The image, lens and object planes were parallel. The laser beam was expanded into a streamwise–wall-normal sheet ~ 2 mm (figure 2.4), using the LaVision divergent sheet optics (two telescope lenses to adjust the sheet thickness and a divergent cylindrical lens with a focal length of -20 mm to adjust the sheet height). The water height was 0.4 ± 0.05m and the average temperature T $= 23°$C.

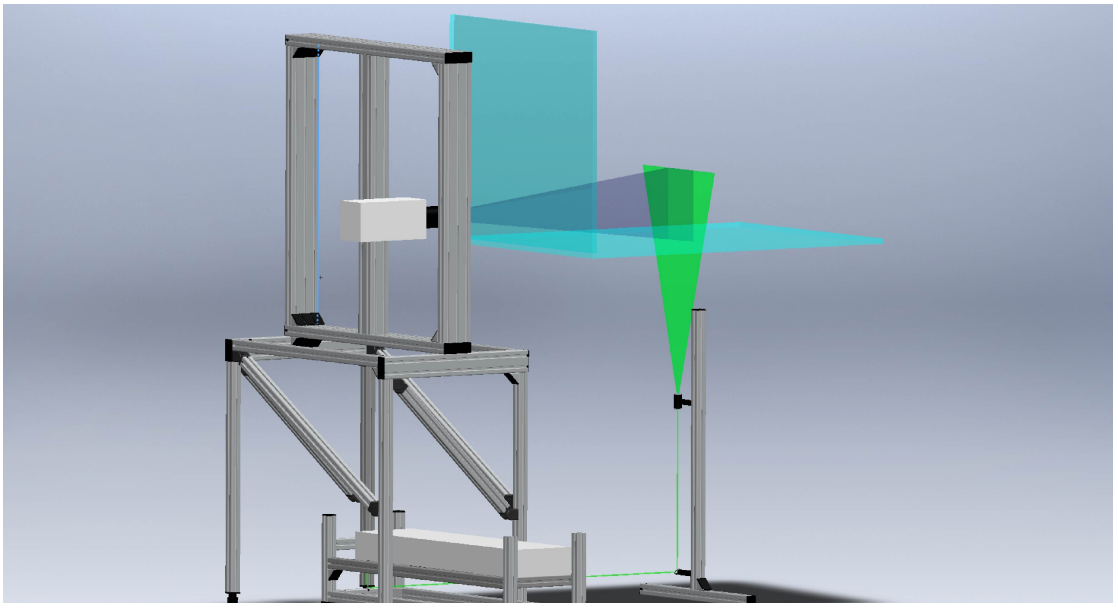

Figure 2.4. Schematic (rendering) of the Planar PIV setup.

The camera captured a field of view (FOV) approximately 0.07 m $\times 0.22$ m, in x and y (starting from the wall), at 800 Hz, with a resulting digital resolution of 11 pix/mm. We acquired approximately 405000 images using DaVis 8.2 (in 37 independent time-resolved sets of 10947 images each, covering around 500 seconds of flow in total), which we subsequently processed using the same software applying an iterative correlation with a final interrogation window of 16×16 pixels with an overlap factor of 50%.

The nominal flow conditions, based on the 400,000 evaluated vector fields were: $U_\infty \approx 0.97$ m/s, $\delta \approx 0.14$ m, $Re_\tau \approx 5300$, while the resulting FOV was approximately $0.5\delta \times 1.8\delta$ in the streamwise and wall-normal direction respectively (table 2.1). Following the temporal resolution limits discussed by Hutchins et al. (2009), due to the high acquisition frequency used, the dataset was additionally filtered in time, using a moving-average filter with a window length of 3 points in time resulting in an effective timestep of $dt^+ = 5.1$. The main aim of this set of experiments

Friction velocity *Re* number	Re_τ	5300
Momentum thickness *Re* number	Re_θ	12200
Friction velocity	U_τ	$0.036\ [\mathrm{m \cdot s^{-1}}]$
Viscosity	ν	$0.935 \cdot 10^{-6}\ [\mathrm{m^2 \cdot s^{-1}}]$
Domain length	$L_x \times L_y$	$0.5\delta \times 1.8\delta$ [m]
Interrogation volume size	$l_x^+ \times l_y^+$	54×54
Timestep	dt^+	1.7

Table 2.1. TBL flow, planar-PIV field ($Re_\tau = 5300$). Nominal flow conditions and processing parameters.

was to capture the boundary layer for long evolution times in order to get converged statistics and accurate structure/interface time-evolution information. For the latter and more specifically when identifying uniform momentum zones (for a detailed definition see Adrian et al., 2000) which is crucial in our analysis (see Chapter 4), potential pixel-locking effects were shown to be very important, to the point of masking the underlying modal velocities (see Kwon et al., 2014; de Silva et al., 2014, 2016). Thus, the temporal filtering applied to the data, also served to mitigate the bias error due to the pixel-locking inherent in the PIV images (see figure 2.5). Following de Silva et al. (2014), we computed the probability density function (pdf) of the

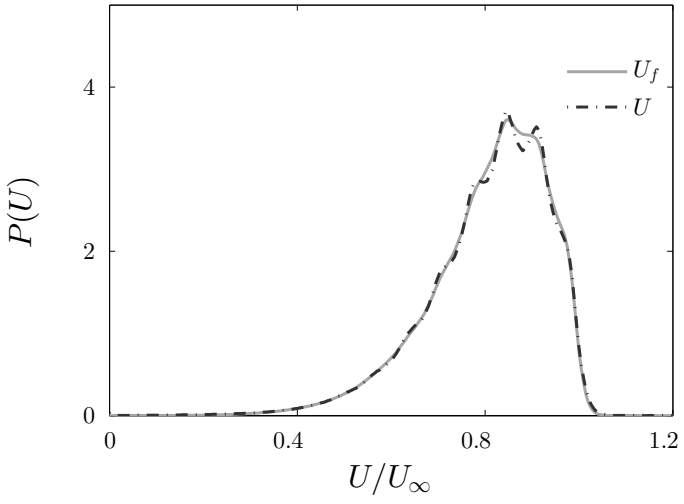

Figure 2.5. TBL flow, planar-PIV field ($Re_\tau = 5300$). Pdf of $\mathbf{u}/U_\infty$ for all the vectors below $y = 0.5\delta$ before and after filtering.

streamwise velocity for all the vectors below $y = 0.5\delta$. The results showed that even though pixel-locking effects were not severe, a clear bias was present in the pdf distribution (figure 2.5, dash-dot black line). Further to the temporal filtering, and based on the initial vector overlap (50%), a spatial 2D Gaussian filter with a 3×3 point kernel was applied, such that the effective spatial resolution of the data remained unaltered. After both spatial and temporal filtering, the resulting velocity pdf showed that the pixel-locking effects were suppressed (figure 2.5, solid grey line).

The mean velocity profile displayed a log region ($\kappa = 0.38$, $B = 4.1$ according to Österlund et al., 2000) for $200 < y^+ < 0.15\delta$ (figure 2.6). For the computation of the momentum thickness, θ, Spalding's law of the wall (Spalding, 1961) was employed for the region from the wall ($y^+ = 0$) up to the first independent velocity point (i.e the first point not influenced by the wall in the volume correlation process).

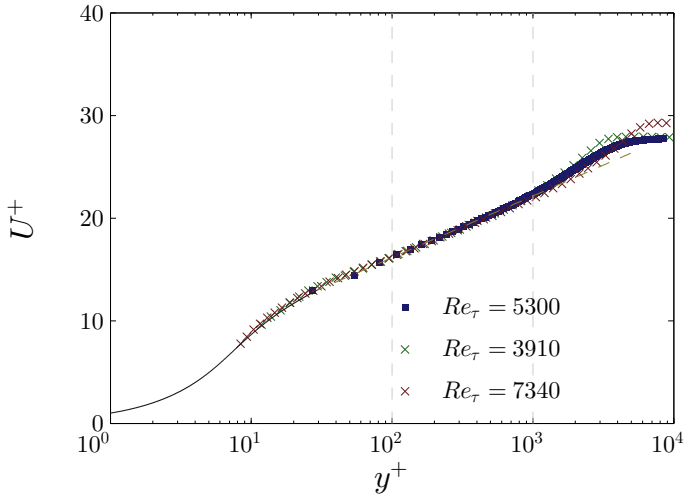

Figure 2.6. TBL flow, planar-PIV field ($Re_\tau = 5300$). Inner normalised mean velocity profile. $\times$ symbols are hotwire data from Hutchins et al. (2009). Solid black line denotes Spalding's law of the wall (Spalding, 1961).

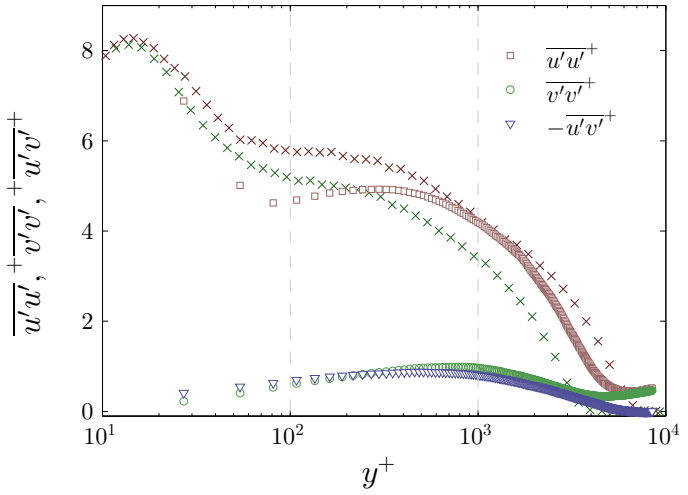

Figure 2.7. TBL flow, planar-PIV field ($Re_\tau = 5300$). Inner normalised turbulence intensity profiles of the streamwise and wall-normal components and Reynolds shear stress profile. $\times$ symbols are hotwire data from Hutchins et al. (2009).

This dataset was used for the analysis of the temporal evolution of the turbulent/non-turbulent interface and internal layers and the results are presented in chapters 4 and 5. Due to the large wall-normal extent of the FOV, it also served for the characterisation of the boundary layer flow

(identical flow conditions as in section 2.4.2). The pressure estimation method (analysed and validated in chapter 3), was also applied to the velocity data, and results on the structure of pressure fluctuations and their association with internal layers and the freestream boundary are presented in chapter 6. The variety of applications for this dataset, called for some comparison with other published studies with better spatial resolution in order to evaluate the range of applicability. Turbulence intensity profiles of the streamwise and wall-normal components as well as the Reynolds stress profile are shown in figure 2.7, together with streamwise turbulence intensity profiles from hot-wire data (Hutchins et al., 2009) of a turbulent boundary layer with a higher and lower Reynolds number ($Re_\tau = 3910$ and 7340). The profile of the current dataset lies in between those of the two delimiting Reynolds number datasets for the largest part of the boundary layer. Spatial resolutions effects, inherent to PIV, can be seen close to the wall, however in cases where large structures are the main interest, these effects are not expected to influence the results.

2.4 Time-resolved tomographic PIV measurements

Two different tomographic PIV experiments were carried out, at the same streamwise location with varying wall-normal extend. For both of them, the same optics, camera setup and calibration process – outlined below – were used.

Camera and optics

The initial laser beam, steered through the set of mirrors (figure 2.3), was enlarged with a beam expander, before being finally expanded into a 20 mm thick volume through the combination of LaVision Module A and C Volume Optics (figure 2.9b). The end volume was cropped to obtain a rectangular cross-section and well-defined edges using a LaVision adjustable aperture. Four cameras were used in a cross-like configuration. Elsinga et al. (2006) showed that the quality of the tomographic reconstruction is very high (larger than 0.9) when four cameras are used, while Scarano (2013) noted than a cross-like configuration results in higher accuracy than a linear one, especially for small aperture (planar) angles, as is the case here. The bottom two cameras were positioned normal to the volume middle plane, while the top ones were inclined downwards at approximately 10° (figure 2.8). The planar angle between both sets of cameras was $\sim 15^\circ$. For tomographic setups, the reconstruction quality is shown to be optimal for planar angles around 30° (Elsinga et al., 2006; Scarano, 2013), however in our case larger angles would not be possible due to practical restrictions. The aluminium frame where the cameras where mounted, did not allow for larger spacing between the cameras and Scheimpflug effects would become much more pronounced for larger viewing angles. Therefore, the goal was to maximise the accuracy (around 0.75 for the reconstruction quality, Elsinga et al. 2006) within the given constraints. It should also be noted here that, with respect to the vertical angles, for the intermediate dataset outlined below (sec. 2.4.2), the cameras were further inclined downwards in order to capture

the wall. This requirement was the most challenging one, due to the size of the cameras – that did not allow for large angles and at the same time full overlap of FOV for the tomographic reconstruction – the steel bar in front of the glass section (figure 2.11) – that obstructed part of the window – and the large optical distortions arising for large viewing angles.

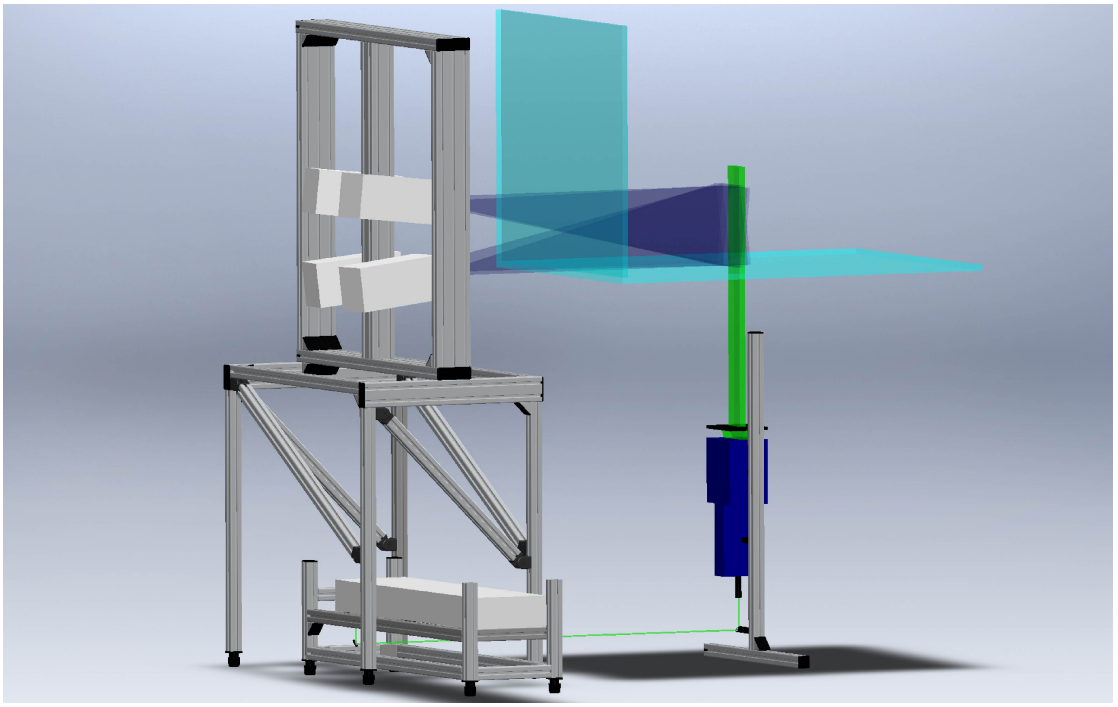

Figure 2.8. Schematic (rendering) of the tomo-PIV setup.

Calibration

Tomo-PIV requires a volume camera calibration. In our work, we used 3 coplanar equidistant views ($dz = 10$ mm) of a 2D calibration plate (figure 2.9a) to calibrate the four cameras, employing a polynomial fit.

The three equidistant views at spanwise locations $z = -10$, 0, and 10 mm corresponding to the back, middle, and front plane of the volume were selected such that the whole measurement volume was encompassed, as proposed by the LaVision manual. To translate the plate along the z-axis we mounted it on a single-axis motor-driven Velmex BiSlide positioning system and it could be translated in equidistant steps in the spanwise direction through a VMX stepping motor controller.

2.4.1 Long vertical field of view ($\approx 2\delta$)

For this set of experiments, the cameras were fitted with Sigma f/2.8 EX DG Macro lenses with a focal length of 105 mm and an aperture stop of f/11. The laser was used to illuminate a volume

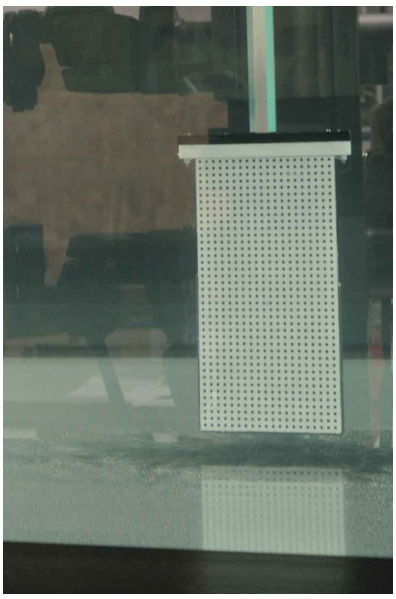

(a) Translating calibration plate.

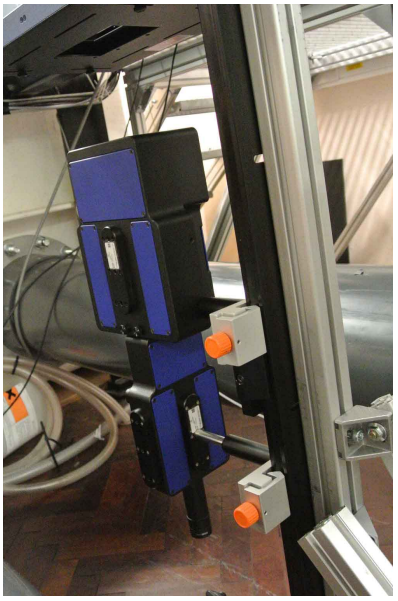

(b) Beam expander, volume optics and adjustable aperture.

Figure 2.9. Tomo-PIV equipment.

approximately 0.08 m $\times$ 0.18 m $\times$ 0.02 m, in x, y, and z, with a resulting digital resolution of 13 pix/mm. The water height was 0.37 m and the average temperature T $= 13°$C.

Friction velocity *Re* number	Re_τ	2370
Momentum thickness *Re* number	Re_θ	4840
Friction velocity	U_τ	$0.0254\ [\mathrm{m \cdot s^{-1}}]$
Viscosity	ν	$1.16 \cdot 10^{-6}\ [\mathrm{m^2 \cdot s^{-1}}]$
Domain length	$L_x \times L_y \times L_z$	$0.8\delta \times 2\delta \times 0.18\delta$ [m]
Interrogation volume size	$l_x^+ \times l_y^+ \times l_z^+$	$104 \times 104 \times 104$
Timestep	dt^+	0.38
Voxel size	l_v^+	1.62

Table 2.2. TBL flow, tomo-PIV field ($Re_\tau = 2300$, long vertical field of view). Nominal flow conditions and processing parameters.

Using DaVis 8.2, we acquired a set of 3300 particle images at 1.45 kHz, which we subsequently processed with the same software using an iterative volume correlation with a final interrogation volume of $64 \times 64 \times 64$ pixels with an overlap factor of 75%. The nominal flow conditions, based on the 3,300 evaluated vector fields were: $U_\infty \approx 0.66$ m/s, $\delta \approx 0.10$ m, $Re_\tau \approx 2400$, while the resulting FOV was approximately $0.8\delta \times 2\delta \times 0.18\delta$ in the streamwise, wall-normal and spanwise direction respectively (Table 2.2).

The mean velocity profile displayed a log region ($\kappa = 0.38$, $B = 4.1$ according to Österlund et al., 2000) for $200 < y^+ < 0.15\delta$ (figure 2.10). For the computation of the momentum thickness, θ, Spalding's law of the wall (Spalding, 1961) was employed for the region from the wall ($y^+ = 0$)

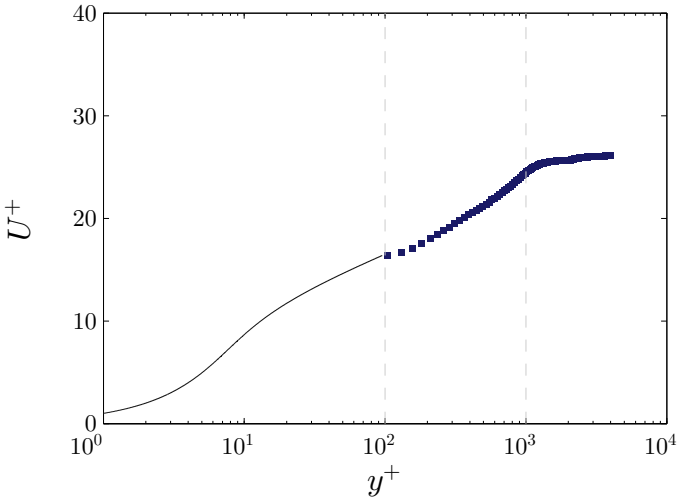

Figure 2.10. TBL flow, tomo-PIV field ($Re_\tau = 2300$, long vertical field of view). Inner normalised mean velocity profile. Solid black line denotes Spalding's law of the wall (Spalding, 1961).

up to the first independent velocity point (i.e the first point not influenced by the wall in the volume correlation process).

This dataset was used for the experimental assessment of the pressure determination methods outlined in chapter 3, section 3.1.

2.4.2 Intermediate vertical field of view ($\approx 2/3\delta$)

The setup for this set of experiments was very similar to the one of the long vertical field of view in the previous section (sec. 2.4.1) with just a few notable differences. The cameras were fitted with Nikon f/4 ED-IF AF Micro-Nikkor lenses with a focal length of 200 mm with an aperture stop of f/22 to reduce optical distortions (see also section 2.1.3). The bottom cameras were also slightly inclined downwards (4°) in this experimental set, in order to capture the wall. The planar angle remained roughly the same (15°) for both sets. The final volume was 0.04 m $\times$ 0.09 m $\times$ 0.02 m, in x, y, and z, with a resulting digital resolution of 27 pix/mm. The water height was 0.4 $\pm$0.05m and the average temperature T $=$ 23°C.

Using DaVis 8.2, we acquired 10 independent sets of 5468 particle images each, at 1.45 kHz, covering 38 seconds of flow, which we subsequently processed with the same software using an iterative volume correlation with a final interrogation volume of $64 \times 64 \times 64$ pixels and an overlap factor of 75%. For this dataset, the main aim was to capture the majority of the boundary layer in the wall-normal direction but also attain a high enough spatial resolution, as opposed to the first, long vertical field of view experiment. The nominal flow conditions were identical to the planar measurements (section 2.3) where the whole boundary layer height was captured and the resulting FOV was approximately $0.3\delta \times 0.7\delta \times 0.15\delta$ in the streamwise, wall-normal and spanwise direction respectively (table 2.3).

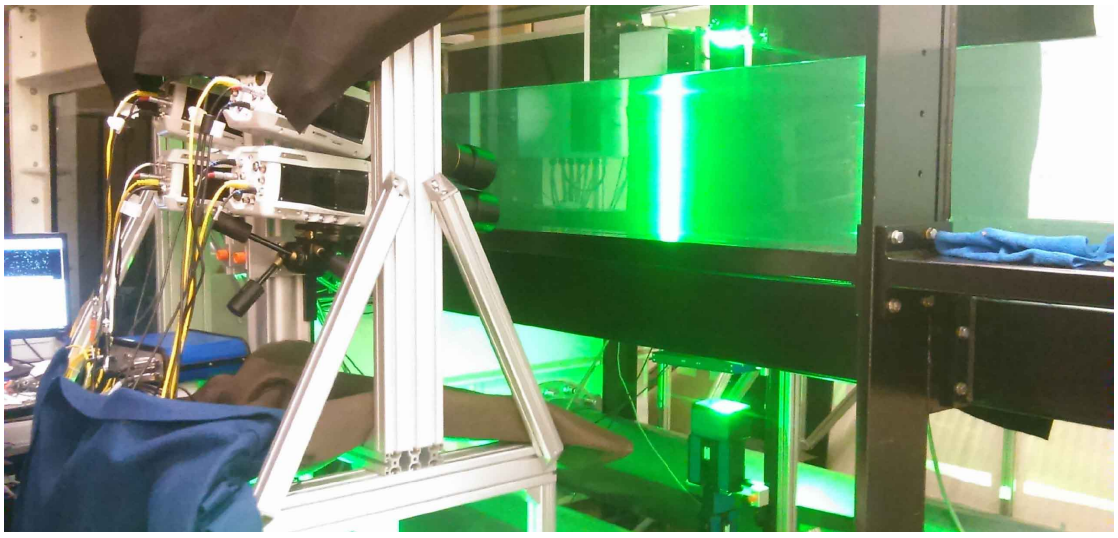

Figure 2.11. TBL flow, tomo-PIV field (Intermediate vertical field of view). Experimental setup capture.

Friction velocity *Re* number	Re_τ	5300
Momentum thickness *Re* number	Re_θ	12200
Friction velocity	U_τ	$0.036\ [\mathrm{m}\cdot\mathrm{s}^{-1}]$
Viscosity	ν	$0.935\cdot10^{-6}\ [\mathrm{m}^2\cdot\mathrm{s}^{-1}]$
Domain length	$L_x\times L_y\times L_z$	$0.3\delta\times0.7\delta\times0.15\delta$ [m]
Interrogation volume size	$l_x^+\times l_y^+\times l_z^+$	$92\times92\times92$
Timestep	dt^+	0.95

Table 2.3. TBL flow, tomo-PIV field ($Re_\tau = 5300$, intermediate vertical field of view). Nominal flow conditions and processing parameters

This dataset was also used for assessment of the pressure determination methods outlined in chapter 3, section 3.1.

Chapter 3

Determination of pressure fluctuations from PIV

In this chapter, a pressure estimation method based on Taylor's hypothesis, initially developed by de Kat and Ganapathisubramani (2013) and applied to 3C planar PIV data, is analysed and expanded to account for volumetric velocity data, while its performance is also compared with an Eulerian and a pseudo-Lagrangian approach in both synthetic and experimental data. More specifically, the corresponding uncertainty estimates of all methods are presented (section 3.1.5) and the three approaches are subsequently validated using synthetic PIV data of a turbulent channel flow (section 3.2) and are also applied in experimental turbulent boundary layer data of two different Reynolds numbers (sections 3.4 and 3.3).

3.1 Methodology

As mentioned in chapter 1, Navier–Stokes (NS) equations provide the link between pressure and velocity that can be exploited to extract full pressure fields from velocity data. In this section and throughout the rest of this thesis, we use the coordinate system x, y, and z to denote the streamwise, wall-normal and spanwise directions respectively and u, v, and w to denote the corresponding velocity components. The incompressible NS equations can be rewritten, solving for the pressure gradient, as follows:

$$\nabla p = -\rho \left\{ \frac{\partial \mathbf{u}}{\partial t} + (\mathbf{u} \cdot \nabla)\,\mathbf{u} - \nu \nabla^2 \mathbf{u} \right\} \tag{3.1}$$

where $\mathbf{u}$ is the velocity vector field, p is the pressure field, ρ is the fluid's density and ν its kinematic viscosity. Taking the divergence of the pressure gradient, the result is a Poisson equation 3.2, which can be solved by spatial integration using a Poisson solver (see de Kat and

Ganapathisubramani, 2013). The boundary conditions used are Neumann using equation 3.1.

$$\begin{aligned}\nabla \cdot \nabla p &= \frac{\partial^2 p}{\partial x^2} + \frac{\partial^2 p}{\partial y^2} + \frac{\partial^2 p}{\partial z^2} \\ &= \frac{\partial}{\partial x}\left(\frac{\partial p}{\partial x}\right) + \frac{\partial}{\partial y}\left(\frac{\partial p}{\partial y}\right) + \frac{\partial}{\partial z}\left(\frac{\partial p}{\partial z}\right)\end{aligned} \tag{3.2}$$

The convective and viscous terms in equation 3.1 can be readily computed, from full 3D velocity fields. If time information is also provided (time-resolved measurements), the acceleration can be computed using an Eulerian or a pseudo-Lagrangian approach and the pressure gradients are fully defined. It is important to also note that, by taking the divergence of the pressure gradient and using the continuity equation, the viscous term drops out in the Poisson formulation.

3.1.1 Eulerian approach (EU)

Assuming that the temporal velocity gradient is approximately constant or linear in time within the time interval between the two snapshots, dt, and for all spatial locations (Jakobsen et al., 1997), the acceleration at time t (equation 3.3), as well as the pressure gradient (equation 3.4) can then be evaluated.

$$\frac{\partial \mathbf{u}}{\partial t} = \frac{1}{2dt}\left\{\mathbf{u}|_{(\mathbf{x},t+dt)} - \mathbf{u}|_{(\mathbf{x},t-dt)}\right\} \tag{3.3}$$

$$\nabla p = -\rho\left\{\frac{1}{2dt}\left\{\mathbf{u}|_{(\mathbf{x},t+dt)} - \mathbf{u}|_{(\mathbf{x},t-dt)}\right\} + (\mathbf{u}\cdot\nabla)\,\mathbf{u} - \nu\nabla^2\mathbf{u}\right\} \tag{3.4}$$

For time-resolved data, another common approach to compute the material acceleration is by following particle trajectories (Lagrangian). A pseudo-Lagrangian approach is outlined in the next section.

3.1.2 Pseudo-Lagrangian approach (pLA)

Following de Kat and van Oudheusden (2012), we define a pseudo-Lagrangian description of the flow by reconstructing fluid-parcel trajectories using a pseudo-tracking approach. More specifically, using Taylor's expansion for a time interval, τ and following an iterative procedure, any fluid-parcel particle trajectory can be estimated for iteration k, as follows:

$$\mathbf{x}_p^k(t,\tau) = \mathbf{x} + \mathbf{u}(\mathbf{x},t)\tau + \frac{1}{2}\frac{D\mathbf{u}^k}{Dt}(\mathbf{x},t)\tau^2 \tag{3.5}$$

At the next iteration level, indicated with the subscript $k+1$, the material acceleration is then computed (equation 3.6) and the pressure gradient (equation 3.2) can be fully determined (equation 3.7).

$$\frac{D\mathbf{u}}{Dt}^{k+1}(\mathbf{x},t) = \frac{\mathbf{u}(\mathbf{x}_p^k(t,\Delta t),t+\Delta t) - \mathbf{u}(\mathbf{x}_p^k(t,-\Delta t),t-\Delta t)}{2\Delta t} \tag{3.6}$$

$$\nabla p = -\rho \left\{ \frac{D\mathbf{u}}{Dt}(\mathbf{x},t) - \nu\nabla^2\mathbf{u} \right\} \tag{3.7}$$

Even though here we focus only on a pseudo-Lagrangian approach, for completeness it should also be noted that recently, new techniques have been developed that allow for highly accurate, fully Lagrangian particle tracking information. Most notably, Schanz et al. (2013, 2014) developed the 'Shake the box' algorithm (STB) which, for a single timestep, reconstructs a particle track for previous timesteps, predicts the position of the particle in the next timestep and corrects this position by shaking the particles to fit in the measurement volume, using image matching (Schanz et al., 2014). The procedure is completed by finding new particles and their tracks, removing those that left the volume and repeating the image matching where necessary. It was shown that when converged, STB can accurately detect almost all particles residing in the measurement volume with fairly low position errors. In this way, velocity gradients and material acceleration information – that are very difficult to estimate accurately from PIV data – become available and provide a very promising input to the pressure estimation schemes discussed above.

Regardless of the reconstruction method used however, the acquisition of three-dimensional, time-resolved data is challenging and in cases where this is not possible, alternative methods have to be used. For example, when time-resolution is not sufficient, a Taylor's hypothesis approach can be used, which is described in the following section.

3.1.3 Taylor's hypothesis approach (TH)

Taylor's hypothesis states that, if the mean velocity is significantly larger than turbulent fluctuations, turbulent eddies are 'frozen' in time and are simply convected by the mean flow (Taylor, 1938). In the case of grid generated decaying turbulence, for which it was originally developed, the hypothesis was shown to perform well (Favre et al., 1955). In shear flows however, which are of interest here, the hypothesis breaks down (Lin, 1953) since the turbulent fluctuations are transported with convection velocities that differ from the mean (Fisher and Davies, 1964; Zaman and Hussain, 1981; Kim and Hussain, 1993; Davoust and Jacquin, 2011, among others). Structures of different sizes are expected to behave differently and even different parts of the same structure might move with different velocities as the structure evolves over time, making a complete definition of the convection velocity quite challenging (Krögstad et al., 1998). Previous studies have used spectral information to estimate it (del Álamo and Jiménez, 2009; Davoust and Jacquin, 2011), showing that small scales are indeed travelling with the local mean, following the original form of Taylor's hypothesis, however this isn't true for low frequencies

corresponding in larger modes. De Kat and Ganapathisubramani (2013) showed that using an in-plane filtered axial velocity in a turbulent jet as the convection velocity, yields more promising results for pressure, than using the mean. More recently, Geng et al. (2015) tested the validity of using the mean as the convection velocity in the case of a turbulent channel and concluded that the assumption holds well in the logarithmic and outer layer but fails close to the wall. In the present study, different convection velocities will be tested, so a generalised form of Taylor's hypothesis, with a spatially changing convection velocity, $\mathbf{U_c} = (U_c, V_c, W_c)$ will be used:

$$\frac{D\mathbf{u}'}{Dt} = \frac{\partial \mathbf{u}'}{\partial t} + (\mathbf{U_c} \cdot \nabla)\,\mathbf{u}' = 0 \tag{3.8}$$

When only volumetric velocity snapshots are available (3D-volumetric PIV or DNS), the missing temporal information can then be extracted from equation 3.8 as:

$$\frac{\partial \mathbf{u}'}{\partial t} = -(\mathbf{U_c} \cdot \nabla)\,\mathbf{u}' \tag{3.9}$$

To examine the implications of using this hypothesis on the governing equations, we start from the momentum equation, rewriting it so as to include the chosen convection velocity (see Geng et al., 2015) and using Reynold's decomposition:

$$\frac{\partial \mathbf{u}}{\partial t} = -\left\{\frac{1}{\rho}\nabla p + (\mathbf{u}\cdot\nabla)\,\mathbf{u} - \nu\nabla^2\mathbf{u}\right\} \Rightarrow$$

$$\frac{\partial \mathbf{u}'}{\partial t} = -(\mathbf{U_c}\cdot\nabla)\,\mathbf{u}' - \left\{\frac{1}{\rho}\nabla p + ([\mathbf{U}-\mathbf{U_c}]\cdot\nabla)\mathbf{u}' + (\mathbf{u}'\cdot\nabla)\,\mathbf{u} + (\mathbf{U}\cdot\nabla)\,\mathbf{U} - \nu\nabla^2\mathbf{u}\right\} \tag{3.10}$$

It then follows that, Taylor's hypothesis is well satisfied, if the *sum* of the pressure, convective and viscous terms (enclosed in brackets) is negligible (Geng et al., 2015).

$$\frac{1}{\rho}\nabla p + ([\mathbf{U}-\mathbf{U_c}]\cdot\nabla)\mathbf{u}' + (\mathbf{u}'\cdot\nabla)\,\mathbf{u} + (\mathbf{U}\cdot\nabla)\,\mathbf{U} - \nu\nabla^2\mathbf{u} = 0 \Rightarrow$$

$$\nabla p = -\rho\left\{([\mathbf{U}-\mathbf{U_c}]\cdot\nabla)\mathbf{u}' + (\mathbf{u}'\cdot\nabla)\mathbf{u} + (\mathbf{U}\cdot\nabla)\,\mathbf{U} - \nu\nabla^2\mathbf{u}\right\} \tag{3.11}$$

It is the last equation, that fully determines the pressure gradient, which is subsequently integrated and solved (equation 3.2). In regions where the choice of convection velocity is not correct, the pressure gradient equation is no longer balanced and the resulting pressure fields start to deviate from the exact solution.

3.1.4 Taylor's hypothesis using 2D velocity data (TH-2D)

Recent developments in PIV and PTV techniques (see for example Schanz et al., 2016) show that, in a scientific context, the progress of pressure estimation methods is clearly oriented towards state-of-the-art equipment to acquire high-resolution velocity data and complex computational algorithms to subsequently extract pressure. On the other hand, for cases when such equipment is not accessible or affordable and especially in an industrial context, minimisation

of cost and complexity of experiments and processing time is critical, even at the expense of accuracy. It is therefore valuable to quantify how loss of information (either in terms of time or space) affects the accuracy of pressure estimation methods, so that a balance between cost and performance can be found for different applications. To this end, the above analysis shows that Taylor's hypothesis can be used to estimate pressure in a significantly simplified manner, both in terms of computational cost and equipment (time information is not needed). A detailed comparison of the performance of this method with most other pressure estimation techniques available can be found in Blinde et al. (2016) for the case of a 3D separated flow. In the present work, both a numerical and an experimental assessment of the method are presented for a 3D channel and turbulent boundary layer flow respectively. However, such applications, although simplified, still require the knowledge of the full 3D velocity field, which can be very challenging to acquire experimentally outside of very-well equipped scientific laboratories. For this reason, apart from the 3D estimations we further use TH to estimate pressure in both the numerical and the experimental study (see sections 3.2 and 3.4, 3.3 respectively) for the case of 2D velocity data (effectively neglecting temporal and reducing spatial information), that can be acquired from the simplest form of PIV (2D-planar). Instead of using the 3D volumetric velocity fields, we extract each individual streamwise-wall normal plane of every volume, we subsequently compute pressure using the same equations (3.8 and 3.11) in their 2D form and we compare the results with the ones acquired using the full 3D information. In this way, we can quantify the loss of accuracy in pressure estimation when time or space information is not available and potentially suggest whether the estimated result is valuable and to which extent for different applications.

3.1.5 Pressure estimation uncertainty

In this work, pressure is estimated from experimental – and therefore imperfect – velocity data. It is important to evaluate how an initial uncertainty, ε_u, on the velocity field would propagate down to the derived quantity, namely here, pressure. Following a linear uncertainty propagation procedure, outlined by de Kat and van Oudheusden (2012) (for more details see JCGM 100:2008, 2008) each measured quantity, x, involved in the estimation of a derived quantity, r, is associated with its uncertainty, ε_x, and its sensitivity coefficient, $\theta_x = \partial r/\partial x$, which determines the influence of this uncertainty on the uncertainty of the derived quantity. The product of the uncertainty with the sensitivity coefficient gives the contribution of each measured quantity, x, towards the total uncertainty of the derived quantity. This total uncertainty, ε_r, is proportional to the square root of the sum of the square of the contributions from all the measured quantities involved in the derivation. More specifically, using equation 3.4, the total uncertainty on the pressure field using EU can be written as:

$$\varepsilon_{P,EU} \propto \varepsilon_u \sqrt{\Big[\underbrace{\frac{1}{2}\Big(\frac{h}{\Delta t}\Big)^2}_{I} + \underbrace{\frac{|\mathbf{u}|^2}{2}}_{II} + \underbrace{h^2\frac{|\nabla u|^2+|\nabla v|^2+|\nabla w|^2}{3}}_{III}} \tag{3.12}$$

where $\varepsilon_{P,EU}$ is the total uncertainty on the estimated pressure field, Δt is the time separation of the velocity fields, $|\mathbf{u}|$ is the magnitude of the velocity vector, ∇u, ∇v, and ∇w are the magnitudes of the streamwise, wall-normal and spanwise velocity gradients respectively and $h = \Delta x = \Delta y = \Delta z$, is the grid resolution.

Considering a linear fluid-parcel trajectory and following equations 3.5 and 3.6 once, the total uncertainty on the estimated pressure field for pLA is:

$$\varepsilon_{P,pLA} \propto \quad \varepsilon_u \sqrt{\Big[\underbrace{\frac{1}{2}\Big(\frac{h}{\Delta t}\Big)^2}_{I} + \underbrace{h^2 \frac{|\nabla u|^2+|\nabla v|^2+|\nabla w|^2}{6}}_{III}} \tag{3.13}$$

Finally, for TH, following equation (3.11), the total uncertainty on the resulting pressure field can be estimated as follows:

$$\begin{aligned} \varepsilon_{P,TH} \propto \quad & \varepsilon_{U_c} \sqrt{\Big[\underbrace{h^2 \frac{|\nabla u'|^2+|\nabla v'|^2+|\nabla w'|^2}{3}}_{III}\Big]} + \varepsilon_U A_U \\ & + \varepsilon_u \sqrt{\Big[\underbrace{\frac{1}{2}|\mathbf{U}-\mathbf{U_c}|^2+\frac{|\mathbf{u}'|^2}{2}}_{II} + \underbrace{h^2 \frac{|\nabla u|^2+|\nabla v|^2+|\nabla w|^2}{3}}_{III}\Big]} \end{aligned} \tag{3.14}$$

where $\varepsilon_{P,TH}$ is the total uncertainty on the estimated pressure field, ε_{U_c} is the uncertainty on the convection velocity estimation, ε_U is the uncertainty on the mean velocity, $|\mathbf{u}'|$ is the magnitude of the velocity fluctuation, $|\mathbf{U}|$ is the magnitude of the mean velocity vector and $|\nabla u'|, |\nabla v'|, |\nabla w'|$ are the magnitudes of the gradient of the streamwise, wall-normal and spanwise velocity fluctuation components respectively. With A_U we denote the sensitivity coefficient of the uncertainty on the mean velocity, which is defined as follows:

$$\begin{aligned} A_U = \quad & \varepsilon_U \sqrt{\Big[\frac{1}{2}|\mathbf{U}-\mathbf{U_c}|^2 + h^2 \frac{|\nabla u|^2+|\nabla v|^2+|\nabla w|^2}{3}\Big]} \\ & + \varepsilon_U \sqrt{\Big[+\frac{|\mathbf{U}|^2}{2} + h^2 \frac{|\nabla u'|^2+|\nabla v'|^2+|\nabla w'|^2}{3}\Big]} \\ & + \varepsilon_U \sqrt{\Big[h^2 \frac{|\nabla U|^2+|\nabla V|^2+|\nabla W|^2}{3}\Big]} \end{aligned} \tag{3.15}$$

For all methods, the letters I, II, and III are used to denote the uncertainties corresponding to the time, velocity and velocity gradient terms respectively, for reference in the sections that follow. For TH only the terms related to the uncertainty in the total velocity field, ε_u, and in the convection velocity, ε_{U_c} are highlighted, since for well converged mean fields, ε_U is expected to be small (as a statistical uncertainty) and its contribution inconsequential with respect to the other terms. It should also be noted here that, for all methods, the uncertainty from the viscous term is neglected because, as mentioned above, the viscous term present in the pressure gradient equation drops out in the Poisson formulation.

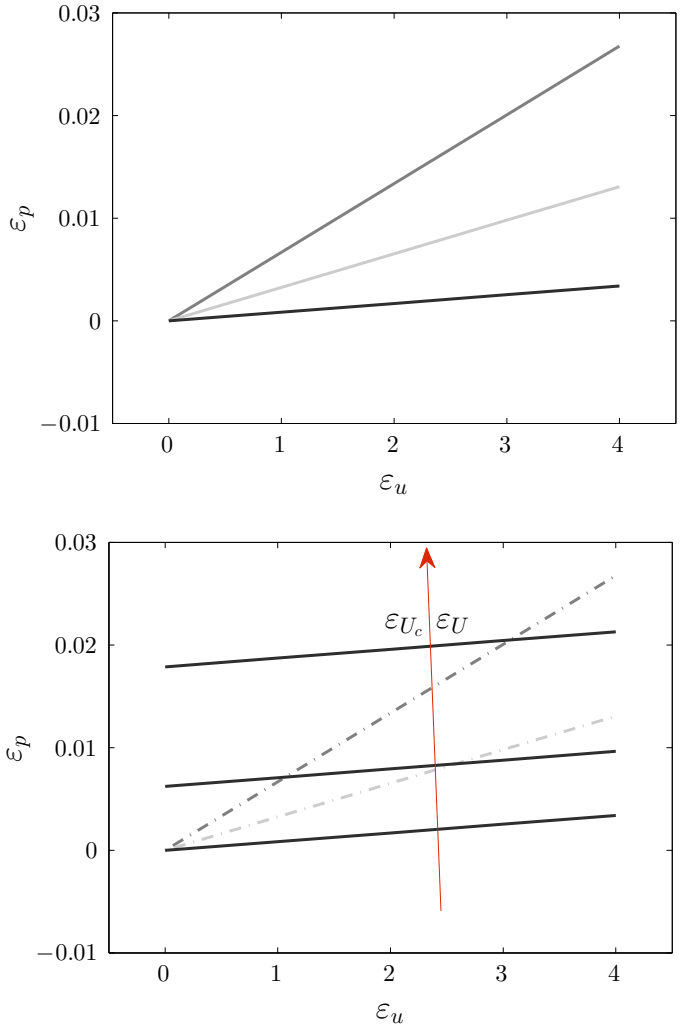

Figure 3.1. Total uncertainty on the pressure estimation following equation (3.12)–(3.14) for all methods (top). Total uncertainty on the pressure estimation for TH with increasing levels of ε_{U_c} and ε_U (bottom). Colours: TH, EU, pLA.

Using equations 3.12–3.14 on a single DNS velocity volume (see sect. 3.2) – to have a realistic estimates of the velocity and gradient terms – the total uncertainty on the pressure estimation for each method is computed, for increasing levels of measurement uncertainty on the velocity field (figure 3.1, top). For TH (using the streamwise mean velocity as the convection velocity), different levels of the convection velocity uncertainty, ε_{U_c}, and mean velocity uncertainty, ε_U, are also presented (figure 3.1, bottom). As already mentioned, for zero measurement noise on the velocity field, both EU and pLA have zero uncertainty propagating on the estimated pressure. With increasing velocity uncertainty level, there is a linear increase in the resulting uncertainty in pressure for both methods, with EU having a much steeper increase due to the extra velocity term, *II*, in equation 3.12. For TH, if both the uncertainty on the convection and mean velocity are zero, the propagation uncertainty on the pressure is zero as well (figure 3.1 top and lower limit, figure 3.1, bottom). However, a perfect estimate for the convection velocity is unlikely to be found, so a more realistic situation would include uncertainties on both the convection

and the mean velocity (figure 3.1, bottom) with the latter being minimal, as already mentioned above. In the case of a moderate uncertainty on the convection velocity, $\varepsilon_{U_c} = 4\%$, and a small uncertainty on the mean velocity, $\varepsilon_U = 0.5\%$ (middle black line in figure 3.1, bottom), TH appears to outperform EU for all velocity uncertainty levels and pLA for uncertainties on the velocity larger than 2%, (figure 3.1, top). Finally, for a moderate level of uncertainty on both convection and mean velocity $\varepsilon_{U_c} = 4\%$, $\varepsilon_{U_c} = 2\%$, TH shows larger uncertainty with respect to pLA for all velocity uncertainty levels and provides slightly more accurate pressure estimates than EU for velocity measurement uncertainties of 4 and 5%, (upper limit, figure 3.1, bottom).

To conclude, for small uncertainty levels on the convection mean velocity estimation TH can provide a good accuracy for pressure estimation with respect to the other two approaches, especially for high velocity measurement uncertainties (which are likely to occur in high-Reynolds-number measurements due to the large dynamic range in velocity scales).

3.2 Numerical assessment

The methods described in section 3.1, are applied on DNS data from the Johns Hopkins University channel flow database (Li et al., 2008; Perlman et al., 2007; Graham et al., 2013). Since the ultimate goal of this work is to estimate pressure using experimental data, we use this DNS dataset to simulate synthetic 3D PIV velocity snapshots on which we then implement the different approaches and assess their accuracy using the provided DNS pressure fields. The main simulation parameters and flow statistics of the dataset are shown in table 3.1 (non-dimensional) and the grid spacing (in wall units) in table 3.2.

Friction velocity *Re* number	Re_τ	999.713
Database timestep	dt	0.00650
Friction velocity	U_τ	0.05
Bulk velocity	U_b	0.99992
Viscosity	ν	$5 \cdot 10^{-5}$
Domain length	$L_x \times L_y \times L_z$	$8\pi h \times 2h \times 3\pi h$
Grid	$N_x \times N_y \times N_z$	$2048 \times 512 \times 1536$

Table 3.1. Channel flow, synthetic PIV field ($Re_\tau = 1000$), simulation Parameters.

x-direction	Δ_x^+	12.2683
y-direction-first point	$\Delta_{y_1}^+$	0.01653
y-direction-centreline	$\Delta_{y_c}^+$	6.15728
z-direction	Δ_z^+	6.13416

Table 3.2. Channel flow, synthetic PIV field ($Re_\tau = 1000$), grid spacing.

3.2.1 Numerical set up

From the full channel pressure and velocity datasets, an initial volume of $88 \times 101 \times 96$ points in x, y, and z respectively, is chosen. The volume is located in the middle of the channel in the streamwise and spanwise direction and spreads from the viscous sublayer up to the wake region of the boundary layer ($y^+ = 2$ up to $y/\delta = 0.3$) in the wall normal direction.

In order to simulate the effect of synthetic PIV, the first step is to interpolate this data onto an equidistant grid in x, y, and z. Additionally, the data also needs to be filtered, since it has been shown that image cross correlation procedure of the PIV techniques have a similar effect as a moving average filter (Foucaut et al., 2004). The interpolation onto an equidistant grid and the filtering are performed in a single step in order to avoid aliasing. For filtering a Hanning window is applied. Also, since the original data is non-uniformly spaced in the wall normal direction, the filtering in y is combined with a weighting function to counteract the bias induced due to the non-uniform spacing. The volume is subsequently cropped to avoid edge effects of filtering. The final volume, after interpolation, filtering and cropping is located entirely in the log region in the wall normal direction and in the middle of the channel width and length. The final size of the resulting FOV is $240 \times 120 \times 180$ (in wall units) in x, y, and z respectively.

In order to assess the dependence of the methods in grid resolution, three different interrogation volume sizes are tested. Simulating an overlap factor (OF) of 75% in all three directions, the resulting number of vectors for each resolution is (table 3.3):

Interrogation volume size	Grid spacing	Resulting number of vectors
l^+	$(\Delta h^+ = \Delta x^+ = \Delta y^+ = \Delta z^+)$	(x,y,z)
12	3	$81 \times 41 \times 61$
24	6	$41 \times 21 \times 31$
48	12	$21 \times 11 \times 16$

Table 3.3. Channel flow, synthetic PIV field ($Re_\tau = 1000$), resolutions tested.

Besides the filtering effect mentioned above, PIV has been shown to create additional noise on the velocity field, on top of the physical noise originated from the particle motion (Foucaut et al., 2004). To simulate this influence, separate random noise fields are generated, filtered and cropped, following the same procedure described above and subsequently added to the three velocity components. To evaluate the dependence of the different techniques on the noise level, four different noise magnitudes are tested, each one scaled so that its root-mean-square (rms) value, ε_u, is given as a percentage of the maximum velocity occurring in the flow (de Kat and Ganapathisubramani, 2013).

In order to adequately assess the average performance of the three techniques, a sufficient number of different samples should be processed. Therefore, from the available time history 30 time

frames are chosen, several timesteps away from each other so that they can be considered independent. All the performance measures that will follow are averaged over this set of samples.

As mentioned above, TH includes the choice of an appropriate convection velocity (equation 3.9). In this work, three different convection velocities are tested. More specifically, both the streamwise mean velocity, $U_c = U(y)$, constant in the x–z plane, and the filtered version of it, $U_c = U_f$, (which yielded a locally varying velocity field) are tested. A three dimensional convection velocity is also examined, where the values of the three components are the mean values of the respective flow velocity components: $\mathbf{U_c} = (U(y),V(y),W(y))$. It should be noted here that, all the mean fields mentioned above imply time-averaged fields.

Finally, regarding EU and pLA, the dependence of the methods on the frame time-separation is examined. More specifically, for each of the 30 selected time frames (denoted 0 in Figure 3.2) where the pressure is computed, snapshots located one ($n = 1$), two ($n = 2$), four ($n = 4$) and eight ($n = 8$) time steps before and after are also selected and used to compute the acceleration on the central snapshot (equation 3.3 and 3.6). Because of the large parameter space involved,

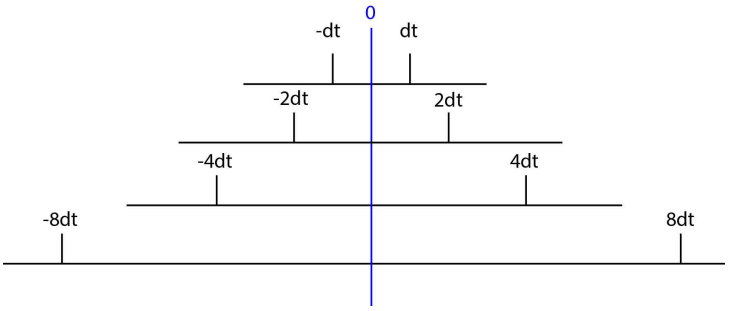

Figure 3.2. Channel flow, synthetic PIV field ($Re_\tau = 1000$). Different time separations for EU and pLA approaches.

we first select the convection velocity and time separation that give the most accurate results for TH and EU and pLA respectively. Using these values, which represent the best performance of each method, we can then compare across the different methods and also assess their dependence on grid resolution and noise levels. For the methods' performance assessment, four different measures were computed, all with respect to the exact and estimated pressure fields. More specifically, these were the normalised variance of the difference between the two fields, their correlation coefficient, their coefficient of determination (R-squared error), and the mean squared error between their probability density functions (pdfs). For brevity and since all three measures indicated similar behaviour, only the correlation coefficient results will be discussed in the following sections. It should also be noted here that for the presentation of the results that follows, unless indicated otherwise: $U_c = U$, $l^+ = 12$, $\varepsilon_u = 1\%$.

3.2.2 Convection velocity dependence

For TH, pressure is determined using the three convection velocities outlined above. The resulting fields have a higher average correlation coefficient with the DNS field when the streamwise

mean velocity is used as convection velocity, although all methods exhibit correlation coefficients above 0.74 (Table 3.4 and figure 3.3).

	$U_c = U$	$U_c = U_f$	$\mathbf{U_c} = U,V,W$
$\boldsymbol{r_{p_i}}$	0.79	0.74	0.76

Table 3.4. Channel flow, synthetic PIV field ($Re_\tau = 1000$). Average performance measures for different convection velocities ($\varepsilon_u/U_{max} = 1\%$, $l^+ = 12$). Using the streamwise mean velocity as the convection velocity yields the best results.

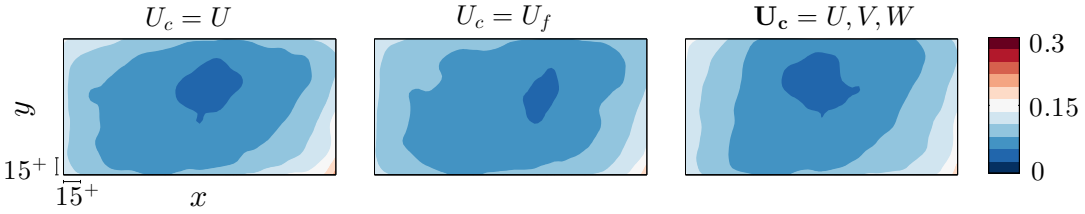

Figure 3.3. Channel flow, synthetic PIV field ($Re_\tau = 1000$). Convection velocity dependence for TH approach. Streamwise–wall-normal contours of rms error normalised with the dynamic range of the DNS pressure field at each snapshot, and averaged over all snapshots and spanwise locations ($\varepsilon_u/U_{max} = 1\%$, $l^+ = 12$).

Rms errors, normalised with the dynamic range of the DNS pressure field at each snapshot, show similar results, with the filtered version of the streamwise velocity performing better at the boundaries, although all methods again have similar accuracy. Based on these observations and following Geng et al. (2015), who showed that for the logarithmic region of the boundary layer, using the mean velocity as the convection velocity is an adequately accurate assumption, this is the convection velocity used for the rest of the study.

3.2.3 Time-separation dependence

For the EU and pLA approaches, pressure fields are estimated using the different time separations to compute acceleration, as outlined above (based on the flow statistics on table 2.1, one timestep corresponds to $dt^+ = 0.32$, in wall units). The results for the average correlation coefficient show that for EU the noise level present in the data influences the dependence of the method on the time-separation. In the case of $\varepsilon_u/U_{max} = 1\%$ (figure 3.4), an increase of time separation up to 1.28 results in higher correlation values but the accuracy decreases for larger timesteps (see also rms error in figure 3.6, top). In contrast to that, for the zero noise case, there is a monotonic decrease in correlation as the timestep increases (figure 3.5 top line). This is expected since, for EU, an increase of time separation, dt, decreases the precision error, associated with the uncertainty on the velocity field, but intensifies the truncation error, stemming from the discretisation scheme (see van Oudheusden, 2013). Therefore, for good quality data, as is the case of zero noise, it is the truncation error that is more prominent and dictates small time separations to be used. However, for higher noise level (or experimental results), a small increase of

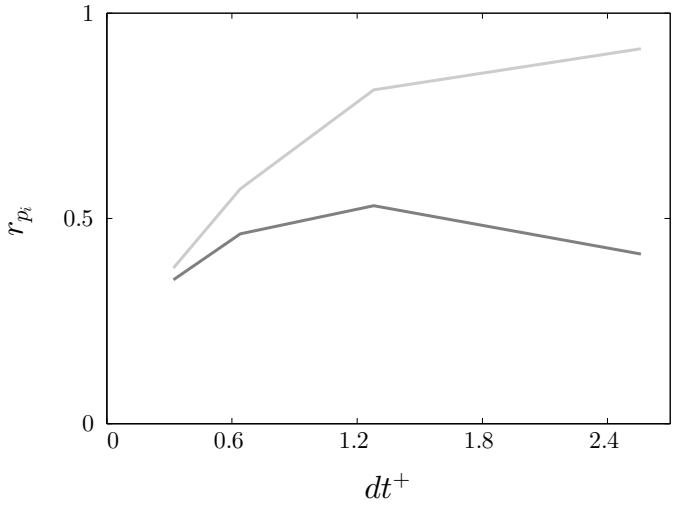

Figure 3.4. Channel flow, synthetic PIV field ($Re_\tau = 1000$). Average correlation coefficient with varying frame time-separation ($\varepsilon_u/U_{max} = 1\%$, $l^+ = 12$). Colours: —— EU, —— pLA. For pLA the largest timestep yields the best results. The performance of EU increases for moderate timesteps but deteriorates again for the largest timesteps used.

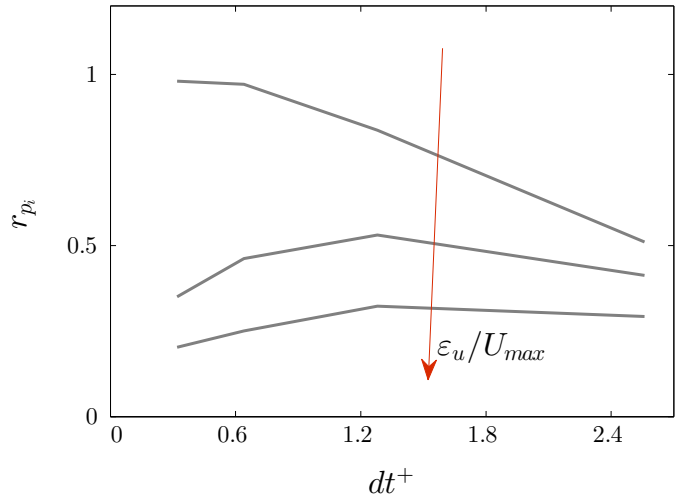

Figure 3.5. Channel flow, synthetic PIV field ($Re_\tau = 1000$). Average correlation coefficient with varying frame time-separation and noise for EU ($l^+ = 12$). When noise is present in the data a moderate increase in timestep improves the performance, while for zero noise the minimum timestep yields the most accurate results.

dt might provide a better balance between the two error sources (figure 3.5, middle and bottom line). A larger increase of *dt* though, would lead to an increasing truncation error representing the receding correlation between the velocity fields used for the computation of the acceleration. For an Eulerian approach this would in turn lead to an increasing error on the acceleration. Moreover, the time derivative for the computation of the acceleration implies that an increasing timestep will also lead to aliasing. This explains the drop in correlation for timesteps larger than

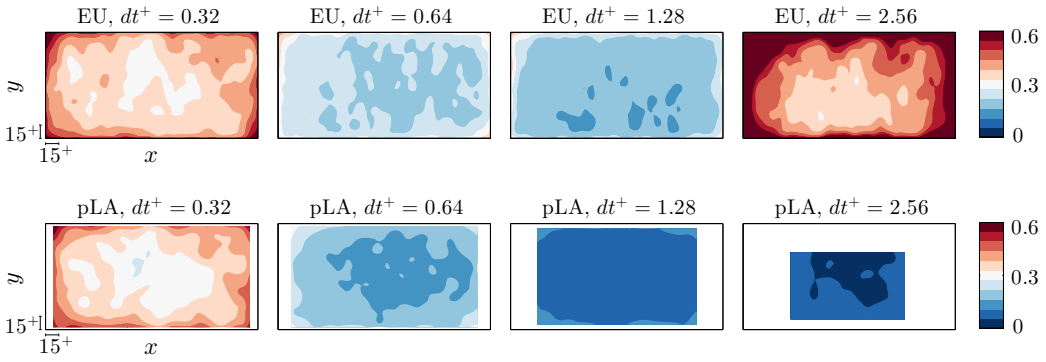

Figure 3.6. Channel flow, synthetic PIV field ($Re_\tau = 1000$). Time separation dependence for EU and pLA. Streamwise–wall-normal contours of rms error normalised with the dynamic range of the DNS pressure field at each snapshot, and averaged over all snapshots and spanwise locations ($\varepsilon_u/U_{max} = 0\%$ for EU, $\varepsilon_u/U_{max} = 1\%$ for pLA, $l^+ = 12$). EU performs worse with increasing time separation while pLA shows the opposite behaviour.

1.28 for the case of $\varepsilon_u/U_{max} = 1$ and 2% (figure 3.5, middle and bottom line). Therefore, for EU, the a moderate frame separation is chosen for the rest of the study ($dt^+ = 1.28$).

In the case of the pseudo-Lagrangian approach, the situation is reversed. Using the largest timestep yields the most accurate results with a correlation coefficient of 0.83, while for the smallest time separation ($dt^+ = 0.32$) the correlation coefficient drops around 20% (figure 3.4). This is also highlighted in the resulting rms errors ($\varepsilon_u/U_{max} = 1\%$) where, for the case of small timesteps (figure 3.6, bottom), there is a significant deviation from the DNS pressure. For the large frame separations, the error progressively decreases. However, it should be noted here, that pLA, due to the reconstruction of particle trajectories involved, suffers from edge effects which are intensified for larger time frame separations, resulting in smaller pressure volumes. So, even though the largest time separation ($dt^+ = 2.56$) yields the best results, it also leads to a loss of more than 60% of the volume. For this reason, we select an intermediate value ($dt^+ = 1.28$) for the rest of the study, where less than 40% of the volume is lost.

3.2.4 Noise dependence

As already mentioned, four different noise levels were filtered and added to the velocity fields, with the rms value of the final noise fields, ε_u, being a percentage of the maximum velocity present in the flow. Based on the choices of frame time separation and convection velocity outlined in the previous section, for the three methods tested pressure fields are estimated for all these levels of noise and the average correlation coefficient between the DNS and estimated pressure fields with respect to noise is determined (figure 3.7). For the zero noise level, pLA provides very accurate results (correlation coefficient close to one) outperforming TH, which reaches values around 0.8. EU has a slightly lower accuracy than pLA (because, as mentioned above, the timestep selected improves the performance only when noise is present) but still

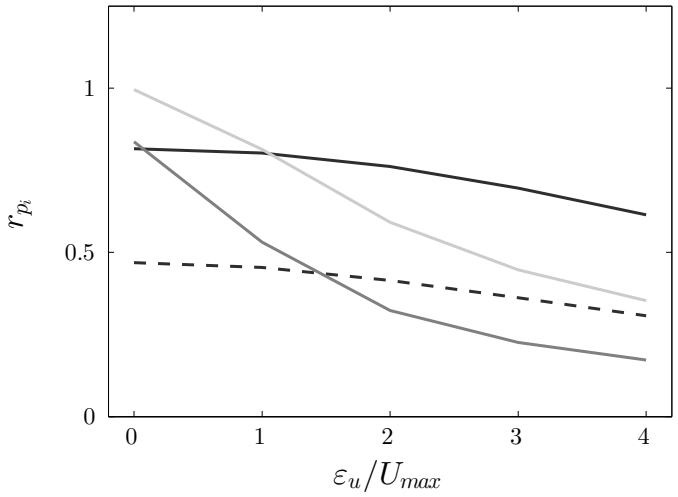

Figure 3.7. Channel flow, synthetic PIV field ($Re_\tau = 1000$). Average correlation coefficient with varying noise level ($dt^+ = 1.28$ for EU and pLA, $U_c = U$ for TH, $l^+ = 12$). Colours: —— TH, - - - TH-2D, —— EU, —— pLA. All methods show decrease in correlation with increasing noise, with TH being the least sensitive to noise and EU suffering the most. TH-2D shows a constant drop of about 40% from the 3D estimation, however it is still robust with respect to noise and outperforms EU for high noise levels.

outperforms TH. With increasing noise, the correlation coefficient follows a decreasing trend for all methods, however TH appears to be the least influenced and outperforms the other two approaches for all noise levels considered. This is evident in the case of $\varepsilon_u/U_{max} = 4\%$, where TH results in a maximum decrease of correlation around 20%, while pLA results in a correlation close to 0.4 marking a decrease of 60%, and EU suffering most from the noise shows a decrease of 80% in accuracy, implying no correlation with the exact field (figure 3.8, top row).

These observations for the three methods are in line with the error propagation analysis on section 3.1.5, where it was shown that for zero noise on the velocity field, pressure estimates with either Eulerian or pseudo-Lagrangian approach shouldn't have any error propagating through (equation 3.12 and 3.13), while pressure estimates using TH would have an error relating to an incorrect convection velocity chosen. However, as the error on the velocity increases, EU and pLA suffer significantly more, as the error on the estimated pressure grows progressively, while TH still retains similar levels of accuracy even at the largest noise level (figure 3.1, top). These correlation coefficient values appear to match the case of some small but non-zero errors on the convection and mean velocity for TH (figure 3.1, bottom), which lead to a smaller resulting error on the pressure field for high noise levels with respect to pLA and for all noise levels with respect to EU.

In the case of TH-2D, the average correlation coefficient based on instantaneous snapshots is significantly reduced (drop of about 40% from the 3D estimation), however it is still robust with respect to noise when compared to the EU and pLA approaches and even outperforms EU for high noise levels.

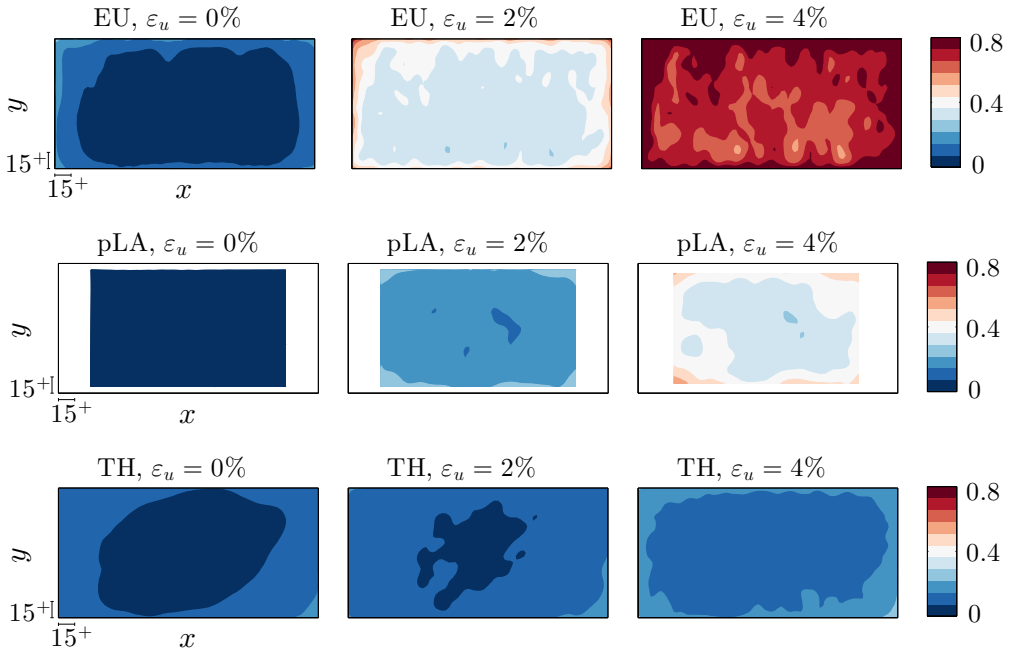

Figure 3.8. Channel flow, synthetic PIV field ($Re_\tau = 1000$). Noise dependence for all methods. Streamwise–wall-normal contours of rms error normalised with the dynamic range of the DNS pressure field at each snapshot, and averaged over all snapshots and spanwise locations ($dt^+ = 1.28$ for EU and pLA, $U_c = U$ for TH, $l^+ = 12$). All methods show decrease in accuracy with increasing noise, with TH being the least sensitive to noise and EU suffering the most.

3.2.5 Resolution dependence

Finally, pressure is estimated for the different grid resolutions outlined above (table 3.3) and the average correlation coefficient between the exact and estimated pressure fields is determined (figure 3.9).

Decrease in grid resolution leads to poorer performance for all three methods. Similar to the influence of noise on TH (figure 3.7), lower grid resolution results in a decrease of the pressure correlation coefficient from about 0.79 for the best resolution, to about 0.6. On the other hand and in line with the noise dependency results, TH-2D shows a significant correlation drop for all resolutions tested when compared to the full 3D method. However, it is also quite robust with respect to resolution (drop from 0.43 to 0.37) and performs similarly to both EU and pLA for the coarsest grid. EU follows a slightly sharper decreasing trend, from a correlation coefficient around 0.53 dropping to 0.3 for the worst resolution. It should also be noted here that it is the noise effect ($\varepsilon_u/U_{max} = 1\%$) on EU, that is responsible for the much lower values of correlation coefficient with respect to the other 3D methods. For the pLA approach, there is a much sharper decrease (more than 50%) in accuracy with decreasing resolution which can be of significant importance in the case of experimental data, where high spatial resolution is be hard to attain (especially when time-resolved volumetric velocity fields are required). This behaviour can also be seen in the rms error results which show that TH is the most robust method with respect to

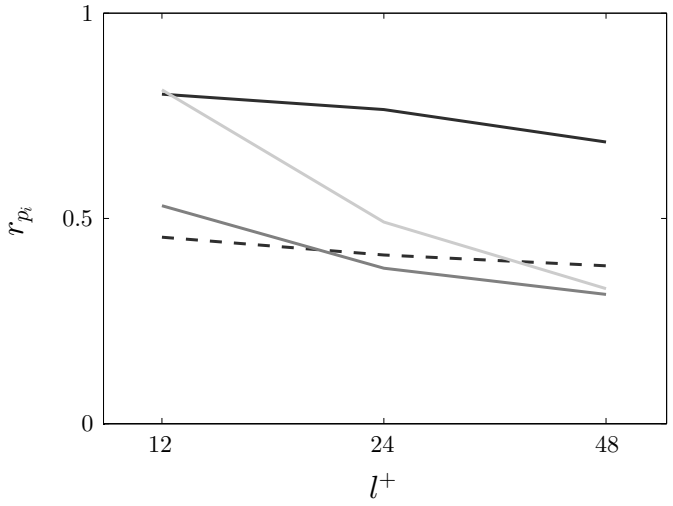

Figure 3.9. Channel flow, synthetic PIV field ($Re_\tau = 1000$). Average correlation coefficient with varying resolution ($dt^+ = 1.28$ for EU and pLA, $U_c = U$ for TH, $\varepsilon_u/U_{max} = 1\%$). Colours: —— TH, - - - TH-2D, —— EU, —— pLA. Decrease in correlation for lower resolution for all methods with TH showing the slowest decrease. TH-2D has the lowest accuracy for the finest grid, however performs better than either EU or pLA for the coarsest one.

resolution (figure 3.10). On the other hand, although pLA has the best performance at the finer grid, its accuracy shows the largest drop with decreasing resolution, resulting in errors of the same order of EU in the coarsest grid.

3.2.6 Pressure Statistics

All previous performance assessments of the different methods were based on the estimation of instantaneous pressure. However, in many applications, statistical information is also crucial, so here we also present rms pressure values for all methods and how they compare with DNS results. It should be noted here that, due to the small size and low number of available synthetic volumes when compared to the full database, the mean and rms values of DNS pressure differ significantly from the converged database statistics (Li et al., 2008; Perlman et al., 2007; Graham et al., 2013). Also, for the estimated pressures, for lack of appropriate Dirichlet boundary condition, the average pressure on each volume is set to zero. Therefore, in order to be consistent in the comparison of DNS and estimated pressures, we effectively set the average DNS pressure of each volume to zero and compute the rms pressures for both DNS and TH by averaging only over the number of data points available. Both TH and pLA provide statistics very close to the DNS values, whereas EU is more influenced by noise ($\varepsilon_u/U_{max} = 1\%$, for all methods) and also suffers from stronger edge effects (figure 3.11). Regarding the TH-2D approach, as was mentioned above, in terms of instantaneous pressure fields, using 2D velocity data leads to a 40% drop in correlation from the 3D data case (figure 3.7). Nevertheless, the method still shows robustness to noise influence and the resulting pressure statistics are relatively unaltered when

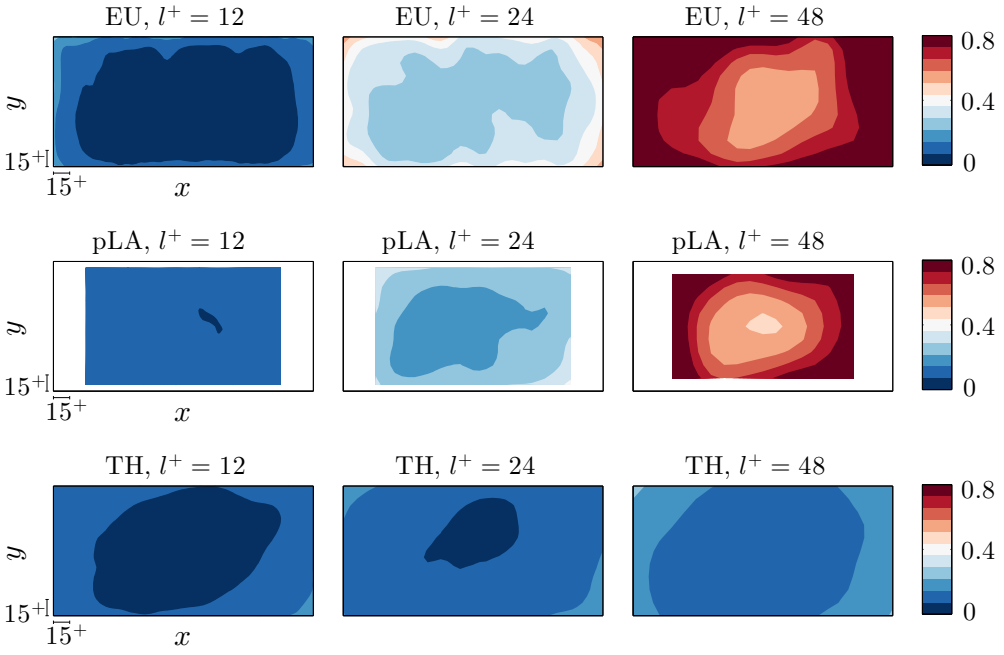

Figure 3.10. Channel flow, synthetic PIV field ($Re_\tau = 1000$). Resolution dependence fot all methods. Streamwise–wall-normal contours of rms error normalised with the dynamic range of the DNS pressure field at each snapshot, and averaged over all snapshots and spanwise locations ($dt^+ = 1.28$ for EU and pLA, $U_c = U$ for TH, $\varepsilon_u/U_{max} = 1\%$).

compared to the 3D case. Based on these results and given the fact that TH does not require time information, it can be a valuable alternative for getting pressure statistics in cases where only 2D velocity snapshots are available (see chapter 6 for such an application).

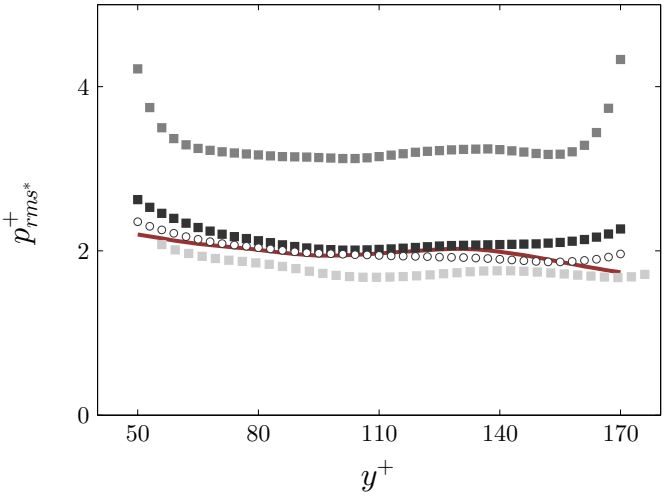

Figure 3.11. Channel flow, synthetic PIV field ($Re_\tau = 1000$). Rms pressure normalised with inner variables for all methods ($dt^+ = 1.28$ for EU and pLA, $U_c = U$ for TH, $l^+ = 12$). ■ TH, ○ TH-2D, ■ EU, ■ pLA, — DNS.

For completeness, we also present a 3D volume of the DNS pressure field, together with the best estimates for all methods, with zero noise ($\varepsilon_u/U_{max} = 0\%$) and highest resolution ($l^+ = 12$). That is, using the streamwise mean velocity ($U_c = U$) for the TH approach, a separation of one timestep ($dt^+ = 0.32$) for the EU acceleration term (since the noise level is zero), and four timesteps ($dt^+ = 1.28$) for the acceleration term in the pseudo-Lagrangian approach (figure 3.12).

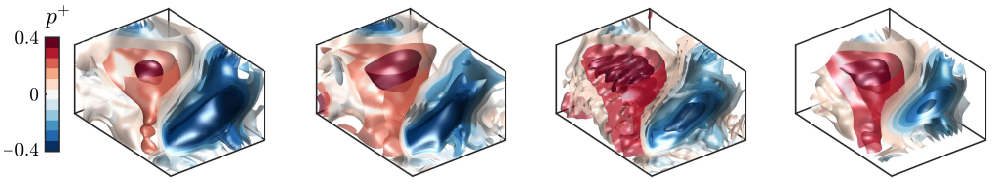

(a) DNS **(b)** TH **(c)** EU **(d)** pLA

Figure 3.12. Channel flow, synthetic PIV field ($Re_\tau = 1000$), pressure volumes. Comparison of best performance for all methods ($\varepsilon_u/U_{max} = 0\%$, $l^+ = 12$).

All methods represent the field with good accuracy, with TH and pLA being smoother than EU, but a little less accurate. However, as explained above, this is the best these methods can perform at the current dataset and their accuracy is restricted severely when noise is added or the resolution decreases. The waviness introduced in the field estimated using EU (figure 3.12c), is apparent only in the case of zero noise, and for all other cases, the noise magnitude is larger and masks this effect. The same pattern is also observed on the pressure gradient term (equation 3.4) which indicates that it is not a product of the pressure integration method. Since EU is the only approach that employs a direct central difference scheme for the time derivative and we do not use filter in time, aliasing effects might be an explanation for this behaviour. Notably, the waviness disappears in the low resolution case, where the grid spacing, $h^+ = 12$, is the same as the original DNS data. Another possible explanation therefore, is that the oversampling in space for the other two resolutions tested ($h^+ =$ [3, 6]) combined with the direct central difference scheme for the time derivative employed in EU is the source of this artefact.

3.3 Experimental assessment - TBL long vertical field of view

3.3.1 Instantaneous pressure fields

The data used for the experimental assessment of the methods outlined in section 3.1, are the tomo-PIV (Long vertical field of view) velocity fields acquired in the set-up described in chapter 2, sec. 2.4.1. The methods are implemented on the acquired volumetric PIV velocity data using the streamwise mean as the convection velocity for TH and, initially, a single timestep as the frame time-separation for EU and pLA. Since the FOV extends up to the freestream, we can then apply Dirichlet boundary conditions to the top surface of the volumes for the Poisson equation (equation 3.2). More specifically, pressure is prescribed ($p = 0$) for a single point at the top

surface of the volume, located in the freestream. Additionally, the average pressure of the that surface is also set to zero. Based on the aforementioned nominal flow conditions, the resulting interrogation window size is $l^+ = 104$, much coarser than the different resolutions ($l^+ = 12$, 24, and 48) tested on the DNS dataset, but the timesteps are comparable: $dt^+ = 0.38$ for the experimental dataset and $dt^+ = 0.32$ for DNS.

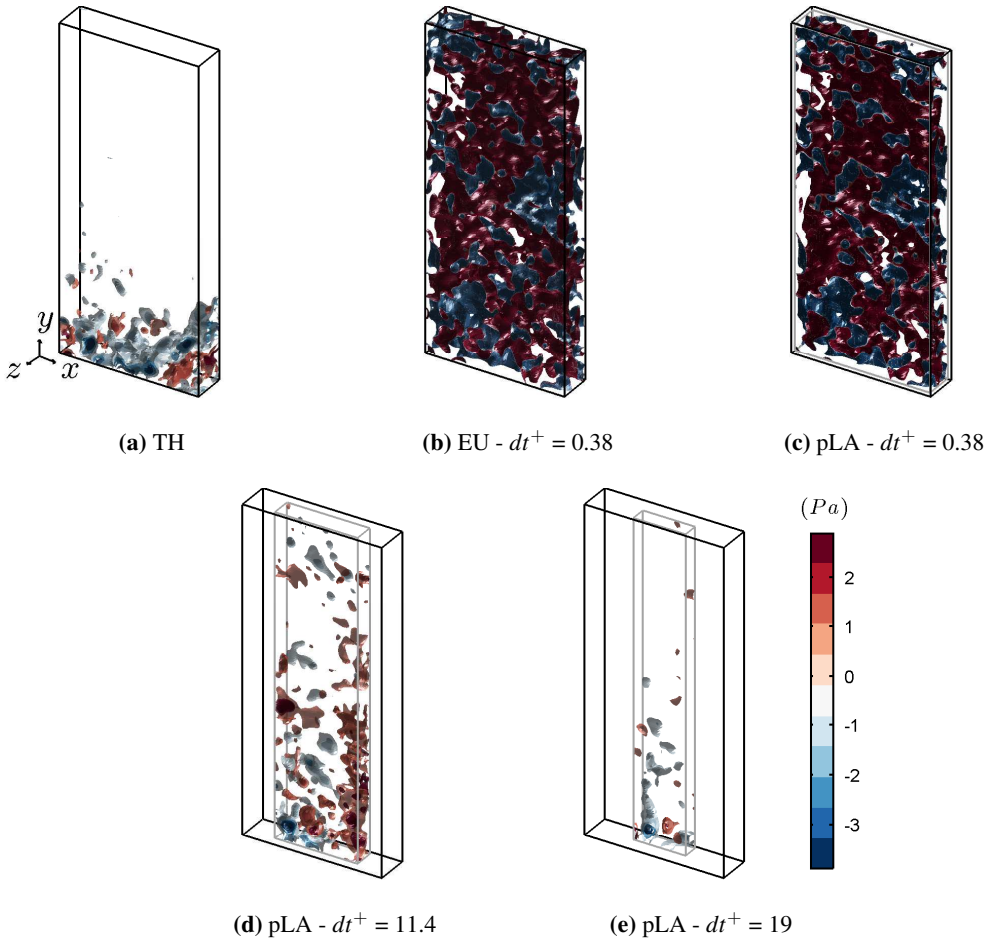

(a) TH **(b)** EU - dt^+ = 0.38 **(c)** pLA - dt^+ = 0.38

(d) pLA - dt^+ = 11.4 **(e)** pLA - dt^+ = 19

Figure 3.13. TBL flow, tomo-PIV field ($Re_\tau = 2300$, long vertical field of view). Contour plots of pressure for all methods. Flow is from left to right, axes as appearing on the left, each 200^+ long. TH seems to be the least affected by noise and EU the most while pLA performs much better for very large timesteps but the resulting volume is greatly reduced.

The results show that for a single timestep ($dt^+ = 0.38$), both pLA and EU are greatly affected from noise (figure 4.1b and c), to the point where no individual structures can be identified. The pressure fields using TH (figure 3.13a) seem to be less noisy and some individual formations are discernible. This is consistent with the observations of the previous section, where high levels of noise (more than 3%) present in the velocity fields, led to a rapid decrease in accuracy for both EU and pLA approaches (figure 3.7), while TH was less influenced. Numerical assessment in the previous section showed that pLA suffered the most with poor spatial resolution (figure 3.9). Even for a resolution of $l^+ = 48$, pLA showed a 50% decrease in correlation with the exact pressure field, so we would expect the current resolution of $l^+ = 104$ to be, besides noise, the

other main factor responsible for the poor performance (figure 3.13c). However, it is also shown that, in terms of frame separation, larger timesteps could potentially improve the performance for pLA (figure 3.4), with the limitation being the greatly reduced volumes due to particles leaving the FOV. To test this observation, we implement pLA for several different time separations (figures 3.13d and 3.13e). The results show that indeed, for larger timesteps, the evaluated pressure fields are less noisy and some structural details can be detected. Due to the much coarser spatial resolution and high noise levels included, the frame time separation needed in order for pLA to show a marked improvement ($dt^+ = 11.4$) is an order of magnitude larger than the one used for the DNS dataset ($dt^+ = 1.28$). However, also due to the larger FOV and coarse resolution, the loss in volume due to particles leaving the FOV is also more limited, which allowed for these large frame separations to be used.

Since no reference pressure is available, it is unclear how much these formations, discernible with Taylor's hypothesis and the pseudo-Lagrangian approach, resembled the ones present in the flow. However, we choose to assess the performance of each method using the inner normalised rms values of pressure $p^+_{rms} = p_{rms}/(\rho U_\tau^2)$ – averaged in space and time – and comparing them with DNS results of similar Re numbers. Therefore, pressure distributions from turbulent boundary layers of $Re_\theta = 5000$ ($Re_\tau = 1460$) and $Re_\theta = 6500$ ($Re_\tau = 1990$) (Sillero et al., 2013, 2014; Borrell et al., 2013; Simens et al., 2009) are plotted together with experimental results (figures 3.14–3.18). The two DNS datasets are selected so that the former approximately matches the Re_θ of the present experiments and the latter the Re_τ.

3.3.2 Pressure statistics

Eulerian approach

The numerical study in the previous section showed that EU gave the most accurate results for minimal time separation in case of very good quality data. However, for increasing noise present in the data, as is the case of the experimental results, a moderate increase of timestep improved the performance (figure 3.4 and 3.5). For this reason we test different time-separations ($dt^+ = 0.38 - 11.4$) and plot the resulting pressure fields (figure 4.2) together with the DNS data (Sillero et al., 2013, 2014; Borrell et al., 2013; Simens et al., 2009).

Results show that for all time separations the pressure values are an order of magnitude higher than the DNS data, in line with the pressure contour plots in figure 3.13b. There is however a decreasing trend with increasing frame separation, which is more pronounced between $dt^+ = 0.38$ and $dt^+ = 1.9$. This improvement is – besides the aforementioned decrease in precision error – due to the coarse spatial resolution of the data in conjunction with oversampling in time. For the last two timesteps tested ($dt^+ =$ [7.6, 11.4]), the near wall region values deviate significantly from the DNS curve and this could be due to the increasing truncation error (figure 4.12a). In the freestream, especially for the smallest frame separation, there was an upward branching of the values, probably due to the boundary conditions imposed. In order to better

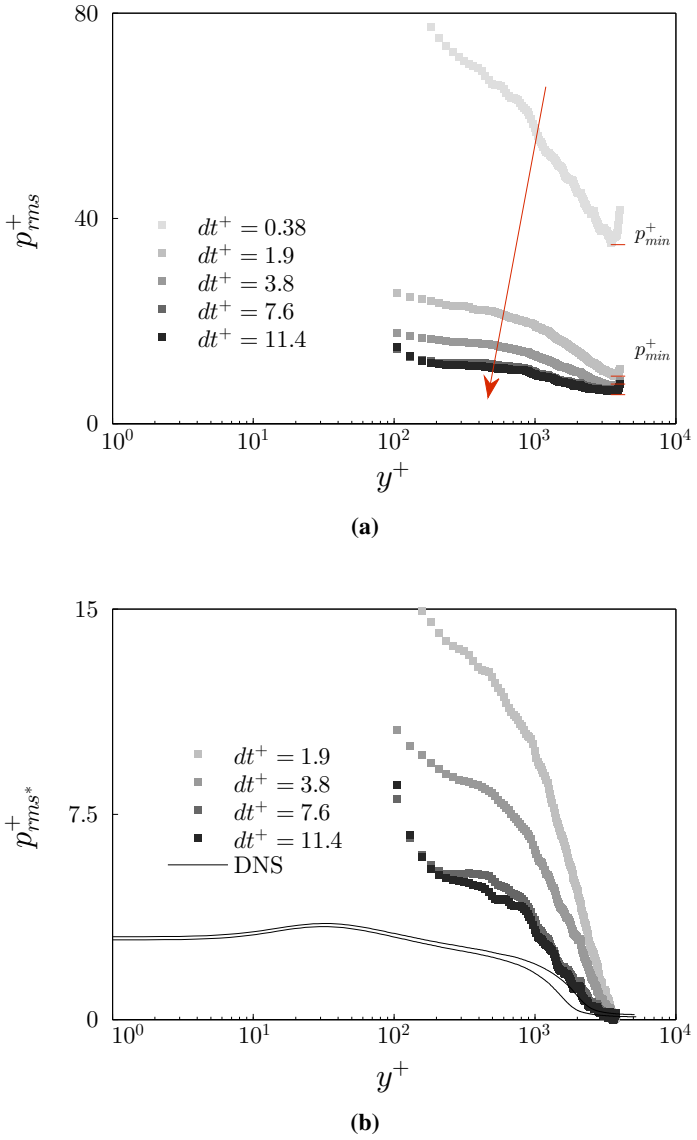

Figure 3.14. TBL flow, tomo-PIV field ($Re_\tau = 2300$, long vertical field of view). Rms pressure, normalised with inner variables, using EU. (a) Results for increasing frame separation ($dt^+ = 0.38 - -11.4$). (b) Same results translated downwards using a reference pressure and replotted together with DNS (Sillero et al., 2013, 2014; Borrell et al., 2013; Simens et al., 2009) at $Re_\theta = 5000$ ($Re_\tau = 1460$) and $Re_\theta = 6500$ ($Re_\tau = 1990$), solid lines.

compare with the DNS data, we removed these end points and subtracted the minimum rms pressure: $p^+_{rms^*} = p^+_{rms} - p^+_{min}$, from all values (see figure 3.14a), effectively setting the pressure fluctuations at the freestream to zero. This was a similar – albeit more simplistic – approach to the de-noising of pressure measurements employed by Tsuji et al. (2012). The resulting plot (figure 3.14b) shows that, even when a constant noise level (corresponding to the p_{min}) is subtracted, the pressure distribution deviates significantly from the DNS data.

Pseudo-Lagrangian approach

The pressure contours in figure 3.13d and 3.13e and the numerical study results for pLA showed an improvement in performance for increasing time separation, leading however to a decrease in volume. For this reason, similar to EU, we test several frame separations for pLA and plot the results together with DNS data (Sillero et al., 2013, 2014; Borrell et al., 2013; Simens et al., 2009).

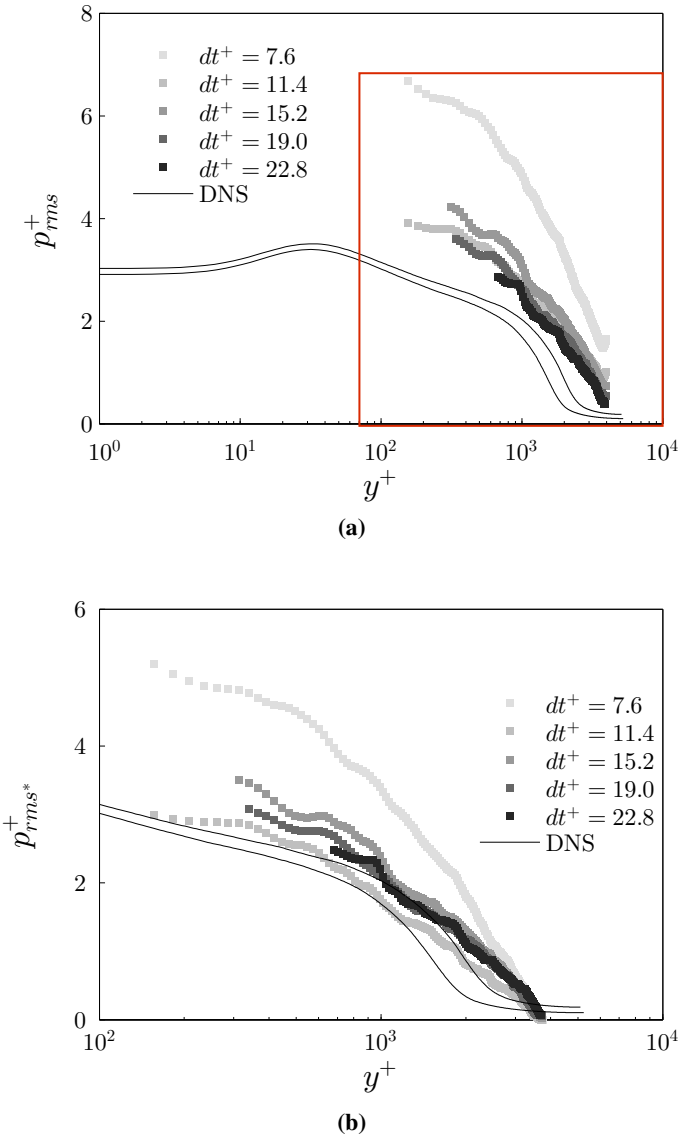

Figure 3.15. TBL flow, tomo-PIV field ($Re_\tau = 2300$, long vertical field of view). Rms pressure, normalised with inner variables, using pLA together with DNS results (Sillero et al., 2013, 2014; Borrell et al., 2013; Simens et al., 2009) at $Re_\theta = 5000$ ($Re_\tau = 1460$) and $Re_\theta = 6500$ ($Re_\tau = 1990$), solid lines. (a) Results for increasing frame separation ($dt^+ = 7.6 - 22.8$). (b) Zoomed-in region in (a) showing increasing time-scales with increasing y^+.

For the first few timesteps used ($dt^+ = 0.38 - 7.6$), there is a marked improvement with increasing dt^+ as expected, however the overall pressure values are much higher than the DNS data and not shown here. For larger timesteps ($dt^+ = 7.6 - 22.8$) the values are comparable with the DNS results (figure 3.15a), but there is no clear trend with increasing frame separation. As already mentioned for EU, the maximum allowable timesteps for the method to perform adequately, besides the limitation of volume loss, are also dictated by the combination of a coarse resolution in space with a very high resolution in time. Looking more closely at the area where the experimental points lie (highlighted rectangle in figure 3.15a), it is clear that the frame separations that perform best tend to increase with increasing distance from the wall (figure 3.15b). It has to be noted that here in favour of consistency, following the same procedure as with the EU results, the end points were removed and the minimum rms pressure was subtracted from the distributions as well. Using $dt^+ = 11.4$ yields the best results for a region up to $y^+ \approx 800$, while for $800 < y^+ < 2500$, the best choice is $dt^+ = 19$ and above that, $dt^+ = 22.8$, even though at that point, the remaining volume is reduced to a plane (figure 3.15b and 3.13e). Although the exact limits of these regions are quite uncertain, the general trend agrees with the increase of streamwise velocity away from the wall. Therefore, it is noted that a more suitable implementation of pLA should include a frame separation $dt^+(y^+)$, increasing with y^+.

Taylor's hypothesis approach

Comparing with the DNS data (Sillero et al., 2013, 2014; Borrell et al., 2013; Simens et al., 2009), shows that TH is the method least influenced by noise and the pressure distribution follows a similar trend as the DNS results (figure 3.16).

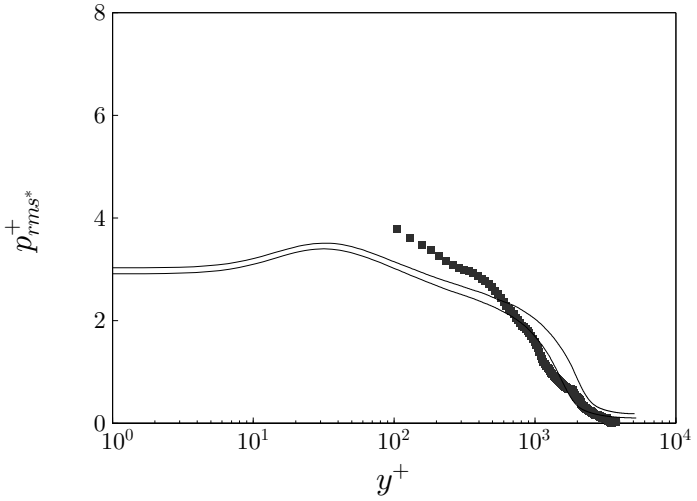

Figure 3.16. TBL flow, tomo-PIV field ($Re_\tau = 2300$, long vertical field of view). Rms pressure, normalised with inner variables, using TH together with DNS results (Sillero et al., 2013, 2014; Borrell et al., 2013; Simens et al., 2009) at $Re_\theta = 5000$ ($Re_\tau = 1460$) and $Re_\theta = 6500$ ($Re_\tau = 1990$), solid lines.

Similar to EU and pLA results, the end points were removed and the minimum rms pressure was subtracted from the distribution. With the freestream noise subtraction mentioned above, the rms pressure distribution approximately follows the lower Re DNS dataset (which has a comparable Re_θ with the experimental results), away from the wall. As expected, larger discrepancies can be seen closer to the wall, where the convection velocities likely deviate from the mean (Geng et al., 2015).

Time and resolution dependence

As already mentioned, the cross-correlation of particle images, which is the core of PIV, acts similar to a low-pass filter in space. In our case the data are also time-resolved and the finite acquisition frequency imposes a similar filter in time. Regarding the spatial filtering effects, unlike the numerical study, where high-resolution data were available and the effects of different filter sizes were evident (figure 3.9), the experimental data are already quite coarse in space ($l^+ = 104$) and even though further decrease of resolution was tested, the effects on the final pressure values were minimal.

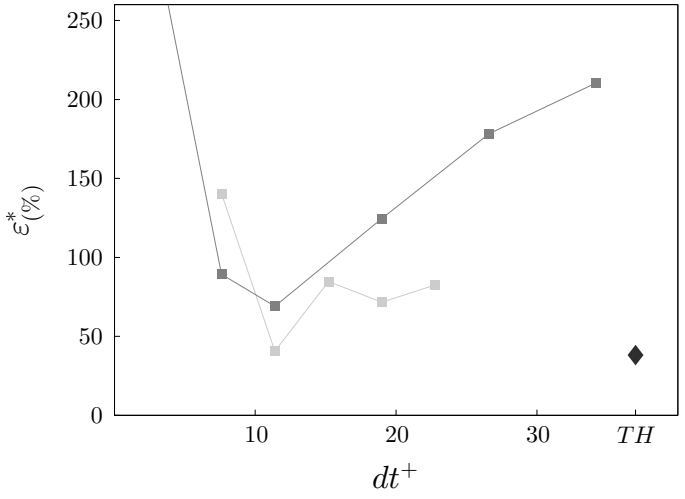

Figure 3.17. TBL flow, tomo-PIV field ($Re_\tau = 2300$, long vertical field of view). Average error (in %) of all methods with respect to DNS results. ♦ TH, —■— EU, —■— pLA. For pLA a moderate timestep $\sim dt^+ = 10$ yields the best results, even though for larger timesteps the error remains at similar – albeit a bit higher – levels. The performance of EU improves for moderate timesteps but deteriorates again for the largest timesteps used. TH is not time dependent and shows quite low error levels

The dependence of each method on frame time-separation was already tested above, however to highlight the differences between methods and similar to figure 3.4 of the numerical study, the normalised errors (in %) between the estimated and DNS values (Sillero et al., 2013, 2014; Borrell et al., 2013; Simens et al., 2009) were plotted against the different timesteps used (figure 3.17). The normalised error, ε^*, is computed for every wall-normal location, y^+, as the average

deviation of the estimated pressure values from the two corresponding DNS ones and is then averaged across all y^+ locations. The star denotes the procedure followed in the previous sections where for all approaches, the end points were removed and the minimum rms pressure was subtracted from the distribution. It is also important to note here that, because of the volume losses mentioned above, the error computed for pLA is based on fewer points as the timestep increases. The results show that both EU and pLA approaches improve with larger timesteps, even though for EU the distribution in the near-wall region deviates significantly from the DNS values for very large timesteps (see figure 4.2b). When increasing the timestep further ($dt^+ > 10$), the performance of EU starts to deteriorate mirroring the trend of figure 3.4 in the numerical study. On the other hand pLA shows lower error levels, some slight oscillations (in line with the behaviour shown in figure 3.15b) and the performance does not deteriorate significantly even for the maximum allowable timestep (despite the volume loss). TH does not use time information and is represented by a single point at the right side of the figure, symbolizing the equivalent of an infinite timestep approach. The TH point corresponds to error levels much lower than EU and comparable to pLA when very large timesteps are used. Following the previous observations a $dt^+ = 11.4$ is chosen for both EU and pLA, since it corresponds to the minimum deviation between estimated and DNS distributions for both approaches. With the timesteps chosen, the corresponding pressure distributions of the three approaches can then be compared with each other and the DNS results, as shown in the next section.

Method comparison

Finally, the best results from each method are compared (figure 3.18). Both TH and pLA match the low *Re* DNS dataset, with TH performing better away from the wall, as expected. The Eulerian approach has the poorest performance. Based on the numerical study in the previous sections, the large discrepancies observed for EU can be attributed to the extra velocity term, *II*, in equation 3.12 in the uncertainty analysis. This term does not appear in the uncertainty formulation for pLA, whereas for TH, it involves the magnitude of the velocity fluctuations, $\mathbf{u}'$ and of the difference between the mean and the convection velocity, $\mathbf{U} - \mathbf{U_c}$, which are both much smaller. It is obvious that for the present experimental conditions, both pLA and TH can provide reasonable results, the former with a considerable loss in volume and noise sensitivity. For pLA it should also be noted that, apart from noise, the coarse resolution might influence significantly the accuracy, based on the results of the numerical study (figure 3.9). An experimental dataset with improved resolution could perhaps reveal with more detail whether pLA could improve significantly in performance, or could bring TH within the resolution limits of the DNS study (figure 3.9) so that we we would be able to predict its accuracy with more certainty. However, we are already reaching the limits of the state-of-the art equipment and significant improvements in spatial resolution are not possible without losing time resolution or part of the FOV (which would in turn render the Dirichlet condition at the freestream, used in the Poisson formulation, invalid and the pressure estimation less accurate).

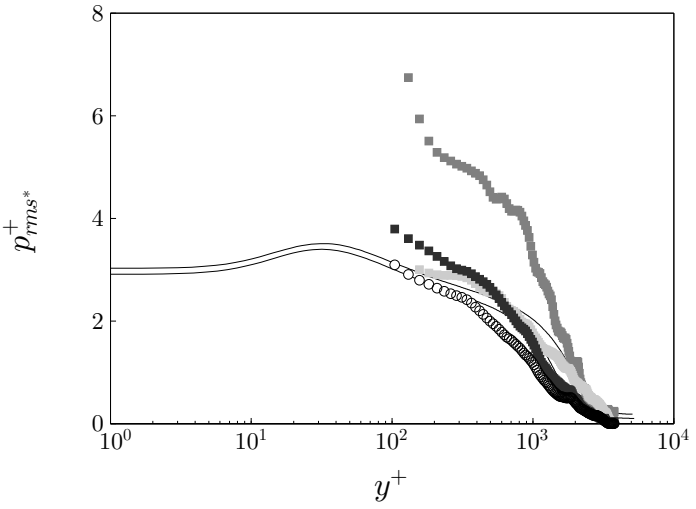

Figure 3.18. TBL flow, tomo-PIV field ($Re_\tau = 2300$, long vertical field of view). Comparison of all methods together with DNS results (solid lines) (Sillero et al., 2013, 2014; Borrell et al., 2013; Simens et al., 2009). ■ TH, ○ TH-2D, ■ EU, ■ pLA. TH seems to be the least affected by noise while pLA performs much better for large timesteps ($dt^+ = 11.4$) but the resulting volume is greatly reduced. TH-2D also provides reliable pressure values in a statistical sense.

3.4 Experimental assessment - TBL intermediate vertical field of view

Following the experimental results presented above, an assessment of the three methods in a high-Reynolds number turbulent boundary layer with increased spatial resolution is also worth briefly discussing here. The second experimental dataset of time-resolved tomographic PIV measurements acquired is used (section 2.4.2), which covers approximately two thirds of the boundary layer in height – half the height of the volume in the previous experiment – in an effort to improve the spatial resolution. The free-stream velocity is also increased, in order to achieve a high Reynolds number, and these different flow conditions also necessitated the planar-PIV dataset (see section 2.3), which had a FOV that reached up to the freestream, in order to characterise the flow.

3.4.1 Instantaneous pressure fields

The three methods described above are subsequently implemented on the acquired volumetric PIV velocity data using the streamwise mean as the convection velocity for TH and, initially, a single timestep as the frame time-separation for EU and pLA. Neumann boundary conditions are applied to all the edges, except the top plane of the domain where Dirichlet boundary conditions are enforced, for which, since the FOV did not extend to the freestream, the pressure was set using a corrected formulation of Bernoulli's equation, following de Kat and van Oudheusden (2012). Based on the aforementioned nominal flow conditions, the resulting interrogation

window size is $l^+ = 92$, still much coarser than the different resolutions ($l^+ = 12$, 24, and 48) tested on the DNS dataset, but slightly finer than the previous experimental dataset ($l^+ = 104$).

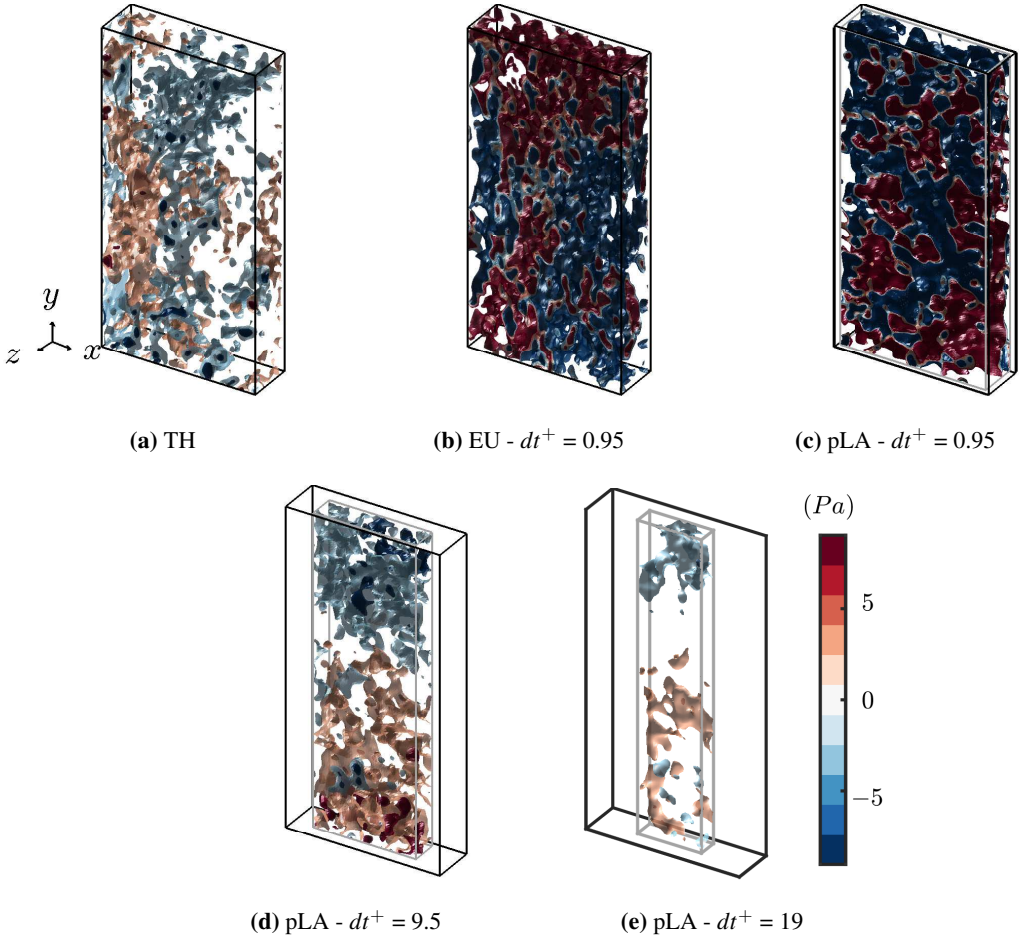

(a) TH **(b)** EU - dt^+ = 0.95 **(c)** pLA - dt^+ = 0.95

(d) pLA - dt^+ = 9.5 **(e)** pLA - dt^+ = 19

Figure 3.19. TBL flow, tomo-PIV field ($Re_\tau = 5300$, intermediate vertical field of view). Contour plots of pressure for all methods. Flow is from left to right, axes as appearing on the left, each 200^+ long. TH seems to be the least affected by noise and EU the most while pLA performs much better for very large timesteps but the resulting volume is greatly reduced.

Mirroring the previous numerical and experimental results, the pressure fields show that for a single timestep ($dt^+ = 9.5$), both pLA and EU are greatly affected from noise (figure 3.19b and 3.19c), to the point where no individual structures can be identified. The pressure fields using TH (figure 3.19a) seem again to be less noisy while individual formations are discernible. For larger timesteps, the evaluated pressure fields with pLA are, as expected, less noisy and some structural details can be detected.

3.4.2 Pressure statistics

Following the procedure in the previous section, we choose to assess the performance of each method, using the inner normalised rms values of pressure $p^+_{rms^*} = p^+_{rms} - p^+_{min}$ – averaged in

space and time – and comparing them with experimental results of similar *Re* numbers. Therefore, pressure distributions from direct pressure measurements in turbulent boundary layers of $Re_\theta = 12100$ and $Re_\theta = 15200$ (Tsuji et al., 2007) are plotted together with the present experimental results (figure 3.20). The dependence of EU and pLA were discussed in the previous section, so here we just present their comparison with TH for the timesteps with which they perform the best.

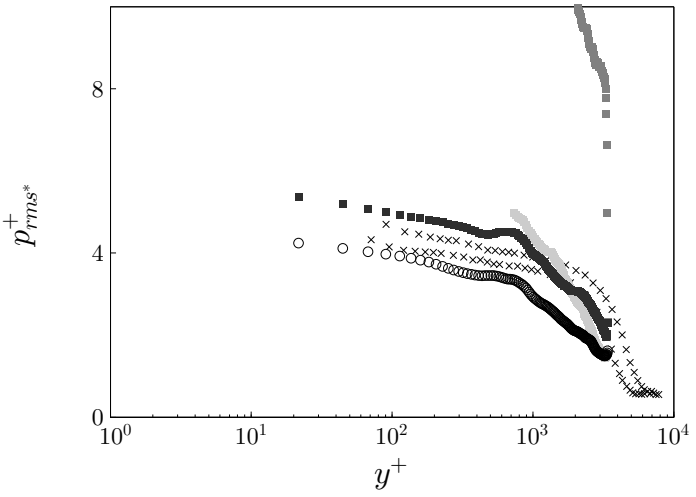

Figure 3.20. TBL flow, tomo-PIV field ($Re_\tau = 5300$, intermediate vertical field of view). Comparison of all methods together with direct pressure measurement results (×, Tsuji et al., 2007). ■ TH, ○ TH-2D, ■ EU, ■ pLA. TH seems to be the least affected by noise while pLA performs much better for large timesteps ($dt^+ = 19$) but the resulting volume is greatly reduced. TH-2D shows again a good statistical representation of the pressure values.

The rms pressure values support the observations from the snapshots (figure 3.19), namely that TH is the method least affected by noise and provides results comparable with those from direct pressure measurements, while EU suffers from noise the most (to the point where it is difficult to plot all results together). For pLA, larger timesteps significantly improve the performance (with the aforementioned volume losses, which in this case are more pronounced than in the previous dataset). TH-2D slightly underestimates pressure when compared to the 3D approach, as was also shown in both the experimental and numerical assessment above. However, the estimated rms pressure values are still in very good agreement with the experimental results and can provide a reliable alternative to extract pressure statistics when only 2D velocity data is available – a fact that is exploited in chapter 6.

Chapter 4

Velocity fluctuations and entrainment at the freestream boundary

This chapter includes the detection and analysis of turbulent/non-turbulent interfaces (TNTIs) in a turbulent boundary layer, using the time-resolved planar PIV data described with detail in chapter 2 section 2.3.

4.1 Detection of the freestream boundary

The detection of the TNTI has been, in itself, the point of focus of a variety of studies over the years and many different methods have been developed, mainly corresponding to the experimental or numerical method used to acquire the data. While details on the subject are out of the scope of this work, a brief outline on the chosen detection method follows for completeness.

Since only velocity information is available in a 2D domain and based on the limitations of using a vorticity threshold on a noisy freestream, we chose to use a kinetic energy deficit threshold, as described in Chauhan et al. (2014a,b). A local instantaneous kinetic energy deficit, K, over a 3×3 region, on a coordinate system moving with the freestream velocity, U_∞, is given by:

$$K = 100 \times \frac{1}{9U_\infty^2} \sum_{m,n=-1}^{1} [(U_{m,n} - U_\infty)^2 + V_{m,n}^2] \tag{4.1}$$

Above the TNTI, i.e at the freestream, $U \approx U_\infty$ and $V \approx 0$, therefore K is expected to be very small, whereas below the interface and towards the wall, where the turbulent fluctuations are more energetic, the value of K rapidly increases. A threshold, K_{th} can then be computed, using the average turbulent kinetic energy in the freestream from all the available velocity snapshots, above which the flow is considered turbulent. For the present data, the average kinetic energy deficit computed in the freestream was 0.16. Based on this threshold, a binary representation

of the flow is computed for which, regions with a local K below the threshold are assumed to be non-turbulent (and are assigned a value of 1), while regions with $K > K_{th}$ are considered turbulent (and are assigned a value of 0). Then the interface location is estimated as the shortest continuous contour line with a value of 0.5. However, the ultimate choice of a momentum deficit threshold (starting from the average value in the freestream), is subject to a number of considerations, in order for the TNTI definition to be consistent with the boundary layer thickness. Chauhan et al. (2014a) suggested that the final threshold should ensure that $Y_i + 3\sigma_i \approx \delta$, where Y_i, σ_i are the mean and standard deviation of the TNTI location, while the intermittency profile is required to follow an error-function. Their final chosen value was $K_{th} = 0.12$, which resulted in a Gaussian distribution for y_i and an average TNTI location of $Y_i = 0.67\delta$. In our case, a

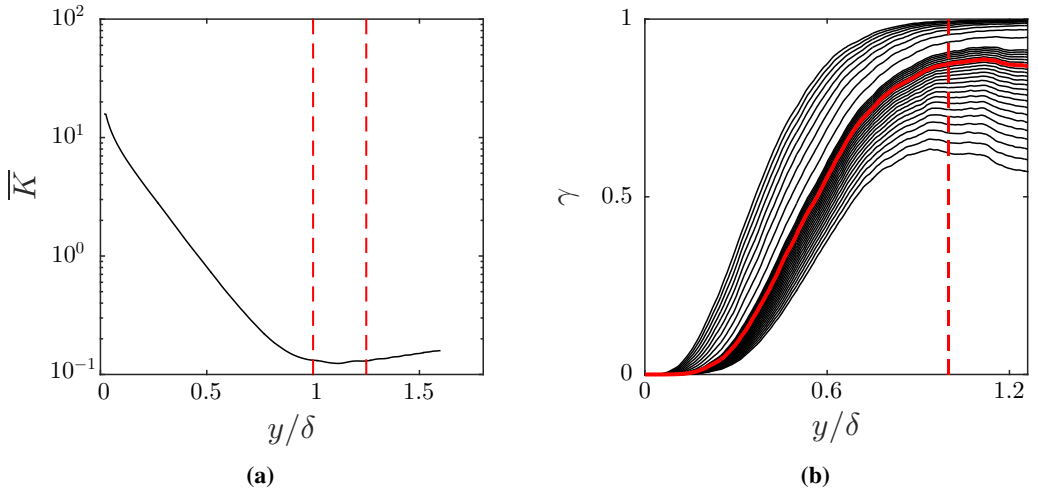

Figure 4.1. TBL flow, planar-PIV field ($Re_\tau = 5300$). (a) Average kinetic energy deficit, $\overline{K}$ with wall normal location. Red dashed lines indicate the region where $\overline{K}$ is approximately constant in the freestream. (b) Variation of the intermittency profile with K_{th}. Fully turbulent flow at $\gamma = 0$, while no turbulent activity is considered at the limit of $\gamma = 1$. Solid red line marks the chosen threshold $K_{th} = 0.26$ and dashed red line denotes the boundary layer thickness above which the kinetic energy deficit profile should be approximately constant.

similar procedure as in Chauhan et al. (2014a) is followed, however due to increased turbulence in the freestream, a balance between the proposed conditions and the resulting statistics has to be found. Firstly, the increased turbulent activity at the freestream leads to a slight upsurge of the average kinetic energy deficit, $\overline{K}$, (see figure 4.1a) in the outer part of the freestream region, while just above δ the values are approximately constant (marked with red dashed lines in figure 4.1a). Consequently, for all following calculations, we only include vectors up to $y = 1.25\delta$, such that only the constant kinetic energy deficit region is included. Different threshold values in increments of 0.01 up to $K_{th} = 0.3$ and in increments of 0.1 up to $K_{th} = 1.2$ are then tested in a subset of 1370 independent snapshots and the results show that, in order to fulfil all requirements, values larger than $K_{th} = 1$ have to be used (figures 4.2a, 4.2b). This essentially means that due to instances where the freestream turbulence is elevated, the required threshold (applied

to all snapshots) would have to increase significantly in order to achieve a proper distinction of turbulent and non-turbulent regions in these cases. This however, would lead to a bias towards the wall for the average TNTI location (see figure 4.2b). Thus, an intermediate value for K_{th} has to be chosen. Based on the variation of both the intermittency profiles as well as the TNTI

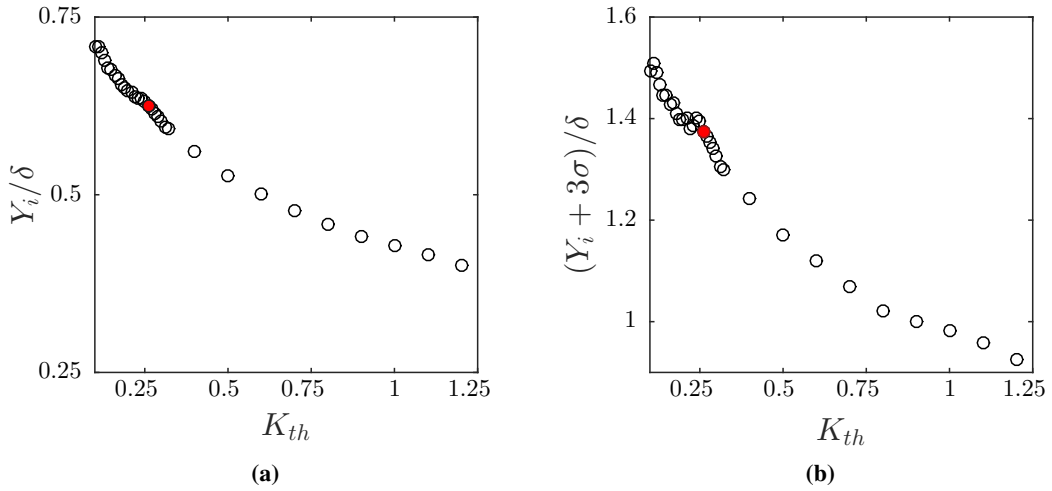

Figure 4.2. TBL flow, planar-PIV field ($Re_\tau = 5300$). Variation of statistics with K_{th} (open circles). (a) Mean TNTI location, Y_i. (b) $Y_i + 3\sigma_i$. Solid red circles denote the chosen threshold $K_{th} = 0.26$.

statistics with K_{th}, a threshold of $K_{th} = 0.26$ is eventually chosen, such that the resulting intermittency profile (marked with red in figure 4.1b) is approximately constant above δ, while also $Y_i + 3\sigma_i < 1.4\delta$, and $Y_i \approx 0.6\delta$. Using this threshold, the mean location of the TNTI is found to be at $Y_i = 0.58\delta$. Finally, it should be noted here that, the process described above does not always result in a continuous contour covering the streamwise extent of the FOV in its entirety. Since these cases counted for a relatively small percentage (5%) of the total number of images (which included more than 405000 snapshots), these instances were not included in any of the presented results.

4.2 Characteristics of the freestream boundary

4.2.1 Geometrical characteristics

After the TNTI is detected in all available snapshots, some statistical characteristics of the interface can be estimated and compared with other published results. First of all, the probability density function (pdf) of the vertical TNTI location is calculated, including all points from each interface. The resulting pdf exhibits a positive skewness towards the wall when compared to a Gaussian distribution (figure 4.3). This behaviour, which was not documented in similar studies of turbulent boundary layers (see Chauhan et al., 2014a; Eisma et al., 2015 among others), is

attributed to the increased freestream turbulence intensity in our facility. This is also the reason of the slightly lower average TNTI location ($Y_i = 0.58\delta$), when compared to the results of Chauhan et al. (2014a).

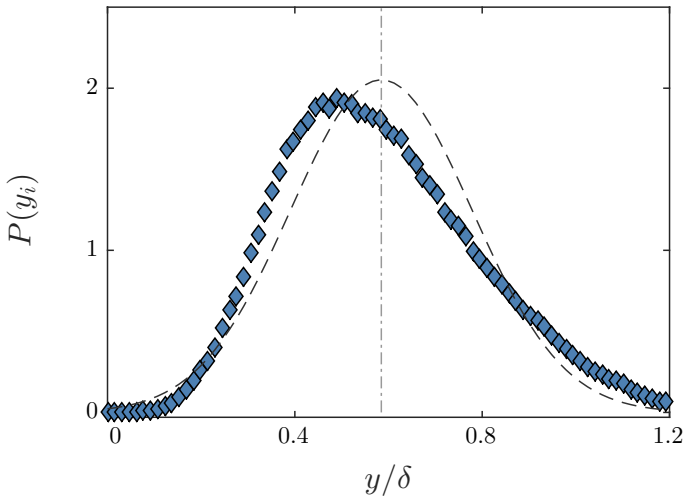

Figure 4.3. TBL flow, planar-PIV field ($Re_\tau = 5300$). Pdf of TNTI location, Y_i. Dashed line denotes the corresponding Gaussian distribution with $\mu = Y_i$, $\sigma = \sigma_i$. Dotted-dashed line denotes $Y_i = 0.58\delta$.

One of the most prominent characteristics of the TNTI, visually observed very early on (Corrsin and Kistler, 1955), is its sharp and convoluted outline. Sreenivasan and Meneveau (1986) were the first to show experimentally that this outline exhibits a fractal-like scaling, while recently de Silva et al. (2013), using PIV supported this argument and further estimated the fractal dimension of high-Reynolds-number boundary layer to be $D_f \approx 2.3-2.4$. Here, we do not attempt to analyse such concepts, however we use the total length of the convoluted interface, L_s, normalised with the streamwise extent of the interface, L_x (figure 4.4), as a representative measure of its multi-scale geometry. On average, the normalised length is shown to be around twice the length of the streamwise extent, while it can reach up to $6L_x$ (figure 4.5a), in line with results reported by Chauhan et al. (2014a). It should be noted here that the available streamwise extent was limited to 0.5δ, therefore larger scale contortions of the interface do not contribute to the presented statistics.

The normalised total length, L_s/L_x, provides information on the convoluted shape of the TNTI and the scales involved in it, but does not explicitly describe the vertical expansion of the interface. For this reason we introduce a second normalisation parameter, namely the maximum wall-normal extent of the interface, L_y, that describes how the total length is distributed in the vertical direction (figure 4.4). As expected, when normalised with L_y, the average ratio is larger ($\overline{L_s/L_y} \approx 5.5$), while on some occasions the total length reaches up to 15 times the wall-normal extent of the TNTI (figure 4.5b).

Both normalisations result in strongly skewed distributions of strictly positive values, with low mean values and large variances thus pointing us towards a comparison with lognormal fits

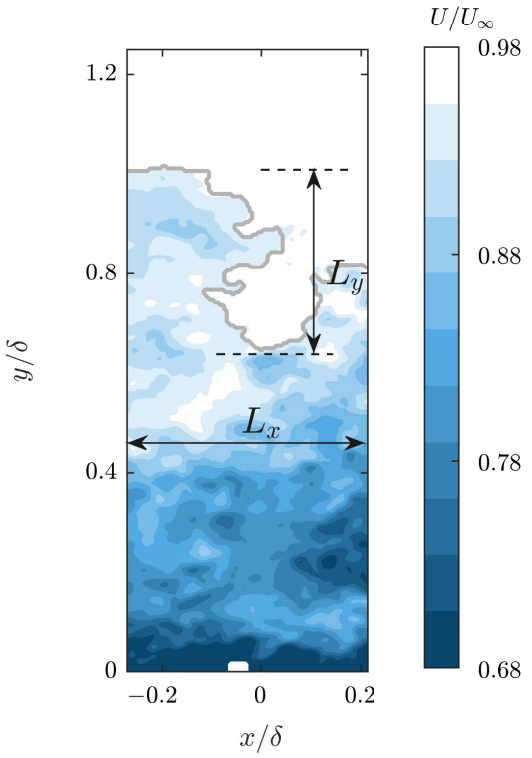

Figure 4.4. TBL flow, planar-PIV field ($Re_\tau = 5300$). Velocity contours of a single snapshot. The TNTI is marked with grey solid line, while the streamwise (L_x) and wall-normal (L_y) extent of the interface are shown in black.

(marked with yellow in figure 4.5). Lognormal distributions are observed in many scientific fields ranging from chemistry, medicine, and biology to finance and sociology and they have been shown to provide more accurate representations of certain physical phenomena than normal distributions (Grönholm and Annila, 2007; Limpert et al., 2001; Limpert and Stahel, 2011 among others). The lognormal fit is seen to match L_s/L_x to some extent, arguably better than a Gaussian fit, while it provides an excellent fit for L_s/L_y, and thus it is worth adding some further comments on its physical meaning. The main difference between a normal and a lognormal distribution is that although both result from a range of random inputs independent of each other, the former only considers additive results while the latter, multiplicative (and divisive) ones (Limpert and Stahel, 2011), thus making it suitable to describe growth processes or indicate an underlying law of proportionate effect. Grönholm and Annila (2007) further suggested that these distributions represent natural processes resulting from the principle of increasing entropy and that they typically describe phenomena arising from small non-linear fluctuations in subsequent steps. The convoluted shape of the TNTI reflects the presence of various scales that influence its geometry and therefore this lognormal behaviour might be indicative of its growth mechanism (the law of proportionate effect could for example indicate that the rate of change of L_s/L_y at any instance is independent of the value of L_s/L_y at that instance). The concept of successive small independent factors, combined in a multiplicative fashion to produce a lognormal distribution of the length of the interface, can be further supported from the autocorrelation of the

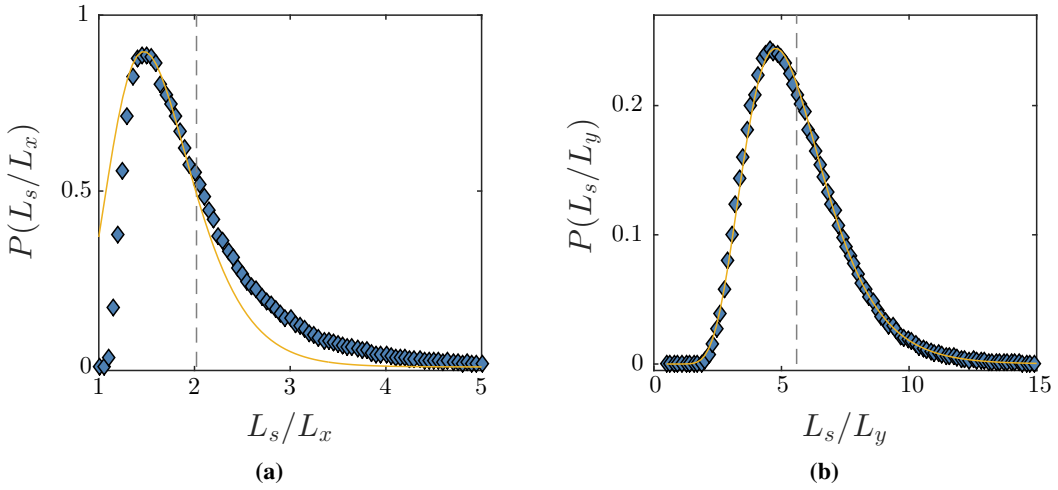

Figure 4.5. TBL flow, planar-PIV field ($Re_\tau = 5300$). Pdf of total length, when normalised with (a) the streamwise extent, L_x and (b) the wall-normal extent, L_y. Dashed lines denote mean values, solid yellow lines mark lognormal fits.

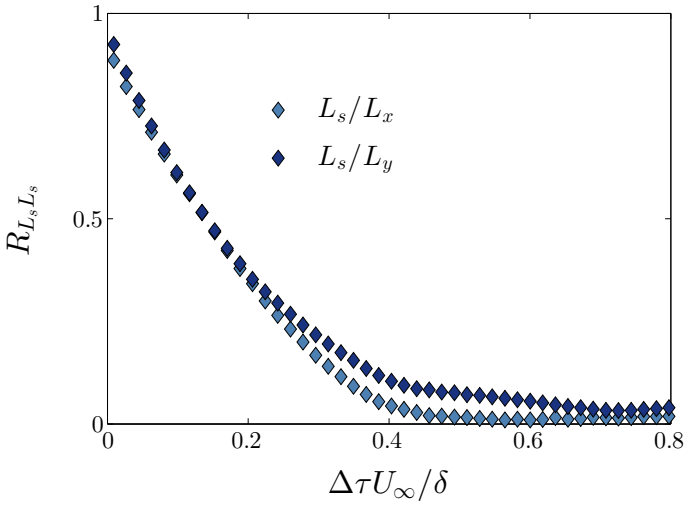

Figure 4.6. TBL flow, planar-PIV field ($Re_\tau = 5300$). Temporal autocorrelation of L_s/L_x and L_s/L_y.

temporal evolution of the two normalised lengths (figure 4.6, using two sets of 10944 consecutive snapshots). It is clear that, both quantities have a limited temporal coherence ($< 0.3U_\infty/\delta$), indicating that they result from many small-scale variations of the interface geometry, thus supporting the observed lognormal distribution. Although a more detailed analysis on the subject is out of scope of the current work, it could be an interesting point for further studies due to the physical implications.

As was shown above (figure 4.3), the TNTI location varies significantly across the different velocity snapshots so it is interesting to assess any potential influence of this variation on the total length of the TNTI. When normalised with the streamwise extent, the total length exhibits

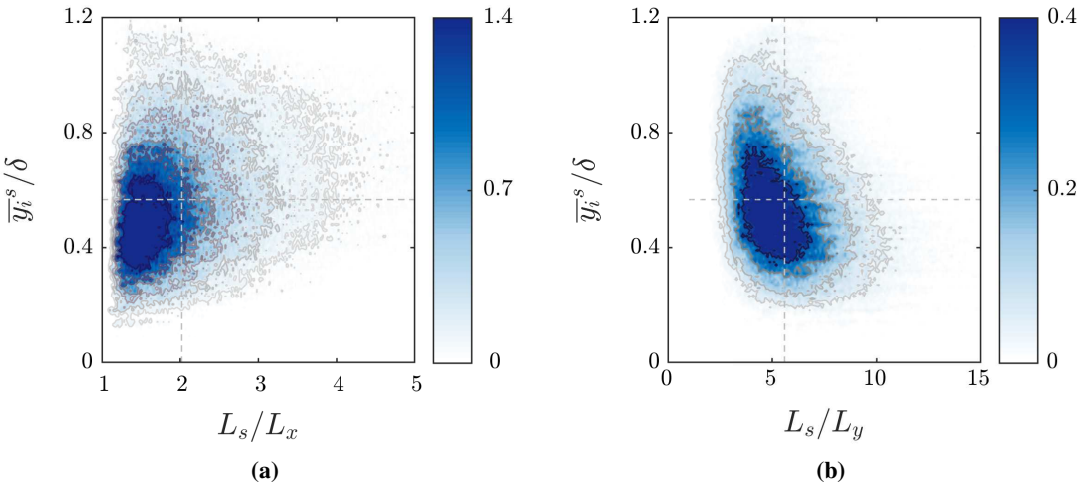

Figure 4.7. TBL flow, planar-PIV field ($Re_\tau = 5300$). Joint pdf of average TNTI location, $\overline{y_i}^s$ with total length, when normalised with (a) the streamwise extent, L_x and (b) the wall-normal extent, L_y. Dashed lines denote mean values.

a maximum at $\overline{y_i}^s \approx 0.7\delta$ (figure 4.7a), where $\overline{y_i}^s$ is the average TNTI location at every time instance. On the other hand, a normalisation with the wall-normal extent shows a decreasing trend with increasing wall-normal location (figure 4.7b). This behaviour suggests that the TNTI has a limited wall-normal extent for $\overline{y_i}^s < 0.5\delta$, which leads to high values of L_s/L_y in that region. For higher wall-normal locations, the ratio rapidly decreases, indicating an increase of L_y that matches the trend observed for L_s.

4.2.2 Conditional statistics across the interface

The use of conditional statistics to identify the sharp changes in flow quantities across the TNTI was first employed by Bisset et al. (2002), who observed both a velocity and a temperature jump again in a turbulent wake. These observations were further extended to turbulent jets (Westerweel et al., 2005, 2009; da Silva et al., 2011) and boundary layers (Hunt et al., 2011; da Silva et al., 2014b; Philip et al., 2014; Chauhan et al., 2014a; Ishihara et al., 2015; Eisma et al., 2015). The thickness of the jump, δ_ω, was unilaterally regarded as a direct measure for the shear across the interface and a crucial parameter of the scales that were involved in the transport mechanisms (Chauhan et al., 2014a).

Following this line of work, in the present section, conditional averages of the main flow quantities across the interface are computed and the average thickness of the TNTI is estimated. As was mentioned above, the average location of the TNTI per snapshot, $\overline{y_i}^s$, varies significantly in time and that variation was shown to have an effect on the geometrical characteristics of the interface. The large number of available velocity snapshots ($\approx 400,000$) allowed us to also assess any potential influence of the TNTI wall-normal location on the conditional statistics across the interface, which, to the authors knowledge was only partially discussed in the work of Chauhan

et al. (2014a). It should also be noted here that, following the works of Kwon et al. (2014) and Chauhan et al. (2014a), in situations where the interface folds on itself, the lower 'envelope' of the interface is considered to ensure that only turbulent regions are considered below it.

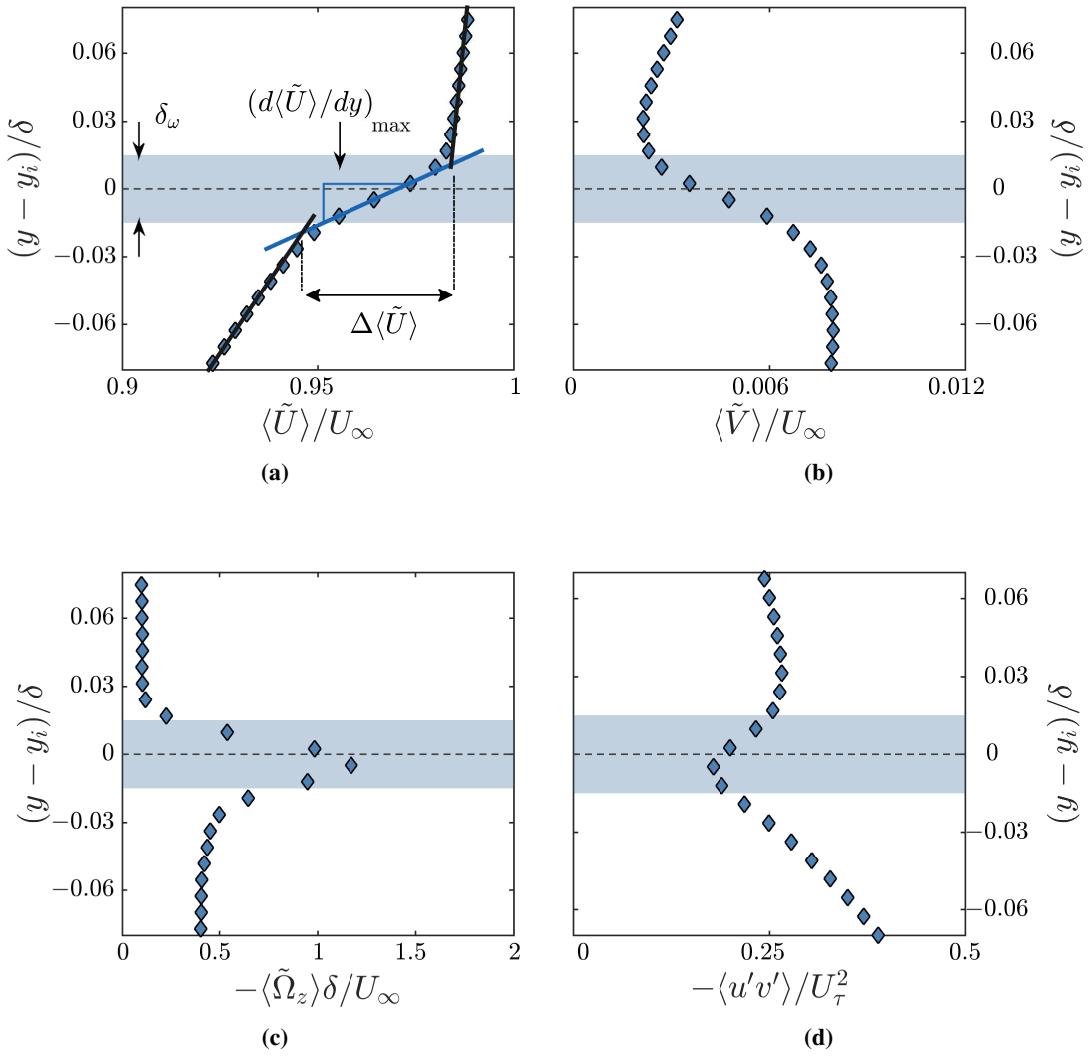

Figure 4.8. TBL flow, planar-PIV field ($Re_\tau = 5300$). Conditionally averaged flow statistics across the interface, y_i. Coloured region indicates the vorticity thickness, δ_ω, estimated following Chauhan et al. (2014a). (a) Streamwise velocity, $\langle\tilde{U}\rangle/U_\infty$. (b) Wall-normal velocity, $\langle\tilde{V}\rangle/U_\infty$. (c) Out-of-plane vorticity, $\langle\tilde{\Omega}_z\rangle\delta/U_\infty$. (d) Reynolds stress, $\langle u'v'\rangle/{U_\tau}^2$.

Conditional statistics for the main flow quantities (denoted with $\langle\,\tilde{}\,\rangle$ in figure 4.8) exhibit clear jumps across the TNTI, thus confirming that the kinetic energy deficit threshold used ($K_{th} = 0.26$) successfully demarcates the turbulent from the non-turbulent region. The step-change of the streamwise velocity, $\Delta\langle\tilde{U}\rangle$ is approximately 4% of the freestream velocity U_∞, in line with results from Chauhan et al. (2014a) and Eisma et al. (2015). When normalised with inner variables, $\Delta\langle\tilde{U}\rangle/u_\tau \approx 1.07$, which is slightly lower than the value of $1.15u_\tau$, suggested by

Chauhan et al. (2014b) who used turbulent boundary layer data of a range of Reynolds numbers ($Re_\tau = 1200 - 14500$) to assess the scaling of the TNTI. This discrepancy could be due to the higher uncertainties on the calculation of the friction velocity u_τ. Following Chauhan et al. (2014a), we define the thickness of the jump as

$$\delta_\omega = \frac{\Delta\langle\tilde{U}\rangle}{\left.\frac{d\langle\tilde{U}\rangle}{dy}\right|_{max}} \tag{4.2}$$

where $d\langle\tilde{U}\rangle/dy\big|_{max}$ is the maximum value of the local gradient. The resulting value for the vorticity thickness is $\delta_\omega = 0.03\delta$ (see also table 4.1), which is in good agreement with the Reynolds number scaling documented by Chauhan et al. (2014b) (see figure 4.9). It has been suggested by several studies (da Silva et al., 2011; Chauhan et al., 2014b; Eisma et al., 2015; Borrell and Jiménez, 2016) that, in turbulent boundary layers, δ_ω is of the order of and scales with the local Taylor microscale (λ_τ). In the present case, $\delta_\omega \approx 0.4\lambda_\tau$ (see also table 4.1), in agreement with results from Eisma et al. (2015). The importance of the vorticity thickness and its scaling has been discussed in several previous works (Bisset et al., 2002; Westerweel et al., 2005; da Silva and Taveira, 2010; da Silva et al., 2011 among others), however a note should be made regarding the terminology adopted here and the limitations imposed by the dataset available. As was also mentioned in chapter 1, Bisset et al. (2002) were the first to postulate the presence of two distinct layers that compose the TNTI, an idea that could only be validated using high-resolution DNS data, able to resolve structures below the Kolmogorov scale (da Silva and Taveira, 2010; da Silva et al., 2011, 2014a). It was subsequently proposed that within the outer 'viscous' superlayer, viscous diffusion is prominent, while the peak in vorticity occurs in the inner interface. The resolution of the present data ($l_x/\eta \approx 4.6$ in the outer layer, where l_x is the interrogation window size) does not allow for such a distinction so here we use the term TNTI to describe the region where a peak in vorticity occurs. Also, following the analysis and relevant considerations of Chauhan et al. (2014a) on a dataset of similar resolution, it is noted that δ_ω, as estimated here, can only provide an upper bound for the actual thickness of the interface. However, since δ_ω scales with λ_τ and in the outer region $l_x/\lambda \approx 0.14$, the resolution allows for the detection of such a jump and we can still gain some valuable insight on how this jump scales for different TNTI locations and whether it is significant for the internal layers below the interface (see chapter 5).

The wall-normal velocity, V (figure 4.8b), exhibits a much less sharp change across the TNTI and follows the trend presented by Eisma et al. (2015). The conditionally averaged out-of-plane vorticity, $\langle\tilde{\Omega}_z\rangle$, shows a strong peak within δ_ω, while it drops to almost zero at the freestream. Finally, the conditionally averaged Reynolds stress profile follows the model suggested by Eisma et al. (2015), although higher values are observed at the freestream, possibly due to the elevated freestream turbulence levels.

When the profiles are conditioned upon the average TNTI location, Y_i, some notable differences can be seen for all flow quantities (figure 4.10 and table 4.1), although the main trends remain

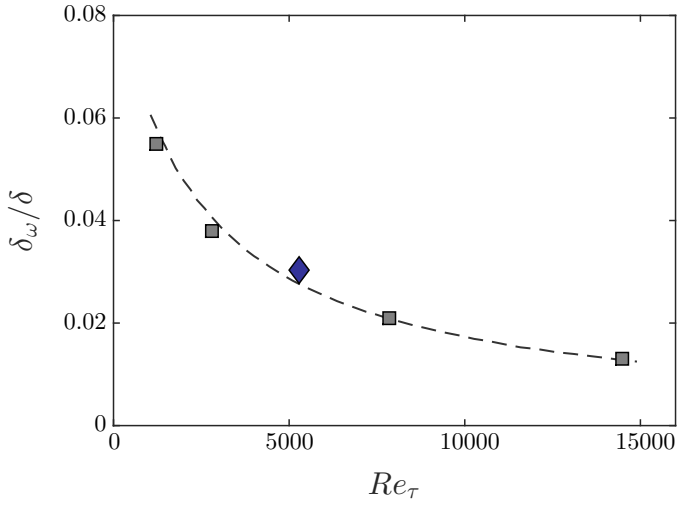

Figure 4.9. TBL flow, planar-PIV field ($Re_\tau = 5300$). Vorticity jump, δ_ω/δ, with Reynolds number from Chauhan et al. (2014b). Present data denoted with ♦.

mostly unaltered. The streamwise velocity jump exhibits a slight increase as the TNTI location decreases, mostly due to the lower velocities present below the interface when it is closer to the wall, while above the interface (figure 4.10a). Above the TNTI, the profiles collapse, indicating similar freestream characteristics regardless of the wall-normal position of the TNTI. For the estimation of the upper limit on the vorticity thickness, δ_ω, we follow the same procedure as described above, this time for the different TNTI locations. Results show that, when normalised with the boundary layer thickness, δ, the estimated thickness decreases as the interface moves closer to the wall (see table 4.1). In addition, δ_ω also exhibits an approximate scaling with the Taylor microscale $\delta_\omega \approx 0.4\lambda_\tau$, in agreement with similar results from Eisma et al. (2015) in the case of internal layers of high shear below the TNTI.

		$\Delta\langle\tilde{U}\rangle/U_\infty$	δ_ω/δ	$\delta_\omega/\lambda_\tau$
All		0.038	0.030	0.36
High	$(\overline{y_i}^s \geq 0.75\delta)$	0.033	0.036	0.43
Average	$(0.45 \leq \overline{y_i}^s < 0.75\delta)$	0.038	0.031	0.36
Low	$(\overline{y_i}^s < 0.45\delta)$	0.039	0.025	0.33

Table 4.1. TBL flow, planar-PIV field ($Re_\tau = 5300$). Velocity jump and vorticity thickness for different wall-normal locations. Taylor microscale, λ_τ, estimated for each wall normal location as $\sqrt{\overline{u'^2}/\overline{(\partial u/\partial x^2)}}$.

The vertical velocity profile, in line with observations from Chauhan et al. (2014a), shows a decreasing trend with decreasing TNTI location, reaching negative values for the lowest interface locations, thus indicating a downwards movement in correlation with low wall-normal TNTI location (figure 4.10b). The out-of-plane vorticity profiles, similar to the streamwise velocity ones, collapse well in the irrotational freestream region above the TNTI, for all TNTI locations, while below the interface, the vorticity peak increases as the TNTI moves closer to the wall

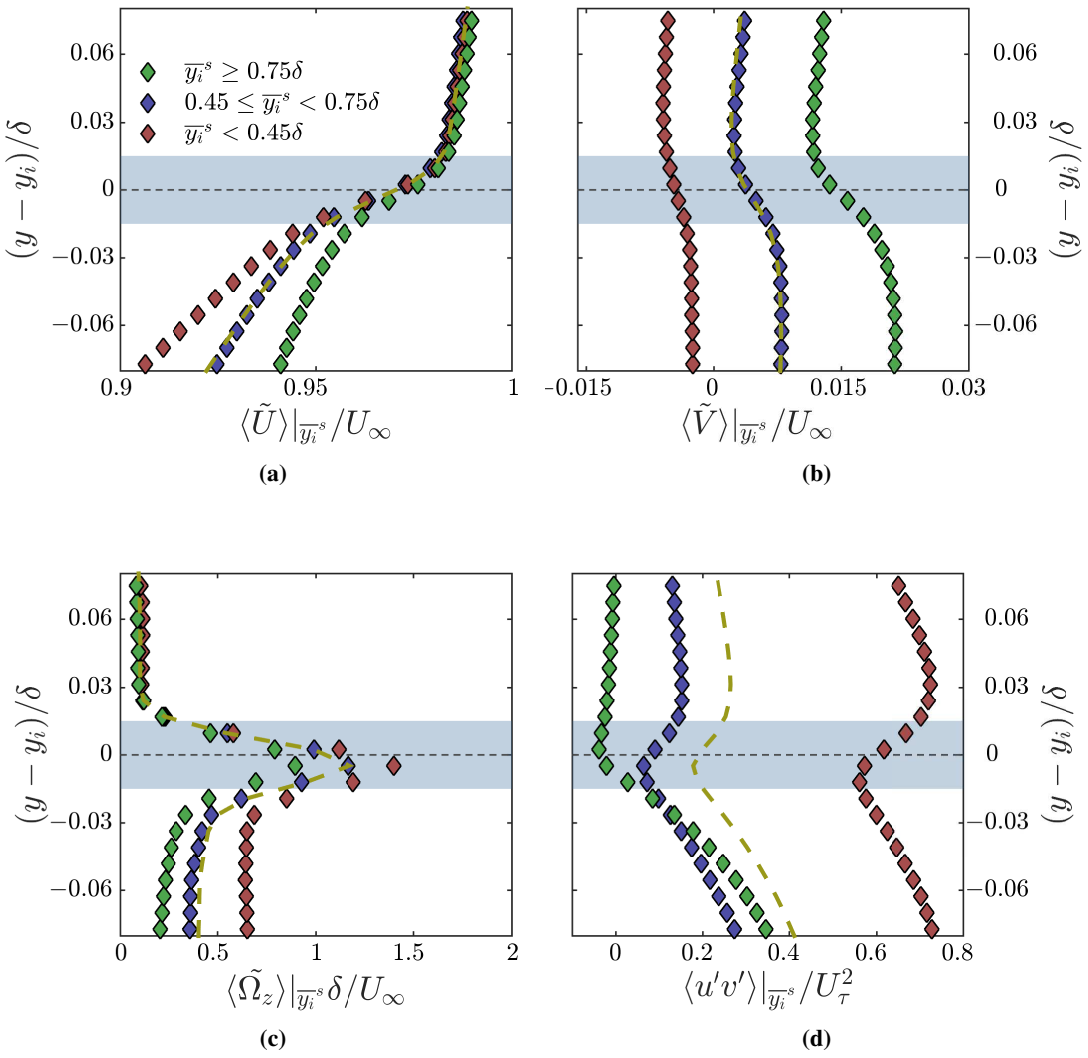

Figure 4.10. TBL flow, planar-PIV field ($Re_\tau = 5300$). Conditionally averaged flow statistics across the interface, conditioned upon the average interface location at each snapshot, $\overline{y_i}^s$: ♦ for $\overline{y_i}^s \geq 0.75\delta$, ♦ for $0.45 \leq \overline{y_i}^s < 0.75\delta$, and ♦ for $\overline{y_i}^s < 0.45\delta$. Coloured region indicates the global vorticity thickness, δ_ω. Dashed lines indicate the global averages in figure 4.8. (a) Streamwise velocity, $\langle \tilde{U} \rangle|_{\overline{y_i}^s}/U_\infty$. (b) Wall-normal velocity, $\langle \tilde{V} \rangle|_{\overline{y_i}^s}/U_\infty$. (c) Out-of-plane vorticity, $\langle \tilde{\Omega}_z|_{\overline{y_i}^s} \rangle \delta/U_\infty$. (d) Reynolds stress, $\langle u'v' \rangle|_{\overline{y_i}^s}/{U_\tau}^2$.

(figure 4.10c). The Reynolds stress profiles are those that show the largest change with decreasing TNTI location (figure 4.10d). For the highest interface locations ($\overline{y_i}^s \geq 0.75\delta$), the profile closely resembles the results from Chauhan et al. (2014a), indicating almost zero values for the Reynolds stress at the interface, while it rapidly increases within the turbulent region. Above the TNTI on the other hand, there is a change in sign and the profile reaches an almost constant value, which was not observed in the global averages (figure 4.8d). For lower TNTI locations, the value of the Reynolds stress increases significantly, while there is also a second inflection

point in the non-turbulent region, which becomes more pronounced as the TNTI location decreases further ($\overline{y_i}^s \leq 0.45\delta$).

It should be noted here that when the velocity, vorticity, and Reynolds stress profiles are conditioned upon the length of the interface, L_s/L_x, which was the other main geometrical characteristic of the TNTI, all trends observed for an increase in length are similar, albeit to a lesser extent, to those observed for an increase in $\overline{y_i}^s$ (see figure 4.10) and as such are not presented here. This similarity in behaviour follows from the sharp increase in length observed for higher wall-normal locations, in figure 4.7.

As was mentioned previously, the TNTI is a thin region of high shear. In their seminal conceptual model of vortical structures in boundary layers, Adrian et al. (2000) depicted the formation of shear layers within the boundary layer as inclined regions, extending from stagnation points due to opposing $Q4$ and $Q2$ events above and below the layers respectively. In an attempt to statistically assess this observation in the case of the TNTI, we compute the contributions of $Q2$ and $Q4$ events on the resulting Reynolds stress profiles (figure 4.10d) separately, as a percentage of the total number of events for each wall normal location across the interface. The resulting profiles show that, below the interface, the two events have similar contributions, however the ejections are slightly more prominent, with a percentage around 40% of the total uv events. A distinct change in percentage is observed across the interface, with $Q4$ events increasing in number and becoming dominant ($> 50\%$) with only 10% of the total belonging to $Q2$ ones, both remaining at these levels throughout the irrotational region.

These trends, are also shown to be strongly influenced by the average TNTI location in each snapshot. Specifically, the percentage of $Q2$ events increases with increasing TNTI location, while as expected the $Q4$ ones follow the opposite trend, thus keeping the percentage of negative uv events approximately constant at 75%. For the highest TNTI locations ($\overline{y_i}^s \geq 0.75\delta$), there are almost no sweeps present below the interface, while when the TNTI is very close to the wall ($\overline{y_i}^s \leq 0.45\delta$), the percentage of ejections above the interface reaches zero. This behaviour is in line with the vertical velocity profile variation presented in figure 4.10c, which showed that for a decrease in the average TNTI location, the vertical velocities across the interface become increasingly negative, thus intensifying the presence of $Q4$ events in these cases. Following the line of work from Adrian et al. (2000), the presence of $Q2$ events can be linked with the flow induced by the presence of vortex cores belonging to hairpin-like structures within the boundary layer. Opposing $Q4$ events, on the other hand, can be explained as either a result of downwash from upstream eddies or of hairpin-like structures that are surrounded by faster moving fluid. We can therefore assume that, in the case of the freestream boundary, above which the turbulent activity is expected to be negligible, $Q4$ events above the boundary would in most cases be the result of structures below it, moving slower than the surrounding fluid. This assumption, combined with the increase of the velocity jump across the TNTI for locations closer to the wall (see figure 4.10a), can explain the increase of $Q4$ events in those cases. On the other hand, when the TNTI is far from the wall, the difference in streamwise velocity across the interface is much

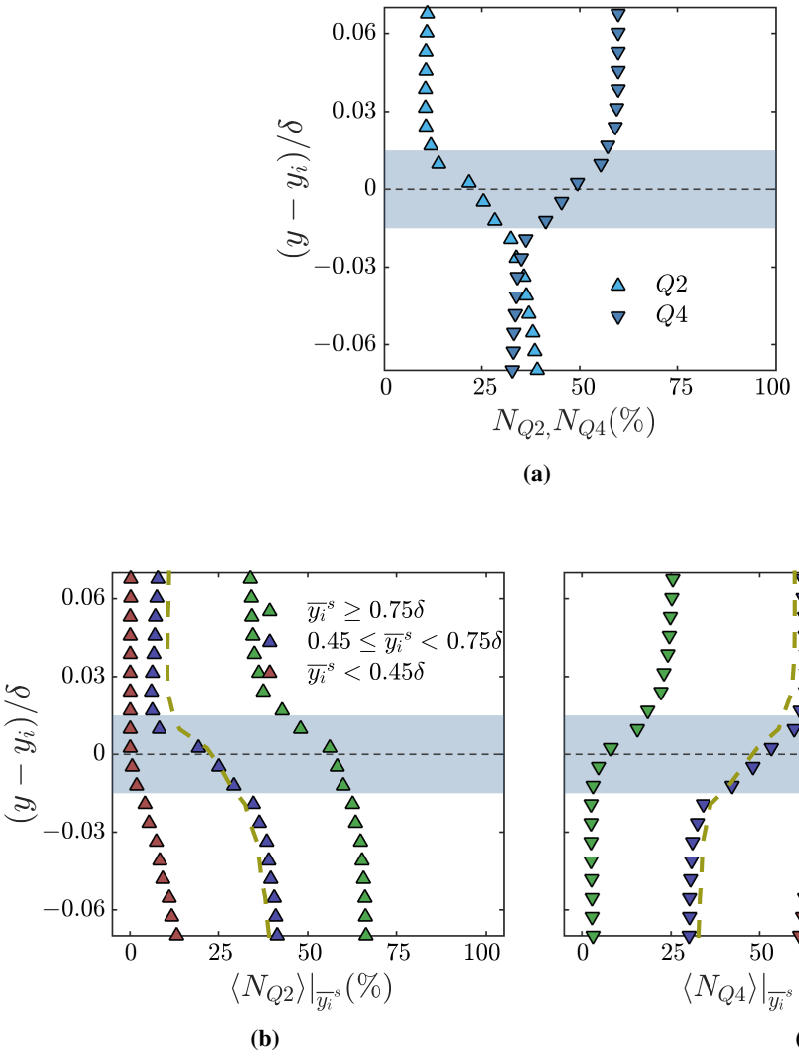

Figure 4.11. TBL flow, planar-PIV field ($Re_\tau = 5300$). Number of $Q2$ and $Q4$ events across the TNTI as a percentage of the total number of uv events at each wall-normal location. (a) $Q2$ and $Q4$ events for all time instances. (b) Percentage of $Q2$ events conditioned upon the average interface location at each snapshot, $\langle N_{Q2}\rangle|_{\overline{y_i}^s}$. (b) Percentage of $Q4$ events conditioned upon the average interface location at each snapshot, $\langle N_{Q4}\rangle|_{\overline{y_i}^s}$: ♦ for $\overline{y_i}^s \geq 0.75\delta$,♦ for $0.45 \leq \overline{y_i}^s < 0.75\delta$, and ♦ for $\overline{y_i}^s < 0.45\delta$.

smaller, and therefore we can assume that most structures below the TNTI are convecting with velocities similar to the freestream, thus resulting in a sharp drop of $Q4$ events for these cases.

Finally, it is important to note that, the instantaneous TNTI location denotes the end of the turbulent region regardless of its location from the wall. As such, the flow behaviour above the interface is not expected to vary significantly, regardless of the interface location with respect to the wall. Although that is indeed the case for the streamwise velocity and vorticity above the interface (reaching freestream and zero values respectively), there are significant differences observed for the vertical velocity and quadrant events as discussed above. Following

the work of Kwon et al. (2016), some of these observations can be traced back to the Reynolds-decomposition of the flow. The authors argued that such a decomposition might alter results in the case of the outer region, where the flow is strongly intermittent. They specifically remarked that this would lead to positive velocity fluctuations for a low TNTI location, since in a time-average sense, freestream values at that location would be higher than the global mean – an observation indeed supported in the present work (see figure 4.11b). In the context of a Reynolds decomposition of the flow this is mathematically sound, however $Q4$ events detected in the freestream region in this way should not be considered turbulent. This indicates that, some of the discrepancies observed for a variation of the interface location analysed in this section reflect the effect of the tools used to analyse the flow, namely here the velocity decomposition scheme. However, that mainly refers to quadrant event behaviour, since it is their estimation that involves a decomposition of the flow. Also, as was suggested in Kwon et al. (2016), the intermittent nature of the flow affects mostly the streamwise velocity component, while the other two components are not significantly altered. Therefore, the prominence of $Q4$ events above the TNTI, for low interface locations, is partly a result of an increase of higher than average streamwise velocity events (inherent to a Reynolds decomposition of the flow) however, the negative vertical velocity fluctuations associated with these events can be traced back to the decreasing trend of the full vertical velocity profile across the interface (see figure 4.10b). As such, these events do indeed indicate a different behaviour of the irrotational flow close to the TNTI, induced by the turbulent region beneath it. Specifically, an average downwards movement of the turbulent region is shown to be linked with a negative vertical velocity also in the irrotational region in the vicinity of the TNTI (see figure 4.10b). On the other hand an upwards movement of the turbulent region is associated with a positive vertical velocity, albeit smaller in magnitude, of the region above the TNTI. These contrasting behaviours could potentially be linked with different entrainment rates as will be discussed in the following section.

4.3 Entrainment

Following the statistical analysis of the main characteristics of the TNTI in the previous section, an attempt is made here to quantify the entrainment rate across the interface, exploiting the time-resolved data available. Previous studies have used time-resolved information to estimate entrainment in the case of a turbulent jet (see Wolf et al., 2012; Watanabe et al., 2016; Mistry et al., 2016), however, to the authors' knowledge, such analysis has not yet been achieved for turbulent boundary layers. Notable works on the subject (Chauhan et al., 2014a,b; Philip et al., 2014; Eisma et al., 2015) employed 2D velocity snapshots and based the entrainment analysis on theoretical concepts. Our aim here is to apply the methodology described in Mistry et al. (2016) for turbulent jets and adjust it accordingly for the case of a turbulent boundary layer, in order to estimate the entrainment rate across the TNTI and compare it with previously suggested theoretical estimations.

4.3.1 Method Analysis

The method used for the estimation of the entrainment rate, denoted v_n, is based on the process described in Mistry et al. (2016), appropriately altered to account for the temporal and spatial resolution of our database for the case of a much more rapidly evolving flow. More specifically, the interface is detected at two time instances, t and $t+dt$. Mistry et al. (2016) suggested that the change of the interface geometry between these two times would be a result of local advection and entrainment. Therefore, in order to isolate the effect of entrainment, the interface at time $t+dt$ is translated by a distance $-u_I dt$, assuming a linear advection with velocity u_I. The difference between the translated interface and the interface detected at time t, representing the entrainment change, is estimated as the normal distance between the two curves at each point, $\boldsymbol{dl}\cdot\boldsymbol{n}$, where $\boldsymbol{n}$ is the outward normal vector, and the local entrainment velocity is computed as $v_n = \boldsymbol{dl}\cdot\boldsymbol{n}/dt$. This approach is shown to work well in the case of a turbulent jet, where the TNTI is detected using a passive scalar and the entrainment velocity is estimated to be of the order of the Kolmogorov microscale (Mistry et al., 2016). In a turbulent boundary layer however, the entrainment velocity is expected to scale with the friction velocity (Chauhan et al., 2014b), which is almost an order of magnitude higher than the Kolmogorov velocity at the edge of the boundary layer (Herpin et al., 2010), and as such requires a much finer temporal resolution to be accurately measured. In the present case, the frame rate ($f = 800\ Hz$, $dt^+ = 1.7$) results in much larger deformations of the interface geometry at each timestep, than what could be approximated using the surface normal vectors. Therefore, in order to estimate the entrainment at each time instance, we still follow the initial steps described in Mistry et al. (2016) however, instead of a point-by-point approach using the surface normal vectors, we compute an average entrainment rate for the interface at each time instance. Specifically, the entrainment or mass flux is computed as the difference in area, dA, below the translated interface at time $t+dt$ and the initial interface at time t (see figure 4.12). Since the interface demarcates the end of the turbulent region, this essentially represents the amount of fluid parcels that move from the irrotational to the turbulent region (and vice versa) from one time instance to the other. Negative values indicate a decrease in the turbulent area below the interface (detrainment), while increase of the turbulent region over time is represented with positive values. The entrainment or mass flux rate is then $\dot{M} = dA/dt$, and the entrainment velocity $v_n = \dot{M}/L_s$, for each snapshot, where L_s is the interface length as described in the previous section. Additionally, instead of a linear approximation, we chose a second order Lagrangian approach (see chapter 3) to estimate the change of the interface geometry due to local advection. The time interval used was the minimum allowed by the acquisition frequency ($dt^+ = 1.7$). In order to get converged entrainment values but based on independent samples, velocity snapshot pairs that were at least half a flow-through time apart ($\Delta t U_\infty/\delta = 0.2$) were chosen from the initial database. These were further conditioned upon the correlation of the interface outline between the two snapshots (chosen to be above 0.9), in order to remove extreme excursions of the interface geometry, mainly due to the freestream turbulence present in the flow. The final number of image pairs processed for all entrainment results presented here was $N_{pairs} = 16358$.

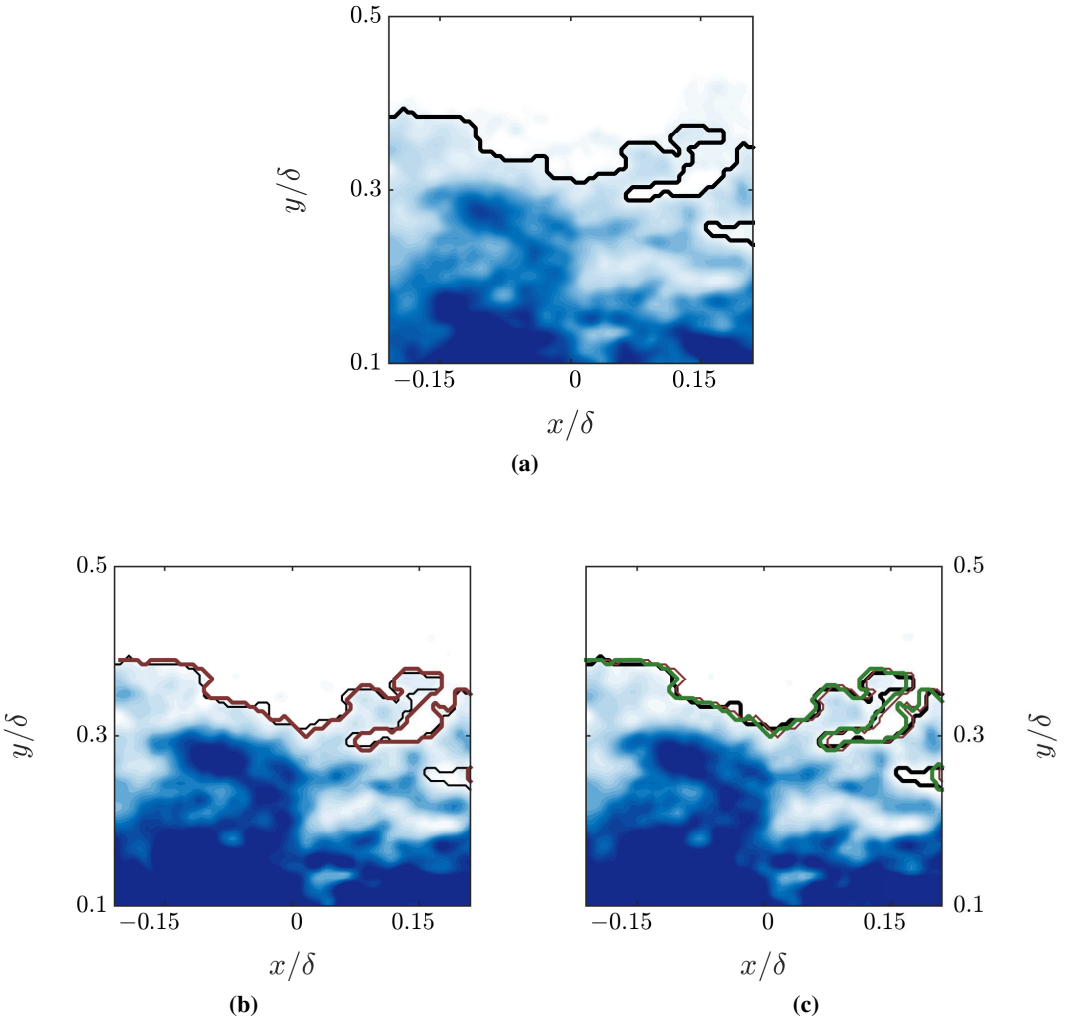

Figure 4.12. TBL flow, planar-PIV field ($Re_\tau = 5300$). Velocity contours and interface outline at time t and $t + dt$ with and without subtracting local advection. (a) Velocity contours and interface outline at time t (black solid line). (b) Velocity contours and interface outline at time $t + dt$ (brown solid line). (b) Velocity contours at time t and interface outline at time $t + dt$ when the local advection is subtracted (green solid line).

4.3.2 Effects of streamwise extent

The entrainment estimation process as described above, can only provide an average entrainment velocity for each snapshot and although the streamwise extent of the FOV is limited ($\approx 0.5\delta$), some deviations from a point approach as described in Mistry et al. (2016) are expected. To assess this influence, we divide the TNTI at each time instance in N equidistant segments of decreasing length, ΔL_x and estimate the mass flux at each segment separately. ΔL_x varies linearly from 0.5δ (single segment) to 0.03δ, which is the limit after which the number of interface points at each segment becomes too small for an accurate estimate of an area change. It should be noted here that, in general, the resulting streamwise extent of each interface segment L_{x_i} should be equal to ΔL_x, however due to edge effects from the Lagrangian translation described

above, the resulting values of L_{x_i} are slightly lower. For consistency, in all the results that follow, the variation of L_{x_i} is presented. At each snapshot, the sum of mass-flux estimates of all segments equals the mass flux computed for the entire TNTI, while also the total length of each path equals the total length of the TNTI (equation 4.3).

$$\sum_{i=1}^{N} L_{s_i} = L_s, \qquad \sum_{i=1}^{N} dA_i = dA \tag{4.3}$$

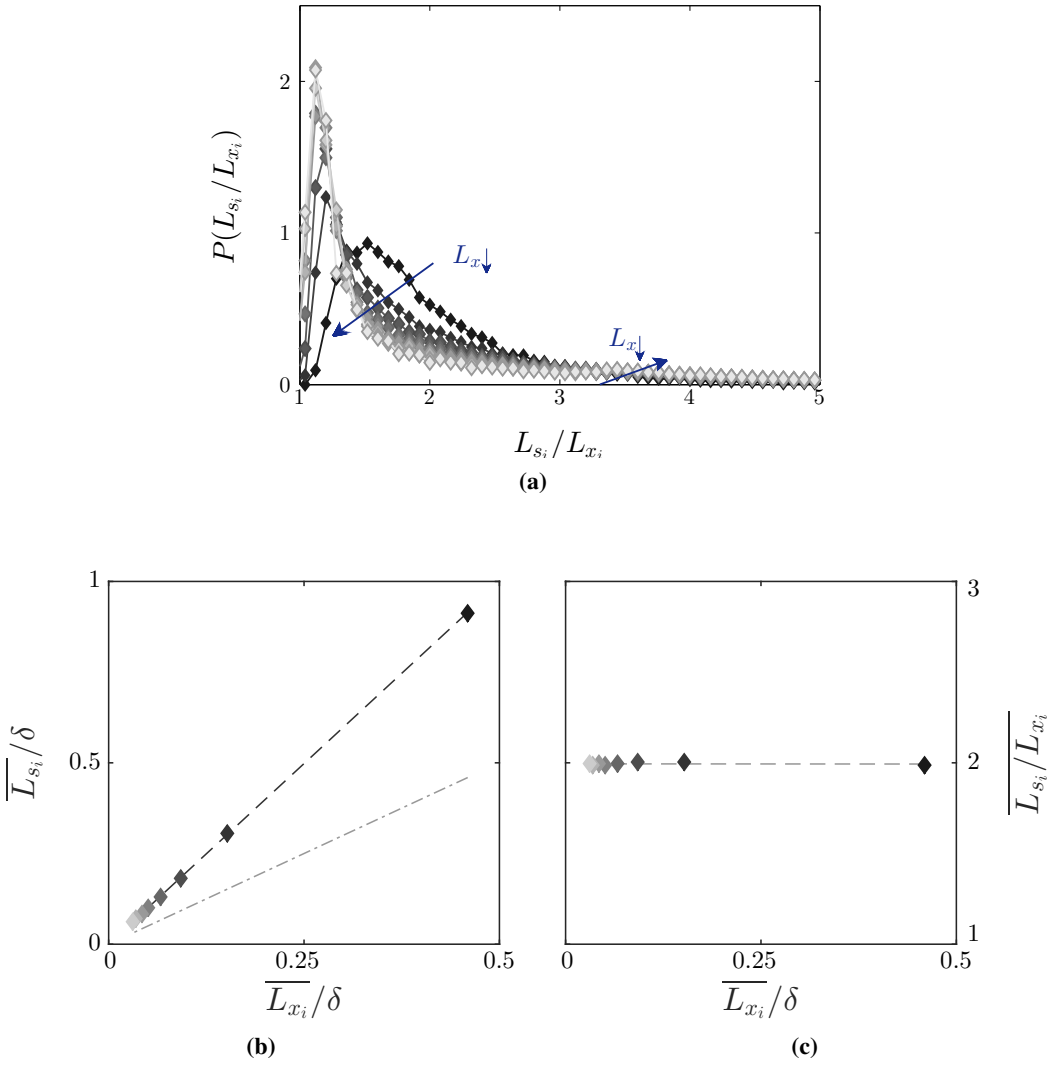

Figure 4.13. TBL flow, planar-PIV field ($Re_\tau = 5300$). (a) Pdf of normalised length, L_{s_i}/L_{x_i}, with varying streamwise extent. Blue arrows indicate decrease of ΔL_x from 0.03δ to 0.5δ. (b) Variation of $\overline{L_{s_i}}$ with $\overline{L_{x_i}}$ for $\Delta L_x : 0.03\delta - 0.5\delta$. Dashed line indicates linear fit for $\overline{L_{s_i}}$ and dot-dashed line shows the unit slope of $\overline{L_{x_i}}$ for comparison. (c) Variation of $\overline{L_{s_i}/L_{x_i}}$ with $\overline{L_{x_i}}$ for $\Delta L_x : 0.03\delta - 0.5\delta$ (linear fit marked with dashed line).

Locally however, low/high values of the interface length L_{s_i} when limited to a certain streamwise extent would lead to a significant decrease/increase of the normalised length L_{s_i}/L_{x_i}. This can be seen from the pdf of L_{s_i}/L_{x_i}, when the TNTI is divided into segments of different streamwise

extents (figure 4.13a). An increase in the number of segments, shifts the peak of the distribution to lower values, while the tail also becomes wider. On average though, these differences are much less pronounced. A linear increase of L_{x_i} (unit slope in figure 4.13b marked with dot-dashed line) will also lead to a linear increase of the average interface path, $\overline{L_s}$, with only a difference in slope (symbols in figure 4.13b) which would lead to an almost constant ratio of the two lengths. As expected, the resulting values of $\overline{L_{s_i}/L_{x_i}}$ (symbols in figure 4.13c) agree well with the expected constant ratio, thus ensuring that, on average the mass flux estimations should not vary significantly from a point-by-point approach. To further assess this notion, entrainment

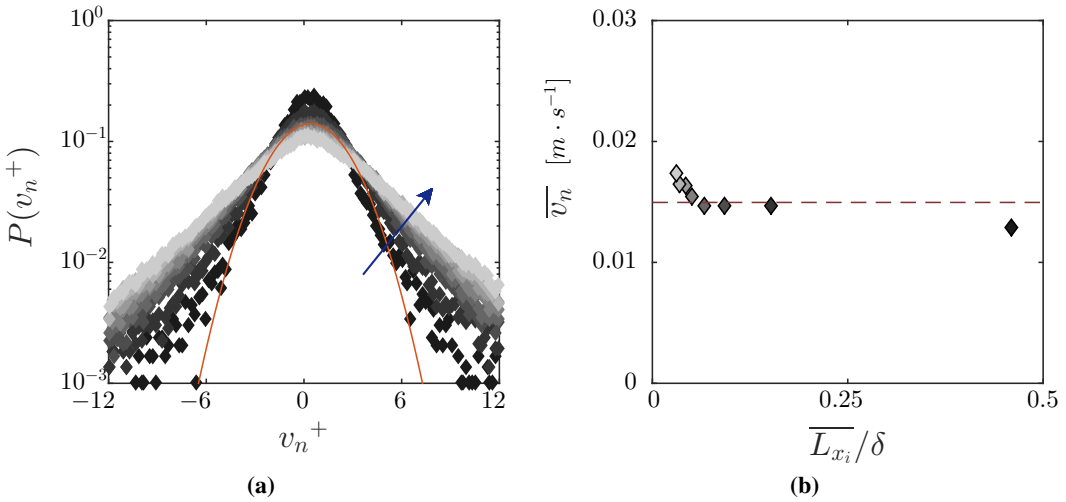

Figure 4.14. TBL flow, planar-PIV field ($Re_\tau = 5300$). (a) Pdf of inner normalised entrainment velocity v_n^+ for $\Delta L_x : 0.03\delta - 0.5\delta$. Blue arrow indicates increase in the number of segments and a Gaussian fit is marked with red solid line. (b) Variation of the average entrainment velocity, $\overline{v_n}$ for $\Delta L_x : 0.03\delta - 0.5\delta$. Dashed line indicates average mass flux rate as estimated in Chauhan et al. (2014a) (see equation 4.4).

velocities v_n, are also computed for an increasing number of TNTI segments (figure 4.14a). The resulting v_n values are of the order of the friction velocity u_τ, as suggested by Chauhan et al. (2014b), while the average entrainment velocity for all cases considered is positive. Additionally, the shape of the distribution, which is much wider than a Gaussian distribution (red solid line in figure 4.14a), agrees well with the results from Mistry et al. (2016), with the most notable difference being the scaling (v_n scales with the Kolmogorov velocity in a turbulent jet) as was already discussed above. As the number of segments increases, the pdf becomes wider, due to aforementioned locally higher values of L_{s_i}, while it also shows better convergence due to the higher number of points included. The average values of the entrainment velocity, $\overline{v_n}$, reach a plateau for average segment lengths ($\Delta L_x : 0.06\delta - 0.15\delta$, figure 4.14a), although they exhibit larger discrepancies from a constant trend than $\overline{L_{s_i}/L_{x_i}}$, especially for small segment lengths. Interestingly, the resulting values agree well with the theoretical estimation of the average rate of mass per unit area as described in Chauhan et al. (2014a) (see equation 4.4, the density is

omitted from the original equation for comparison).

$$v_n = \frac{\dot{M}}{L_s} \approx \frac{d\dot{M}}{dx} = U_\infty \left[\frac{d\delta}{dx} - \frac{d\delta^*}{dx} \right] \tag{4.4}$$

4.3.3 Entrainment for different interface geometries

Finally, after the entrainment estimation process has been analysed and compared with previous theoretical results, we can assess the dependence of the mass flux on the geometrical properties discussed in the previous section. More specifically, the influence of the average TNTI location

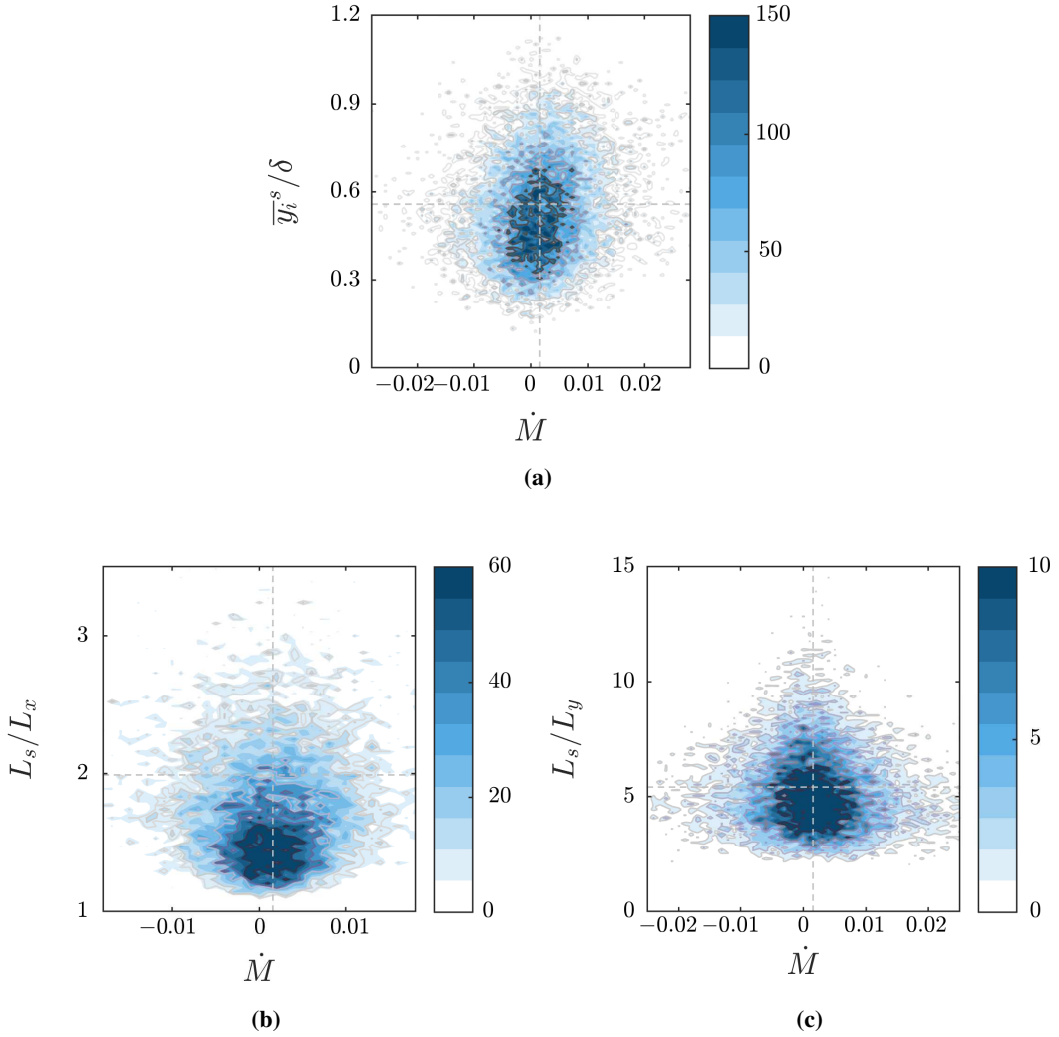

Figure 4.15. TBL flow, planar-PIV field ($Re_\tau = 5300$). Joint pdfs of the mass flux rate, $\dot{M}$ with (a) the average TNTI location at each time instance $\overline{y_i}^s$, (b) the interface length normalised with the streamwise interface extent, L_s/L_x, and (c) the interface length normalised with the wall-normal interface extent, L_s/L_y. Dashed lines indicate average values.

at each time instance, $\overline{y_i}^s$ and of the total interface length, L_s, when normalised with the streamwise (L_x) and wall-normal (L_y) interface extent, are considered (figure 4.15). For all the results

presented here, the entire interface at each time instance is considered, using the full streamwise extent of the FOV. The average TNTI location is shown to have a moderate effect on the resulting mass flux rate, with positive entrainment values being slightly more prominent on higher than average $\overline{y_i}^s$ locations (figure 4.15a). Taking into account the distribution of the velocity components and Reynolds stress events discussed above, we can assume that for lower than average TNTI locations, it is mainly the vertical downwards motion that is relevant in the prominence of $Q4$ above the TNTI, since the streamwise component remains at freestream values regardless of the TNTI location. This negative vertical velocity, shown on average to be larger in amplitude than the velocity of the turbulent region, might then act as an inhibition for the growth of the boundary layer (figure 4.11), opposing the small percentage of $Q2$ events within the turbulent region. This opposing motion could be the reason for the increase of detrainment (figure 4.15a) and the much flatter interface outlines (figure 4.7b), in those cases. When the TNTI is far away from the wall on the other hand, there is a much greater part of the turbulent region with velocities close to the freestream, moving upwards, also inducing a positive vertical velocity in the freestream region, which however is smaller in amplitude. These observations indicate that a strong upwards motion within the turbulent region potentially brings about larger entrainment rates without the opposing presence of negative vertical velocity fluctuations above the interface, thus explaining the bias towards positive entrainment values in those cases. This view, conceptually is very similar to the models presented by Praturi and Brodkey (1978) and acknowledges a prominent role for sweep events above the interface; it is their strong presence that is shown to be linked with lower interface locations and detrainment, and their absence that allows the $Q2$ events within the turbulent region to grow upwards.

The total length of the interface, when normalised with the streamwise extent does not show a clear trend with $\dot{M}$, however it is interesting to note that more convoluted interfaces, in terms of total length, are not necessarily linked with higher entrainment values (figure 4.15b). It is mostly interfaces with a L_s/L_x slightly above average (dashed horizontal line in figure 4.15b) that are shown to be linked with larger mass flux rates, although these fluxes can be either positive or negative with almost equal probabilities. This symmetry is also observed in the joint pdf of the mass flux with L_s/L_y, with only a small net positive $\dot{M}$ (dashed vertical line in figure 4.15c), reflecting the trend observed for the entrainment velocity in the previous subsection (figure 4.14a). However, in terms of magnitude, $\dot{M}$ shows a clear decreasing trend with L_s/L_y, reaching a maximum for L_s/L_y values just below the average (dashed horizontal line in figure 4.15c). This observation when combined with the variation of $\dot{M}$ with L_s/L_x, indicates that larger entrainment/detrainment fluxes are linked with interfaces of an average path length and a comparable wall normal extent. Interfaces with these characteristics were shown to reside on higher than average wall-normal locations (figure 4.7b). The wall-normal extent can be linked with a large-scale variation of the interface geometry (see figure 4.4), while the total path-length is a measure of the convolution of the interface at different scales. Highly convoluted interfaces with limited wall normal extent (high L_s/L_y ratios) exhibit mass fluxes much smaller in magnitude.

Combining the previous comments, it is evident that, although positive entrainment values are observed for higher than average TNTI locations (figure 4.15a), where the interface is also shown to be highly convoluted (figure 4.7b), the opposite correlation does not exist: highly convoluted interfaces are not necessarily linked with positive net entrainment values. Further, very long interfaces (high values of both L_s/L_x and L_s/L_y in figures 4.15b and 4.15c), result in a sharp decrease of both positive and negative entrainment values. Taking into account that these geometries are also rarely observable (figure 4.5), it seems rather unlikely that a 'nibbling' mechanism of the small scales could account for large entrainment changes. However, with the current dataset it is not possible to fully ascertain whether large-scale engulfment results in larger entrainment rates either, since the streamwise field of view is limited ($L_x = 0.5\delta$). To conclude, what could be suggested with some certainty is that the location of the freestream boundary influences the observed jumps in velocity, vorticity and Reynolds stress and also the resulting entrainment rates, with lower TNTI locations mostly inhibiting boundary layer growth, a behaviour mainly associated with the vertical velocity component.

Potential changes in the balance between negative and positive velocity fluctuations also in the case of uniform momentum zones below the TNTI, could further highlight the structural organisation of the flow, and will be the main point focus of the following chapter.

Chapter 5

Temporal evolution of velocity fluctuations within the turbulent region

In the previous chapter the characteristics and evolution of the TNTI in the case of a turbulent boundary layer were presented. Here, we extend further the structural analysis of the boundary layer by looking at the temporal evolution of uniform momentum zones (UMZs) below the freestream boundary using the same time-resolved planar PIV database (chapter 2, section 2.3).

5.1 Detection of instantaneous uniform momentum zones

We adopt the term 'internal layers' from Eisma et al. (2015) to describe regions of high shear occurring throughout the boundary layer and separate regions of uniform momentum. In order to identify these layers, we follow the methodology used by Adrian et al. (2000) and recently by de Silva et al. (2016), altered to some extent in order to account for time-resolved data and tracking purposes. The instantaneous method is based on detecting the local peaks of the probability density function (pdf) of the streamwise velocity component for every velocity snapshot. It has been shown that these peaks represent the modal velocities that characterise each UMZ (Meinhart and Adrian, 1995; Adrian et al., 2000; de Silva et al., 2016). However, as suggested by de Silva et al. (2016), only the vectors below the turbulent/non-turbulent interface (TNTI) should be included, so that the significantly higher outer peak of the non-turbulent region would not overshadow the ones of the internal layers. For this reason and since the freestream boundary location was previously estimated (see chapter 4), we also construct the pdf of the streamwise velocity component for every snapshot by identifying the vectors belonging to the turbulent region only. The local peaks observed in the constructed pdf represent the modal velocities that characterise the different UMZs present in the flow. Conversely, the edges of the zones lie at points of local minimum, or they can be estimated by the mid-point between the modal peaks (see de Silva et al., 2016). Two representative snapshots of this detection procedure can be seen

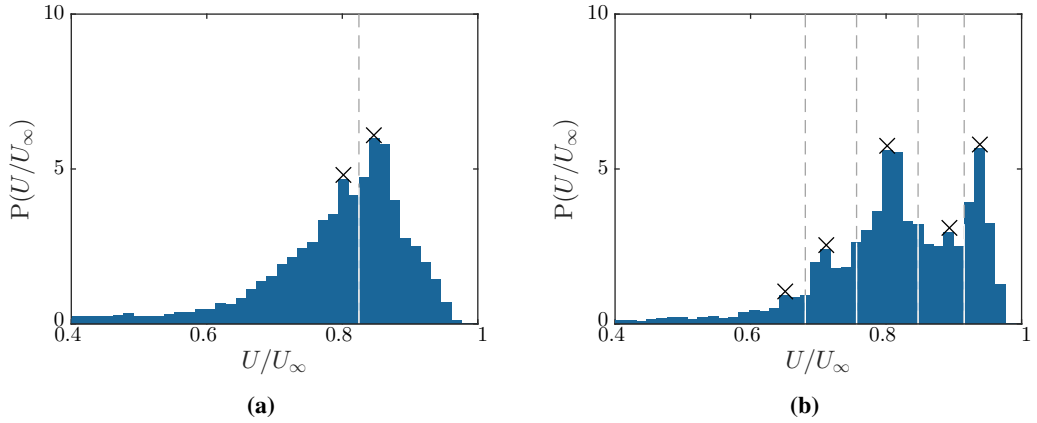

Figure 5.1. TBL flow, planar-PIV field ($Re_\tau = 5300$). Pdf of U/U_∞ for two independent snapshots. Detected peaks denoted with $\times$.

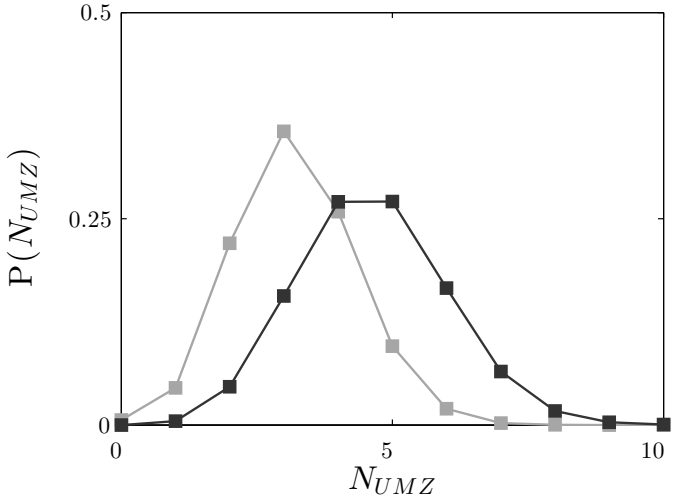

Figure 5.2. TBL flow, planar-PIV field ($Re_\tau = 5300$). Pdf of the total number of peaks detected, following a snapshot (black symbols) and a time-resolved (grey symbols) approach.

in figure 5.1. We apply this detection process to all the available velocity snapshots independently and, on average ≈ 4.5 peaks are detected for $Re_\tau = 5300$, with a distribution shown in figure 5.2 (black symbols), which agrees with the results of de Silva et al. (2016). For the detection of the zones' edges, the same procedure is followed, this time searching for troughs of the velocity pdf. Because the zones and their edges are treated independently, it is not always certain that each peak would be bounded by two edges, so for the peaks that are unbounded, the mid-distance between two peaks is chosen as the edge location.

5.1.1 Influence of peak detection thresholds

There are some important considerations regarding the detection process and the resulting number of peaks that are worth discussing briefly here. Firstly, the streamwise extent of the data and consequently the number of vectors available were shown by de Silva et al. (2016) to be important factors when detecting the modal velocities. Based on a range of experimental and numerical datasets of different Reynolds numbers, the authors concluded that the required streamwise extent should be scaled in viscous units and be large enough so that that good convergence is ensured, but also small enough to allow for the lowest modal velocities to manifest their peaks. A combination of a streamwise extent $\approx$ 2000 viscous units, including $\approx$ 5000 vectors (below the TNTI) divided in 50 bins was shown to be an appropriate choice and even in cases where the number of vectors varied significantly the detected number of peaks remained unaffected (de Silva et al., 2016). In our case, the available streamwise extent is $\approx$ 2600 viscous units (0.5δ), including on average 6500 vectors below the TNTI (depending on its vertical location) that were distributed in 50 bins. We choose to use the full streamwise extent available for the detection process, even though it is larger than what was reported in the literature. However for completeness, we repeated the process while reducing the field of view to 2000 viscous units; even though there were instantaneous discrepancies in individual snapshots, the resulting statistics were similar while the trends discussed in following sections remained unaltered. Further, we found that the most important factor in the resulting number of peaks was the thresholds used in the peak detection algorithm itself. These could include the allowed distance between two peaks, the minimum height for a peak to be considered detectable and its difference in height with the neighbouring points. Depending on these parameters, the resulting average number of detected peaks is found to vary significantly (figure 5.3). An increase of the minimum required prominence of the peaks with respect to their neighbours, results (as expected) in a gradual decrease of the average detected number of peaks (from 6 to almost 3). Similarly, when the allowed distance between peaks is significantly increased, no more than 4 peaks on average can be detected. When the peaks are allowed to be next to each other though, the number of detected peaks can reach up to 7, however in that case differentiating between different UMZs would be almost impossible. Finally, the range of the minimum required peak heights tested here, seemed to have only an imperceptible influence on the resulting number of peaks (increasing height leads to slightly lower N_{UMZ}).

In order to facilitate comparison with previous results, we choose a parameter set such that the average number of peaks follows the Reynolds number dependency found by de Silva et al., 2016. These includes a minimum peak height of 0.3 with a prominence of at least 0.05 from neighbouring values, and a minimum distance of two bins between detected peaks.

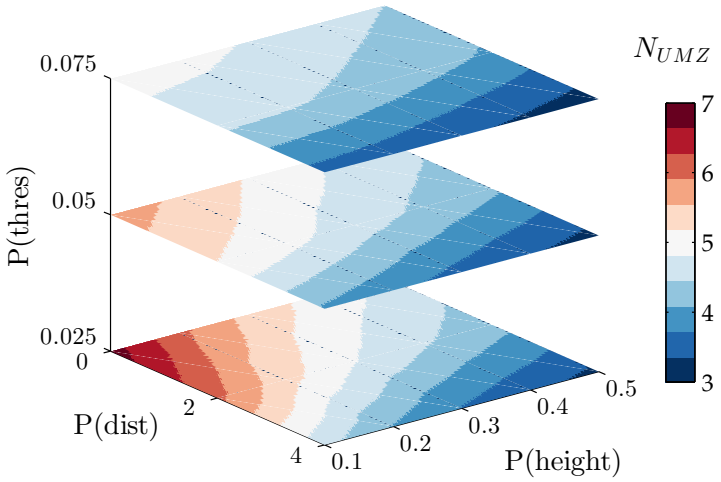

Figure 5.3. TBL flow, planar-PIV field ($Re_\tau = 5300$). Contours of the average number of peaks detected, with varying minimum peak height, minimum peak distance and minimum peak threshold (prominence from neighbouring points) in the peak-detection algorithm.

5.2 Detection of time-coherent uniform momentum zones

Following the process described above, we can successfully identify UMZs and their edges in all available snapshots, however tracking them in time becomes increasingly difficult for a multitude of reasons. From a physical perspective, even when identified correctly, not all modal velocities and zones that appear instantaneously necessarily last longer than a single snapshot in time. Furthermore, while identifying local maxima in independent distributions can be successful most of the time, following the same procedure in a time-series does not always result in a smooth evolution of the detected peaks. The same applies to the evolution of the edges of these zones, which makes their tracking in time very challenging. For these reasons, to identify the peaks and edges in the available time-resolved data, we still use an instantaneous detection for each velocity snapshot, but we further set a temporal threshold (ten consecutive snapshots or $\tau^+ \approx 20$) to remove peaks that remain within the measurement plane for short times (referred to as residence times, τ). Since the characteristic velocity (modal velocity) of each peak is the basis of its instantaneous detection, we also use it to evaluate its temporal coherence. More specifically, peaks that are detected in successive snapshots and vary their modal velocity within a band of $\pm 0.5U_\tau$ (corresponding to a shift of a single bin in the velocity pdf in either direction) from one snapshot to the other, are considered coherent between these snapshots. The chosen temporal threshold, taking into account the initial temporal filter applied, ensures that a UMZ is present in at least 4 uncorrelated consecutive snapshots. It is important

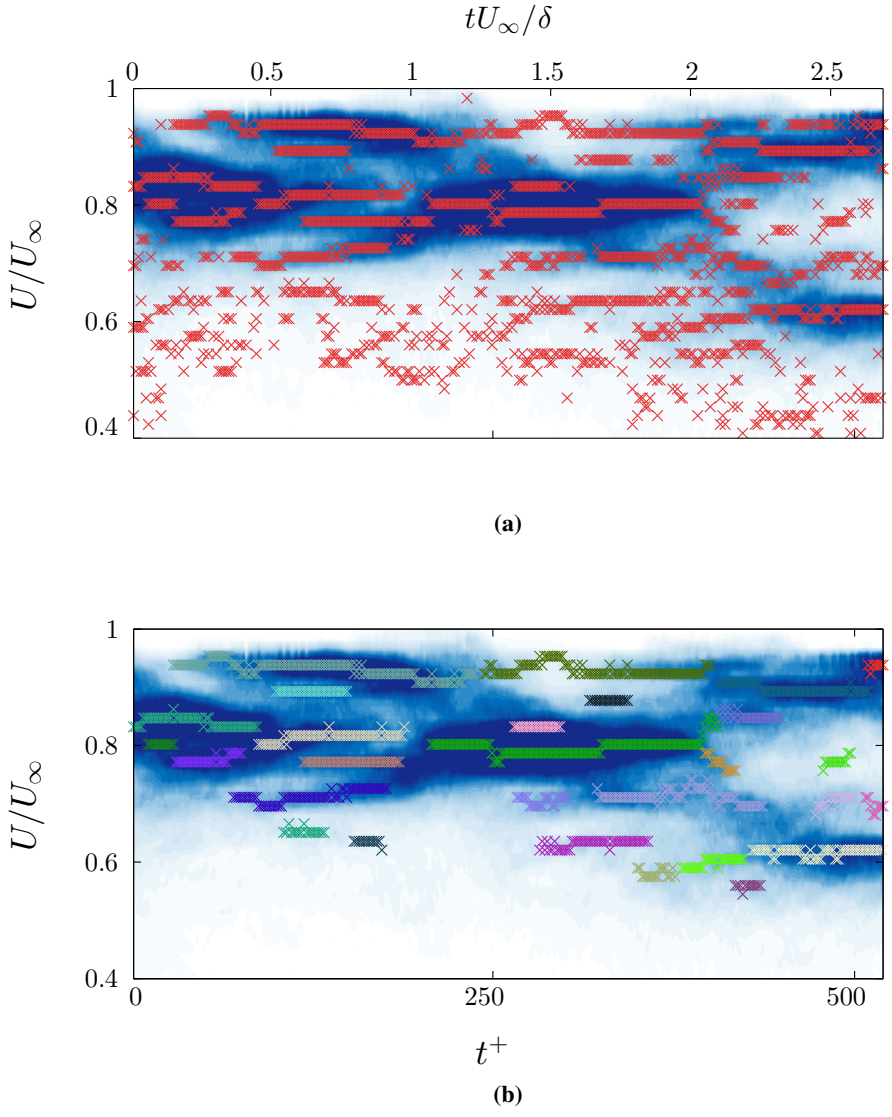

Figure 5.4. TBL flow, planar-PIV field ($Re_\tau = 5300$). Contour plot of the time evolution of the pdf of U/U_∞ for 300 consecutive images. (a) Red $\times$ symbols denote all detected modal velocities. (b) Modal peaks that have time-scales shorter than $\tau^+ \approx 20$ are removed and all remaining peaks are coloured separately.

to note that, a spatial filter has already been used for the detection of the UMZs, in the form of the instantaneous pdfs, which include all the vectors of each snapshot spanning 0.5δ in the streamwise direction. Therefore, all the results presented here refer to structures spanning at least 0.5δ in length ($\approx$2600 viscous units). This process leads to a significant decrease in the total number of peaks, without however altering the overall evolution of the number of zones. This can be seen in the pdf of N_{UMZ} after removal of shorter peaks (figure 5.2, grey symbols).

In the following sections, the geometric characteristics of time-coherent UMZs and associated flow statistics are discussed in detail. It should be noted this analysis was also performed for snapshot UMZs (i.e. before applying temporal threshold) and the results were mostly similar

to those observed for time-coherent UMZs with only some notable differences that are also discussed.

5.3 Characteristics of time-coherent uniform momentum zones

Some important characteristics of the time-coherent UMZs are the velocity range and thickness of the zones as well as their total number and how it influences the flow statistics.

Due to the large amount of data available and in order to represent the results in a clear fashion, a grouping of the UMZs is necessary. Following de Silva et al. (2016), a straightforward way to group the different UMZs in order to analyse their characteristics is by using the inner normalised momentum deficit of their associated modal velocities. Even though this classification clearly distinguishes between zones closer to the wall (where the corresponding momentum deficit is large) and the ones closer to the freestream (low momentum deficit levels), it does not take into account how these momentum deficit levels are distributed in the different UMZs present in each snapshot. As was shown in figure 5.2, the overall number of zones varies between 1 and 10 and this fluctuation might indicate different structural behaviour. Therefore, we introduce a new classification scheme, where each instantaneous zone is ranked using a top-down approach starting from the one with the highest modal velocity (that is closest to the freestream). For each image, the total number of time-coherent zones is determined and the different zones are then ranked in ascending order according to their momentum deficit level, effectively labelling the zone closest to the freestream as rank one, while the rank of the zone closest to the wall is equal to the total number of zones, N_{UMZ}, present in that particular image (see figure 5.5).

5.3.1 Velocity range

When the UMZs are classified based on their momentum deficit level, each class contains a constant range of modal velocities, with a certain distribution that is seen to vary slightly with the total number of zones (figure 5.6a). More specifically, the class of the largest momentum deficit is the one that shows the largest variation as the number of zones increases, with its mean value decreasing and its distribution becoming wider. A similar change, albeit to a lesser extent, can be seen for the class of the intermediate momentum deficit, while the zone closest to the freestream shows virtually no change as the number of zones increases. This behaviour indicates that, when the number of UMZs increases, the newest zones appear near the wall and therefore have a larger momentum deficit, while the ones already present shift to slightly larger modal velocity values to accommodate for that addition. This process is more clear, when the zones are classified based on their rank (figure 5.6c). For a low N_{UMZ}, the existing peaks have modal velocities close to U_∞, with wide distributions, mostly skewed towards the freestream (a representative example can be seen in figure 5.6d).

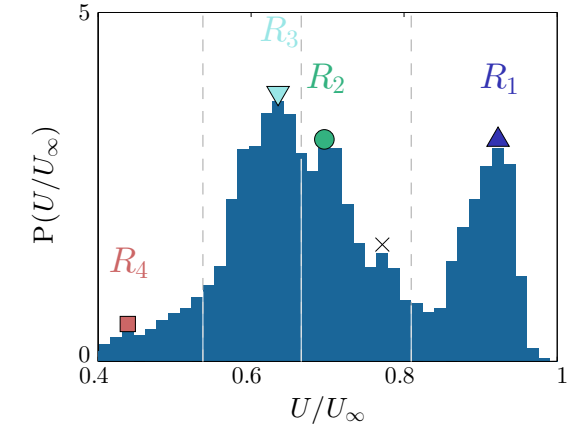

(a)

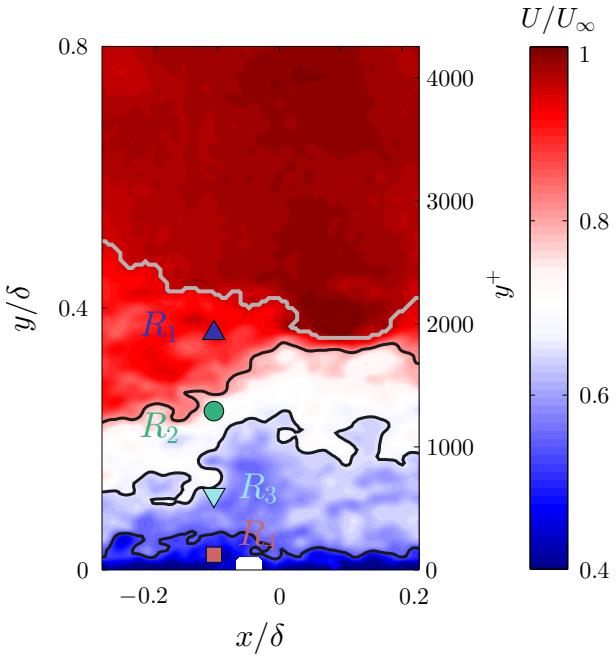

(b)

Figure 5.5. TBL flow, planar-PIV field ($Re_\tau = 5300$). Classification system based on zone rank. The zone closest to the freestream is defined as rank one (▲, R_1) while the others below it follow in ascending order. (a) Pdf of U/U_∞ for an instantaneous velocity field with $N_{UMZ} = 4$. Grey dashed lines mark the internal layers that distinguish the different UMZs and the modal velocity of each zone is marked with coloured symbols according to rank. × symbol denotes an instantaneously detected, short-lived peak that was discarded. (b) Velocity contours of the same velocity snapshot as in (a). Black solid lines denote the boundaries of each zone while the TNTI is marked with grey.

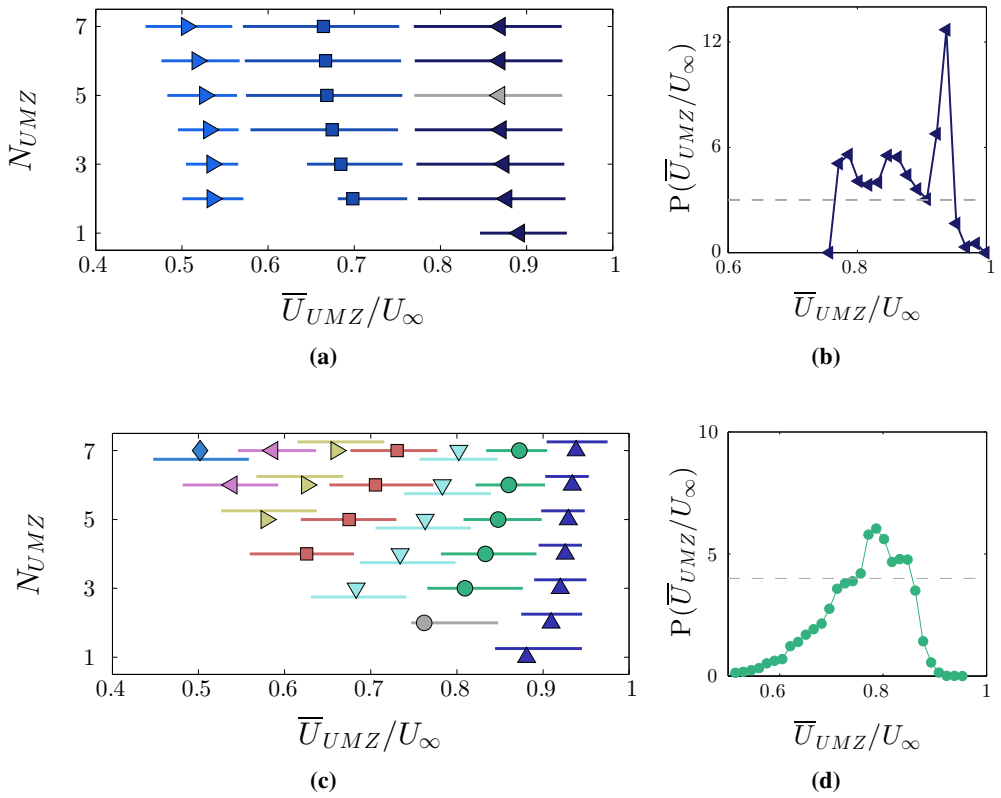

Figure 5.6. TBL flow, planar-PIV field ($Re_\tau = 5300$). Mean values and extent of the pdf of the normalised modal velocities, varying with the total number of UMZs detected, N_{UMZ}. (a,b) Classification based on momentum deficit, $(U_\infty - U_m)/U_\tau$: ◀ 0-6, ■ 6-12, ▶ 12-18. (a) Symbols denote mean values and solid lines the pdf extent, taken at a constant height of 3 (grey dashed line on subfigure b). Grey coloured symbols denote the mean and extent of the example distribution shown in (b). UMZs with low momentum deficit show little variation with increasing N_{UMZ}, while the group of the largest deficit moves to lower modal velocities as new zones appear close to the wall. (c,d) Classification based on zone rank. Symbols as in figure 5.5. Pdf extent taken at a constant height of 4 (grey dashed line in subfigure d). Grey coloured symbols denote the mean and extent of the example distribution shown in (d). All ranks move to higher modal velocities as N_{UMZ} increases.

As the number of zones increases, all ranks are shown to move to higher values while the distribution of the modal velocity values within each rank becomes progressively narrower. Zones that are closer to the wall show the largest velocity increase, while the ones close to the freestream reach slightly higher values, and their distribution becomes less skewed. It should also be noted here that, the appearance of newer zones of larger momentum deficit, close to the wall, is in agreement with the attached eddy model which assumes that the origin of the vortical structures populating the boundary layer is at the wall (see Perry and Chong, 1982 and Head and Bandyopadhyay, 1981).

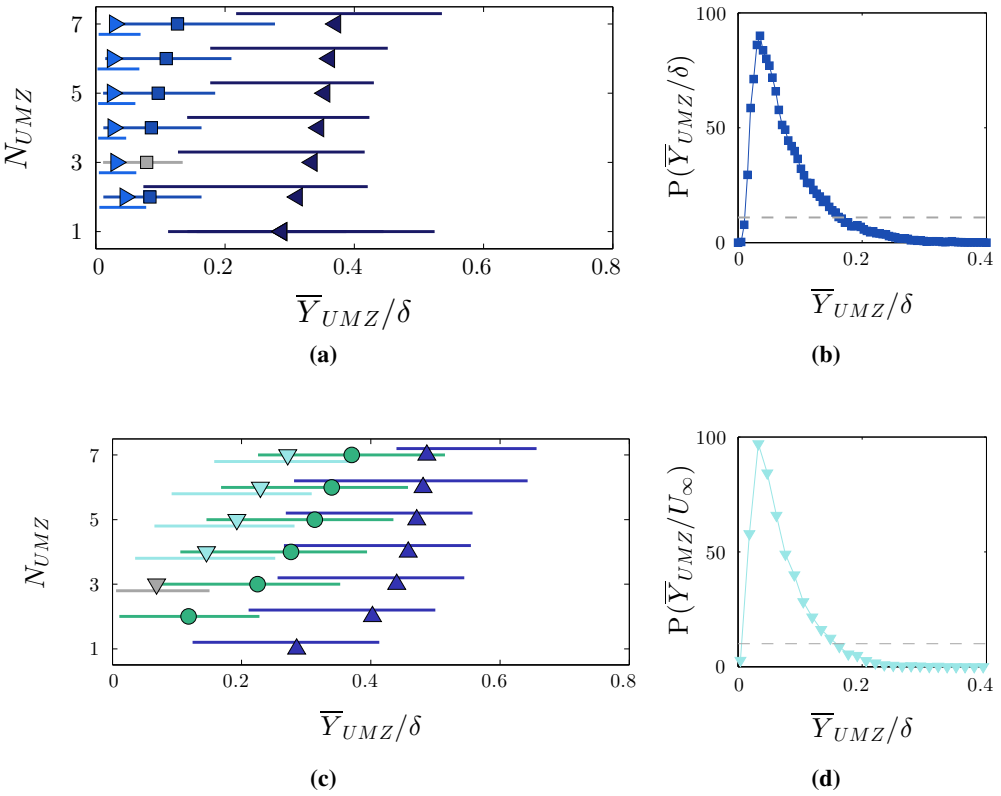

Figure 5.7. TBL flow, planar-PIV field ($Re_\tau = 5300$). Mean values and extent of the pdf of the normalised wall-normal location, varying with the total number of UMZs detected N_{UMZ}. Colours and symbols as in figure 5.6. (a, b) Classification based on momentum deficit, $(U_\infty - U_m)/U_\tau$. Pdf extent taken at a constant height of 11 (grey dashed line in subfigure b). For an increase in N_{UMZ}, the zones with the lowest momentum deficit move to higher wall-normal locations, to account for the newest ones that appear near the wall. (c, d) Classification based on zone rank, pdf extent taken at a constant height of 10 (grey dashed line in subfigure d). Only the first three ranks are shown for clarity, however the trend is similar for all following ranks. All ranks move upwards while new zones of higher rank appear below them.

5.3.2 Wall-normal location and thickness

Apart from the differences in velocity range, the UMZs are characterised in physical space by their average wall-normal location, $\overline{Y}_{UMZ}$ and thickness, $\bar{t}_{UMZ}$ (as described in de Silva et al., 2016). When the zones are classified based on their momentum deficit level, there is a clear distinction in both the mean values and distributions of the average wall-normal location for the different groups. As expected, the zones with the largest momentum deficit are the ones closest to the wall, with a narrow distribution around their mean wall-normal location (figure 5.7a), which moves to lower values as N_{UMZ} increases and new zones appear at the wall. Conversely, the group of zones with the smallest momentum deficit is at the largest distance from the wall, while the distribution around its mean wall-normal location is the widest of all groups. This group also shows the largest change in wall-normal location as N_{UMZ} increases, indicating an

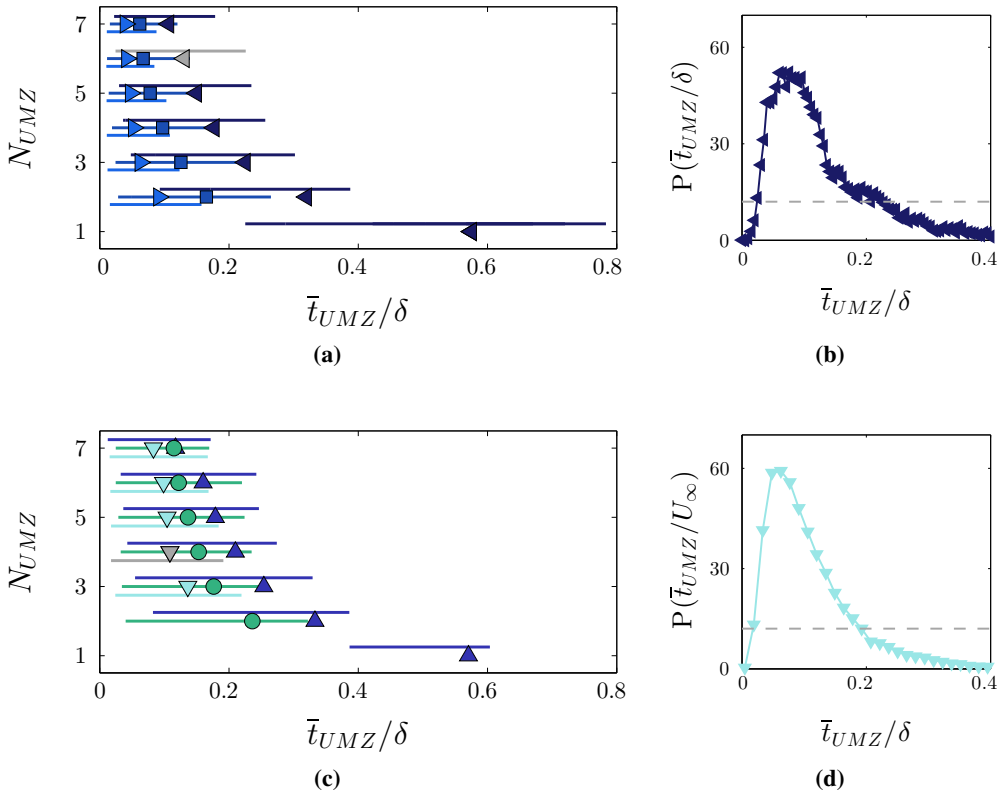

Figure 5.8. TBL flow, planar-PIV field ($Re_\tau = 5300$). Mean values and extent of the pdf of the normalised zone thickness, varying with the total number of UMZs detected, N_{UMZ}. Colours and symbols as in figure 5.6. (a, b) Classification based on momentum deficit, $(U_\infty - U_m)/U_\tau$. Pdf extent, taken at a constant height of 12 (grey dashed line in subfigure b). (c, d) Classification based on zone rank, pdf extent taken at a constant height of 12 (grey dashed line in subfigure d). Only the first three ranks are shown for clarity, however the trend is similar for all following ranks. Both systems show similar trends of decreasing thickness with increasing N_{UMZ}. Zones close to the wall have shorter wall-normal extent on average and with a much narrower distribution around it.

upwards movement to account for the appearance of newer zones at the wall. This change can be seen more clearly when the zones are classified depending on their rank (figure 5.7c). The trends are very similar, since this classification still takes into account the momentum deficit of each zone, although it is clear now that for an increase in N_{UMZ} all ranks move upwards while new zones of higher rank appear below them.

The mean thickness of the different UMZs is also presented for the two different classification systems (figure 5.8). When the zones are classified according to their momentum deficit level and in-line with the observations from de Silva et al. (2016), the thickness increases with distance from the wall and its distribution becomes wider (figure 5.6a). The mean thickness of all the groups and the fluctuations around it show a decreasing trend with increasing number of zones. A very similar behaviour can be seen when the zones are classified according to their

rank (figures 5.8c and 5.8d). An increasing number of zones, will compress the thickness of all the zones, although their wall-normal position will increase (figures 5.8c and 5.6d).

5.3.3 Total number of zones

Based on the observations of the previous section, the total number of zones present at a given snapshot in time is a critical factor influencing UMZ characteristics. This influence could possibly indicate further structural differences of the flow, so here we present some basic statistical properties of the flow when conditioned on N_{UMZ}.

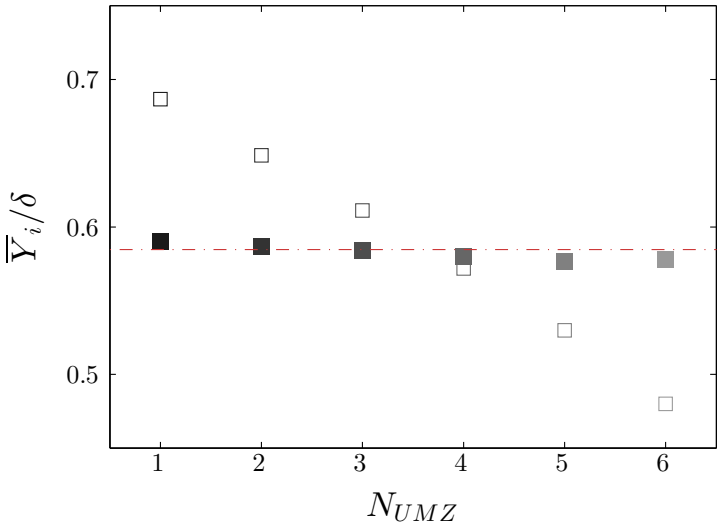

Figure 5.9. TBL flow, planar-PIV field ($Re_\tau = 5300$). Variation of the mean location of the TNTI, $\overline{Y}_i$, with the number of UMZs detected below it. Colour gradient from dark to light denotes increasing number of time-coherent zones. Open symbols mark results before applying the temporal threshold. Red dotted line denotes the global average location of the TNTI.

As mentioned above, when the total number of zones increases, the thickness of all zones decreases, while their average wall-normal position increases. The combination of these two trends results in an almost constant TNTI location for an increasing N_{UMZ} (figure 5.9). This is also the most notable difference we found between instantaneously detected and time-coherent peaks. More specifically, when all modal peaks are considered, and no temporal threshold is applied, the thickness of all zones still follows a decreasing trend for an increasing N_{UMZ} however, their wall-normal position decreases as well. That leads to significantly lower TNTI location for a high number of zones (open symbols in figure 5.9, see section 5.3.6 for more details).

Apart from the TNTI location, flow statistics also show a strong dependence on N_{UMZ}. A large number of zones leads to a strong momentum deficit in the region near the wall ($y < 0.25\delta$) (figures 5.10a and 5.10b). This is in line with the conclusions from the previous section, where it was shown that an increasing number of zones leads to a decrease of the mean modal velocity

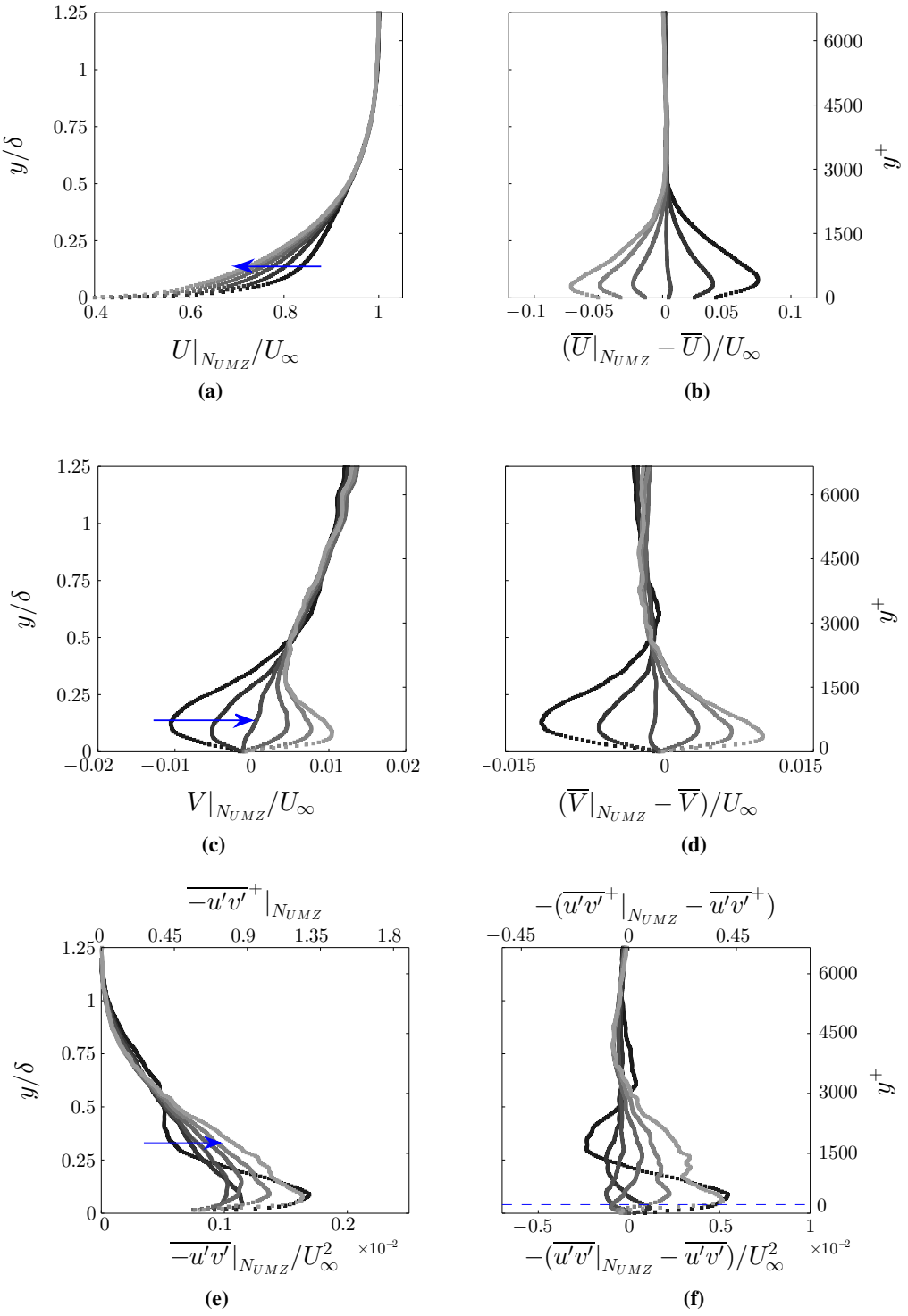

Figure 5.10. TBL flow, planar-PIV field ($Re_\tau = 5300$). Conditionally averaged statistics with varying number of UMZs present in the flow. Blue arrows indicate increasing number of zones (from 1 to 8). (a) Outer normalised mean streamwise velocity profile. (b) Difference from global streamwise average. (c) Outer normalised mean wall-normal velocity profile. (b) Difference from global wall-normal average. (e) Root-mean-square profile of the Reynolds shear stress. (f) Difference from global Reynolds stress profile.

of the lower UMZs (figure 5.6b), because new zones tend to appear closer to the wall therefore adding to the momentum deficit in that region. At the same time, within that region, the vertical velocity component is shown to be significantly increased compared to the global average (figure 5.10b). This combined behaviour of U and V statistics indicates a large-scale $Q2$ event in the log region for a high N_{UMZ}. When N_{UMZ} is low, the opposite trends are observed in both the streamwise and the wall-normal velocity profiles. Close to the wall there is a strong downward motion (figures 5.10c and 5.10d), pushing high speed flow to regions of lower momentum, thus creating a slight increase of U, reflected in a fuller streamwise velocity profile (figures 5.10a and 5.10b). These two trends suggest the presence of a large scale $Q4$ event in the log region for a low N_{UMZ}. The region closer to the freestream shows no significant variation, in line with the almost constant average TNTI location (figure 5.9).

Finally, conditional averages of the Reynolds stress profiles show that closer to the wall, there is increased turbulent activity when compared to the global average for a low number of zones, which then rapidly decreases and only slightly re-surges close to the freestream. In contrast, a high number of zones is coupled with low turbulent activity very close to the wall, which then significantly increases in the logarithmic region and gradually reaches the global average farther away from the wall. This behaviour can potentially be linked with previously documented small-scale activity when conditioned to a large-scale log-layer structure. More specifically, Hutchins and Marusic (2007b) showed that the presence of large-scale high-speed events ('superstructures') in the logarithmic layer (corresponding to an outer spectral peak $\approx 6\delta$), creates an increase of small-scale activity very close to the wall, while low-speed log-structures have the opposite effect. They further noticed that this behaviour is reversed after a certain distance from the wall (termed the 'crossover' point) and that this point of reversal is Reynolds number dependent. Later, Mathis et al. (2009) supported this observation and proposed that the point where the correlation between the large-scale component with the envelope of the small-scale component crosses zero, happens within the logarithmic region, at an estimated $y_c^+ \propto \sqrt{Re_\tau}$ (blue dashed line in figure 5.10f, located at 0.04δ in the present data), an estimation also supported by Ganapathisubramani et al. (2012). Similar results were presented by Dennis and Nickels (2011), who showed that increased Reynolds stress regions were correlated with long low-speed structures while the high-speed ones did not exhibit a similar correlation.

In the present case, when the number of zones is low, there is a significant increase of streamwise momentum in the log-region that could signify the passage of high-speed structures. Following the amplitude modulation reasoning and noting that the majority of the available vectors are above the cross-over point (blue dashed line in figure 5.10f), this would lead to a decrease in the amplitude of the small-scales, as is indeed observed in the Reynolds stress profile. Below the crossover point the situation reverses and the passage of a high-speed structure in the log region is expected to amplify small-scale activity. The current resolution does not provide sufficient data of that region, however it is possible that new zones are created there that are not detected using the available vectors. Conversely, when the number of zones is high, the log region is

characterised by a significant momentum deficit, which in turn can be linked to low-speed structures and increased small scale activity would be expected. Results again support this argument, with the Reynolds stress values significantly increased from the global average, when a large number of zones is present in the flow (figure 5.10f).

5.3.4 $Q2$ and $Q4$ events in the log region

The above discussion on amplitude modulation is based on the assumption that the observed large-scale $Q2$ and $Q4$ events in the log region indicate the passage of low and high speed structures that have a substantial coherence in space. Since the available velocity snapshots are time-resolved, the time for which such events reside within our FOV can be computed and their spatial extent can be subsequently estimated. In order to assess this concept we first classify all available snapshots based on whether they match the resulting profiles on figures 5.10b and 5.10d. More specifically, for every velocity snapshot, the deviation, in the log-layer, of the (streamwise averaged) U and V velocity profiles from the global mean, is estimated. The signed integral between the resulting profiles (see figure 5.11) and the y-axis is the basis of our definition for the log-layer events. We define as a large-scale $Q2$ event a combination of a negative integral $U-\overline{U}$ value and a positive integral $V-\overline{V}$ value, in the log-region (a representative example is depicted on figure 5.11a and 5.11b). The opposite behaviour (figure 5.11c and 5.11d) is classified as $Q4$ event. Overall, such events are found to account for 74% of all instantaneous fields. This is in line with the results on three-dimensional structures in a turbulent boundary layer by Dennis and Nickels (2011), who documented a high correlation of increased streamwise momentum with a downwards motion and a momentum deficit region with an upwards movement.

The resulting residence times show that (figure 5.12) on average, these profiles persist for $0.5\delta/U_\infty$ within the measurement domain and the longest of them reach times of $3\delta/U_\infty$ (maximum recorded event of $6\delta/U_\infty$). It should be stressed here that the profiles in figure 5.11 are a result of streamwise averaging and therefore indicate that the events considered are at least 0.5δ long. Assuming moreover that the events move with approximately the local mean velocity, the average time-scales found indicate high-speed structures that are at least 0.9δ long while low-speed ones are at least 0.8δ long. While such an assumption on the convection velocities has long been disputed (see Fisher and Davies, 1964; Zaman and Hussain, 1981; Kim and Hussain, 1993; Davoust and Jacquin, 2011, among others), recently, Geng et al. (2015) showed that in the logarithmic region of turbulent boundary layers, which is of interest here, the use of the streamwise mean as the convection velocity is a good approximation. The maximum recorded residence times suggest the passage of structures of up to 6δ, in line with reported scales of large-scale motions and superstrucures in the logarithmic layer (see Hutchins and Marusic, 2007b; Ganapathisubramani et al., 2003; Tomkins and Adrian, 2005; Dennis and Nickels, 2011, among others). On average however, both $Q2$ and $Q4$ events have similar but

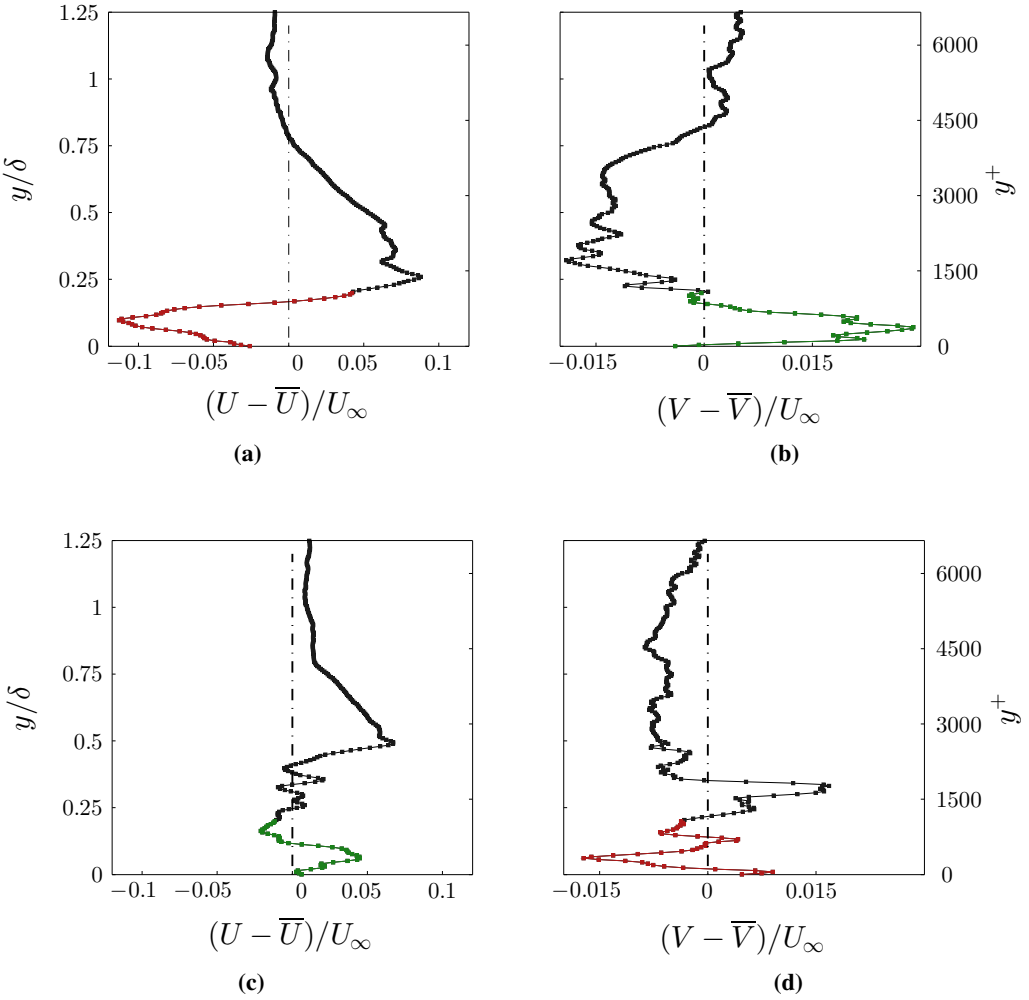

Figure 5.11. TBL flow, planar-PIV field ($Re_\tau = 5300$). Streamwised averaged velocity profiles for two different snapshots representing a large-scale $Q2$ (a, b) and $Q4$ (c, d) event at the log region.

significantly shorter spatial extents. The main reason behind this is the much shorter temporal coherence of the vertical velocity V when compared to the streamwise one. The reported long-scales in the literature mainly refer to low or high streamwise velocity structures. In the present data, when only a low or high U velocity event is tracked in time, the resulting residence times have a similar distribution to the $Q2$ and $Q4$ events (figure 5.12), but are on average twice as long ($1.2\delta/U_\infty$), suggesting spatial extents closer to the documented values, albeit still shorter. Another reason for this is that our measurement domain is a streamwise–wall-normal plane and that very long high- and low-momentum structures have been shown to alternate in the log region while also exhibiting a meandering motion in the spanwise direction (Hutchins and Marusic, 2007a,b; Zheng and Longmire, 2014). Therefore, it can be argued that this presence of $Q2$ and $Q4$ events, observed in the velocity profiles, signifies the passage of low- and high-momentum structures through our field of view and their recorded time-scale depends on their streamwise alignment with the measurement plane. A similar organisation of side-by-side

$Q2$ and $Q4$ events in the logarithmic region of channels was also presented by Lozano Duran et al. (2012), who showed that these events form a predominant structure which is completed by a vortex cluster primarily located within the $Q2$ event but extending slightly underneath the $Q4$ as well.

The previous results have shown that velocity profiles exhibit a large, ejection-like behaviour in the log-region for cases of a high number of zones present in the flow, while large-scale sweep-like events dominate for low N_{UMZ}. The TNTI location is shown to be almost constant when conditioned on the number of zones (figure 5.9), although a strong decreasing trend with increasing N_{UMZ} was observed for an instantaneous peak detection (see section 5.3.6 for more details). In order to further investigate the correlation between N_{UMZ}, $\overline{Y}_i$, and the presence of these low- or high-speed log-structures, conditional averaging is used again. This time however, the latter two parameters are used as conditions, while the resulting variations in N_{UMZ} are recorded. We follow the procedure discussed above to identity $Q2$ and $Q4$ events in the log-region and we subsequently estimate their magnitude together with the instantaneous TNTI location in every snapshot. The joint pdf of these two parameters is computed, showing how many times a certain combination of events takes place (figure 5.13b). The average number of zones over these realisations is subsequently estimated (figure 5.13a) and the resulting map of $\overline{N}_{UMZ}$ shows that, indeed, a similar correlation as the one shown in figures 5.9 and 5.10 exists.

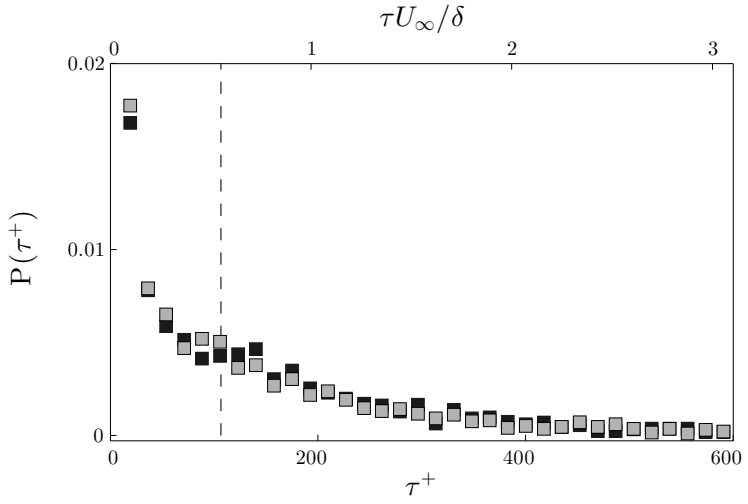

Figure 5.12. TBL flow, planar-PIV field ($Re_\tau = 5300$). Pdf of residence times within the FOV; ■ for $Q2$ events and ■ for $Q4$ events.

More specifically, a $Q2$ event in the log-layer results on average in a high number of zones ($\overline{N}_{UMZ} \geq 5$), a number which tends to increase further with increasing ejection magnitude. The presence of a $Q4$ event on the other hand results in a low number of zones, in line with the conditional averages in figure 5.10. The TNTI location is again shown to have a limited effect on the resulting number of zones (see also figure 5.9).

Previous results were based on the presence of either a $Q2$- or $Q4$-like large scale event in the log region. Overall such events occur in 74% of the total snapshots available and therefore

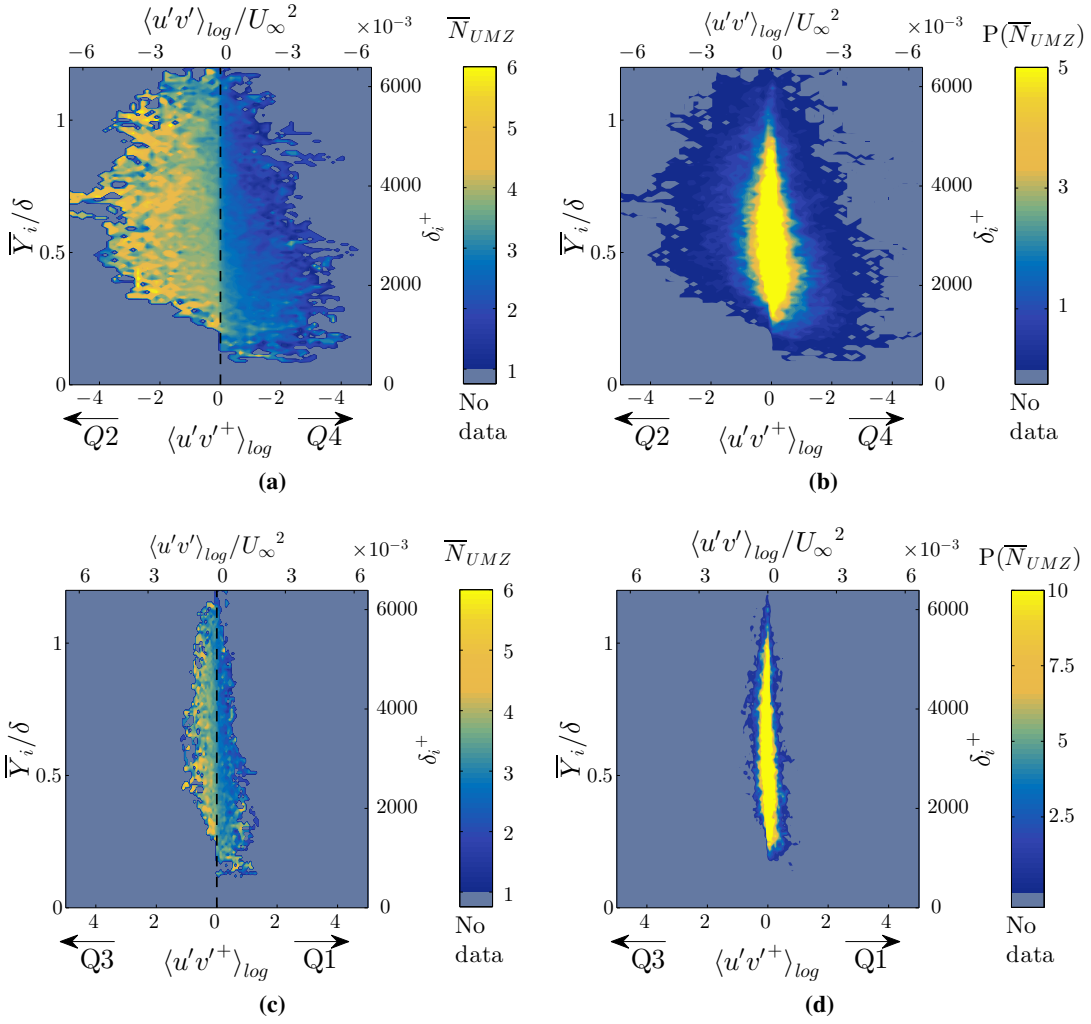

Figure 5.13. TBL flow, planar-PIV field ($Re_\tau = 5300$). Pdf of the average number of zones present in the flow, $\overline{N}_{UMZ}$, for varying TNTI location, $\overline{Y}_i$ and magnitude of log-region events. Average number of zones (a) and pdf of realisations for large-scale $Q2$, $Q4$ events in the log region (b). In total, they occur in 74% of all cases. Average number of zones (c) and pdf of realisations (d), for large-scale $Q1$, $Q3$ events in the log region (26% of all cases). For all plots, events on the left represent lower than average streamwise velocities, while the opposite holds for events on the right.

the trends observed in figures 5.13a and 5.13b will be the ones dominating in a global sense. However, for completeness, a similar map of $\overline{N}_{UMZ}$ is presented for the other type of events, namely the $Q1$ (outward) and $Q3$ (inward) events (figures 5.13c and 5.13d). The resulting pdfs show that these events are significantly weaker in magnitude and they mostly represent cases of average N_{UMZ}. Even though there is no clear segregation of extremes like the one in figure 5.13a (instances with very low number of zones are almost non-existent), there is still a strong trend of increasing $\overline{N}_{UMZ}$ for low-speed structures $Q3$ present in the log region. Considering all quadrant events, an increase of the streamwise velocity is shown to be correlated with a decrease in the number of zones ($Q1$ and $Q4$ events), while a lower than average streamwise velocity has

the opposite effect ($Q2$ and $Q3$ events). When the large-scale high-speed events are combined with a downwards motion there is a further decrease in the number of zones. Conversely, when the low-speed events are combined with a positive vertical velocity ($Q2$ events), the number of zones increases further.

Finally, a comment should be made regarding the temporal coherence of the large-scale events in the log region and how it could affect the time-scales of UMZs. As mentioned above, large-scale $Q2$ and $Q4$ events in the log layer that have average residence times of $0.5\delta/U_\infty$, can potentially trigger the organisation of the flow into either low or high number of UMZs, respectively. Individual UMZs however, represent flow regions that have an almost constant modal velocity, either higher or lower than the local mean, and as such are generally expected to have shorter time-scales than the large-scale log events (which include regions of all flow velocities higher or lower than the local mean).

5.3.5 Conditional statistics across the internal layers

As was previously discussed, the term internal layers is used to describe the regions of high shear that bound each UMZ. Eisma et al. (2015) have shown that, when identified using the shear component of the velocity gradient tensor, these layers show similar characteristics with the TNTI, especially in terms of the conditional statistics and entrainment across the interface. They further suggested that since these layers are believed to be linked with the presence of UMZs in the flow, they might be indicative of the evolution of large-scale structures in a turbulent boundary layer. In the present work, internal layers are identified as velocity contours at the mid distance of the modal velocity peaks, that delimit UMZs and as such are more directly linked with large-scale motions in the flow per definition. Therefore, our aim is to assess whether such a definition still provides similar observations for the detected internal layers, how these characteristics vary with respect to each zone rank, and how they compare with the results presented on the TNTI (see chapter 4). For all layers presented here, $40,515$ snapshots were selected from the initial time-resolved database that were $dt = 0.1U_\infty/\delta$ apart, in an effort to minimise time dependence but still get converged statistics for all cases. Following the classification based on zone rank described above, each internal layer is the lower bound of the zone rank that describes it (see figure 5.14). For example, the internal layer associated with the zone of rank 1 (R_1) is the edge between R_1 and R_2, while the last layer presented, associated with zone of rank R_5, is the edge between R_5 and R_6. The streamwise velocity profile conditioned across the layers shows a clear jump for all layers similar to the one observed for the TNTI (dashed line in figure 5.14a). As expected, for increasing zone rank – generally linked with a wall-normal position closer to the wall (see also figure 5.7c) – the profiles move to lower velocities although exhibiting similar distributions. For the estimation of the jump thickness, δ_ω we follow the procedure described in chapter 4, section 4.2, for the TNTI. Results show that, in line with observations from Eisma et al. (2015), the velocity jump, $\Delta\langle\tilde{U}\rangle/U_\infty$, increases for layers closer to the wall, while the thickness scales approximately with the local Taylor microscale (λ_τ)

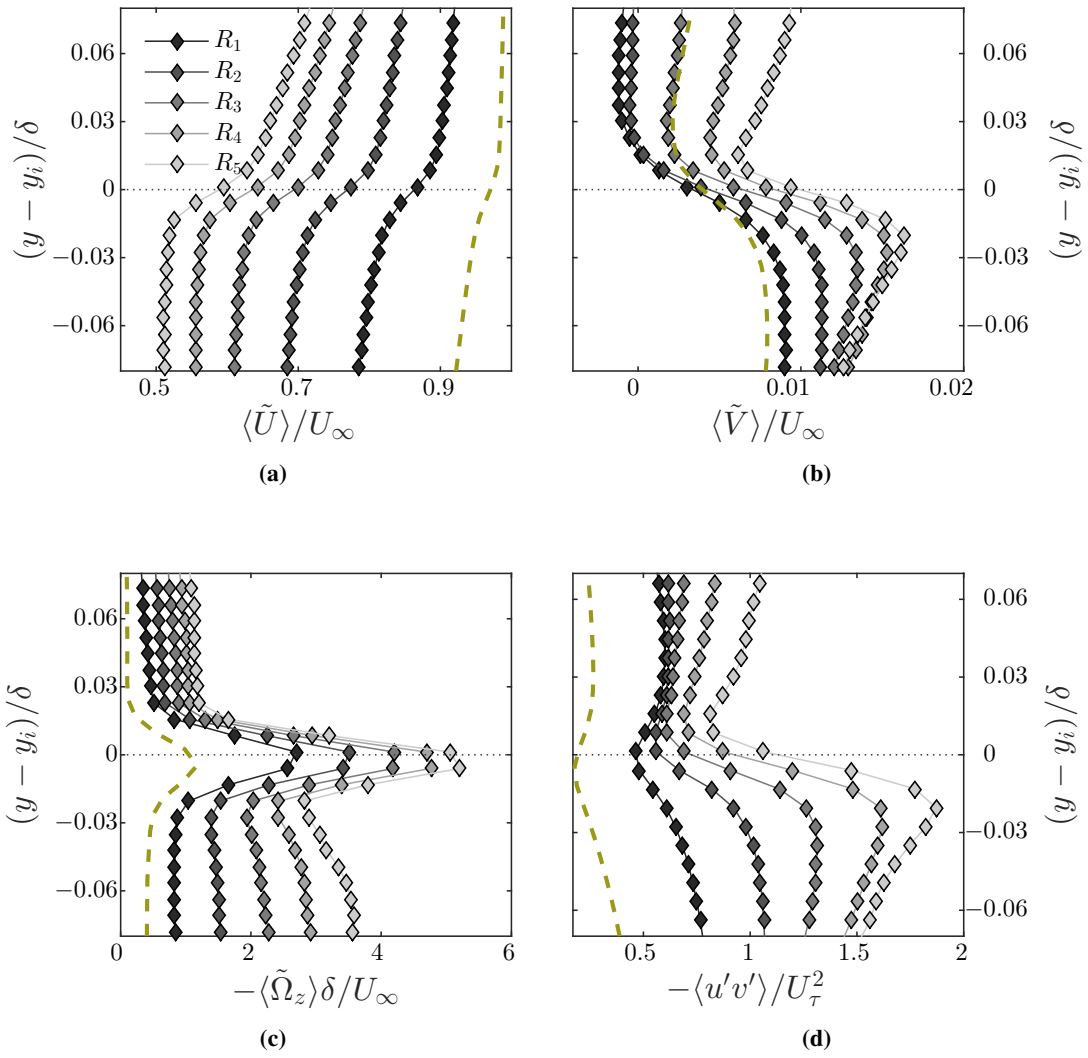

Figure 5.14. TBL flow, planar-PIV field ($Re_\tau = 5300$). Conditionally averaged flow statistics across the internal layers that bound each UMZ. Dashed lines indicate the profiles across the TNTI (see chapter 4). (a) $\langle \tilde{U} \rangle / U_\infty$ (b) $\langle \tilde{V} \rangle / U_\infty$ (c) $\langle \tilde{\Omega}_z \rangle \delta / U_\infty$ (d) $\langle u'v' \rangle / {U_\tau}^2$.

for the average wall-normal location of each layer (see table 5.1). It should be noted here that, the larger discrepancies observed in the scaling when compared to the TNTI results are mainly due to the fact that internal layers are not grouped by their wall-normal location but the rank of the zone they bound. Therefore, even though their average wall-normal location decreases with increasing zone rank, the corresponding λ_τ, might not be a representative scaling for the whole range of the wall-normal locations around that average (see also figures 5.7c and 5.7d for the resulting distributions).

The conditional vertical velocity profiles across the internal layers exhibit the largest changes when compared with the TNTI results (figure 5.14b). More specifically, the wall normal velocities below each layer show a clear increase with increasing zone rank. On the contrary, results

	$\Delta\langle\tilde{U}\rangle/U_\infty$	δ_ω/δ	$\delta_\omega/\lambda_\tau$
R_1	0.09	0.031	0.41
R_2	0.11	0.030	0.47
R_3	0.12	0.029	0.49
R_4	0.13	0.028	0.52
R_5	0.13	0.026	0.52

Table 5.1. TBL flow, planar-PIV field ($Re_\tau = 5300$). Velocity jump and vorticity thickness for internal layers bounding different zone ranks. Taylor microscale, λ_τ, estimated for each average wall-normal location as $\sqrt{\overline{u'^2}/\overline{(\partial u/\partial x^2)}}$.

for the TNTI, for wall-normal locations closer to the wall showed the opposite behaviour, moving towards negative velocities. The vertical velocities above each layer show a similar increase for zone ranks higher than R_3, while for the two lower ranks they move towards negative values, as was observed for the TNTI (see figure 4.10b). This difference can be explained when taking into account the large-scale events that were shown to be linked with a high number of zones in the previous sections. A high number of zones case was linked with a large-scale $Q2$ event in the log region, while a low N_{UMZ} was found to be linked with a large-scale $Q4$ one. Internal layers of high zone ranks exist only in cases where N_{UMZ} is high and therefore the increasing trend for $\langle\tilde{V}\rangle$ further supports the presence of an ejection event in those cases. Internal layers of lower ranks on the other hand exist for a much larger range of N_{UMZ} and therefore any effects of a high or low number of zones are expected to balance out. This is indeed the case for velocities above internal layers of zone ranks R_1 and R_2, although such a trend does not extend to the velocities below these layers.

Conditional profiles for the out-of-plane vorticity (figure 5.14c) and Reynolds stress (figure 5.14d), both move to higher values for the layers representing higher zone ranks, following the trends observed for the TNTI (see figures 4.10c and 4.10d), indicating that a peak in vorticity is present across internal layers and its magnitude increases for layers closer to the wall. In those cases, the Reynolds stress values are also elevated and they exhibit a larger jump, again similar to the profiles acquired for TNTI locations close to the wall (see figure 4.10d).

Finally, profiles of the number of $Q2$ and $Q4$ events as a percentage of the total uv events across the layers are presented and compared with the corresponding ones from the TNTI analysis (figure 5.15). The distributions across all internal layers are similar to the one across the TNTI (dashed lines in figures 5.15a and 5.15b), with the percentage of $Q2$ events increasing below the layers while above them, it is the percentage of $Q4$ that increases. For the internal layers of zone ranks R_1 and R_2, $Q2$ events are prominent below the layers, while $Q4$ ones are prominent above, following the observations from the events across the TNTI and the conceptual description of the shear layers by Adrian et al. (2000) (inclined layers extending from stagnation points of opposing $Q2$ and $Q4$ events). Although this trend extends to TNTI locations closer to the wall (see figure 4.11), the same is not observed for internal layers closer to the wall. Reflecting the discrepancies of the vertical velocity profiles, zones of higher rank, exhibit an increasing number

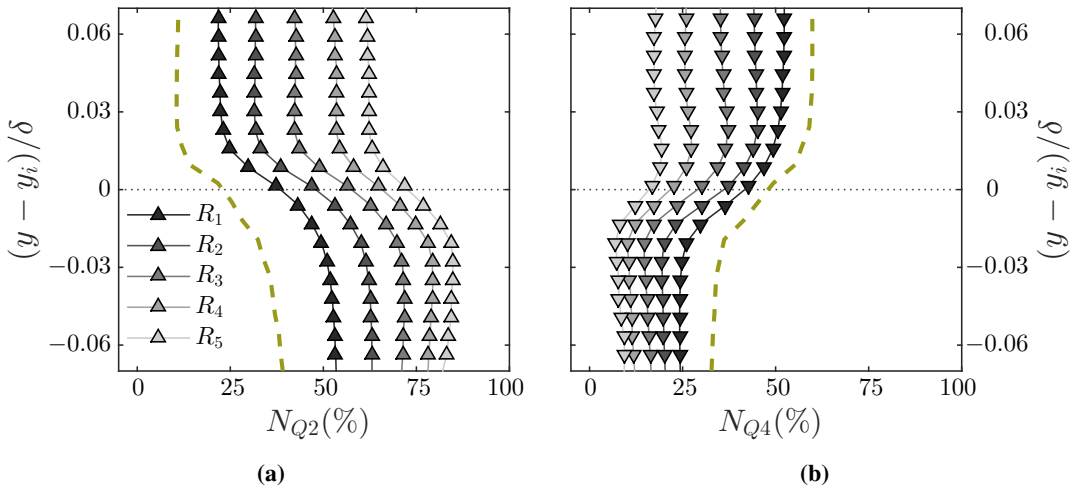

Figure 5.15. TBL flow, planar-PIV field ($Re_\tau = 5300$). Number of $Q2$ and $Q4$ events across the internal layers that bound each UMZ as a percentage of the total number of vectors averaged at each wall-normal location.

of $Q2$ events for all wall-normal locations across the layers, while the percentage of $Q4$ events reaches zero for the highest ranks. As mentioned above, this behaviour is a result of the high N_{UMZ} for these cases, which is linked with a large scale $Q2$ event in the log region. Internal layers of higher rank, exist only in high-zone-number states and as such exhibit an increase of $Q2$ events, evident in both $Q2/Q4$ and V profiles across the layers.

5.3.6 A note on the influence of bin count and time-coherence

After analysing the main characteristics of UMZs and the internal layers that bound them, a discussion on relevant time-scales follows in the next section. However, a final comment should first be made regarding the effect of bin count and time-coherence on the detected peaks and the trends observed in this chapter. For all the results presented, UMZs that have a temporal coherence shorter than $\tau^+ \approx 20$ are removed. This leads to an expected decrease in the average number of peaks detected (see figure 5.2), and also to some notable differences in the conditional averages presented in figures 5.9 and 5.13. More specifically, the average TNTI location, $\overline{Y}_i$, shows a strong variation with the number of zones, N_{UMZ} (open symbols in figure 5.9). Interestingly, a low $\overline{Y}_i$ leads to a large N_{UMZ} and vice-versa.

This observation could be traced back to the physical description of the zones. UMZs are defined as local peaks of the streamwise velocity pdf. If the freestream velocity is considered relatively constant within all available snapshots, the wall-normal location of the TNTI leads to a variation in the total amount of velocity vectors below the interface. This means that, in physical space, a UMZ that is detected below a TNTI located far away from the wall, should cover a much greater wall-normal extent than in situations where the TNTI is very close to the wall, a fact that could

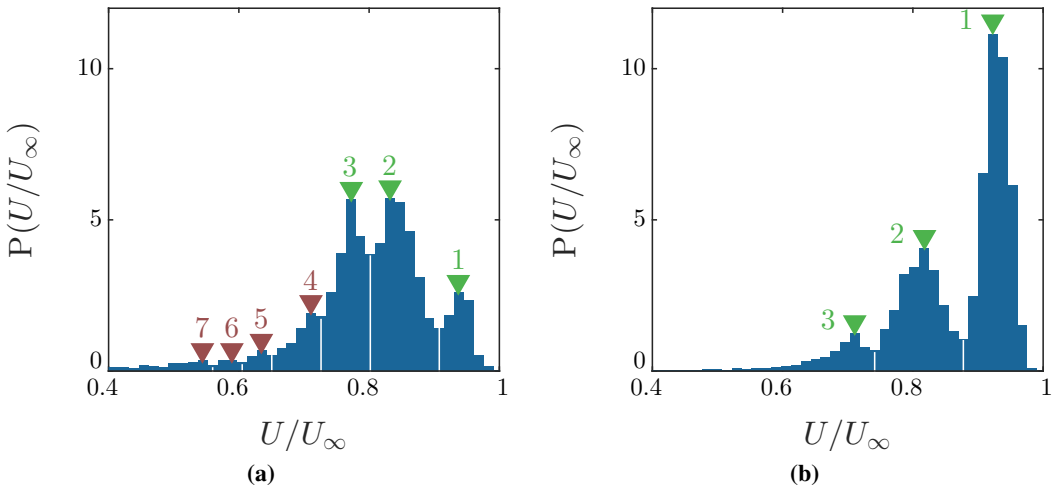

Figure 5.16. TBL flow, planar-PIV field ($Re_\tau = 5300$). Pdf of U/U_∞ for two independent velocity snapshots representing lower and higher than average TNTI location and how that infulences the detection of modal peaks. Red and green triangles denote peaks with streamwise extent below and above the defined threshold respectively. White lines mark the local minimum between two consecutive peaks. (a) $\overline{Y}_i = 0.46\delta$. (b) $\overline{Y}_i = 0.98\delta$.

explain the lower number of zones in such flow states. On the other hand, when the TNTI is located very close to the wall, a much smaller amount of vectors of the same velocity band can form a detectable UMZ, thus enabling the formation of multiple zones, smaller in size, that are also expected to have smaller time-scales. The use of a temporal threshold to remove short-lived peaks, would therefore act as a balance for the large increase in N_{UMZ} observed for low TNTI locations. Additionally, a higher than average TNTI location, is in many cases a result of snapshots with elevated freestream turbulence intensity, the presence of which might interrupt the time-coherence of the peaks detected below it. Removal of short-lived peaks will therefore tend to balance the TNTI variation further, leading to an almost constant TNTI location for all N_{UMZ} (figure 5.9).

It is therefore interesting to check whether this behaviour is indeed a result of the physical description of UMZs or stems from a bias of the instantaneous detection procedure, which would compromise the validity of detected peaks due to the decrease in bin counts and increase of detection noise in the case of low $\overline{Y}_i$.

The detection of a local peak is based on its prominence with respect to the neighbouring points. For each peak, this can be represented as the difference in bin counts, between the peak itself, and the neighbouring local minimum $\Delta N = N_{peak} - N_{min}$. Since the number of vectors in each bin, N, is a result of a counting procedure, it is associated with a Poisson distribution and therefore its uncertainty estimate is the standard deviation of the Poisson distribution for the counted value, $\sqrt{N}$. Following a linear propagation analysis (JCGM 100:2008, 2008), the corresponding

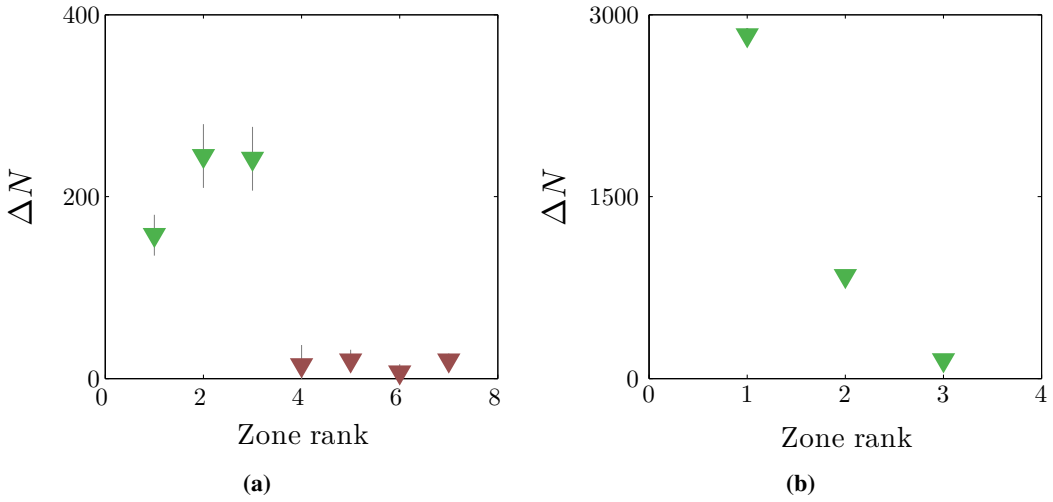

Figure 5.17. TBL flow, planar-PIV field ($Re_\tau = 5300$). Difference in vector counts, $\Delta N = N_{peak} - N_{min}$, between the modal peaks in figure 5.16 and the greater of the two local minima that surround them. Grey lines mark the uncertainty on the detection of each peak, defined as $\sqrt{N_{peak} + N_{min}}$. (a) $\overline{Y}_i = 0.46\delta$. (b) $\overline{Y}_i = 0.98\delta$.

uncertainty on the difference of bin counts can then be estimated as $\sqrt{N_{peak} + N_{min}}$. So, the certainty with which a peak is detected depends on whether its prominence from the neighbouring bins is greater than the uncertainty involved in its detection. It should be noted here that, since each peak is bounded by two local minima, the greater of the two is chosen in order to account for the worst-case scenario.

A typical example of a low TNTI (figure 5.16a, $\overline{Y}_i = 0.46\delta$), shows that in total, seven peaks are detected instantaneously, of which only the first three (starting at the freestream, marked with green triangles in figure 5.16a) are time-coherent. On the other hand, a higher-than-average TNTI location (figure 5.16a, $\overline{Y}_i = 0.98\delta$) leads to the detection of three peaks that are all time-coherent. As expected, when the TNTI is low, there is a significant decrease in the bin count, especially for the peaks that are short-lived (red triangles in figure 5.17a), for which the corresponding uncertainty is comparable although still lower than the prominence of the peaks. For the time-coherent peaks, although the uncertainty is increased, it is still an order of magnitude less than the peak prominence, ensuring that these peaks are well-defined. On the other hand, when the TNTI is far away from the wall, the number of vectors for each detected peak is much larger (an order of magnitude larger for the peaks closest to the freestream), and the corresponding uncertainty is statistically insignificant for the detection of the peaks (figure 5.17b).

The previous two cases show that instantaneously, a peak detection algorithm will distinguish local maxima in the streamwise velocity pdf, based on the relative parameters discussed in section 5.1. However, the number of vector counts for each peak with respect to its neighbouring minimum is another crucial parameter that influences the confidence bound with which each peak is detected. In cases where the TNTI is located very close to the wall and only a small

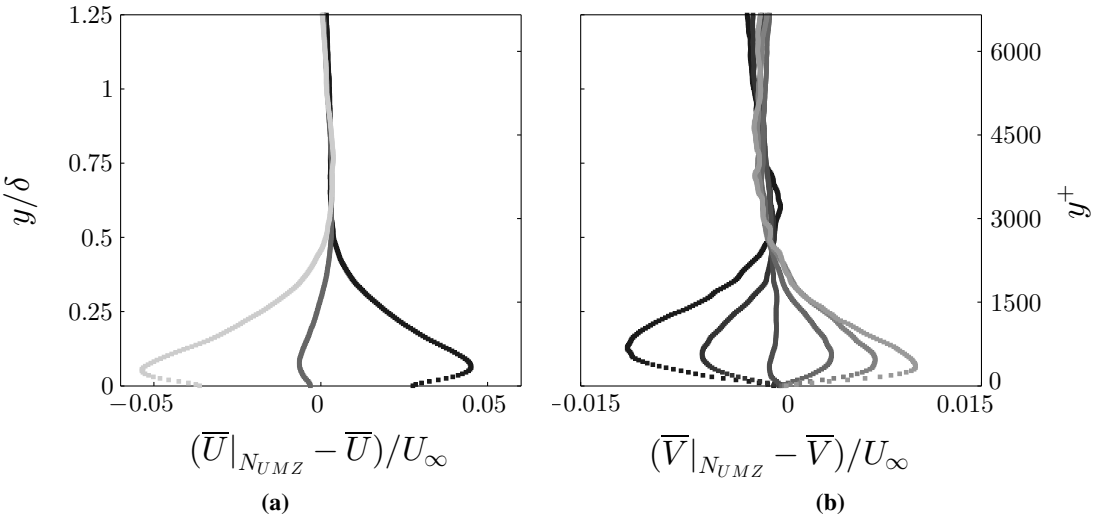

Figure 5.18. TBL flow, planar-PIV field ($Re_\tau = 5300$). Conditionally averaged velocities for each characteristic region. (b) Difference from global streamwise average. (c) Difference from global wall-normal average. Colours denote the classification of N_{UMZ} into three characreistic regions: ■ for $N_{UMZ} < 3$,■ for $3 \leq N_{UMZ} < 5$,■ for $N_{UMZ} \geq 5$.

number of velocity vectors are available below it, more peaks are detected on average but with much higher uncertainty levels. Therefore, care should be taken especially for the short-lived modal peaks, since in some cases their prominence with respect to neighbouring points is of the order of their detection uncertainty. Interestingly, time-coherence of the peaks seems to ensure a prominence much greater than the relevant uncertainty, even in cases where the TNTI is very close to the wall.

5.4 Time-scales

Apart from flow statistics, the time information available allows us to estimate time-scales for the different events discussed above. In order to facilitate the discussion in the following paragraphs and based on the average number of peaks ($\overline{N}_{UMZ} \approx 3.2$) we define three characteristic regions: $N_{UMZ} < 3$, representing low number of zones; $3 \leq N_{UMZ} < 5$ average number of zones; $N_{UMZ} \geq 5$ large number of zones. The regions are defined in such a way that a high number of zones represents a large-scale $Q2$ event in the log region, while the low-zone-number group represents a large-scale $Q4$. Both velocity components are close to the global average for the average-zone-number group (see figures 5.18a and 5.18b).

5.4.1 Number of zones

Since UMZs with short temporal coherence have been removed, we can estimate the time for which a certain N_{UMZ} resides within our FOV and how often it reappears. This definition is

shown schematically in figure 5.19a for an example of 300 consecutive images, where τ_w^+ denotes the residence time of a certain number of zones or group of zones (the large number of zones group is highlighted here) inside the measurement plane, and τ_f^+ denotes the time after which the same N_{UMZ} or group of zones reappears.

The average residence time of the different zone-number states is found to be of the order of 10 viscous time units and exhibits only a very slight decreasing trend as N_{UMZ} increases (figure 5.19b). The frequency with which each number of zones appears in time reflects the pdf distribution of N_{UMZ} (figure 5.2): increase in frequency is observed for an average number of zones, while both extremes appear progressively less often. A change in the relative time-scales is expectedly observed when instead of individual zones, the three zone divisions are considered. The average-zone-number group exhibits residence times almost twice as long as either of the high or low-zone-number group and it is also the most frequent state (as was expected from the of distribution of N_{UMZ}). As can be seen in figure 5.19a, the transition from the average state to either extreme is not monotonic. This implies that, starting at the most frequent state of an average N_{UMZ}, there is often a shift towards an extreme (either high or low), a return to an average number of zones, and a shift again towards the same extreme. The time-scales of all such transitions were reported above, however it was the presence of one extreme or the other that was shown in the previous section to be linked with large-scale structures in the log layer. Therefore, the residence time of a high- or average-zone-number state ($\sim 0.33\delta/U_\infty$) that does not get into a low-zone behaviour (marked with ⧫ in figure 5.19b), could be indicative of the presence, within our measurement plane, of a large-scale ejection that was shown to be linked with this behaviour. Conversely, the significantly higher residence time of a low or average number of zones ($\sim 0.58\delta/U_\infty$), could indicate the presence of a high-speed structure that was previously shown to be linked with it.

Apart from the time-scales, we can further investigate the evolution of this structuring process by finding the most probable number of UMZs at a time $t+dt$, given that at time t, the flow is organised into N number of zones. As was discussed, the timestep dt after which a change occurs, has a weak dependence on the number of zones at time t and is of the order of 10 viscous time units. Results show that the division of an average number of zones ($3 \leq N_{UMZ} < 5$) is the most preferable state (figure 5.20). Given a low N_{UMZ} the most probable change will be towards a higher number, while given a high number of UMZs at time t, the opposite trend is observed. For an average N_{UMZ}, there is almost equal probability of moving towards either a lower or a higher number of zones. It is interesting to note that most zone-number changes are symmetric. For example a change from a structuring of $N_{UMZ} = 5$ to one with $N_{UMZ} = 3$ will happen approximately as many times as the reverse ($P(N_{UMZ} = 3 \rightarrow 5) \approx P(N_{UMZ} = 5 \rightarrow 3)$). Due to this symmetry, when estimating the most probable situation that preceded (at time $t-dt$) each realisation at time t, the results are almost identical to the ones presented in figure 5.20.

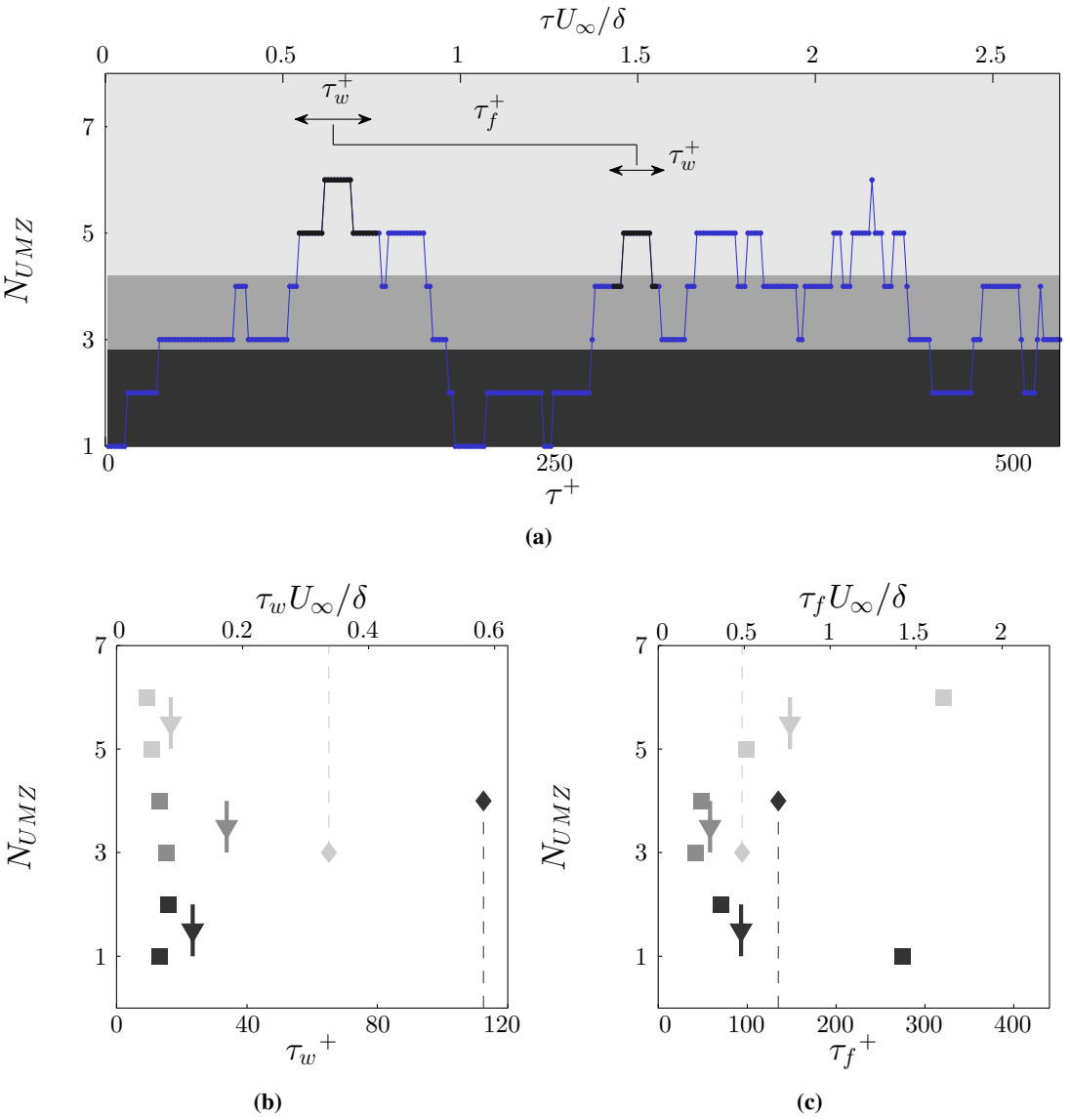

Figure 5.19. TBL flow, planar-PIV field ($Re_\tau = 5300$). (a) Time-evolution of the number of time-coherent peaks for the same 300 consecutive images as in figure 5.4. Background colours denote the classification of N_{UMZ} into the three regions defined in figure 5.4. Examples of how long a high number of zones resides within the measurement plane, τ_w^+, and how often it reappears, τ_f^+, denoted with black. (c,d) For how long, on average, the boundary layer is structured into a certain number of zones (left) and the frequency of repetition of this structuring (right). Squares denote each number of zones independently and triangles each group of zones: ▼ for $3 < N_{UMZ}$,▼ for $3 \leq N_{UMZ} < 5$,▼ for $N_{UMZ} \geq 5$. Solid lines mark the range of each group. Dashed lines denote the time (left) and frequency (right) for which the boundary layer is structured in an average or high number zones (♦) or in a low or average number of zones (♦).

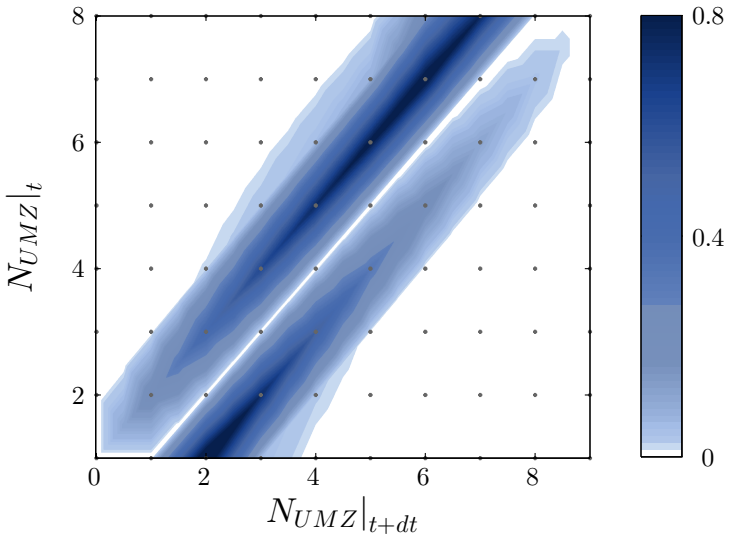

Figure 5.20. TBL flow, planar-PIV field ($Re_\tau = 5300$). Pdf of the number of zones at time $t + dt$, based on the number of zones at time t. Grey dots denote data-points. Linear interpolation was used on a finer mesh for visual clarity.

5.4.2 Individual UMZs

The analysis of the previous section was relevant to the time-scales and evolution of the structuring process of the boundary layer into a given number of zones. However, the results did not include information on the temporal coherence of individual UMZs. Each zone is detected based on modal velocities that are present in each snapshot. Several of the detected peaks also appear in following snapshots, while others die away. Based on the change of each peak's modal velocity in consecutive snapshots, individual UMZs can be tracked. For all time-scale evaluations we only consider peaks that persist inside the FOV for longer than $\tau^+ \approx 20$ (an example of the remaining peaks can be seen in figure 5.4b, each one with a different colour). For the remaining peaks, the average residence time is $\approx 0.35\delta/U_\infty$ and shows that these structures persist within our FOV for time-scales shorter than δ/U_∞ (figure 5.21). As was mentioned in the previous section, UMZs are shown to be linked with large-scale structures in the log region, however their temporal coherence is based on the time that a single modal velocity persists within the measurement plane and as such are generally expected to have much shorter time-scales than the corresponding log region events. The largest residence times found (6–$7\delta/U_\infty$), show that there are cases where individual UMZs do indeed reach time-scales that, assuming convection velocities that range from 0.5–$0.9U_\infty$, may indicate structures with lengths larger than 3δ (LSMs) and reaching up to 6δ (superstructures).

Large scale structures and superstructures are also known to meander in the spanwise direction and therefore it is likely for them to appear and disappear from our streamwise–wall-normal measurement plane, effectively breaking their observed time-coherence and as such the residence times of UMZs as well, depending on their meandering amplitude and alignment with the FOV. Another explanation for the lack of longer residence times, comes from recent studies

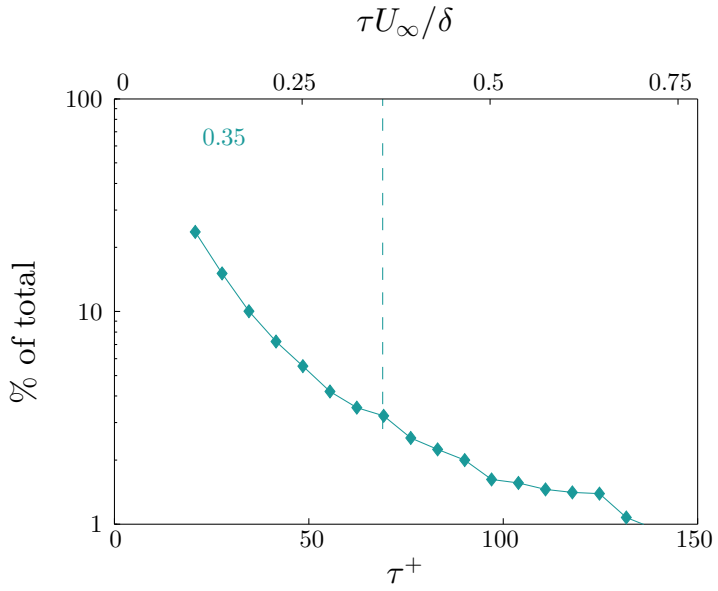

Figure 5.21. TBL flow, planar-PIV field ($Re_\tau = 5300$). Frequency of appearance of time-coherent UMZs (in % of the total), depending on their residence time, τ. Dashed line denotes average residence time.

suggesting that the observed spectral peaks in the outer-region that have been linked to the presence of very-large structures, might be due to a sequence of structures that are repeated in time for very long distances, without necessarily an elongated spatial coherence: Kim and Adrian (1999) and later Baltzer et al. (2013) suggested that the large-scale motions (LSMs) observed in high *Re* number pipe flows align to form VLSMs, an observation later supported by Lee and Sung (2011) for superstructures in turbulent boundary layers. Following this reasoning, Hellström et al. (2015) and Ahn et al. (2015) using experimental and numerical data of a pipe flow respectively, showed that the observed coherence of the very-large structures in the frequency domain does not infer spatial coherence of the same size and that the emerging outer spectral peak reflects an alignment of smaller structures.

Throughout each zone's residence time within the FOV, both their respective rank as well as the number of zones present at every snapshot vary. The naturally arising question is whether the modal velocity of each zone and the total number of zones present in the flow during each zone's residence time have any influence on that characteristic time. The time sequence presented in figure 5.4 shows that zones with large modal velocities have larger time-scales than the ones that appear closer to the wall. This is further supported from the residence time of structures that, during this time, have a modal velocity belonging to one of the four modal velocity groups shown (figure 5.22a). Each zone might contribute to all groups (only once to each though), according to the different modal velocities it corresponds to during its residence time. Although each modal velocity band contains zones that persist within the measurement plane for various times, there is a clear increase of the average residence time (denoted with dashed lines), for zones closer to the freestream. Also, even though low modal velocity bands include some UMZs with long residence times, the majority of their observation time includes UMZs with shorter time-scales

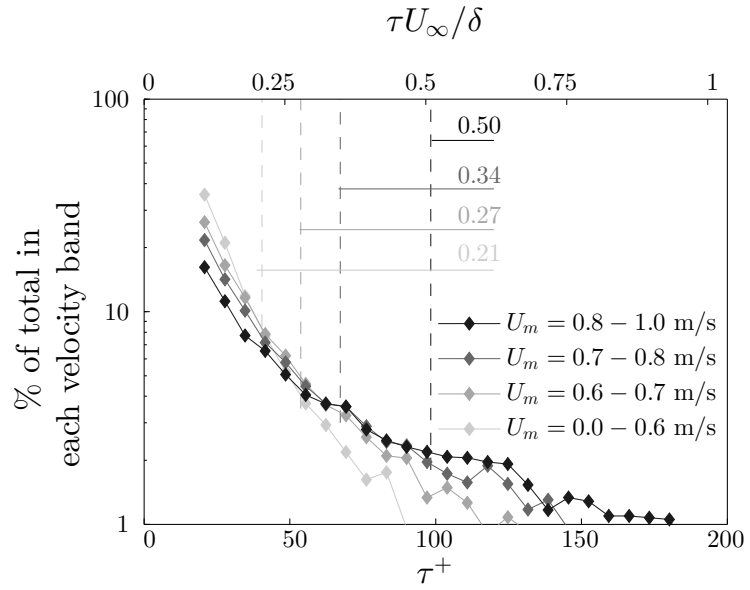

(a)

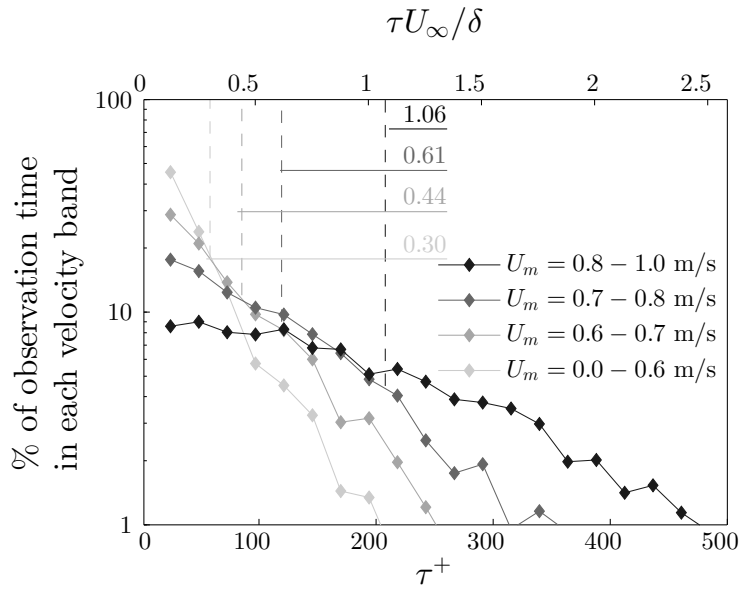

(b)

Figure 5.22. TBL flow, planar-PIV field ($Re_\tau = 5300$). UMZs are classified according to whether they reach at least once during their residence time, τ, a modal velocity, U_m belonging to each of the three shown velocity bands. (a) Frequency of appearance of UMZs within each velocity band (in % of the total UMZs within that band), depending on their residence time. Each UMZ might contribute to multiple bands, only once to each, according to the different modal velocities it corresponds to during its residence time. Dashed lines denote the average residence time of UMZs within each band. (b) Duration of observation of UMZs within each velocity band (in % of the total observation time of all UMZs within that band) according to their residence time. Each UMZ might contribute to multiple bands, every time it reaches a modal velocity belonging to any of them. Dashed lines denote the average observation time of UMZs in each group.

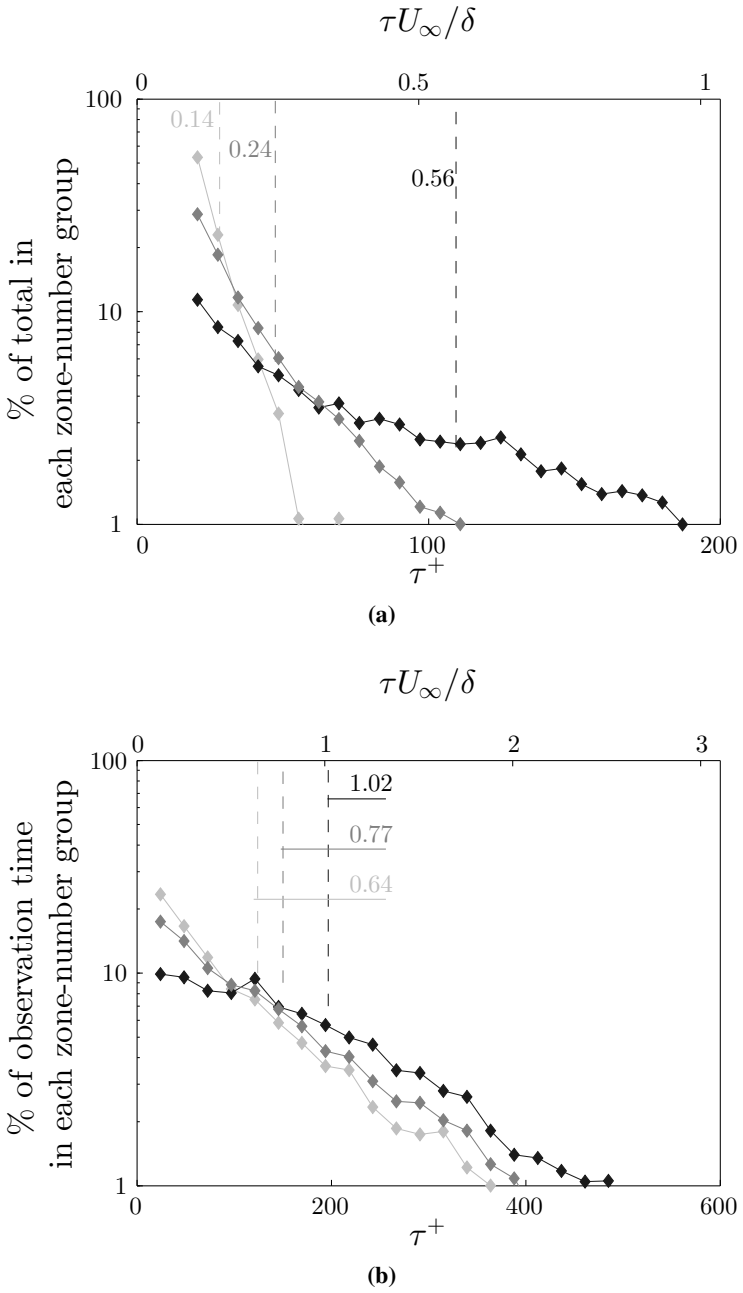

Figure 5.23. TBL flow, planar-PIV field ($Re_\tau = 5300$). UMZs are classified according to whether they encounter at least once during their residence time, τ, any of these zone-groups: —— for $\overline{N}_{UMZ} < 3$, —— for $3 \leq \overline{N}_{UMZ} < 5$, —— for $\overline{N}_{UMZ} \geq 5$. (a) Frequency of appearance of UMZs, within each zone-number group (in % of the total within that group), depending on their residence time. Each UMZ might contribute to multiple groups, only once to each, according to the number of other zones appearing and dying away during its residence time. Dashed lines denote the average residence time of UMZs within each group. (b) Duration of observation of UMZs within each zone-number group (in % of the total observation time of all UMZs within that group) according to their residence time. Each UMZ might contribute to multiple groups, every time it encounters them. Dashed lines denote the average observation time of UMZs in each group.

(see figure 5.22b). For example, 50% of the total observation time of the lowest modal velocity group (denoted with light grey in figure 5.22) is spent on structures with residence times shorter than $\tau^+ = 40$. For the high-modal-velocity bands, the observation time is almost equally spent between structures of all time-scales. This essentially means that for any individual snapshot, it is much more probable for a high-modal-velocity peak to have a long residence time than it is for a low-modal-velocity peak one. Furthermore, the mean observation times of each velocity group show that in any individual snapshot there is also a much higher probability of finding a peak that belongs in a high-velocity group. That trend supports a hierarchical organisation of structures in the wall-normal direction (new slower zones appearing close to the wall, while older faster ones are located closer to the freestream) and is also in line with the schematic depiction of a hairpin packet organisation by Adrian et al. (2000).

When the residence times are now grouped according to N_{UMZ} the results show that, zones appearing in snapshots where the boundary layer is organised into many layers, are less coherent in time (mean residence times of $0.14\delta/U_\infty$) and even the longer ones do not typically exceed residence times of $0.25\delta/U_\infty$ (figure 5.23a). Also, in the high-number-of-zones group, shorter-lived structures are shown to dominate the total time of peak observation (figure 5.23b). This shows that for any snapshot belonging to a high zone number group, there is a much higher possibility that any of the peaks present is a short-lived one. On the other hand, UMZs that exist in snapshots characterised by a low N_{UMZ}, tend to persist longer, with maximum residence times exceeding δ/U_∞ and they are also shown to spend the majority of these residence times in the low zone number group (figure 5.23b). For example, zones with residence times of $\tau^+ = 250$ account for 4.5% of the total observation time of the low zone-number group, while only for 1% of the total observation time of the high zone-number group. This trend can be mapped into a Reynolds number dependence following the scaling of the number of zones with Re_τ (de Silva et al., 2016). More specifically, a low number of zones ($N_{UMZ} < 3$) would correspond to a $Re_\tau \sim 10^3$ while a high number of zones to a $Re_\tau \sim 10^4$ suggesting that the UMZs present in the flow tend to decrease in size and extent as the Reynolds number increases. A similar behavior was reported by Vallikivi et al. (2015), who found that the wavelength of the outer spectral peak increases when normalised with inner variables and decreases in the case of an outer-scale normalisation, suggesting that the scales associated with it decrease in size as the Reynolds number increases. Another explanation for this time-scale variation could come from the organisation of the flow in the log-region. More specifically, it was shown above that a high number of zones is on average correlated with a large-scale $Q2$ event in the log layer, while a $Q4$ most often leads to a low number of zones. Lozano Duran et al. (2012) showed that, large-scale $Q4$ events exist in pairs with $Q2$ structures and that low-speed events are often engulfed by high-speed ones and are significantly smaller in length and width. This documented difference in size, could be the reason for the much larger time-scales observed when the number of zones is low.

In this chapter, the structuring of the boundary layer into UMZs was analysed in terms of flow statistics, while the zones' temporal evolution was also discussed. In the following chapter,

an effort is made to link these observations for UMZs, along with the trends observed for the freestream boundary in chapter 4, with the structural organisation of pressure fluctuations within the boundary layer.

Chapter 6

Structure of pressure fluctuations

In chapter 3, a pressure estimation method based on Taylor's hypothesis was presented and validated using both numerical and experimental datasets. Results showed that, even in cases when only 2D velocity snapshots are available, the method is still robust to noise, while it provides reasonable pressure estimates in a statistical sense. This allows us to apply the method on the time-resolved planar PIV dataset (described with detail in chapter 2 section 2.3), analyse some structural characteristics of the pressure fluctuations and explore potential connections with the presence of the freestream boundary and internal layers below it (see chapters 4 and 5). For the latter, only time-coherent UMZs and the corresponding internal layers that bound them are considered here.

Pressure was estimated following the 2D form of equation 3.11 in chapter 3. The boundary conditions used were Neumann using equation 3.11, for all edges except the top, for which we we could apply Dirichlet boundary conditions since the FOV extended up to the freestream. More specifically, pressure was prescribed ($p = 0$) at the top edge of the plane, located in the freestream. It should also be noted here that, all analysis in chapters 4 and 5, which will be of interest here, was restricted below $y = 1.25\delta$ in the wall-normal direction, which was the limit set for the detection of the freestream boundary (see also section 4.1). To facilitate comparison and since pressure fluctuations are expected to be negligible in the freestream region, the same limit was also applied in the present chapter.

6.1 Spatio-temporal characteristics

Pressure fluctuations exhibit an almost normal distribution centred around zero throughout the boundary layer. The distribution becomes narrower closer to the freestream, as the pressure fluctuations approach zero values (figure 6.1). In order to understand how these fluctuations are organised across the boundary layer, constant two-point correlations in time and space are

employed for five different wall-normal locations (figures 6.2 and 6.3). Similar to early observations from Kim (1989) in a low-Reynolds number turbulent channel flow, the pressure fluctuations are significantly elongated in the wall-normal direction. Kim (1989) also showed that for zero separations in the streamwise and spanwise directions, pressure has larger correlation extent along the wall-normal direction when compared to other quantities (mainly the velocity fluctuations in all three directions).

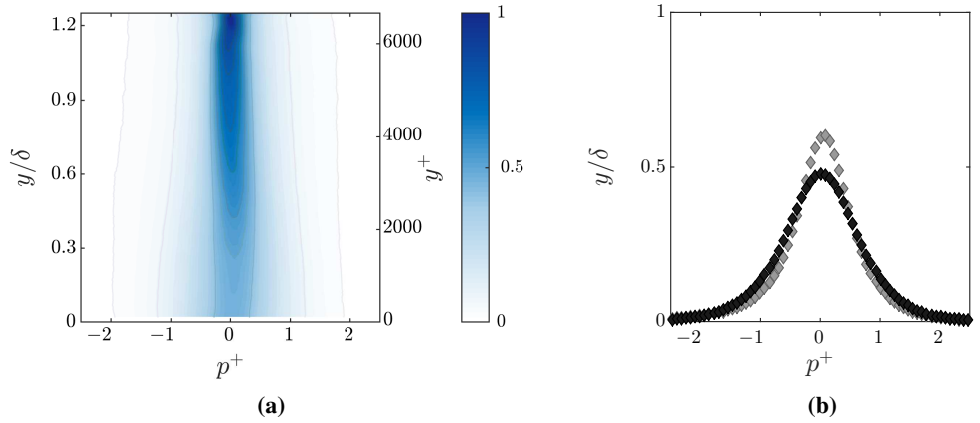

Figure 6.1. TBL flow, planar-PIV field ($Re_\tau = 5300$). (a) Probability density function (pdf) contours of inner-normalised pressure fluctuations, varying with distance from the wall. (b) Pdf profiles of inner-normalised pressure fluctuations for two wall normal locations: $y^+ = 108$ (grey symbols) and $y/\delta = 0.5$.

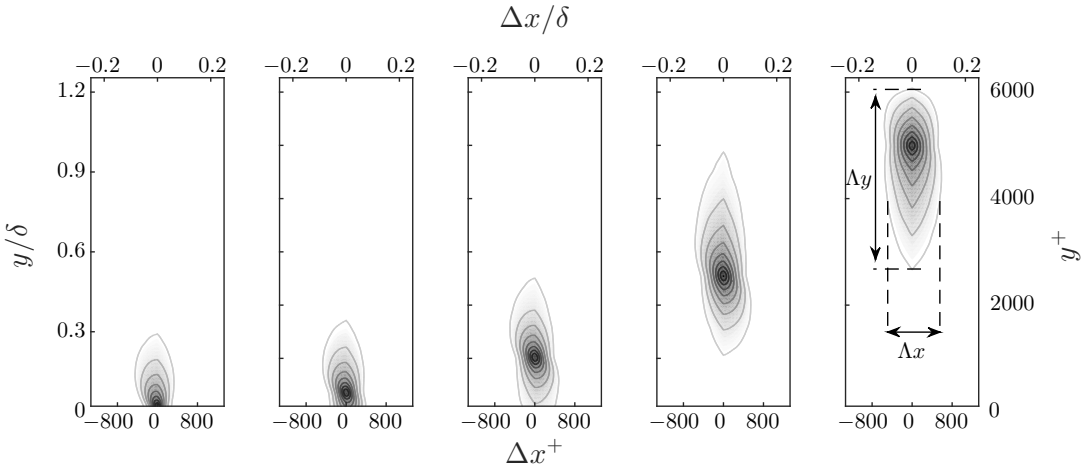

Figure 6.2. TBL flow, planar-PIV field ($Re_\tau = 5300$). Contours of constant two-point correlations of pressure fluctuations R_{pp}, as a function of streamwise and wall-normal separations for $y^+ = 108$, $y^+ = 350$, $y/\delta = 0.2$, $y/\delta = 0.5$, and $y/\delta = 1$. Contour levels ranging from 0.2 to 1 with spacing of 0.1. The maximum streamwise (Λx), and wall-normal (Λy) extents, estimated for a correlation level of 0.3, are also schematically drawn.

To quantify the maximum coherence of pressure fluctuations across the boundary layer, the streamwise and wall-normal extents of the two-point correlations at a level of $R_{pp} = 0.3$ are estimated for every wall-normal location (schematically drawn in figure 6.2). Additionally, based on the minimum location of the vertical coherence, the height of 'pinch-off' from the wall is also computed ($h_p = 0.2\delta$, dashed lines in figure 6.6, slightly above the edge of the logarithmic region). This essentially means that for $y > h_p$, the vertical coherence of the pressure fluctuations no longer reaches the wall.

The maximum streamwise extent shows a moderate variation across the boundary layer (figure 6.3), increasing slightly from the wall until $y/\delta \approx 0.7$, reaching a maximum of $\Lambda x \approx 0.18\delta$ until the edge of the boundary layer, where it drops off towards zero. This indicates that pressure fluctuations are on average coherent for about half the streamwise extent of the measurement plane, throughout the boundary layer.

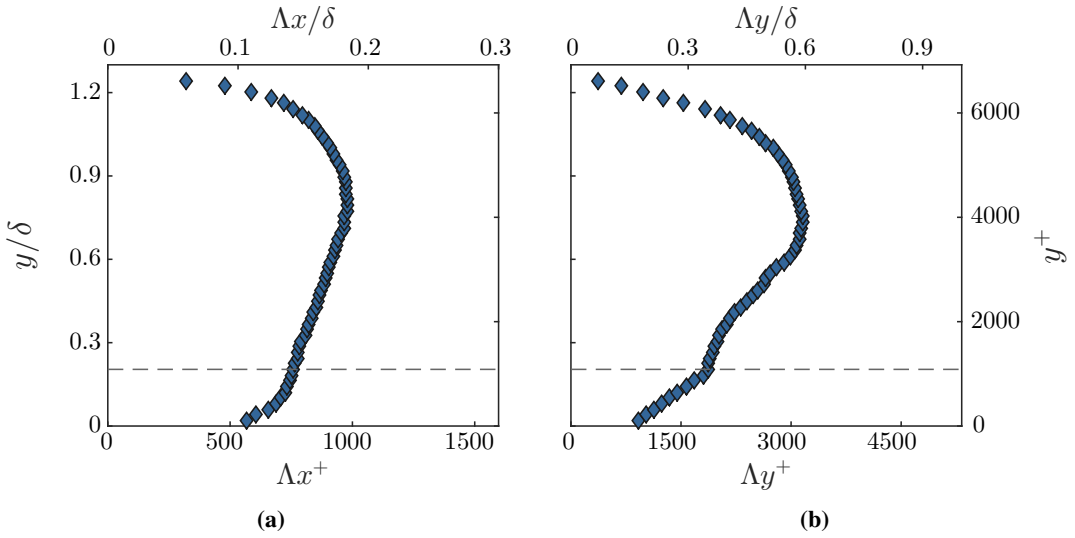

Figure 6.3. TBL flow, planar-PIV field ($Re_\tau = 5300$). Maximum extents of pressure correlations (shown schematically in figure 6.2), varying with distance from the wall.(a) Maximum streamwise (Λx) and (b) wall-normal extent (Λy). Dashed lines denote approximate pinch-off location from the wall.

On the other hand, the wall-normal extent, as was already seen from the two-point correlations (figure 6.2), is up to four times larger and shows a much more pronounced variation across the boundary layer. At the first wall-normal location above the wall where pressure data is available ($y^+ \approx 100$) and which approximately coincides with the beginning of the log region, Λy is almost twice as large as the streamwise coherence ($\Lambda y = 0.18\delta$). It then exhibits a sharp linear increase throughout the logarithmic layer until the pinch-off location. Above the logarithmic layer and up to $y \approx 0.6\delta$, the vertical extent continues to increase, albeit at a slower rate, and it reaches its maximum of $\Lambda y \approx 0.6\delta$ and then drops of slightly towards the edge of the boundary layer. This is indicative of the extensive vertical correlation of pressure structures that spans almost the entire boundary layer thickness, similar to observations from Kim (1989), who found that

in the case of a channel flow, the pressure correlation extents almost to the opposite wall. For heights above 0.9δ, there is a sharp drop towards almost zero values, similar to Λx. Close to the freestream, although the coherence on either direction is expected to decrease due to the almost negligible pressure fluctuations (figure 6.1), the limit imposed on the wall-normal extent of the FOV ($y < 1.25\delta$) is expected to have some additional effect, leading to the sharp decrease towards zero values.

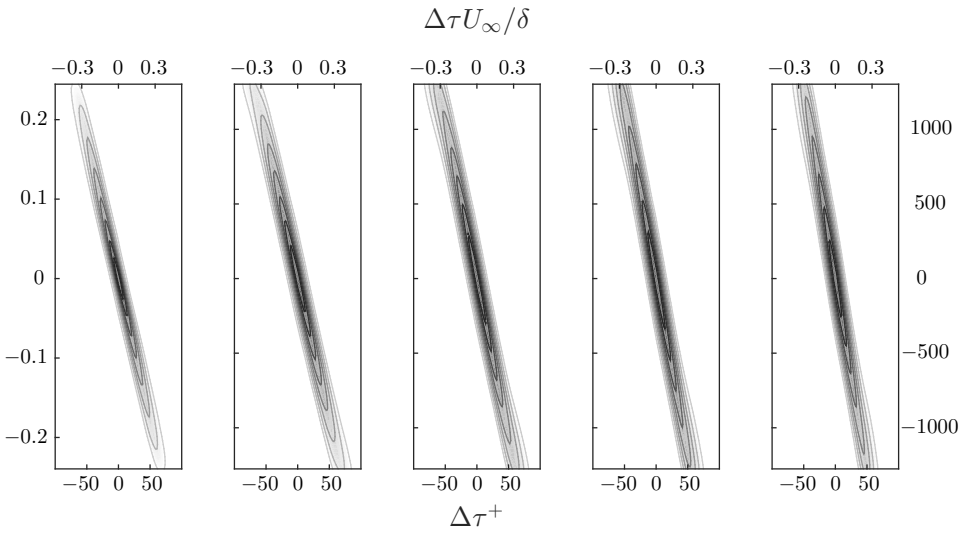

Figure 6.4. TBL flow, planar-PIV field ($Re_\tau = 5300$). Contours of constant two-point correlations of total pressure fluctuations as a function of time and streamwise separation for $y^+ = 108$, $y^+ = 350$, $y/\delta = 0.2$, $y/\delta = 0.5$, and $y/\delta = 1$. Contour levels ranging from 0.2 to 1 with spacing of 0.1.

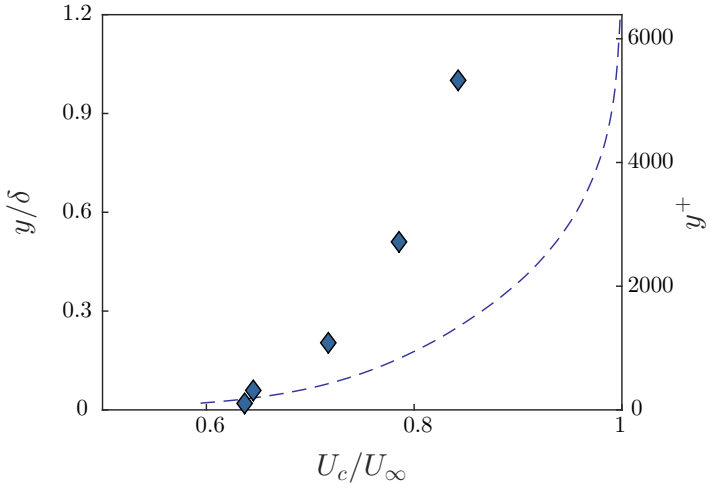

Figure 6.5. TBL flow, planar-PIV field ($Re_\tau = 5300$). Average convection velocities of pressure fluctuations varying with distance from the wall, estimated from a linear fit of the two-point correlation contours in figure 6.4. The mean velocity profile is marked with dashed line.

Two-point correlations as a function of time and streamwise distance for different wall-normal locations (figure 6.4), are indicative of the velocity with which pressure fluctuations convect on the streamwise direction ($U_c = \Delta x/\Delta\tau$). The resulting average convection velocity for the pressure fluctuations, estimated as a linear fit of the contour levels in figure 6.4, is shown to be slightly higher than the local mean velocity close to the wall, while within the log region and above this trend reverses. The streamwise mean velocity was shown to be a good approximation for the convection velocity of velocity fluctuations in the case of wall-bounded flows by Geng et al. (2015), thus indicating that pressure fluctuations convect slightly faster than velocity ones close to the wall, in line with observations from Kim (1989) who estimated that at the wall, pressure fluctuations convect ≈ 1.3 times faster than the velocity and vorticity ones.

6.2 Pressure statistics varying with number of UMZs

The number of uniform momentum zones (UMZs) in the boundary layer, N_{UMZ} was found to be related with different flow velocity conditions (see chapter 5). More specifically, a high number of zones ($N_{UMZ} \geq 5$) was associated with a large-scale $Q2$ event, while a low number of zones ($N_{UMZ} \leq 2$) was linked with a large-scale $Q4$ event in the log region. In the cases where $3 \leq N_{UMZ} \leq 4$, the flow statistic were very close to the global average. Therefore, in this section, we follow a similar analysis to assess any potential influence of N_{UMZ} on the pressure fluctuations statistics and their structure. The root-mean-square (rms) pressure fluctuations, p_{rms} indicate an increase below $y = 0.6\delta$, as N_{UMZ} increases, while the opposite is observed for a low number of zones (figure 6.6).

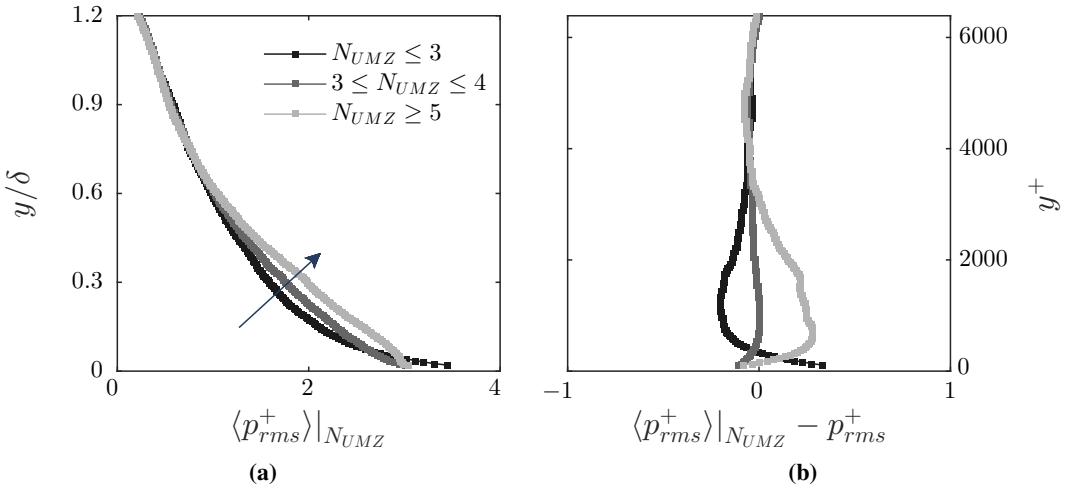

Figure 6.6. TBL flow, planar-PIV field ($Re_\tau = 5300$). Conditionally averaged pressure statistics based on the number of UMZs in the boundary layer, N_{UMZ}. (a) Inner-normalised rms pressure and difference from global rms pressure (b). Pressure rms values are computed with respect to the global time-averaged pressure field.

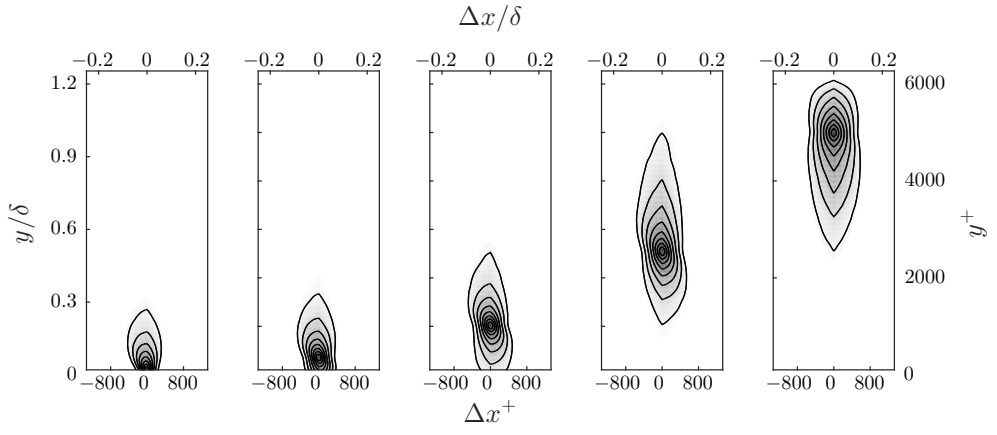

(a)

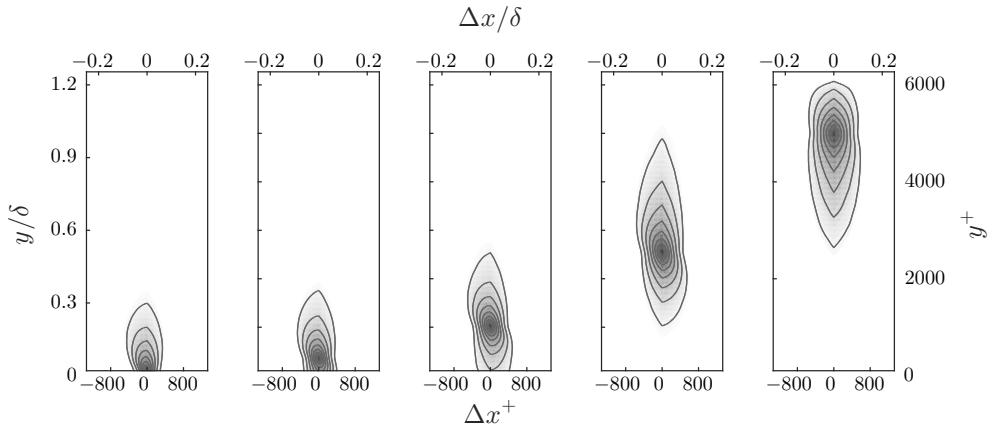

(b)

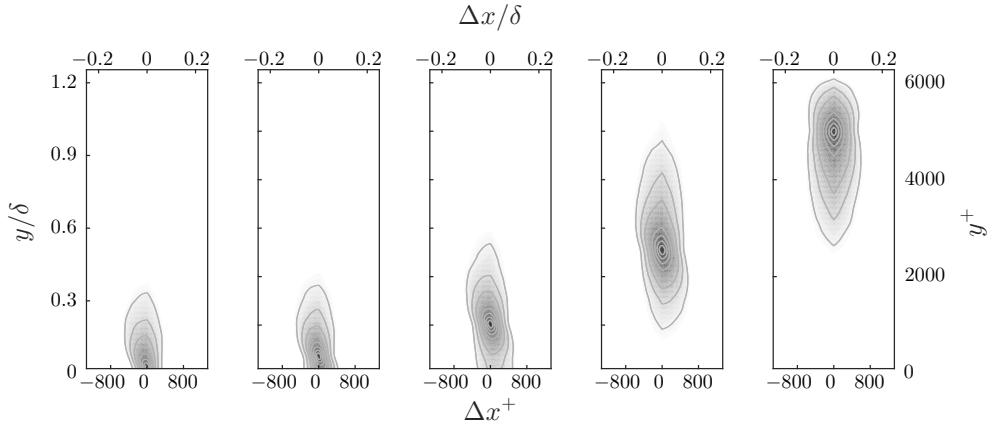

(c)

Figure 6.7. TBL flow, planar-PIV field ($Re_\tau = 5300$). Contours of constant two-point correlations of total pressure fluctuations, as a function of streamwise and wall-normal separations, conditioned upon the number of zones present in the boundary layer, N_{UMZ}, for $y^+ = 108$, $y^+ = 350$, $y/\delta = 0.2$, $y/\delta = 0.5$, and $y/\delta = 1$. (a) $N_{UMZ} < 3$. (b) $3 \leq N_{UMZ} < 5$. (c) $N_{UMZ} \geq 5$. Contour levels ranging from 0.2 to 1 with spacing of 0.1. Pressure fluctuations are computed with respect to the global time-averaged pressure field.

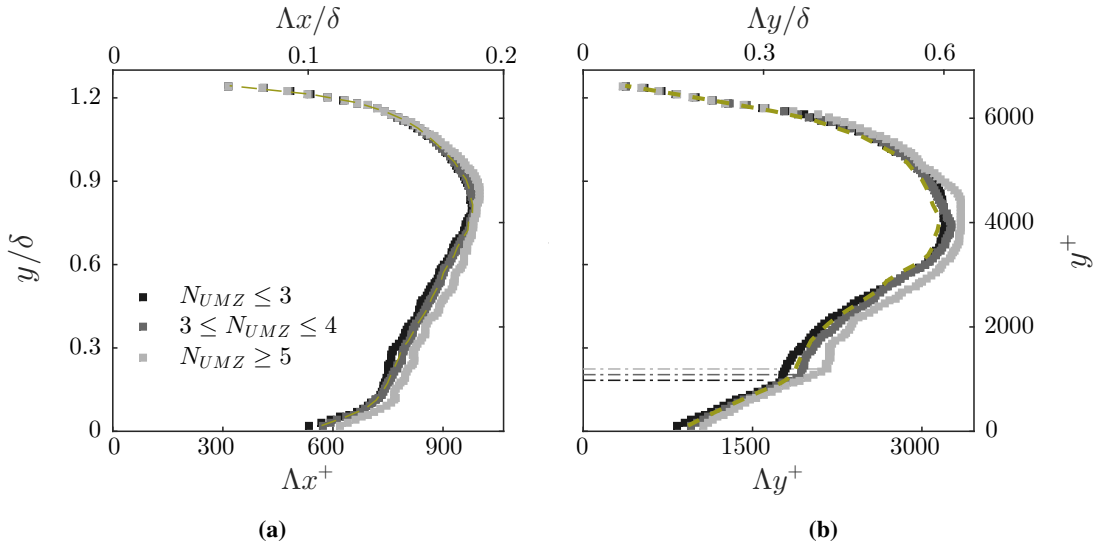

Figure 6.8. TBL flow, planar-PIV field ($Re_\tau = 5300$). Maximum extents of pressure correlations (shown schematically in figure 6.7), varying with distance from the wall and conditioned on N_{UMZ}. (a) Maximum streamwise (Λx) extent. (b) Maximum wall-normal extent (Λy). Dot-dashed horizontal lines denote approximate pinch-off location from the wall. Dashed lines denote the global values for the wall-normal and streamwise extents as were presented in figure 6.6.

This behaviour strongly resembles the conditional velocity statistics (see figures 5.10 and 5.18), associating a $Q2$ event with an increase of pressure fluctuations, and a log-region $Q4$ event with a decrease from the global average. Taking also into account the conditionally averaged Reynolds stress profiles (see figure 5.10f), pressure fluctuations are shown to be similarly amplified within the log region in the presence of a low-speed structure, while a high-speed event is shown to repress both velocity and pressure fluctuations above the crossover point (located at 0.04δ in the present data based on the estimate by Mathis et al., 2009).

Two-point correlations of pressure fluctuations, also indicate a slight change in behaviour for different number of zones present in the flow also in terms of structural organisation (figure 6.7). A low number of zones is shown to limit the vertical extent of the pressure correlation coherence for all wall-normal locations examined. This behaviour becomes more clear when the maximum streamwise and wall-normal extents conditioned to N_{UMZ} are estimated (figure 6.8). Similar to the global pressure correlation extents discussed above and to facilitate the comparison, the conditionally averaged maximum extents are also estimated from the two-point correlations at a level of $R_{pp} = 0.3$.

For an increase in the number of zones, the maximum streamwise extent, Λx, exhibits a slight increase below y/δ, indicating a larger coherence of pressure fluctuations in the streamwise direction, that could not be easily identified from the two-point correlation plots (figure 6.8a). For higher wall-normal locations, the number of zones has no significant effect on the streamwise coherence. The wall-normal extent also shows a marginal increase as N_{UMZ} increases, from the

wall up to the edge of the boundary layer, reaching a maximum of $\Lambda y \approx 0.63$ for a high number of zones, while the corresponding maximum value for a low N_{UMZ} is $\Lambda y \approx 0.6$ (figure 6.8b). The wall-normal location where pressure is not coherent down to the wall (pinch-off location, dotted horizontal lines in figure 6.8b), also shows a small increase, as the number of zones increases, thus further supporting a wider vertical correlation of pressure in those cases. This indicates that, the increase in rms pressure values for high N_{UMZ} (figure 6.6), is also combined with a larger vertical correlation of pressure fluctuations across the boundary layer height. On the contrary, a low number of zones results in a repression of the rms pressure values, while high and low pressure events are also less coherent within the boundary layer both in the x and y direction. Connecting these observations with conditionally averaged flow velocities, a low speed event in the log region leads to an increase of both velocity and pressure fluctuations within that region, with the latter also exhibiting a larger coherence in space. The presence of a high-speed event in the log region though, results in a decrease of turbulent activity, while in particular pressure events have a slightly shorter streamwise and spanwise spatial correlation.

6.3 Pressure statistics across the TNTI and internal layers

In this section the variation of pressure fluctuations across the freestream boundary and internal layers is estimated using conditional averages, following the procedure outlined in chapters 4 and 5 for the velocity, vorticity, and Reynolds stress profiles. The aim here is to assess whether pressure exhibits any significant change across the external and internal layers and how this behaviour might vary with different TNTI locations and zone rank, since these parameters were shown to strongly influence the profiles of all other quantities in the previous chapters. With

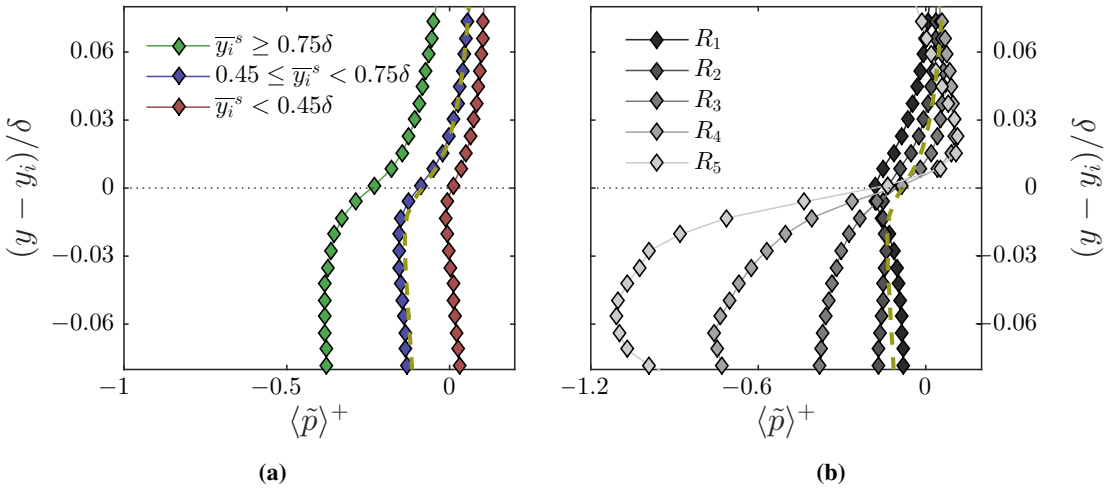

Figure 6.9. TBL flow, planar-PIV field ($Re_\tau = 5300$). Conditionally averaged pressure fluctuations, $\langle \tilde{p} \rangle$, across the TNTI (a), conditioned upon the average interface location at each snapshot, $\overline{y_i}^s$ and across the internal layers (b) that bound each UMZ (see also chapter 5). Dashed lines indicate the global average across the TNTI.

changing TNTI location, pressure fluctuations do exhibit a slight variation, reaching a pressure minimum just below the interface and then remain approximately constant within the turbulent region (figure 6.9a). For TNTI locations above average, where $Q2$ events were shown to be prominent (see figure 4.11b), the magnitude of this pressure drop is shown to increase, while in cases where the interface is very close to the wall and $Q4$ events dominate (see figure 4.11c), pressure fluctuations become increasingly positive. The presence of a pressure minimum below the TNTI was also observed in the work of Taveira and da Silva (2013) and Terashima et al. (2016) in the case of a turbulent jet and was linked with the presence of vortical structures within the interface, the size of which is of the order of the Taylor microscale and defines the characteristics of the interface da Silva et al. (2011). In a broader context, Johansson et al. (1991) and later Ghaemi and Scarano (2013), connected high pressure events with the presence of shear layers, while Johansson et al. (1987) attributed the presence of positive pressure fluctuations to sweep events. On the contrary, Kim et al. (2002), suggested that negative pressure fluctuations are the ones associated with $Q2$ events, while the sweep events are dominant when positive pressure fluctuations are generated. In a statistical sense, the present results agree with those of Kim et al. (2002) in that there is an increasing pressure drop for an increasing percentage of $Q2$ events below the interface, and a trend towards positive values for increasing prominence of sweep events.

Conditional statistics across the internal layers also exhibit significant changes, with an increasing pressure drop below the layers as the zone rank (and consequently N_{UMZ}) increases, while a higher than average pressure is observed above the layers (figure 6.9b). The pressure statistics across the first two layers (R_1 and R_2) are very close to the profiles across the TNTI. For zones of a higher rank, the prominence of $Q2$ events associated with these cases, leads to the sharp drop in pressure below their corresponding layers, similar to the pressure across a high TNTI location, a scenario which was also previously linked with a strong $Q2$ presence just below the interface. In the work by Ghaemi and Scarano (2013), $Q2$ events were shown to originate from the near wall region and specifically from hairpin-like structures, the heads of which were associated with negative pressure events. In the present data, for the cases of a higher than average TNTI location, $Q2$ events that are shown to be prominent across the interface, belong to the outer region of the boundary layer. On the other hand, the large-scale ejection events associated with a high N_{UMZ} belong in the log region and since new zones have been shown to originate at the wall, it can be assumed that these $Q2$ events are a footprint of hairpin vortices originating from the near-wall region and cause the formation of UMZs. Regardless of their location however, $Q2$ events in either case result in a similar pressure drop, indicating the presence of vortical structures below both the TNTI and the internal layers.

Interestingly, an increasing number of zones also leads to an increase in pressure above the internal layers, similarly to the trend observed in the case of a TNTI location close to the wall. The latter is associated with an increase in $Q4$ events above the interface, however the same is not true for an increasing number of zones. In the model proposed by Ghaemi and Scarano (2013), high pressure events were associated with the presence of shear layers within the boundary layer,

where $Q2$ events were found to oppose $Q4$ ones. The present analysis provides overall percentages of quadrant events (chapters 4 and 5) across the total length of the freestream boundary and internal layers, and as such it only allows for a comparison of global behaviour below and above each interface. It is therefore possible that, both in cases of a low TNTI location and of a high-rank internal layer, regardless of the overall prominence of $Q2$ and $Q4$ events above the interfaces, the percentage of instances where the two events are found to oppose each other, are increased, as suggested by Ghaemi and Scarano (2013). That would lead to an increase of high pressure fluctuations in those cases just above the TNTI and internal layers, while below them, the resulting behaviour would still be influenced be the strong presence of $Q2$ events or lack thereof. With respect to internal layers of increasing zone rank, such an assumption can be supported by the hairpin model analysis of Adrian et al. (2000), who associated the presence of such layers with opposing $Q2$ and $Q4$ events, just upstream of hairpin vortical structures populating the boundary layer.

The case of a low TNTI location though, which results in similar high-pressure events above the interface, is slightly different, in that the outer flow above the freestream is generally expected to be quiescent. However, again in line with observations from Adrian et al. (2000) and results from chapter 4, $Q4$ events upstream of hairpin structures might just be a result of structures moving slower that their surrounding fluid. Based on the velocity jump across the interface for different TNTI locations, that could indeed be the case when the interface is close to the wall, where the velocity jump is the largest, as also evidenced by the increase of sweep events above the interface in those conditions. This behaviour was also linked with negative entrainment values in chapter 4, due to the strong opposition of the sweeping motion above the interface towards any upwards movement originating at the wall, leading to 'flatter' (less convoluted) interface geometries. Additionally, both a low TNTI location and a high-rank internal layer case, apart from high pressure values above the interfaces, also lead to an increase of Reynolds stress and vorticity magnitude across the interfaces (see figures 4.10 and 5.14), thus further establishing the existence of a similarity between the two scenarios.

To conclude, in this chapter the structural organisation and convection of pressure fluctuations was analysed. It was shown that the resulting behaviour is strongly influenced by the number of UMZs in the boundary layer, similar to the flow velocity statistics presented in the previous chapters. Also, both the freestream boundary and internal layers below it, are shown to be regions of significant changes in pressure, again in accordance with the variation of velocity and vorticity within those regions.

Chapter 7

Conclusions and future work

The purpose of this work was to enhance the understanding of wall-bounded turbulent flows, with respect to both pressure and velocity fields. An overview of current controversial issues within the research community regarding the velocity field was given in chapter 1, highlighting the specific areas where this work was mostly focused, namely the evolution of freestream boundary and its geometrical characteristics, together with the formation of uniform momentum zones (UMZs) below the interface and their connection to vortical structures. With respect to pressure, an outline of previous studies and recent developments on the subject was given in chapter 1, with emphasis on full-field pressure estimation methods using particle image velocimetry (PIV) data.

Time-resolved tomographic and planar particle image velocimetry (PIV) experiments were performed in a turbulent boundary layer, in order to acquire 2D and volumetric velocity data. In order to also obtain pressure information, a pressure estimation method was presented, that employs Taylor's hypothesis (TH) for the estimation of flow acceleration and can be applied to both 2D and 3D input velocity data. The method was developed by de Kat and Ganapathisubramani (2013) and was shown to provide reliable pressure estimates for 2D-3C velocity data. Here, the method was expanded to allow for volumetric velocity input and it was validated against both synthetic and experimental velocity PIV data together with an Eulerian (EU) and a pseudo-Lagrangian approach (pLA). The techniques were validated numerically, using the channel flow database from Johns Hopkins University (Li et al., 2008; Perlman et al., 2007; Graham et al., 2013). Independent synthetic 3C volumetric PIV snapshots were created from the available data and pressure was using all methods. Initially, it was shown that for TH the use of the streamwise mean as the convection velocity yielded the most accurate results. When noise was present in the data, EU performed best using moderate time-steps which provided a balance between truncation and precision errors. The pseudo-Lagrangian approach performed the best for increasing time frame separation. For very large separations however, even though the accuracy of pLA was improved, there were significant edge effects due to particle paths outside of the FOV, which resulted in much smaller pressure fields (up to 50%). With the convection velocity and frame time-separation chosen so as to get the best possible results, the dependence of all

methods on noise and grid resolution was subsequently tested. It was shown that even though the Eulerian and pseudo-Lagrangian approaches performed better in the case of zero noise and best resolution, their accuracy deteriorated much quicker than the one attained using TH. Especially in the case of high noise levels, both EU and pLA failed completely in determining the pressure, while TH indicated a maximum decrease of correlation of roughly 20%. These results were in agreement with a linear uncertainty propagation procedure for the pressure estimation that was also performed. It was also shown that pLA was the most sensitive of the three methods in terms of grid resolution with a maximum decrease in correlation of more than 50% for a decrease in resolution by a factor of four. Time-resolved volumetric PIV measurements were also performed in a turbulent boundary layer and pressure was estimated on the acquired 3D velocity fields. Results showed that for the minimum time separation, EU and pLA were suffering both from noise and resolution effects, resulting in pressure values an order of magnitude larger than what predicted with DNS at comparable Re numbers. For the pressure fields using TH noise effects were limited and some structural formations were discernible, while the root-mean-square (rms) values of pressure followed closely the distributions from DNS. For larger time-separations, pLA showed a significant improvement, but the resulting volumes were also significantly smaller—in line with the numerical assessment observations. Based on both the numerical and the experimental results, TH seems the most promising approach in these conditions, while pLA can also provide good results for large time separations, increasing with distance from the wall. Experimental data with a higher spatial resolution and of better quality could potentially reinforce these observations, however, large improvements are unlikely due to current limitations in equipment. Better accuracy could also be attained for the Eulerian approach by using more advanced correlation schemes on the 'raw' particle images. The important point however, is that for single snapshots of velocity, TH is the only approach of the three than can provide results and even when time information is available, it outperforms EU and has a similar accuracy with pLA without suffering from volume losses. In addition to the 3D formulation of the method, a 2D TH approach was also tested and it was found that, although it performs significantly worse than the corresponding 3D one instantaneously, it can provide reliable results in a statistical sense, while it is still robust to noise. This indicates the applicability of the method in engineering applications where three dimensional time-resolved data are not always available or affordable and a balance between cost and accuracy is sought after. These results also allowed us to estimate pressure for the planar PIV database and link it with the presence of a turbulent/non-turbulent (TNTI) and of UMZs below it.

Starting at the freestream boundary the structure and evolution of velocity fluctuations within the boundary layer were analysed using the planar PIV database. The TNTI was detected in all available snapshots and its main geomterical characteristics were discussed. Its total length was found to follow an almost lognormal distribution when normalised with either the streamwise or wall-normal extent of the interface. Conditional velocity, vorticity and Reynolds stress profiles exhibited clear jumps across the interface, within a distance that scaled with the local Taylor microscale, in accordance with the scaling of the vorticity thickness suggested from previous studies (da Silva and Taveira, 2010; da Silva et al., 2011; Chauhan et al., 2014b; Eisma et al.,

2015, among others). The interface was also tracked in time and a net positive entrainment rate was estimated that was in agreement with theoretical estimations based on boundary layer growth (Chauhan et al., 2014a). Locations of the TNTI far away from the wall were found to be linked with positive entrainment values, while the opposite was found for TNTI locations close to the wall, a behaviour that was associated with a strong presence of $Q2$ and $Q4$ events across the interface for each case respectively. Below the TNTI, the flow was found to be structured in different UMZs, detected instantaneously following the method suggested by Adrian et al. (2000); de Silva et al. (2016), extended to take into account the temporal coherence of the zones. The main geometrical characteristics of the time-coherent UMZs were presented and it was shown that the total number of zones in the flow is linked with different large-scale events in the log layer. More specifically, a high number of zones was found to be usually linked with a large-scale ejection event. The low-speed fluid moving upwards creates increased small-scale activity above the cross-over point, in line with previous amplitude modulation findings. Conversely, a low number of UMZs corresponds to a large-scale sweep event in the log-region and decreased turbulent activity away from the wall. Earlier studies have reported the existence of alternating large high- and low-speed structures in the log region that meander in the spanwise direction (Hutchins and Marusic, 2007a; Dennis and Nickels, 2011; Jiménez, 2013, among others). Based on these observations, the organisation of the boundary layer into a high or low number of zones can be considered the result of a low- or high-momentum structure moving through the measurement plane respectively. In terms of temporal evolution, it was shown that the presence of a given number of zones is a viscous-scaled phenomenon in time, while the much longer transition from one extreme to the other (high to low N_{UMZ} or vice-versa) could be indicative of the presence of the large-scale log events linked to each scenario respectively. Residence times of individual UMZs (tracked in time based on their modal velocities), indicate that there is a scaling with wall-normal location as suggested by Adrian et al. (2000), with larger zones being located closer to the freestream and moving faster. Furthermore, the events that resided within the FOV for the longest times belonged in their majority to a low-zone-number structuring, while the zones present in high-zone-number cases, exhibited shorter residence times. This behaviour reflects a decrease of time-coherence for conditions that simulate a higher Reynolds number flow. Finally, for all detected UMZs, the corresponding residence times were shown to be much shorter ($\sim \delta/U_\infty$) than the large-scale structures found in boundary layers, thus indicating either very long structures meandering in the spanwise direction or a streamwise alignment of much shorter events. Based on these observations, future research could be directed at datasets of much longer streamwise extent in order to facilitate such a distinction. Also, similar analysis of time-resolved spanwise–wall-normal velocity snapshots could elucidate the spanwise behaviour and extent of UMZs and potentially provide a physical description of what could only be a conceptual interpretation.

Finally, an effort was made to link these observations on the velocity structures, with the spatial organisation of pressure fluctuations. It was shown that a high number of UMZs in the flow is associated with an increase of pressure rms values and a larger coherence of pressure fluctuations in both the streamwise and vertical direction. On the other hand a low number of zones is

linked with decreased pressure activity, which is also slightly less coherent in space. Conditional pressure profiles across both the external (TNTI) and internal layers indicate a pressure drop below the interfaces, reflecting the presence of low-pressure vortical structures, which becomes more prominent when the zone rank and consequently the number of zones increases, in accordance with the model of hairpin vortices and their packets suggested by Adrian et al. (2000). Future work could be aimed at exploring these initial statistical observations, in pressure data of a higher accuracy, in order to analyse further the time-evolution of the pressure fluctuations across the internal layers and their possible effect on entrainment and boundary layer growth.

References

Adrian, R. J., Meinhart, C. D., and Tomkins, C. D. (2000). Vortex organization in the outer region of the turbulent boundary layer. *Journal of Fluid Mechanics*, 422:1–54.

Adrian, R. J. and Westerweel, J. (2011). *Particle Image Velocimetry*. Cambridge University Press.

Ahn, J., Lee, J. H., Lee, J., Kang, J.-h., and Sung, H. J. (2015). Direct numerical simulation of a 30R long turbulent pipe flow at Re_τ= 3008. *Physics of Fluids*, 27(6).

Albertson, J. D., Katul, G. G., Parlange, M. B., and Eichinger, W. E. (1998). Spectral scaling of static pressure fluctuations in the atmospheric surface layer: The interaction between large and small scales. *Physics of Fluids*, 10(7):1725–1732.

Alexopoulos, C. C. and Keffer, J. F. (1971). Turbulent wake in a passively stratified field. *Physics of Fluids*, 14(2):216–224.

Balakumar, B. and Adrian, R. (2007). Large- and very-large-scale motions in channel and boundary-layer flows. *Philosophical Transactions of the Royal Society A: Mathematical, Physical and Engineering Sciences*, 365(1852):665–681.

Baltzer, J. R., Adrian, R. J., and Wu, X. (2013). Structural organization of large and very large scales in turbulent pipe flow simulation. *Journal of Fluid Mechanics*, 720:236–279.

Barenblatt, G. I. (1993). Scaling laws for fully developed turbulent shear flows. Part 1. Basic hypotheses and analysis. *Journal of Fluid Mechanics*, 248:513–520.

Barenblatt, G. I. and Prostokishin, V. M. (1993). Scaling laws for fully developed turbulent shear flows. Part 2. Processing of experimental data. *Journal of Fluid Mechanics*, 248:521–529.

Batchelor, G. K. (1951). Pressure fluctuations in isotropic turbulence. *Mathematical Proceedings of the Cambridge Philosophical Society*, 47:359–374.

Bhaganagar, K., Coleman, G., and Kim, J. (2007). Effect of roughness on pressure fluctuations in a turbulent channel flow. *Physics of Fluids (1994-present)*, 19(2):028103.

Bisset, D. K., Hunt, J. C. R., and Rogers, M. M. (2002). The turbulent/non-turbulent interface bounding a far wake. *Journal of Fluid Mechanics*, 451:383–410.

Blake, W. K. (1970). Turbulent boundary-layer wall-pressure fluctuations on smooth and rough walls. *Journal of Fluid Mechanics*, 44:637–660.

Blinde, P., Michaelis, D., van Oudheusden B., Weiss, P., de Kat, R., Laskari, A., Jeon, Y. J., David, L., Schanz, D., Huhn, F., Gesemann, S., Novara, M., McPhaden, C., Neeteson, N., Rival, D., Schneiders, J. F. G., and Schrijer, F. (2016). Comparative assessment of PIV-based pressure evalutaion techniques applied to a transonic base flow. In *Proc. of the 18th Int Symp on Applications of Laser Techniques to Fluid Mechanics*, Lisbon, Portugal.

Bogey, C. and Bailly, C. (2007). An analysis of the correlations between the turbulent flow and the sound pressure fields of subsonic jets. *Journal of Fluid Mechanics*, 583:71–97.

Borrell, B., Sillero, J., and Jiménez, J. (2013). A code for direct numerical simulation of turbulent boundary layers at high Reynolds numbers in BG/P supercomputers. *Computers & Fluids*, 80:37–43. Selected contributions of the 23rd International Conference on Parallel Fluid Dynamics ParCFD2011.

Borrell, G. and Jiménez, J. (2016). Properties of the turbulent/non-turbulent interface in boundary layers. *Journal of Fluid Mechanics*, 801:554–596.

Brachet, M. E. (1991). Direct simulation of three-dimensional turbulence in the Taylor's Green vortex. *Fluid Dynamics Research*, 8(1-4):1.

Brown, G. and Roshko, A. (1974). On density effects and large structure in turbulent mixing layers. *Journal of Fluid Mechanics*, 64:775–816.

Brown, G. L. and Thomas, A. S. W. (1977). Large structure in a turbulent boundary layer. *Physics of Fluids (1958-1988)*, 20(10):S243–S252.

Charonko, J., King, C., Smith, B., and Vlachos, P. (2010). Assessment of pressure field calculations from particle image velocimetry measurements. *Measurement Science and Technology*, 21(10):105401.

Chauhan, K., Nagib, H., and Monkewitz, P. (2007). Evidence on non-universality of Kármán constant. In *Progress in Turbulence II*, volume 109 of *Springer Proceedings in Physics*, pages 159–163. Springer Berlin Heidelberg.

Chauhan, K., Philip, J., de Silva, C. M., Hutchins, N., and Marusic, I. (2014a). The turbulent/non-turbulent interface and entrainment in a boundary layer. *Journal of Fluid Mechanics*, 742:119–151.

Chauhan, K., Philip, J., and Marusic, I. (2014b). Scaling of the turbulent/non-turbulent interface in boundary layers. *Journal of Fluid Mechanics*, 751:298–328.

Chen, C.-H. P. and Blackwelder, R. F. (1978). Large-scale motion in a turbulent boundary layer: a study using temperature contamination. *Journal of Fluid Mechanics*, 89:1–31.

Chini, G. P., Montemuro, B., White, C. M., and Klewicki, J. (2017). A self-sustaining process model of inertial layer dynamics in high reynolds number turbulent wall flows. *Philosophical Transactions of the Royal Society of London A: Mathematical, Physical and Engineering Sciences*, 375(2089).

Corcos, G. M. (1963). Resolution of pressure in turbulence. *The Journal of the Acoustical Society of America*, 35(2):192–199.

Corino, E. R. and Brodkey, R. (1969). A visual investigation of the wall region in turbulent flow. *Journal of Fluid Mechanics*, 37:1–30.

Corrsin, S. and Kistler, A. L. (1955). Free-stream boundaries of turbulent flows. Technical report, NACA.

da Silva, C. B. and dos Reis, R. J. N. (2011). The role of coherent vortices near the turbulent/non-turbulent interface in a planar jet. *Philosophical Transactions of the Royal Society of London A: Mathematical, Physical and Engineering Sciences*, 369(1937):738–753.

da Silva, C. B., dos Reis, R. J. N., and Pereira, J. C. F. (2011). The intense vorticity structures near the turbulent/non-turbulent interface in a jet. *Journal of Fluid Mechanics*, 685:165–190.

da Silva, C. B., Hunt, J. C., Eames, I., and Westerweel, J. (2014a). Interfacial layers between regions of different turbulence intensity. *Annual Review of Fluid Mechanics*, 46(1):567–590.

da Silva, C. B. and Taveira, R. R. (2010). The thickness of the turbulent/nonturbulent interface is equal to the radius of the large vorticity structures near the edge of the shear layer. *Physics of Fluids*, 22(12):121702.

da Silva, C. B., Taveira, R. R., and Borrell, G. (2014b). Characteristics of the turbulent/non-turbulent interface in boundary layers, jets and shear-free turbulence. *Journal of Physics: Conference Series*, 506(1):012015.

Dahm, W. J. A. and Dimotakis, P. E. (1987). Measurements of entrainment and mixing in turbulent jets. *AIAA Journal*, 25(9):1216–1223.

Davidson, P. A. (2004). *Turbulence: an introduction for scientists and engineers*. Oxford University Press, USA.

Davoust, S. and Jacquin, L. (2011). Taylor's hypothesis convection velocities from mass conservation equation. *Physics of Fluids (1994-present)*, 23(5):051701.

de Kat, R. and Ganapathisubramani, B. (2013). Pressure from particle image velocimetry for convective flows: a Taylor's hypothesis approach. *Measurement Science and Technology*, 24:024002.

de Kat, R. and van Oudheusden, B. (2012). Instantaneous planar pressure determination from PIV in turbulent flow. *Experiments in Fluids*, 52(5):1089–1106.

de Kat, R., van Oudheusden, B., and Scarano, F. (2008). Instantaneous planar pressure field determination around a square-section cylinder based on time-resolved stereo-PIV. In *Proc. of the 14th Int Symp on Applications of Laser Techniques to Fluid Mechanics*, Lisbon, Portugal.

de Silva, C., Marusic, I., and Hutchins, N. (2014). Regions of uniform streamwise momentum in turbulent boundary layers. In *Proc. of the 19th Australasian Fluid Mechanics Conference*, Melbourne, Australia.

de Silva, C. M., Hutchins, N., and Marusic, I. (2016). Uniform momentum zones in turbulent boundary layers. *Journal of Fluid Mechanics*, 786:309–331.

de Silva, C. M., Philip, J., Chauhan, K., Meneveau, C., and Marusic, I. (2013). Multiscale geometry and scaling of the turbulent-nonturbulent interface in high reynolds number boundary layers. *Physical Review Letters*, 111:044501.

de Silva, C. M., Philip, J., Hutchins, N., and Marusic, I. (2017). Interfaces of uniform momentum zones in turbulent boundary layers. *Journal of Fluid Mechanics*, 820:451–478.

del Álamo, J. and Jiménez, J. (2009). Estimation of turbulent convection velocities and corrections to Taylor's approximation. *Journal of Fluid Mechanics*, 640:5–26.

Dennis, D. J. C. and Nickels, T. B. (2011). Experimental measurement of large-scale three-dimensional structures in a turbulent boundary layer. Part 2. Long structures. *Journal of Fluid Mechanics*, 673:218–244.

DeVoria, A. C., Carr, Z. R., and Ringuette, M. J. (2014). On calculating forces from the flow field with application to experimental volume data. *Journal of Fluid Mechanics*, 749:297–319.

Douady, S., Couder, Y., and Brachet, M. E. (1991). Direct observation of the intermittency of intense vorticity filaments in turbulence. *Physics Review Letters*, 67:983–986.

Eisma, J., Westerweel, J., Ooms, G., and Elsinga, G. E. (2015). Interfaces and internal layers in a turbulent boundary layer. *Physics of Fluids*, 27(5):055103.

Elliott, J. A. (1972). Microscale pressure fluctuations measured within the lower atmospheric boundary layer. *Journal of Fluid Mechanics*, 53:351–384.

Elsinga, G., Poelma, C., Schrder, A., Geisler, R., F., S., and Westerweel, J. (2012). Tracking of vortices in a turbulent boundary layer. *Journal of Fluid Mechanics*, 697:273–295.

Elsinga, G., Scarano, F., Wieneke, B., and van Oudheusden, B. (2006). Tomographic particle image velocimetry. *Experiments in Fluids*, 41(6):933–947.

Elsinga, G. E. and Marusic, I. (2010). Evolution and lifetimes of flow topology in a turbulent boundary layer. *Physics of Fluids*, 22(1):015102.

Fabris, G. (1979). Conditional sampling study of the turbulent wake of a cylinder. Part 1. *Journal of Fluid Mechanics*, 94:673–709.

Farabee, T. M. and Casarella, M. J. (1991). Spectral features of wall pressure fluctuations beneath turbulent boundary layers. *Physics of Fluids A: Fluid Dynamics (1989-1993)*, 3(10):2410–2420.

Favre, A., Gaviglio, J., and Dumas, R. (1955). Some measurements of time and space correlation in wind tunnel. Technical Report NACA-TM-1370, National Advisory Committee for Aeronautics, Washington, DC, United States.

Fernholz, H. H., Janke, G., Schober, M., Wagner, P., and Warnack, D. (1996). New developments and applications of skin-friction measuring techniques. *Measurement Science and Technology*, 7(10):1396.

Ferré, J. A., Mumford, J. C., Savill, A. M., and Giralt, F. (1990). Three-dimensional large-eddy motions and fine-scale activity in a plane turbulent wake. *Journal of Fluid Mechanics*, 210:371–414.

Fisher, M. and Davies, P. (1964). Correlation measurements in a non-frozen pattern of turbulence. *Journal of Fluid Mechanics*, 18:97–116.

Flores, O. and Jiménez, J. (2010). Hierarchy of minimal flow units in the logarithmic layer. *Physics of Fluids*, 22(7):071704.

Foucaut, J., Carlier, J., and Stanislas, M. (2004). PIV optimization for the study of turbulent flow using spectral analysis. *Measurement Science and Technology*, 15(6):1046.

Fujisawa, N., Tanahashi, S., and Srinivas, K. (2005). Evaluation of pressure field and fluid forces on a circular cylinder with and without rotational oscillation using velocity data from PIV measurement. *Measurement Science and Technology*, 16(4):989.

Ganapathisubramani, B., Hutchins, N., Hambleton, W. T., Longmire, E. K., and Marusic, I. (2005). Investigation of large-scale coherence in a turbulent boundary layer using two-point correlations. *Journal of Fluid Mechanics*, 524:57–80.

Ganapathisubramani, B., Hutchins, N., Monty, J. P., Chung, D., and Marusic, I. (2012). Amplitude and frequency modulation in wall turbulence. *Journal of Fluid Mechanics*, 712:61–91.

Ganapathisubramani, B., Longmire, E., and Marusic, I. (2003). Characteristics of vortex packets in turbulent boundary layers. *Journal of Fluid Mechanics*, 478:35–46.

Gao, Q., Ortiz-Dueas, C., and Longmire, E. (2013). Evolution of coherent structures in turbulent boundary layers based on moving tomographic PIV. *Experiments in Fluids*, 54(12):1–16.

Geng, C., He, G., Wang, Y., Xu, C., Lozano-Durán, A., and Wallace, J. M. (2015). Taylor's hypothesis in turbulent channel flow considered using a transport equation analysis. *Physics of Fluids (1994-present)*, 27(2):025111.

George, W. K., Beuther, P. D., and Arndt, R. (1984). Pressure spectra in turbulent free shear flows. *Journal of Fluid Mechanics*, 148:155–191.

George, W. K. and Castillo, L. (1997). Zero Pressure Gradient Turbulent Boundary Layer. *Applied Mechanics Reviews*, 50(12):689–729.

Ghaemi, S., Ragni, D., and Scarano, F. (2012). PIV-based pressure fluctuations in the turbulent boundary layer. *Experiments in Fluids*, 53(6):1823–1840.

Ghaemi, S. and Scarano, F. (2013). Turbulent structure of high-amplitude pressure peaks within the turbulent boundary layer. *Journal of Fluid Mechanics*, 735:381–426.

Goldstein, M. (1984). Aeroacoustics of turbulent shear flows. *Annual Review of Fluid Mechanics*, 16(1):263–285.

Graham, J., Lee, M., Malaya, N., Moser, R., Eyink, G., Meneveau, C., Kanov, K., Burns, R., and Szalay, A. (2013). Turbulent channel data set available at: http://turbulence.pha.jhu.edu/docs/readme-channel.pdf.

Grönholm, T. and Annila, A. (2007). Natural distribution. *Mathematical Biosciences*, 210(2):659– 667.

Guala, M., Hommema, S. E., and Adrian, R. J. (2006). Large-scale and very-large-scale motions in turbulent pipe flow. *Journal of Fluid Mechanics*, 554:521–542.

Gurka, R., Liberzon, A., Hefetz, D., Rubinstein, D., and Shavit, U. (1999). Computation of pressure distribution using PIV velocity data. In *Proc. of the 3rd International Workshop on Particle Image Velocimetry*, Santa Barbara, CA.

Harrison, M. (1958). *Pressure fluctuations on the wall adjacent to a turbulent boundary layer*. Washington, D.C. Dept. of the Navy, David Taylor Model Basin.

Head, M. R. and Bandyopadhyay, P. (1981). New aspects of turbulent boundary-layer structure. *Journal of Fluid Mechanics*, 107:297–338.

Hellström, L. H. O., Ganapathisubramani, B., and Smits, A. J. (2015). The evolution of large-scale motions in turbulent pipe flow. *Journal of Fluid Mechanics*, 779:701–715.

Herpin, S., Stanislas, M., and Soria, J. (2010). The organization of near-wall turbulence: a comparison between boundary layer SPIV data and channel flow dns data. *Journal of Turbulence*, 11(47):1–10.

Hoyas, S. and Jiménez, J. (2006). Scaling of the velocity fluctuations in turbulent channels up to $Re_\tau = 2003$. *Physics of Fluids*, 18(1):011702.

Hunt, J. C., Eames, I., and Westerweel, J. (2006). Mechanics of inhomogeneous turbulence and interfacial layers. *Journal of Fluid Mechanics*, 554:499–519.

Hunt, J. C. R., Eames, I., da Silva, C. B., and Westerweel, J. (2011). Interfaces and inhomogeneous turbulence. *Philosophical Transactions of the Royal Society of London A: Mathematical, Physical and Engineering Sciences*, 369(1937):811–832.

Hurther, D., Lemmin, U., and Terray, E. A. (2007). Turbulent transport in the outer region of rough-wall open-channel flows: the contribution of large coherent shear stress structures (lc3s). *Journal of Fluid Mechanics*, 574:465–493.

Hutchins, N. and Marusic, I. (2007a). Evidence of very long meandering features in the logarithmic region of turbulent boundary layers. *Journal of Fluid Mechanics*, 579:1–28.

Hutchins, N. and Marusic, I. (2007b). Large-scale influences in near-wall turbulence. *Philosophical Transactions of the Royal Society A: Mathematical, Physical and Engineering Sciences*, 365(1852):647–664.

Hutchins, N., Monty, J. P., Ganapathisubramani, B., Ng, H. C. H., and Marusic, I. (2011). Three-dimensional conditional structure of a high-Reynolds-number turbulent boundary layer. *Journal of Fluid Mechanics*, 673:255–285.

Hutchins, N., Nickels, T. B., Marusic, I., and Chong, M. (2009). Hot-wire spatial resolution issues in wall-bounded turbulence. *Journal of Fluid Mechanics*, 635:103–136.

Ishihara, T., Ogasawara, H., and Hunt, J. C. (2015). Analysis of conditional statistics obtained near the turbulent/non-turbulent interface of turbulent boundary layers. *Journal of Fluids and Structures*, 53:50–57. Special Issue on Unsteady Separation in Fluid-Structure Interaction–II.

Jakirlić, S. and Hanjalić, S. (2013). A direct numerical simulation-based re-examination of coefficients in the pressurestrain models in second-moment closures. *Fluid Dynamics Research*, 45(5):055509.

Jakobsen, M., Dewhirst, T., and Greated, C. (1997). Particle image velocimetry for predictions of acceleration fields and force within fluid flows. *Measurement Science and Technology*, 8(12):1502.

JCGM 100:2008 (2008). *Evaluation of measurement data Guide to the expression of uncertainty in measurement (GUM 1995 with minor corrections)*, Paris.

Jiménez, J. (2013). Near-wall turbulence. *Physics of Fluids*, 25(10):101302.

Jiménez, J., Kawahara, G., Simens, M. P., Nagata, M., and Shiba, M. (2005). Characterization of near-wall turbulence in terms of equilibrium and 'bursting' solutions. *Physics of Fluids*, 17(1):015105.

Jiménez, J. and Moin, P. (1991). The minimal flow unit in near-wall turbulence. *Journal of Fluid Mechanics*, 225:213–240.

Jiménez, J., Moin, P., Moser, R., and Keefe, L. (1988). Ejection mechanisms in the sublayer of a turbulent channel. *Physics of Fluids (1958-1988)*, 31(6):1311–1313.

Jiménez, J. and Pinelli, A. (1999). The autonomous cycle of near-wall turbulence. *Journal of Fluid Mechanics*, 389:335–359.

Johansson, A. V., Alfredsson, P. H., and Kim, J. (1991). Evolution and dynamics of shear-layer structures in near-wall turbulence. *Journal of Fluid Mechanics*, 224:579–599.

Johansson, A. V., Her, J.-Y., and Haritonidis, J. H. (1987). On the generation of high-amplitude wall-pressure peaks in turbulent boundary layers and spots. *Journal of Fluid Mechanics*, 175:119–142.

Jones, B. G., Adrian, R. J., Nithianandan, C. K., and Planchon Jr., H. P. (1979). Spectra of turbulent static pressure fluctuations in jet mixing layers. *AIAA Journal*, 17(5):449–457.

Khashehchi, M., Ooi, A., Soria, J., and Marusic, I. (2013). Evolution of the turbulent/non-turbulent interface of an axisymmetric turbulent jet. *Experiments in Fluids*, 54(1):1449.

Kida, S. and Miura, H. (1998). Identification and analysis of vortical structures. *European Journal of Mechanics - B/Fluids*, 17(4):471–488. Special Issue Dynamics and Statistics of Concentrated Vortices in Turbulent Flow (Euromech Colloquium 364).

Kim, H. T., Kline, S. J., and Reynolds, W. C. (1971). The production of turbulence near a smooth wall in a turbulent boundary layer. *Journal of Fluid Mechanics*, 50:133–160.

Kim, J. (1989). On the structure of pressure fluctuations in simulated turbulent channel flow. *Journal of Fluid Mechanics*, 205:421–451.

Kim, J., Choi, J.-I., and Sung, H. J. (2002). Relationship between wall pressure fluctuations and streamwise vortices in a turbulent boundary layer. *Physics of Fluids*, 14(2):898–901.

Kim, J. and Hussain, F. (1993). Propagation velocity of perturbations in turbulent channel flow. *Physics of Fluids A: Fluid Dynamics (1989-1993)*, 5(3):695–706.

Kim, J. and Sung, H. (2006). Wall pressure fluctuations and flow-induced noise in a turbulent boundary layer over a bump. *Journal of Fluid Mechanics*, 558:79–102.

Kim, K. C. and Adrian, R. J. (1999). Very large-scale motion in the outer layer. *Physics of Fluids (1994-present)*, 11(2):417–422.

Klewicki, J., Fife, P., Wei, T., and McMurtry, P. (2007). A physical model of the turbulent boundary layer consonant with mean momentum balance structure. *Philosophical Transactions of the Royal Society A: Mathematical, Physical and Engineering Sciences*, 365(1852):823–840.

Klewicki, J. C. (2010). Reynolds Number Dependence, Scaling, and Dynamics of Turbulent Boundary Layers. *Journal of Fluids Engineering*, 132:094001.

Kline, S. J., Reynolds, W. C., Schraub, F. A., and Runstadler, P. (1967). The structure of turbulent boundary layers. *Journal of Fluid Mechanics*, 30:741–773.

Kobashi, Y. (1957). Measurements of pressure fluctuation in the wake of cylinder. *Journal of the Physical Society of Japan*, 12(5):533–543.

Kolmogorov, A. (1941). The local structure of turbulence in incompressible viscous fluid for very large reynolds numbers. *Akademiia Nauk SSSR Doklady*, 30:301–305.

Kovasznay, L. S. G., Kibens, V., and Blackwelder, R. F. (1970). Large-scale motion in the intermittent region of a turbulent boundary layer. *Journal of Fluid Mechanics*, 41:283–325.

Krögstad, P.-Å., Kaspersen, J., and Rimestad, S. (1998). Convection velocities in a turbulent boundary layer. *Physics of Fluids*, 10(4):949–957.

Kwon, Y. S., Hutchins, N., and Monty, J. P. (2016). On the use of the Reynolds decomposition in the intermittent region of turbulent boundary layers. *Journal of Fluid Mechanics*, 794:5–16.

Kwon, Y. S., Philip, J., de Silva, C. M., Hutchins, N., and Monty, J. P. (2014). The quiescent core of turbulent channel flow. *Journal of Fluid Mechanics*, 751:228–254.

LaRue, J. C. and Libby, P. A. (1974). Temperature fluctuations in the plane turbulent wake. *Physics of Fluids*, 17(11):1956–1967.

Laskari, A., de Kat, R., and Ganapathisubramani, B. (2014). Full-field pressure from 3D PIV snapshots in convective turbulent flow. In *Proc. of the 17th Int Symp on Applications of Laser Techniques to Fluid Mechanics*, Lisbon, Portugal.

Laskari, A., de Kat, R., and Ganapathisubramani, B. (2015). Pressure field estimation in convective turbulent flows from 3D PIV velocity fields. In *Proc. of the 11th Int Symp on Particle Image Velocitmetry*, Santa Barbara, California.

Laskari, A., de Kat, R., and Ganapathisubramani, B. (2016). Full-field pressure from snapshot and time-resolved volumetric PIV. *Experiments in Fluids*, 57(3):1–14.

Launder, B. E., Reece, G. J., and Rodi, W. (1975). Progress in the development of a Reynolds-stress turbulence closure. *Journal of Fluid Mechanics*, 68:537–566.

Lee, J. H. and Sung, H. J. (2011). Very-large-scale motions in a turbulent boundary layer. *Journal of Fluid Mechanics*, 673:80–120.

LeHew, J., Guala, M., and McKeon, B. (2013). Time-resolved measurements of coherent structures in the turbulent boundary layer. *Experiments in Fluids*, 54(4):1508.

Li, Y., Perlman, E., Wan, M., Yang, Y., Meneveau, C., Burns, R., Chen, S., Szalay, A., and Eyink, G. (2008). A public turbulence database cluster and applications to study Lagrangian evolution of velocity increments in turbulence. *Journal of Turbulence*, 9(31):1–29.

Limpert, E. and Stahel, W. A. (2011). Problems with using the normal distribution—and ways to improve quality and efficiency of data analysis. *PLOS ONE*, 6(7):1–8.

Limpert, E., Stahel, W. A., and Abbt, M. (2001). Log-normal distributions across the sciences: Keys and clues. *BioScience*, 51(5):341–352.

Lin, C. (1953). On Taylor's Hypothesis and the acceleration terms in the Navier-Stokes equations. *Quarterly of Applied Mathematics*, 10(4):295–306.

Liu, X. and Katz, J. (2006). Instantaneous pressure and material acceleration measurements using a four-exposure PIV system. *Experiments in Fluids*, 41(2):227–240.

Lozano Duran, A., Flores, O., and Jimenez, J. (2012). The three-dimensional structure of momentum transfer in turbulent channels. *Journal of Fluid Mechanics*, 694:100–130.

Lozano-Durán, A. and Jiménez, J. (2011). Time-resolved evolution of the wall-bounded vorticity cascade. *Journal of Physics: Conference Series*, 318(6):062016.

Lumley, J. L. (1979). Computational modeling of turbulent flows. In Yih, C.-S., editor, *Advances in Applied Mechanics*, volume 18 of *Advances in Applied Mechanics*, pages 123–176. Elsevier.

Lumley, J. L., Marshak, R. E., and Panofsky, H. A. (1964). *The structure of atmospheric turbulence*. New York : Interscience Publishers.

Maaloum, A., Kouidri, S., and Rey, R. (2004). Aeroacoustic performance evaluation of axial flow fans based on the unsteady pressure field on the blade surface. *Applied Acoustics*, 65(4):367 – 384.

Mansour, N. N., Kim, J., and Moin, P. (1988). Reynolds-stress and dissipation-rate budgets in a turbulent channel flow. *Journal of Fluid Mechanics*, 194:15–44.

Marusic, I., Mathis, R., and Hutchins, N. (2010a). Predictive model for wall-bounded turbulent flow. *Science*, 329(5988):193–196.

Marusic, I., McKeon, B. J., Monkewitz, P. A., Nagib, H. M., Smits, A. J., and Sreenivasan, K. R. (2010b). Wall-bounded turbulent flows at high Reynolds numbers: Recent advances and key issues. *Physics of Fluids (1994-present)*, 22:065103.

Marusic, I., Monty, J. P., Hultmark, M., and Smits, A. J. (2013). On the logarithmic region in wall turbulence. *Journal of Fluid Mechanics*, 716:1–11.

Mathis, R., Hutchins, N., and Marusic, I. (2009). Large-scale amplitude modulation of the small-scale structures in turbulent boundary layers. *Journal of Fluid Mechanics*, 628:311–337.

McKeon, B. J. (2013). Natural logarithms. *Journal of Fluid Mechanics*, 718:1–4.

McKeon, B. J., Li, J., Jiang, W., Morrison, J. F., and Smits, A. (2004). Further observations on the mean velocity distribution in fully developed pipe flow. *Journal of Fluid Mechanics*, 501:135–147.

Meinhart, C. D. and Adrian, R. J. (1995). On the existence of uniform momentum zones in a turbulent boundary layer. *Physics of Fluids*, 7(4):694–696.

Melling, A. (1997). Tracer particles and seeding for particle image velocimetry. *Measurement Science and Technology*, 8(12):1406.

Mistry, D., Philip, J., Dawson, J. R., and Marusic, I. (2016). Entrainment at multi-scales across the turbulent/non-turbulent interface in an axisymmetric jet. *Journal of Fluid Mechanics*, 802:690–725.

Monin, A. S., Iaglom, A. M., and Lumley, J. L. (1975). *Statistical fluid mechanics : mechanics of turbulence. vol. 2*. MIT press, Cambridge, MA, London.

Monty, J. (2005). *Developments In Smooth Wall Turbulent Duct Flows*. PhD thesis, University of Melbourne.

Morris, S., Stolpa, S. R., Slaboch, P. E., and Klewicki, J. C. (2007). Near-surface particle image velocimetry measurements in a transitionally rough-wall atmospheric boundary layer. *Journal of Fluid Mechanics*, 580:319–338.

Mull, H. R. and Algranti, J. S. (1956). *Preliminary flight survey of aerodynamic noise on an airplane wing*. National Advisory Committee for Aeronautics, Washington, D.C.

Nagib, H. M., Chauhan, K., and Monkewitz, P. A. (2007). Approach to an asymptotic state for zero pressure gradient turbulent boundary layers. *Philosophical Transactions of the Royal Society A: Mathematical, Physical and Engineering Sciences*, 365(1852):755–770.

Nagib, H. M. and Chauhan, K. A. (2008). Variations of von Kármán coefficient in canonical flows. *Physics of Fluids (1994-present)*, 20(10):101518.

Naka, Y., Stanislas, M., Foucaut, J.-M., Coudert, S., Laval, J.-P., and Obi, S. (2015). Space-time pressure-velocity correlations in a turbulent boundary layer. *Journal of Fluid Mechanics*, 771:624–675.

Naughton, J. and Sheplak, M. (2002). Modern developments in shear-stress measurement. *Progress in Aerospace Sciences*, 38(67):515–570.

Ng, H. C. H., Marusic, I., Monty, J. P., Hutchins, N., and Chong, M. S. (2007). Oil film interferometry in high Reynolds number turbulent boundary layers. In *Proc. of the 16th Australasian Fluid Mechanics Conference (AFMC)*, Victoria, Australia. School of Engineering, The University of Queensland.

Noca, F., Shiels, D., and Jeon, D. (1997). Measuring instanteneous fluid dynamic forces on bodies, using only velocity fields and their derivatives. *Journal of Fluids and Structures*, 11(3):345–350.

Offen, G. R. and Kline, S. J. (1975). A proposed model of the bursting process in turbulent boundary layers. *Journal of Fluid Mechanics*, 70:209–228.

Österlund, J., Johansson, A., Nagib, H., and Hites, M. (2000). A note on the overlap region in turbulent boundary layers. *Physics of Fluids*, 12(1):1–4.

Patwardhan, S. S. and Ramesh, O. N. (2014). Scaling of pressure spectrum in turbulent boundary layers. *Journal of Physics: Conference Series*, 506(1):012011.

Perlman, E., Burns, R., Li, Y., and Meneveau, C. (2007). Data exploration of turbulence simulations using a database cluster. In *Supercomputing, 2007. SC '07. Proceedings of the 2007 ACM/IEEE*, pages 1–11.

Perry, A. E. and Chong, M. S. (1982). On the mechanism of wall turbulence. *Journal of Fluid Mechanics*, 119:173–217.

Philip, J., Meneveau, C., de Silva, C. M., and Marusic, I. (2014). Multiscale analysis of fluxes at the turbulent/non-turbulent interface in high Reynolds number boundary layers. *Physics of Fluids*, 26(1):015105.

Phillips, O. M. (1955). The irrotational motion outside a free turbulent boundary. *Mathematical Proceedings of the Cambridge Philosophical Society*, 51:220–229.

Pope, S. (2000). *Turbulent Flows*. Cambridge University Press.

Praturi, A. K. and Brodkey, R. S. (1978). A stereoscopic visual study of coherent structures in turbulent shear flow. *Journal of Fluid Mechanics*, 89(2):251–272.

Pumir, A. (1994). A numerical study of pressure fluctuations in three dimensional, incompressible, homogeneous, isotropic turbulence. *Physics of Fluids (1994-present)*, 6(6):2071–2083.

Raffel, M., Willert, C., Wereley, S., and Kompenhans, J. (2007). *Particle Image Velocimetry: A Practical Guide*. Experimental Fluid Mechanics. Springer Berlin Heidelberg.

Rogers, M. M. (1986). *The structure and modeling of the hydrodynamic and passive scalar fields in homogeneous turbulent shear flow*. PhD thesis, Stanford University.

Rotta, J. (1951). Statistische theorie nichthomogener turbulenz. *Zeitschrift für Physik*, 129(6):547–572.

Scarano, F. (2013). Tomographic PIV: principles and practice. *Measurement Science and Technology*, 24(1):012001.

Schanz, D., Gesemann, S., and Schröder, A. (2016). Shake-the-box: Lagrangian particle tracking at high particle image densities. *Experiments in Fluids*, 57(5):70.

Schanz, D., Schröder, A., and Gesemann, S. (2014). 'Shake the box' - a 4D-PTV algorithm: Accurate and ghostless reconstruction of Lagrangian tracks in densely seeded flows. In *Proc. of the 16th Int Symp on Applications of Laser Techniques to Fluid Mechanics*, Lisbon, Portugal.

Schanz, D., Schröder, A., Gesemann, S., Michaelis, D., and Wieneke, B. (2013). 'Shake the box': A highly efficient and accurate Tomographic Particle Tracking Velocimetry (Tomo-PTV) method using prediction of particle positions. In *Proc. of the 10th Int Symp on Particle Image Velocimetry*, Delft, The Netherlands.

Schoppa, W. and Hussain, F. (2002). Coherent structure generation in near-wall turbulence. *Journal of Fluid Mechanics*, 453:57–108.

Siddon, T. E. (1969). On the response of pressure measuring instrumentation in unsteady flow. *UTIAS Report, No. 136*.

Sillero, J., Jiménez, J., and Moser, R. (2013). One-point statistics for turbulent wall-bounded flows at Reynolds numbers up to $\delta^+ \approx 2000$. *Physics of Fluids*, 25(10):105102.

Sillero, J., Jiménez, J., and Moser, R. (2014). Two-point statistics for turbulent boundary layers and channels at Reynolds numbers up to $\delta^+ \approx 2000$. *Physics of Fluids*, 26(10):105109.

Simens, M. P., Jiménez, J., Hoyas, S., and Mizuno, Y. (2009). A high-resolution code for turbulent boundary layers. *J. Comput. Phys.*, 228(11):4218–4231.

Smits, A. J., McKeon, B. J., and Marusic, I. (2011). High Reynolds number wall turbulence. *Annual Review of Fluid Mechanics*, 43(1):353–375.

Soloff, S. M., Adrian, R. J., and Liu, Z.-C. (1997). Distortion compensation for generalized stereoscopic particle image velocimetry. *Measurement Science and Technology*, 8(12):1441.

Spalding, D. (1961). A single formula for the law of the wall. *Journal of Applied Mechanics*, 28(3):455–458.

Speziale, C. G. (1991). Analytical methods for the development of Reynolds-stress closures in turbulence. *Annu. Rev. Fluid Mech.*, 23(1):107–157.

Speziale, C. G., Gatski, T. B., and Sarkar, S. (1992). On testing models for the pressure-strain correlation of turbulence using direct simulations. *Physics of Fluids A*, 4(12):2887–2899.

Sreenivasan, K. R. and Meneveau, C. (1986). The fractal facets of turbulence. *Journal of Fluid Mechanics*, 173:357–386.

Taveira, R. R. and da Silva, C. B. (2013). Kinetic energy budgets near the turbulent/nonturbulent interface in jets. *Physics of Fluids*, 25(1):015114.

Taylor, G. (1938). The spectrum of turbulence. *Proceedings of the Royal Society of London. Series A - Mathematical and Physical Sciences*, 164(919):476–490.

Terashima, O., Sakai, Y., Nagata, K., Ito, Y., Onishi, K., and Shouji, Y. (2016). Simultaneous measurement of velocity and pressure near the turbulent/non-turbulent interface of a planar turbulent jet. *Experimental Thermal and Fluid Science*, 75:137–146.

Theodorsen, T. (1952). Mechanism of turbulence. In *Proc. of the Midwest Mechanics Symposium*, Columbus, OH.

Tomkins, C. D. and Adrian, R. J. (2005). Energetic spanwise modes in the logarithmic layer of a turbulent boundary layer. *Journal of Fluid Mechanics*, 545:141–162.

Townsend, A. A. (1949). Momentum and energy diffusion in the turbulent wake of a cylinder. *Proceedings of the Royal Society of London A: Mathematical, Physical and Engineering Sciences*, 197(1048):124–140.

Townsend, A. A. (1951). The structure of the turbulent boundary layer. *Mathematical Proceedings of the Cambridge Philosophical Society*, 47:375–395.

Townsend, A. A. (1976). *The structure of turbulent shear flow*. Cambridge University Press Cambridge, New York, 2nd edition.

Tropea, C., Yarin, A., and Foss, J. (2007). *Springer Handbook of Experimental Fluid Mechanics*. Springer Handbook of Experimental Fluid Mechanics. Springer.

Tsuji, Y., Fransson, J., Alfredsson, P., and Johansson, A. (2007). Pressure statistics and their scaling in high-Reynolds-number turbulent boundary layers. *Journal of Fluid Mechanics*, 585:1–40.

Tsuji, Y., Imayama, S., Schlatter, P., Alfredsson, P. H., Johansson, A., Marusic, I., Hutchins, N., and Monty, J. (2012). Pressure fluctuation in high-Reynolds-number turbulent boundary layer: results from experiments and DNS. *Journal of Turbulence*, 13(50):1–19.

Tsuji, Y. and Ishihara, T. (2003). Similarity scaling of pressure fluctuation in turbulence. *Phys. Rev. E*, 68:026309.

Tsuji, Y., Johansson, A., and Marusic, I. (2015). Amplitude modulation of pressure in turbulent boundary layer. In *Proc. of the 9th Int Symp on Turbulence and Shear Flow Phenomena*, Melbourne, Australia.

Turner, J. S. (1986). Turbulent entrainment: the development of the entrainment assumption, and its application to geophysical flows. *Journal of Fluid Mechanics*, 173:431–471.

Tutkun, M., George, W. K., Delville, J., Stanislas, M., Johansson, P. B., Foucaut, J.-M., and Coudert, S. (2009). Two-point correlations in high Reynolds number flat plate turbulent boundary layers. *Journal of Turbulence*, 10(21):1–23.

Uberoi, M. (1953). Quadruple velocity correlations and pressure fluctuations in isotropic turbulence. *Journal of the Aeronautical Sciences (Institute of the Aeronautical Sciences)*, 20(3):197–204.

Vallikivi, M., Ganapathisubramani, B., and Smits, A. J. (2015). Spectral scaling in boundary layers and pipes at very high Reynolds numbers. *Journal of Fluid Mechanics*, 771:303–326.

van Oudheusden, B. (2013). PIV based pressure measurement. *Measurement Science and Technology*, 24(3):032001.

Violato, D., Moore, P., and Scarano, F. (2010). Lagrangian and Eulerian pressure field evaluation of rod–airfoil flow from time-resolved tomographic PIV. *Experiments in Fluids*, 50(4):1057–1070.

Wallace, J. M., Eckelmann, H., and Brodkey, R. S. (1972). The wall region in turbulent shear flow. *Journal of Fluid Mechanics*, 54:39–48.

Wang, G., Senocak, I., Shyy, W., Ikohagi, T., and Cao, S. (2001). Dynamics of attached turbulent cavitating flows. *Progress in Aerospace Sciences*, 37(6):551–581.

Watanabe, T., da Silva, C. B., Sakai, Y., Nagata, K., and Hayase, T. (2016). Lagrangian properties of the entrainment across turbulent/non-turbulent interface layers. *Physics of Fluids*, 28(3):031701.

Wei, T., Fife, P., Klewicki, J., and McMurtry, P. (2005). Properties of the mean momentum balance in turbulent boundary layer, pipe and channel flows. *Journal of Fluid Mechanics*, 522:303–327.

Westerweel, J., Fukushima, C., Pedersen, J. M., and Hunt, J. C. R. (2005). Mechanics of the turbulent-nonturbulent interface of a jet. *Physics Review Letters*, 95:174501.

Westerweel, J., Fukushima, C., Pedersen, J. M., and Hunt, J. C. R. (2009). Momentum and scalar transport at the turbulent/non-turbulent interface of a jet. *Journal of Fluid Mechanics*, 631:199–230.

Wieneke, B. (2008). Volume self-calibration for 3D particle image velocimetry. *Experiments in Fluids*, 45(4):549–556.

Willmarth, W. W. (1956). Wall pressure fluctuations in a turbulent boundary layer. *The Journal of the Acoustical Society of America*, 28(6):1048–1053.

Willmarth, W. W. (1975). Pressure fluctuations beneath turbulent boundary layers. *Annual Review of Fluid Mechanics*, 7(1):13–36.

Winkel, E. S., Elbing, B. R., Ceccio, S. L., Perlin, M., and Dowling, D. R. (2008). High-Reynolds-number turbulent-boundary-layer wall pressure fluctuations with skin-friction reduction by air injection. *The Journal of the Acoustical Society of America*, 123(5):2522–2530.

Wolf, M., Lüthi, B., Holzner, M., Krug, D., Kinzelbach, W., and Tsinober, A. (2012). Investigations on the local entrainment velocity in a turbulent jet. *Physics of Fluids*, 24(10).

Zagarola, M. V. and Smits, A. (1998). Mean-flow scaling of turbulent pipe flow. *Journal of Fluid Mechanics*, 373:33–79.

Zaman, K. and Hussain, A. (1981). Taylor hypothesis and large-scale coherent structures. *Journal of Fluid Mechanics*, 112:379–396.

Zanoun, E.-S., Durst, F., and Nagib, H. (2003). Evaluating the law of the wall in two-dimensional fully developed turbulent channel flows. *Physics of Fluids (1994-present)*, 15(10):3079–3089.

Zheng, S. and Longmire, E. (2014). Perturbing vortex packets in a turbulent boundary layer. *Journal of Fluid Mechanics*, 748:368–398.

Zhou, J., Adrian, R. J., Balachandar, R. S., and Kendall, T. M. (1999). Mechanisms for generating coherent packets of hairpin vortices in channel flow. *Journal of Fluid Mechanics*, 387:353–396.